STRUCTURAL CHEMISTRY OF LEAD-ANTIMONY AND LEAD-BISMUTH SULPHIDES

by

ANICETA SKOWRON

A thesis

submitted to the School of Graduate Studies

in partial fulfilment of the requirements

for the degree

Doctor of Philosophy

McMaster University

January 1991

STRUCTURAL CHEMISTRY OF LEAD-ANTIMONY AND LEAD-BISMUTH SULPHIDES

DOCTOR OF PHILOSOPHY — McMASTER UNIVERSITY

Materials Science and Engineering — Hamilton, Ontario

TITLE: Structural chemistry of lead-antimony and lead-bismuth sulphides.

AUTHOR: Aniceta Skowron

SUPERVISOR: Professor I. D. Brown

NUMBER OF PAGES: xxi, 315

Acknowledgements

I warmly thank Dr I. David Brown for his friendship, stimulation and guidance during all my graduate study.

Also, I thank Dr. R.J.D. Tilley for teaching me the electron microscopy. All the TEM results presented in this thesis were obtained during my research in Dr. R.J.D. Tilley's group.

I greatly appreciate technical assistance with the single crystal X-ray experiments given me by R. Faggiani and financial assistance of the British Council, ICI and McMaster University.

Finally, I thank my family: Krzysztof, for his patience, support and understanding during all these years, my parents and my mother and grandmother-in-law for encouragement and invaluable help at home.

Abstract

The structures in the PbS-rich part of the Ag_2S-PbS-Bi_2S_3 system are composed of PbS-like slabs obtained by twinning the parent PbS (NaCl structure) along the $(311)_{PbS}$ planes. A number of phases, some new and some already encountered in mineral samples, have been found by HREM. In the observed structures the slabs 4 and 7 octahedra wide were the most common. Slabs with width of 8 and 5 octahedra were also encountered, but not those with 6 octahedra. The material was sensitive to the electron beam and the structures often decomposed to galena during the observation. Disappearance of the twin boundary was accompanied by formation of an edge dislocation.

The structures in the PbS-rich part of the PbS-Sb_2S_3 system are composed of ribbons made of back to back square pyramids and arranged in three kinds of topology thus forming three homologous series. The structures of 5 phases were determined and the cation occupancies in the ribbons show that lead atoms occupy the 8- or 7-coordinated sites where the ribbons join, edge to face, while antimony atoms prefer the 7-coordinated sites where the parallel parts of the ribbons overlap.

The observations of the topology and strength of bonding in the PbS-Sb_2S_3 structures served as basis for developing models in which the structures, built of ribbons, are bonded together in variety of ways. The model correctly predicts: 1) stability of three kinds of ribbon arrangements 2) stability limits of the structures in each homologous series 3) lead and antimony distribution in the structures.

Table of contents

List of figures

List of tables

General introduction

Until the discovery of the X-ray diffraction chemists and physicists struggled to understand how atoms are combined to form matter. Since this discovery, much knowledge has been accumulated about the structure of matter and now the challenge is to predict the structures.

Bond valence theory offers one technique for predicting the structures of those inorganic compounds in which the atoms can be formally treated as cations and anions. By careful analysis of many observed structures, the problem of calculating bond distances has been reduced to two network equations. Because these empirical equations are widely obeyed in observed structures, they have a high predictive power, requiring only a knowledge of the bonding topology in the crystal and the atomic valences of the atoms. The method, although quite simple, has been remarkably successful and structures of many inorganic compounds can be predicted and better understood by its use. However, it fails in cases where electronic effects, such as the stereoactivity of the lone electron pairs present in the main group elements in their lower oxidation states, distort the coordination environment around the atoms.

To model such compounds one must carefully study the many structures in which the effect is observed and generalize the observations so that they can be used to predict distortions in other systems. This was the goal of the presented study.

Two systems were chosen, Pb-Sb-S and Pb-Bi-S, since the metals Pb, Sb and Bi all occur in these systems in their lower oxidation states, and their lone electron pairs display stereoactivity to different degrees. The observed structures were examined by two complementary techniques: single crystal X-ray diffraction and high resolution electron microscopy. The former provided precise average geometry of the structures, while the latter in addition to revealing structural defects and disorder, revealed structures that only form in amounts undetectable by X-ray diffraction. Examination of the structural details permits the development of a chemical model which can be used to deduce possible structural topologies and cation distributions in these compounds. This, together with a quantative analysis of the distortion caused by the stereoactive lone pairs, provides sufficient information needed to predict all the structures in the Pb-Sb-S system.

The thesis starts with a review of earlier studies in these systems and, after describing the experimental work, shows how chemical considerations can be used to predict which compounds should occur and what their structures should be.

1 Structural classification of lead-bismuth and lead-antimony sulphides

This chapter gives an account of the up-to-date investigations in the $PbS-Bi_2S_3$, $Ag_2S-PbS-Bi_2S_3$ and $PbS-Sb_2S_3$ systems. The reported phase diagrams are presented first, followed by the structural systematics based on the recent ideas of classification of some complex mineral and synthetic compounds. The systematics are given in a considerable detail since their structural interpretations will be used in the presentation of the results in later chapters.

1.1 Phase diagrams

$PbS-Sb_2S_3$ system

The $PbS-Sb_2S_3$ system includes at least 18 intermediate minerals and has consequently been the subject of several experimental studies (Garvin, 1973; Craig, Chang and Lees, 1973; Hoda and Chang, 1975; Salanci and Moh, 1970; Wang, 1976; Salanci, 1979; Bortnikov, Nekrasov, Mozgova and Tsepin, 1981). The phase diagram of Salanci (1979) is presented in Fig. 1.1. On that, there are six ternary compounds between PbS and Sb_2S_3: phase II; $Pb_3Sb_2S_6$; boulangerite-$Pb_5Sb_4S_{11}$; $Pb_2Sb_2S_5$;

robinsonite-$Pb_4Sb_6S_{13}$, and zinckenite = $PbSb_2S_4$. Wang (1976) found $Pb_2Sb_2S_5$ in two polymorphic forms and he also reported two other compounds: $Pb_5Sb_6S_{14}$ and a compound with composition between $Pb_5Sb_6S_{14}$ and $Pb_2Sb_2S_5$. Bortnikov (1981) also reports a phase with composition close to $Pb_5Sb_6S_{14}$ but it is unclear if this phase is identical with any of the two reported by Wang. All the above compounds melt incongruently and have appreciable composition ranges, summarized in Table 1.1. Crystallographic parameters are given in Table 1.2. Three of the synthesized compounds: boulangerite, robinsonite and zinckenite occur as minerals. In addition a number of other minerals, listed in Table 1.3, have also been reported. The plagionite group minerals, labelled with * in the Table 1.3, which have been obtained in hydro-synthesis experiments at temperatures near 400°C, by Robinson (1948b) and Jambor (1968), fail to appear in the dry system. Heating experiments on natural and synthetic compounds of this group cause their decomposition to phases stable in the dry system. This may indicate, as suggested by Garvin (1973), that the plagionite group minerals contain an additional essential component, probably hydrogen, which is liberated during heating.

PbS-Bi_2S_3 system

The most recent studies of the phase diagram are those of Van Hook (1960), Craig (1967), Salanci and Moh (1969), Otto and Strunz (1968) and Hoda and Chang (1975). The results, summarized

in Table 1.4, are in overall agreement. The phase diagram of Salanci and Moh (1969), Fig. 1.2, shows the presence of the ternary compounds: heyrovskyite-$Pb_6Bi_2S_9$, lillianite-$Pb_3Bi_2S_6$, galenobismutite-$PbBi_2S_4$, and a high temperature V-phase. Three V-phases were later characterized by Takèuchi, Takagi and Yamanaka, (1974); Takèuchi, Ozawa and Takagi, (1979) in this region of composition. All these compounds melt incongruently and dissolve appreciable amounts of Bi_2S_3. All, except the V-phases, are found as minerals. In addition, cosalite and cannizzarite are found as minerals with compositions indicated in Fig. 1.3, but they have not been synthesized from the melts. The synthesis of cosalite was unsuccessful (Hoda and Chang, 1975) in the pure PbS-Bi_2S_3 system (the cosalite minerals are reported to contain small amounts of Cu and Ag) while cannizzarite was synthesized but using the hydrothermal method (Graham, Thompson and Berry, 1953; Williams and Hyde, 1988) so, accordingly, it does not feature in the phase diagrams obtained using dry synthesis.

Ag_2S-PbS-Bi_2S_3 system

A number of minerals, indicated in Fig. 1.3 and listed in Table 1.5 are known but prior to this study their synthesis had not been reported despite several studies of the system (Van Hook (1960), Craig (1967), Hoda and Chang (1975)).

1.2 Structural systematics

In recent years structural classifications of selected groups of minerals or synthetic compounds have been developed in which the observed, complex structures are built up from rather simple archetypes modified by various structure building operations.

In the field of sulphosalts i.e. complex sulphides of As, Sb or Bi with Pb or Sn, this idea was mainly applied by Anderson and Hyde (1974), Takèuchi and Takagi (1974a,b), Hyde, Bagshaw, Andersson and O'Keeffe (1974), Makovicky and Karup-Møller (1977a,b), Makovicky (1977a), Takèuchi (1978), Wuensch (1979), Hyde, Andersson, Bakker, Plug and O'Keeffe (1979), Makovicky and Hyde (1979, 1981), and Makovicky (1981, 1983, 1985). Many of these schemes are rather complex and are often developed in different ways. A simplified description is given below which draws on ideas presented in the above works.

1.2.1 Archetypal structures

In the lead-bismuth and lead-antimony sulphides the cations occur in their lower oxidation states and, accordingly, exhibit stereoactivity of their lone electron pairs. The degree of the stereoactivity, reflected in the degree of deformation of the cations' coordination polyhedra, is small for Pb^{II} and Bi^{III} and increasingly larger for Sn^{II}, Sb^{III} and As^{III}. Corresponding to the different degree of stereoactivity we use four archetype structures. Three of the archetypes: galena, TlI, and SnS, have

been used by Makovicky, (1981, 1985), and Smith and Hyde (1983). The fourth, called here "distorted galena", does not exist in nature but serves to form a conceptual bridge between galena and TlI. Galena and distorted galena are used as archetypes mostly for lead-bismuth sulphides, where the stereoactivity of the bismuth's lone pair is small, TlI and SnS type structures are used for the lead-antimony sulphides where the lone electron pair of antimony is more stereoactive.

Galena

Galena, PbS, has the NaCl structure, Fig. 1.4. Although the lone pair in Pb^{II} is usually stereoactive, in galena it is fully inactive and the coordination around both Pb and S is a regular octahedron.

Distorted galena

This archetype, shown in Fig. 1.5, is obtained by distorting galena, to provide room for a stereoactive electron lone pair. The distortion is such that one of the apical bonds in an octahedron is lengthened and layers composed of back to back square pyramids, with short bonds within the layers and longer bonds between them, are formed. Together with the separation the layers may also be sheared perpendicular to [011] i.e. in the plane of the projection in Fig. 1.5. The cations remain six coordinated but the octahedra are no longer regular. There are five short bonds within the sheet and one longer bond between

sheets (5+1 coordination).

TlI

TlI structure, (B33) (Helmholtz, 1936), is obtained from distorted galena, by introducing a ≅2Å crystallographic shear between the sheets along $[011]_{PbS}$. This results in five short bonds within the sheets and two long bonds between the sheets e.g. 5+2 coordination. In Fig. 1.6 the shear direction is normal to the plane of the figure and gives more room between the sheets to accommodate the lone electron pairs than in the case of the distorted galena.

SnS

The SnS structure, Fig. 1.7, (B16) (Hofmann, 1935; Wiedemeier and von Schnering, 1978; Del Bucchia, Jumas and Maurin, 1980) is obtained from TlI by displacing the cation from the center of the base of the pyramid in such a way as to break the mirror symmetry perpendicular to $[011]_{PbS}$ giving two short and two long basal bonds. The loss of the mirror plane is accompanied by the square base of the pyramid becoming rectangular. The Sn atom has a 3+2 coordination within the sheet and the separation between the sheets is so large that the bonds between the sheets can be neglected.

Phase transformations between the archetypes

The kinship between the archetypes is stressed by the phase transformations occurring between them.

At high pressures the lone pair in Pb^{II} displays pronounced stereochemical activity and with increasing pressure PbS undergoes a phase transition to a SnS-like structure (Bassett, Takahashi and Stook, 1967; Mariano and Chopra 1967).

SnS undergoes a phase transition to the TlI structure on heating to T_c=878K. Von Schnering and Wiedemeier (1981) investigated the transition and found that the transformation occurs in two steps. The first which begins at approximately 680°K involves continuous displacement of the cations towards the centers of the bases of the pyramids together with a continuous change in the shape of the pyramid bases from rectangular (3.98x4.33Å) to square. The second step starts about 5° below T_c and involves further change in lattice parameters and a distortion of the square bases to slightly rectangular (4.18x4.15Å) in opposite sense.

1.2.2 Structure building operations

Following the ideas of Makovicky (1983, 1985) we specify two structure building crystallographic symmetry operations and one operation that does not involve crystallographic symmetry, to

form complex structures from fragments of the archetypes. The symmetry operations: -reflection, either mirror or glide and -translation (shear) lead to series of homologs defined by Makovicky (1989) as *accretional series*. If fragments of archetypes are unrelated by symmetry but share faces that have similar (though slightly different) lattice spacings *variable-fit series* are formed. *Variable-fit* and *accretional* series of lead-bismuth and lead-antimony sulphides are presented below.

Variable-fit structures

Cannizzarite

The structure of cannizzarite (Matzat, 1979; Williams and Hyde, 1988), ≅ $Pb_{46}Bi_{54}S_{127}$ is shown in Fig. 1.8 projected along the short b axis. It consists of two kinds of layers, Q and H. The layer Q is a two atom thick pseudo-tetragonal, (100) section of galena while the layer H is a five atom thick pseudo-hexagonal, (111) section of galena. Each kind of layer has its own short-range periodicity and it takes *m* periods of one layer and *n* periods of the other layer between points where the structures come into register. Because the layers are strictly incommensurate, the formation of commensurate structures requires distortions and a series of structures are formed with different *m/n* ratios. Matzat (1979), found that the two smallest commensurate structures occur for *m/n*=17/10 and 12/7. He postulated further homologs from the combination of these basic structural matches. In his samples Matzat found the combinations

46/27 and 41/24. Williams and Hyde (1988) report only the 17/10 and 12/7 structures in their samples.

Accretional homologous series

In each of *the accretional homologous series* the nature of the archetype and the symmetry operation relating the archetypal fragments remain preserved but the size of the fragment varies.

Structures generated from galena by mirror reflection

Lillianite

The crystal structure of lillianite, $Pb_3Bi_2S_6$, (Otto and Strunz, 1968; Takagi and Takèuchi, 1972) is shown in Fig. 1.9b projected along the short c axis. It is built of slabs of galena twinned along (311) planes of the cubic galena with trigonal prismatic sites created along the twin boundary as shown in Fig. 1.9a. The width of the slabs can be measured by the number of metal octahedra running diagonally across the slab in $[110]_{PbS}$ direction. In lillianite the slabs are four octahedra wide.

A homologous series of phases can be envisaged by varying the thickness of the galena-like slabs adjacent to the (311) twin planes. The following notation is used to briefly describe a homolog. The thickness of the two slabs adjacent to a twin plane

is specified as N_1 and N_2 and the letter L used to signify that structure belongs to the lillianite series. Thus lillianite itself has the symbol L4,4. If $N_1=N_2$, as in lillianite, the unit cell can be orthorhombic since the adjacent slabs will be related by a crystallographic mirror plane in addition to the horizontal mirror plane within the slabs. If $N_1 \neq N_2$ it cannot have a symmetry higher than monoclinic. Only two homologs of the series are known in the pure $PbS-Bi_2S_3$ system: L7,7-heyrovskyite and L4,4-lillianite, (Otto and Strunz, (1968); Tilley and Wright, (1982)). Other members: L4,7-vikingite, L4,8-treasurite, L5,9-eskimoite and L11,11-ourayite were identified by X-ray powder diffraction of mineral samples in the $Ag_2S-PbS-Bi_2S_3$ system (Makovicky and Karup-Møller, 1977b) These authors also identified a mineral called schirmerite with a mosaic structure of small domains, each with a distinct sequence of galena slabs.

The composition of the members of the lillianite series can be derived from their LN_1,N_2 symbols. A slab N_1 octahedra thick has composition $N_1MS + PS_2$, where M denotes the number of metals in octahedral sites within the slabs and P those in trigonal prismatic sites on the boundaries. This corresponds to the chemical formula: $Pb_{N_1-1}Bi_2S_{N_1+2}$. The structures composed of two different slabs with widths N_1 and N_2 will have the formula: $Pb_{N_1+N_2-2}Bi_4S_{N_1+N_2+4}$. The compositions of a few members of the series are indicated along the $PbS-Bi_2S_3$ composition line in

Fig. 1.10.

Because of similar X-ray scattering power of Pb and Bi these two metals cannot be distinguished in an X-ray scattering experiment. The assignment of Pb or Bi in metal sites in usually based on the length of the interatomic distances found in a structure: Bi is placed in smaller and more distorted sites and Pb in larger and more regular ones. The bond-valence method, introduced in chapter 2, is useful in distinguishing Bi and Pb because they occur in different oxidation states but it will only work if the bond lengths are known with precision. The Bi/Pb distribution in lillianite and heyrovskyite proposed by Takagi and Takèuchi (1972) and by Takèuchi and Takagi, (1974a), is close to that obtained using the bond valence method. In both structures lead occupies sites in the twin planes. All the metal sites in the slab have mixed Pb/Bi occupancy in lillianite. In heyrovskyite, L7,7, the sites adjacent to the twin planes have mixed Pb/Bi occupancy and the sites in the inner parts of the slab are occupied by Pb.

No single crystal X-ray study has been performed for the silver containing lillianites to determine their cation occupancies but, because bismuth and silver are known to be able to fully substitute for lead in galena-like $AgBiS_2$ (Geller and Wernick, 1959), it is supposed (Makovicky and Karup-Møller, 1977a,b) that Ag+Bi substitutes for 2Pb. Gustavite, $PbAgBi_3S_6$, found in

mineral samples is thought to be a fully substituted L4,4 and the substitution Ag + Bi ⇔ 2Pb is called (Makovicky, 1977a) the gustavite substitution. The almost vertical line, seen on Fig. 1.10, joining the compositions of silver free L4,4 and gustavite gives the compositions of their solid solution. Similar lines representing the gustavite substitution in other LN_1,N_2 homologs are also shown.

Pavonite

The structure of pavonite, $AgBi_3S_5$, (Makovicky, Mumme and Watts, 1977), is shown in Fig. 1.11 projected along the short b axis and its composition is indicated in Fig. 1.3. The main feature, the (311) twin planes separating the slabs of galena 1 and 5 octahedra wide, is similar to that in lillianites. The difference between lillianite and pavonite comes in the detailed structure of the thinner slab and the twin boundaries. In lillianites the twins have a local mirror symmetry and the metal, always lead, occupies trigonal prismatic sites. In pavonite there is no lead available so the trigonal prismatic sites are occupied by bismuth which is displaced towards the thin slab breaking the mirror symmetry and forming a distinct unit of two square pyramids joined by an octahedron. There are several sulphosalts with a similar thin slab but different widths of the wider slab. They form the pavonite homologous series, (Makovicky, Mumme and Watts, 1977) and are given the symbol PN where N is the number of octahedra running diagonally in the

thicker slab. Of the five known members of the pavonite series only one, P2, $PbBi_4S_7$, forms in the $PbS-Bi_2S_3$ system. The rest are found on $Ag_2S-Bi_2S_3$ joins (Makovicky and Mumme, 1979; Herbert and Mumme, 1981) and $Cu_2S-Bi_2S_3$ (Ohmasa and Nowacki, 1973; Ohmasa, 1973).

V-phases

A series known as "V-phases": V-1, V-2, V-3 occurring in bismuth rich part of $PbS-Bi_2S_3$ diagram, see Fig. 1.2, was characterized by Takèuchi, Takagi, and Yamanaka (1974) and Takèuchi, Ozawa, and Takagi (1979). The structure of V-1, $PbBi_4S_7$, is P2 and V-2, $Pb_2Bi_6S_{11}$, and V-3, $Pb_3Bi_{10}S_{18}$, are twinned variants of V-1 where the twinning occurs only between the thicker B slabs, seen in Figs 1.12a-c. Alternatively, the V-2 and V-3 structures can be seen as ordered intergrowths of P2 and L2,1.

Structures generated from distorted galena by glide reflection

Stibnite

The structure of stibnite Sb_2S_3, (Hofmann, 1933; Bayliss and Nowacki, 1972), which is isomorphous with bismuthinite, Bi_2S_3, (Kupčik and Veselá-Nováková, 1969) and Sb_2Se_3 (Tideswell, Kruse and McCullough. 1957), is shown in Fig. 1.13 projected along the short c axis. It is composed of ribbons made of 4 back to back square pyramidal SbS_5 groups. The ribbons extend indefinitely in the c direction, are one pyramid thick and have a width that

equals twice the basal distance of the SbS_5 pyramid.

A homologous series can be formed from the stibnite structure by adding PbS i.e. inserting the additional PbS_5 pyramids in the middle of the stibnite ribbon. The stoichiometry in the series is determined by the total number of PbS units that have been incorporated as:

$$Sb_2S_3 + (PbS)_{2n} + Sb_2S_3 = 2Pb_nSb_2S_{3+n}$$

where n=0 for stibnite, and 1, 2... for the further members.

By analogy to lillianites, stibnite homologs are described by letter S, to signify that the structure belongs to the stibnite series, and by the number of the SbS_5 pyramids lying diagonally in two neighbouring slabs. Stibnite is S2,2.

Two members of the homologous series, S4,4, $Pb_2Sb_2S_5$, and S5,5, $Pb_3Sb_2S_6$, were synthesized by Wang (1973, 1977) and S4,4 by Smith and Hyde (1983). The latter authors proposed, but did not solve, the structure of S4,4 by analogy with the structures of stibnite and naturally occurring meneghinite, $CuPb_{13}Sb_7S_{24}$ (Euler and Hellner, 1960), a copper bearing analog of S5,5. The second member of the series, S3,3, $PbSb_2S_4$, has not been synthesized in large volume but was found in small regions during an electron microscope study (Tilley, Wright and Smith, 1986). Thus the complete series of four homologs from S2,2 to S5,5 is known to

form.

From the arrangement of the ribbons in S5,5, shown in Fig. 1.14, it can be seen that the stibnite homologous series is derived from the distorted galena archetype with the ribbons facing each other but translated parallel to their width so that only a part of each ribbon overlaps with the next. Cation sites between the ribbons have 5+1 coordination and are occupied mostly by antimony. The other cation sites, in places where the ribbons join, forming a 111/100 boundary (compare with that in cannizzarite), are seven-coordinated and are occupied mostly by lead. The cation distribution proposed by Hyde and Smith (1983) for S4,4 is based on this principle.

Cosalite

The structure of cosalite, $\approx Pb_2Bi_2S_5$, (Srikrishnan and Nowacki, 1974; Macicek, 1988) is shown in Fig. 1.15 projected along the short $\underline{c}$ axis. It is composed of ribbons (shaded)made of back to back square pyramidal $(Pb,Sb)S_5$ groups. The ribbons extend indefinitely in the $\underline{c}$ direction, are one pyramid thick and their width equals four times the basal distance of the $(Pb,Sb)S_5$ pyramid. Two parallel ribbons combine to form a ribbon pair and the metal sites on the facing sides of the ribbons have 5+1 coordination characteristic of the distorted galena structure. These sites are preferred by bismuth. The ribbon pairs are

related by a glide reflection and the sides of the ribbon pairs, which face the edges of the glide related pair, have two eight- and two six-coordinated metal sites. These sites are rich in lead. There is always some silver or copper present in cosalite, both synthetic and natural. Cu seems to stabilize the structure and is placed in tetrahedral positions indicated by squares in Fig. 1.15. Cosalite can be given the symbol C4,4 and could be considered as part of a homologous series but no higher homologs have been reported.

Structures generated from distorted galena by cyclic twinning

Zinckenite

The structure of zinckenite, $\simeq PbSb_2S_4$ (Takeda and Horiuchi, 1971; Portheine and Nowacki, 1975; Lebas and Le Bihan, 1976; Tilley and Wright, 1987), is shown in Fig. 1.16 projected along the short c axis. The structure has a six-fold symmetry and is built of blocks of distorted galena structure. The blocks are infinite in c direction, three octahedra thick and two octahedra wide. They are twinned about three planes containing the six-fold axis with the 60° twin angle characteristic of the 111/100 twin boundary. The sites with 6_3 symmetry are surrounded by ring walls composed of six columns of edge sharing trigonal prisms of Pb or Sb.

Structures generated from TlI by glide reflection

Boulangerite

The structure of boulangerite, $Pb_5Sb_4S_{11}$, (Born and Hellner, 1960; Petrova, Kuznetzov, Belokoneva, Simonov, Pobedimskaya and Belov, 1978), Fig. 1.17, consists of two types of ribbon similar to those described for the stibnite homologous series. The ribbons have different widths: the width of the narrow ribbon equals three times the basal distance of the $(Pb,Sb)S_5$ pyramid while that of the wider one equals six times this distance. The ribbons can be derived conceptually from those in stibnite by inserting two PbS_5 pyramids to form the narrower and eight to form the wider ribbon. In contrast to stibnite the stacking between parallel ribbons is of the TlI type viz. with a shear between the ribbons along the axis of projection shown in Fig. 1.17.

The ribbons stack face to face with a narrow ribbon between each wide one. Where parallel ribbons face each other the cation sites mostly contain five-coordinated antimony. The cation sites on the faces that connect to the edges of other ribbons have higher coordination numbers and are occupied by lead.

A homologous series in which boulangerite is the lowest member can be formed by simultaneous incorporation of further PbS_5 pyramids into both kinds of ribbon. The stoichiometry in the series can be determined by the total number of incorporated PbS

units as:

$$[Sb_2S_3 + (PbS)_{2+2n} + Sb_2S_3] + [Sb_2S_3 + (PbS)_{8+2n} + Sb_2S_3] =$$

narrow ribbon wide ribbon

$$= 2Pb_{5+2n}Sb_4S_{11+2n}$$

where n=0 for boulangerite and 1, 2... for the further members.

Using a short notation, similar to that derived for the lillianites and stibnites, boulangerite can be described as B(3,6)(3,6) which indicates the widths of the two kinds of ribbons and the boulangerite arrangement. The higher homologs are derived by simultaneously increasing the width of both kind of ribbon and are described as B(4,7)(4,7), B(5,8)(5,8) etc.. At the time this study was begun no higher homolog of boulangerite was known.

Robinsonite

The structure of robinsonite, $Pb_4Sb_6S_{13}$, (Petrova, Kaplunnik, Bortnikov, Pobedimskaya and Belov, 1978), Fig. 1.18, also consists of two types of ribbon differing in width. Unlike in boulangerite there are two narrow ribbons for each wide one in robinsonite. The narrow ribbon is identical with the ribbon in stibnite and the other is three times as wide and can be formed

by insertion of four additional pairs of back to back pyramids in the middle of the stibnite ribbon. Antimony favours the five coordinated metal sites where the ribbons face a parallel ribbon and the Pb atoms occupy positions of higher coordination found at sites where the face of one ribbon meets the edge of a second ribbon.

A robinsonite homologous series can be formed by increasing the width of either or both ribbons. The stoichiometry in the series can be determined by the total number of incorporated PbS units as:

$$\underbrace{2[Sb_2S_3 + (PbS)_n + Sb_2S_3]}_{\text{2 narrow ribbons}} + \underbrace{[Sb_2S_3 + (PbS)_{8+2m} + Sb_2S_3]}_{\text{wide ribbon}} = 2Pb_{4+n+m}Sb_6S_{13+n+m}$$

where n and m are zero for robinsonite and 1, 2... for the further members.

In short notation robinsonite can be described as R6,(2,2). Wang (1976) reported two phases with unit cells which could correspond to R7,(2,2) and R7,(3,3) and with single crystal diffraction patterns resembling that of robinsonite, but there was no confirmation that those were part of the robinsonite homologous series.

Combined accretional and variable-fit structures

Galenobismutite

The structure of galenobismutite, $PbBi_2S_4$ (Iitaka and Nowacki, 1962), is shown in Fig. 1.19 projected along the short c axis. Takèuchi and Takagi (1974b) interpreted the structure as built of galena fragments related by a glide. The galena fragments that they use are small and the operation requires severe distortions leaving little resemblance of the resulting complex polyhedra to the original octahedra. Galenobismutite can be seen as an example of the first member of a homologous series that combines the accretional and variable-fit principles where the H and Q type layers, similar to those in cannizzarite, are truncated. In Fig. 1.20 a higher member of the series, weibullite - $Ag_{0.33}Pb_{5.33}Bi_{8.33}(S,Se)_{18}$, is shown to better illustrate such a combination.

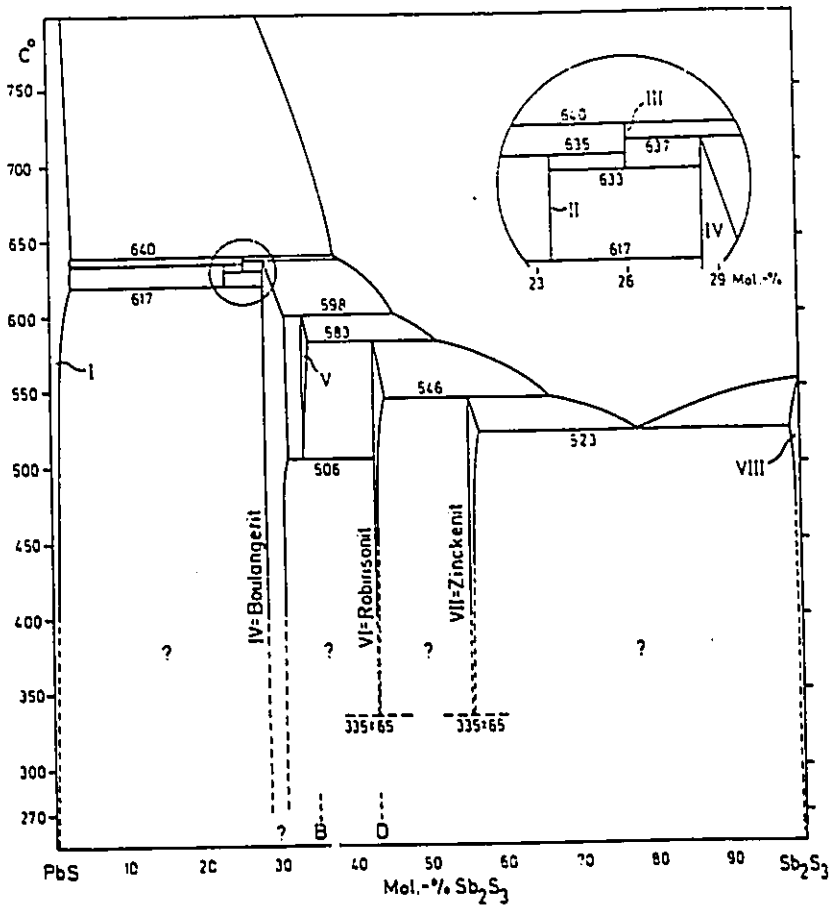

Fig. 1.1: Phase diagram of the PbS-Sb_2S_3 system, (B. Salanci, 1979). Vapour is present in all phase combinations and the pressure of the system is not constant. The phases are: I-galena, II-?, III-3PbS·SbS, IV-boulangerite, V-2PbS·Sb_2S_3 (monoclinic), VI-robinsonite, VII-zinckenite, VIII-stibnite.

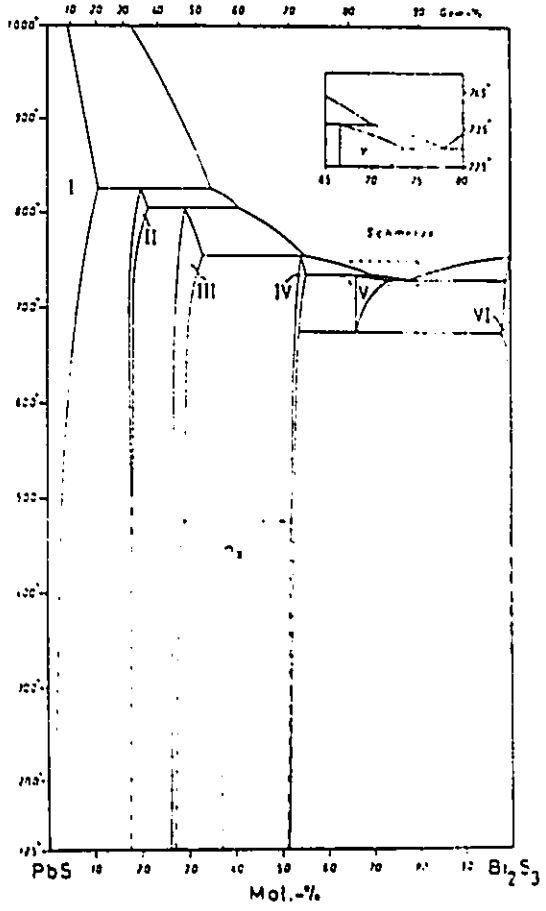

Fig. 1.2: Phase diagram of the PbS-Bi_2S_3 system, (B. Salanci and G. Moh, 1969). The phases are: I-galena, II-heyrovskyite, III-lillianite, IV-galenobismutite, V-V-phase, VI-bismutite, ?x-cosalite.

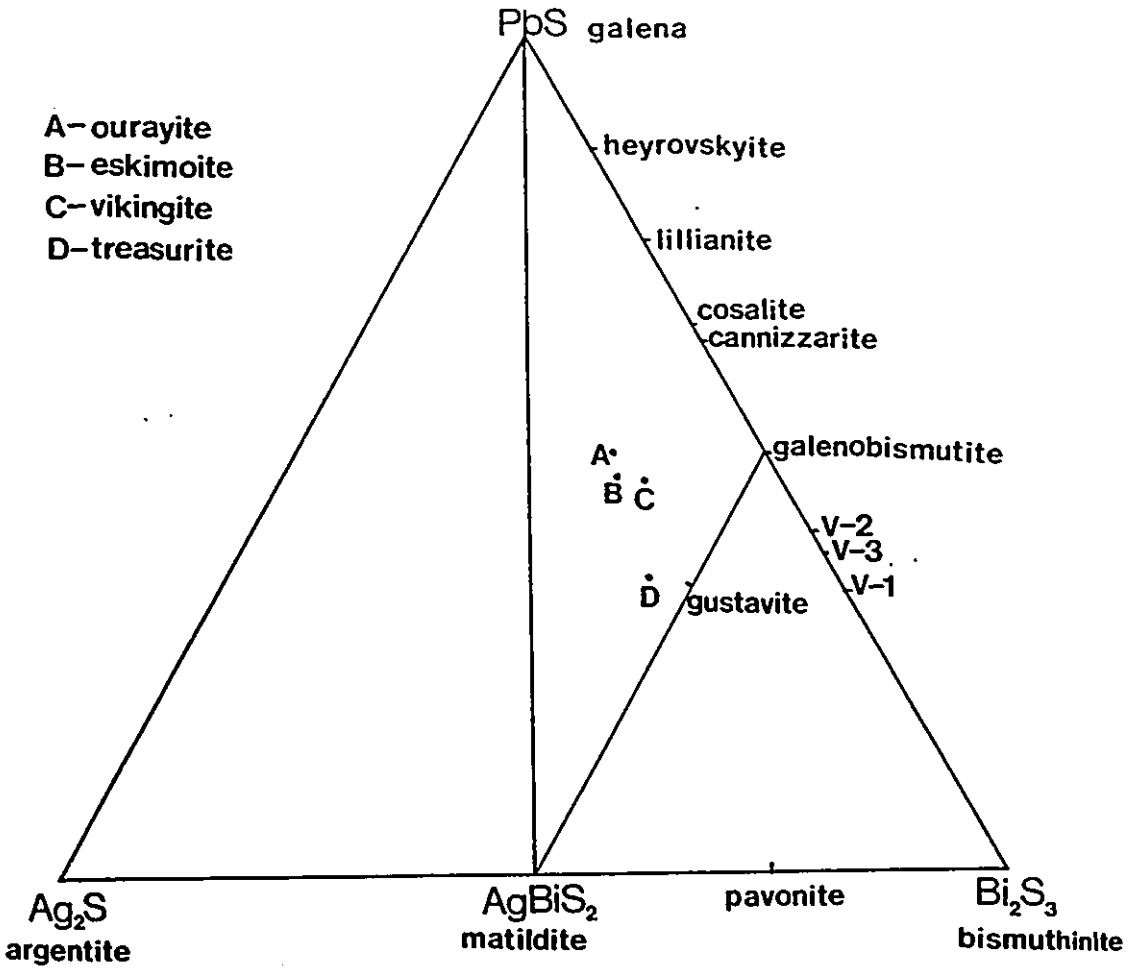

Fig. 1.3: Compositional diagram of both the synthetic and mineral phases reported in the Ag_2S-PbS-Bi_2S_3 system. Chemical formulae and crystallographic parameters are given in Table 1.5.

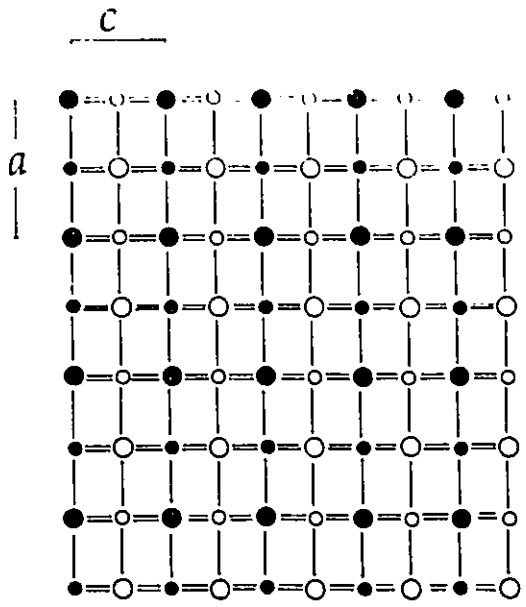

(a)

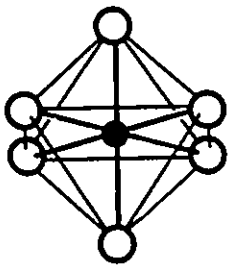

(b)

Fig. 1.4: (a) The crystal structure of galena, NaCl type, viewed down [011]. Two levels at z=0 and z=$\frac{1}{2}$ are respectively denoted as open and shaded circles. The metal atoms have regular octahedral coordination shown in Fig. 1.4(b).

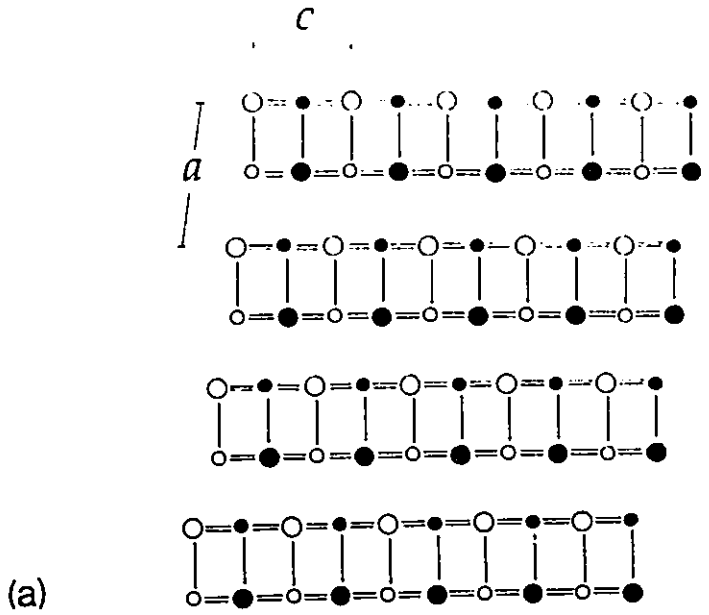

(a)

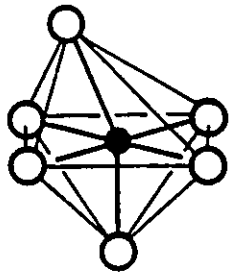

(b)

Fig. 1.5: (a) The structure of distorted galena, viewed down $[011]_{PbS}$, consisting of layers composed of back to back pyramids with five short bonds within the layers and one long bond between the layers. The metals have distorted octahedral coordination, shown in Fig. 1.5(b).

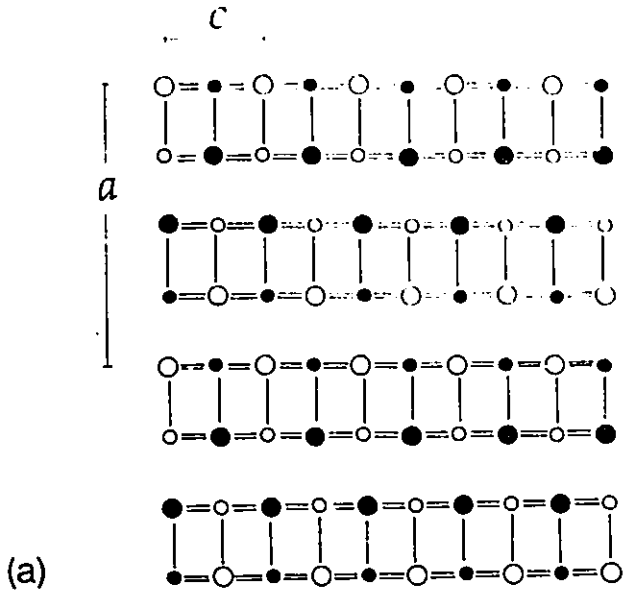

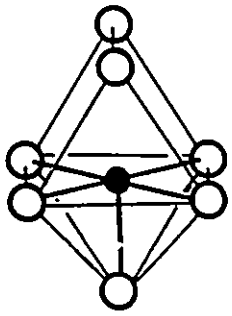

Fig. 1.6: (a) The crystal structure of TlI viewed down $[011]_{PbS}$. Two levels at z=0 and $z=\frac{1}{2}$ are denoted as open and filled circles. The TlI structure can be obtained from distorted galena by applying a shear on $(100)_{PbS}$ and in $[011]_{PbS}$ direction. The back to back square pyramids form sheets (shaded). The 5+2 coordination of the metal atoms is shown in Fig. 1.6(b).

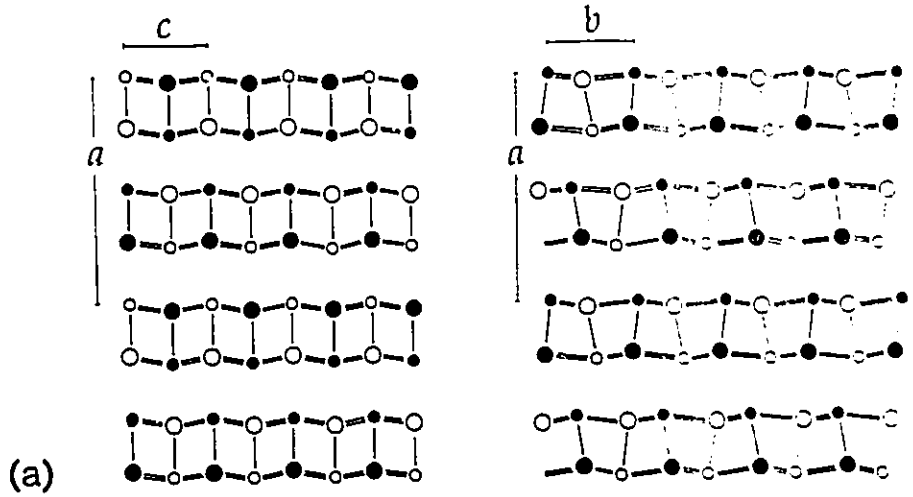

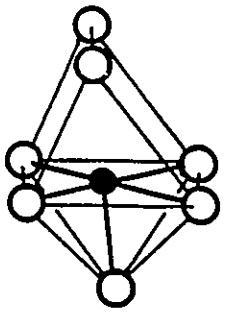

Fig. 1.7: The crystal structure of SnS in two projections. The S atoms (large circles) and the Sn atoms (small circles) that are positioned at $y \cong 0$ and $y \cong \frac{1}{2}$ in the projection along $[011]_{PbS}$ (Fig.7a) are respectively denoted by open and filled circles. In the projection along $[10\bar{1}]_{PbS}$ (Fig.7b) filled circles denote atoms at $z \cong \frac{1}{4}$ and open circles at $z \cong \frac{3}{4}$.

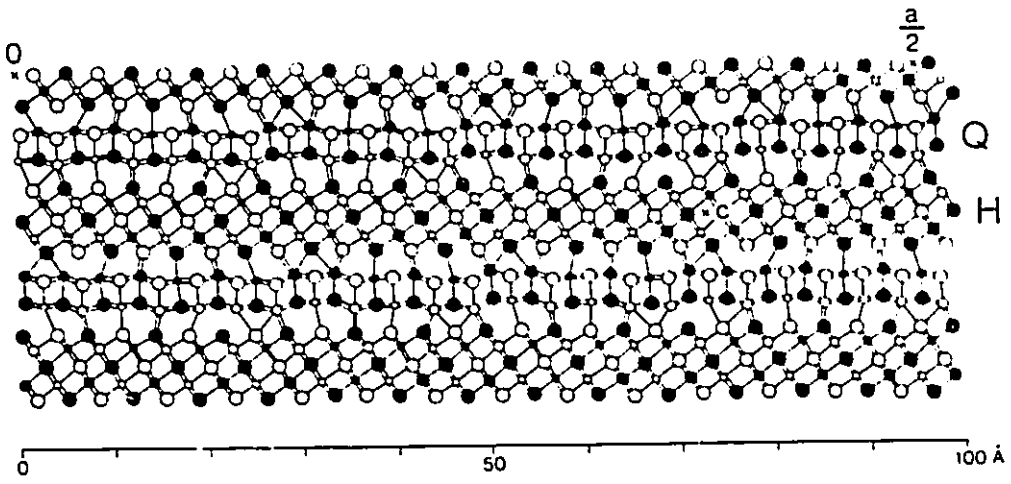

Fig. 1.8: The crystal structure of cannizzarite viewed down [010]. Circles in order of decreasing size represent S, Pb, mixed sites and Bi; colouring denotes atoms at y=0 and $\frac{1}{2}$. In the depicted homolog 46 subcells of the Q type layer match with 27 subcells of the H type layer giving the overall composition $Pb_{46}Bi_{54}S_{127}$.

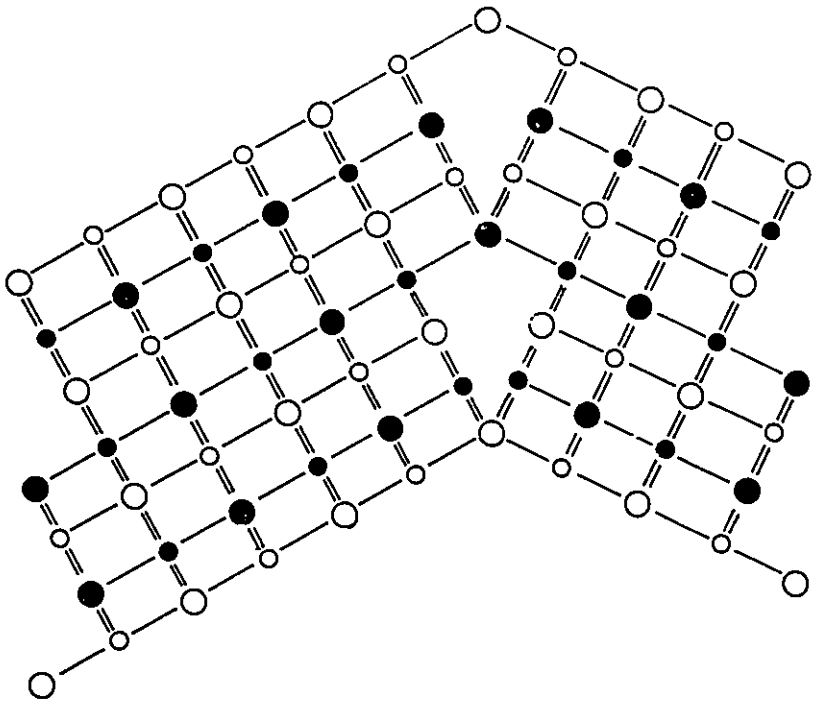

Fig. 1.9(a): Schematic representation of two galena fragments projected along $[011]_{PbS}$ and related by a $(311)_{PbS}$ mirror plane.

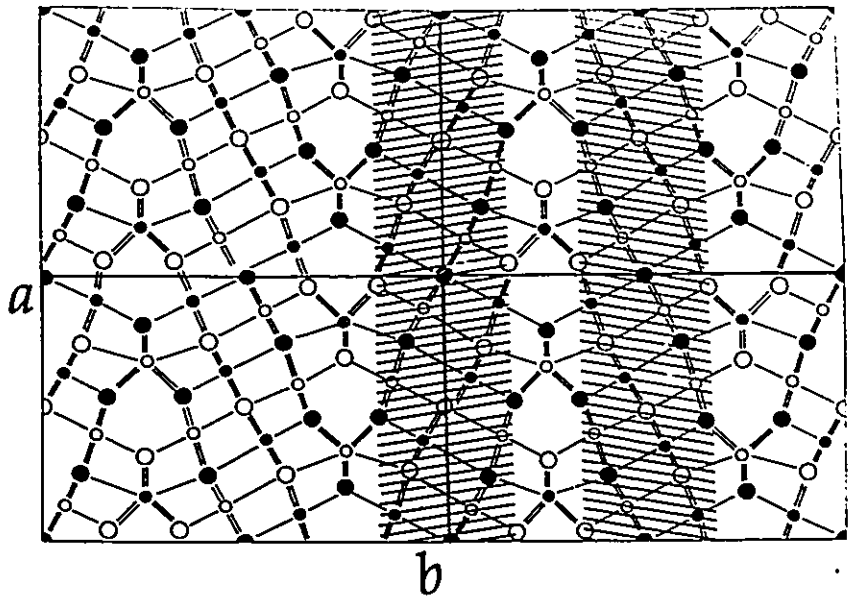

Fig. 1.9(b): The crystal structure of lillianite, $Pb_3Bi_2S_6$, projected along its [001] after removing Pb atoms on the mirror plane. Circles in order of decreasing size represent S, Pb and mixed sites; colouring denotes atoms at y=0 and $\frac{1}{2}$. One Pb atom per trigonal prismatic site is lost as the result of the twinning operation. Galena-like layers are shaded.

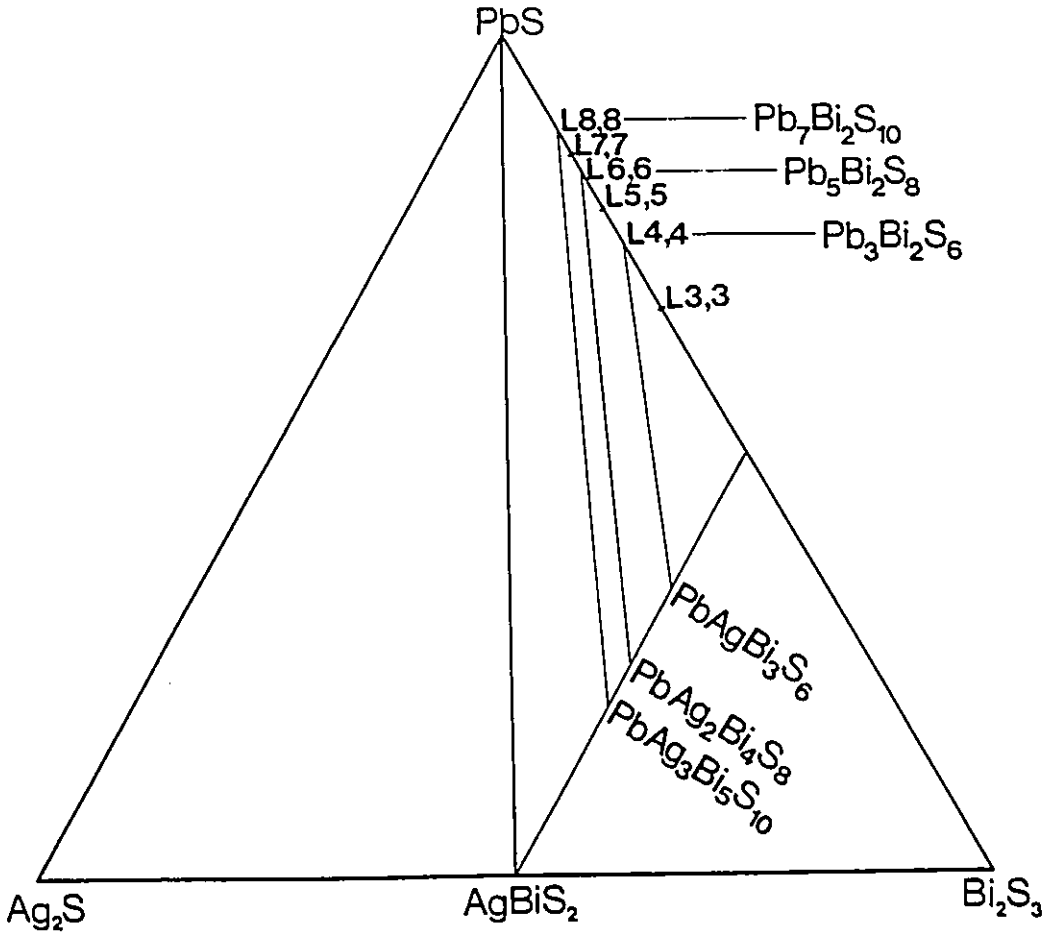

Fig. 1.10: Compositional diagram in the Ag_2S-PbS-Bi_2S_3 system showing the compositions of the solid solutions between lillianite, $Pb_3Bi_2S_6$, and gustavite, $PbAgBi_3S_6$, and between their respective higher homologs.

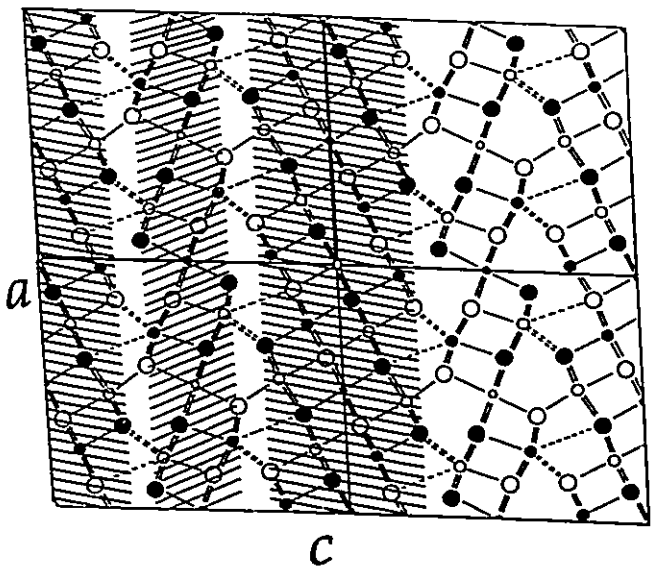

Fig. 1.11: The crystal structure of pavonite, $AgBi_3S_5$, viewed along [010]. Circles in order of decreasing size represent S, Pb and Ag; colouring denotes atoms at y=0 and $\frac{1}{2}$. The galena-like slabs with five octahedra per chain are shaded. Long Bi-S distances are indicated by broken lines.

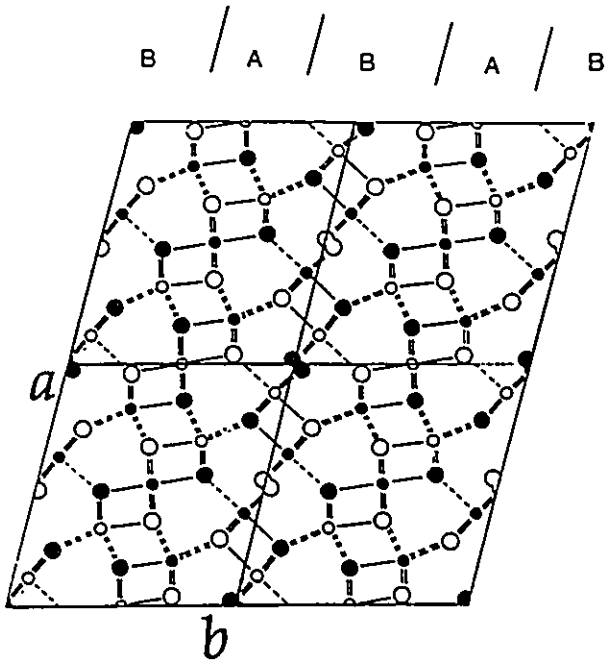

(a)

Fig. 1.12: The crystal structure of (a) V-1, $PbBi_4S_7$, (b) V-2, $Pb_2Bi_6S_{11}$, (c) V-3, $Pb_3Bi_{10}S_{18}$ projected along [001]. Small and large circles denote metal and sulphur atoms respectively; colouring denotes atoms at z=0 and $\frac{1}{2}$. Thinner, A, and thicker, B, slabs are indicated. The V-2 and V-3 structures can be seen as twinned variants of the V-1 structure where the twin planes, marked T, occur only between the thicker, type B, slabs.

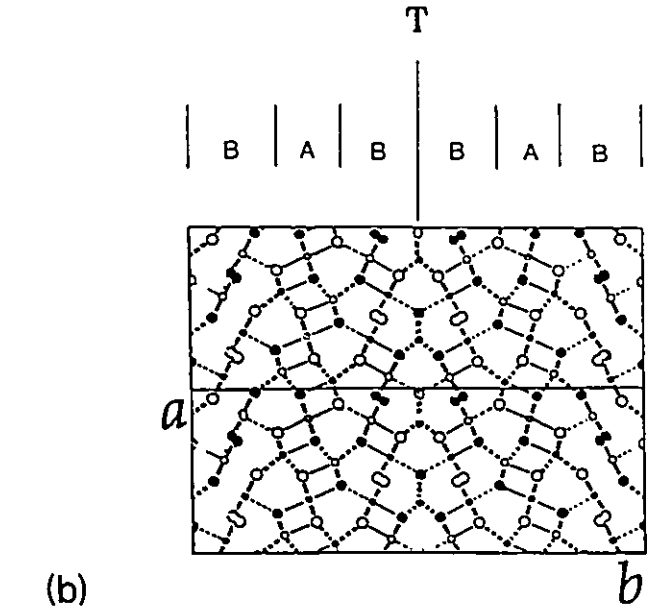

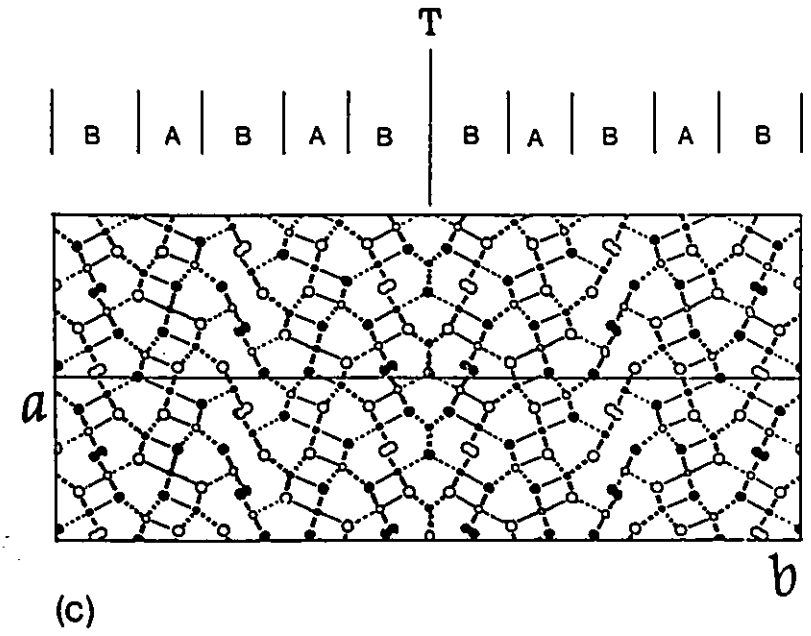

Fig. 1.12(b) and (c)

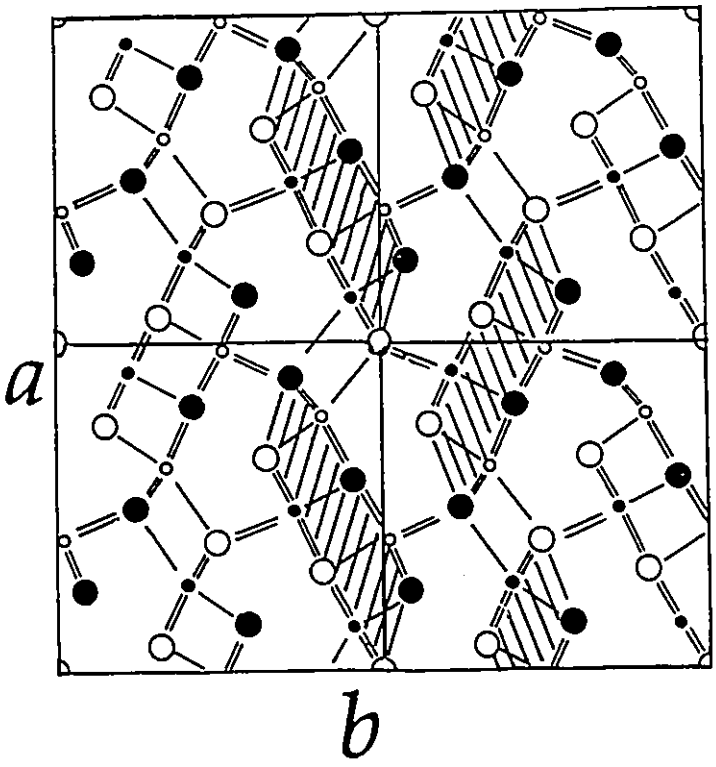

Fig. 1.13: The crystal structure of stibnite, Sb_2S_3, S2,2, projected along [001]. The large circles represent S, the small Sb; colouring denotes atoms at y=0 and $\frac{1}{2}$. The structure is composed of ribbons (ruled) made of back to back square pyramidal SbS_5 groups.

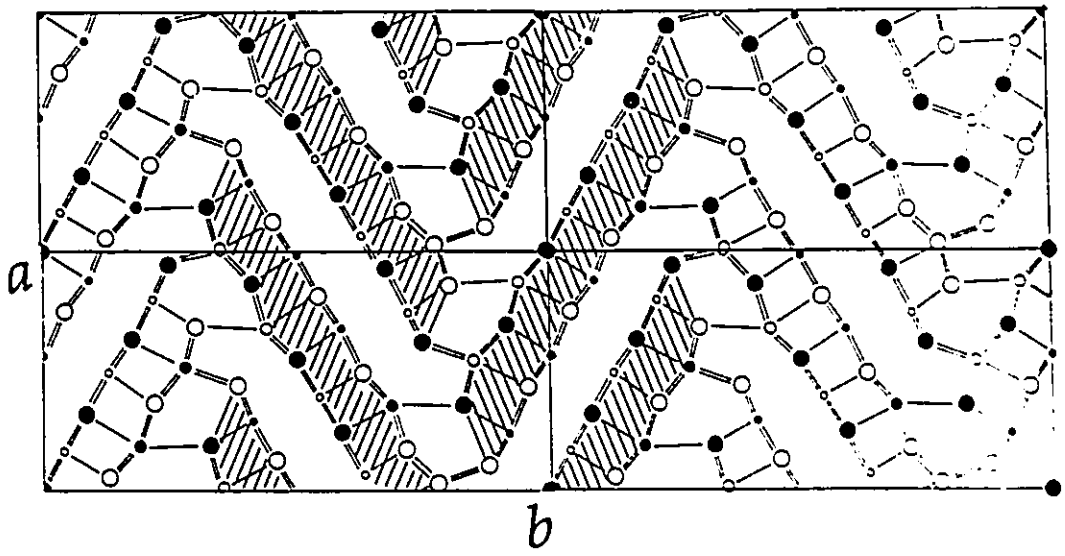

Fig. 1.14: The crystal structure of meneghenite, $CuPb_{13}Sb_7S_{24}$, S5,5, projected along [001] axis. In order of decreasiog size the circles represent S, Pb, ($\frac{1}{2}$Pb +$\frac{1}{2}$Sb) and ($\frac{1}{4}$Pb + $\frac{3}{4}$Sb). The levels at $z=\frac{1}{4}$ and $z=\frac{3}{4}$ are denoted by open and full circles. The unrefined Cu positions are not indicated. The structure is composed of ribbons made of back to back square pyramidal SbS_5 groups (ruled) which are arranged into the distorted galena-like structure.

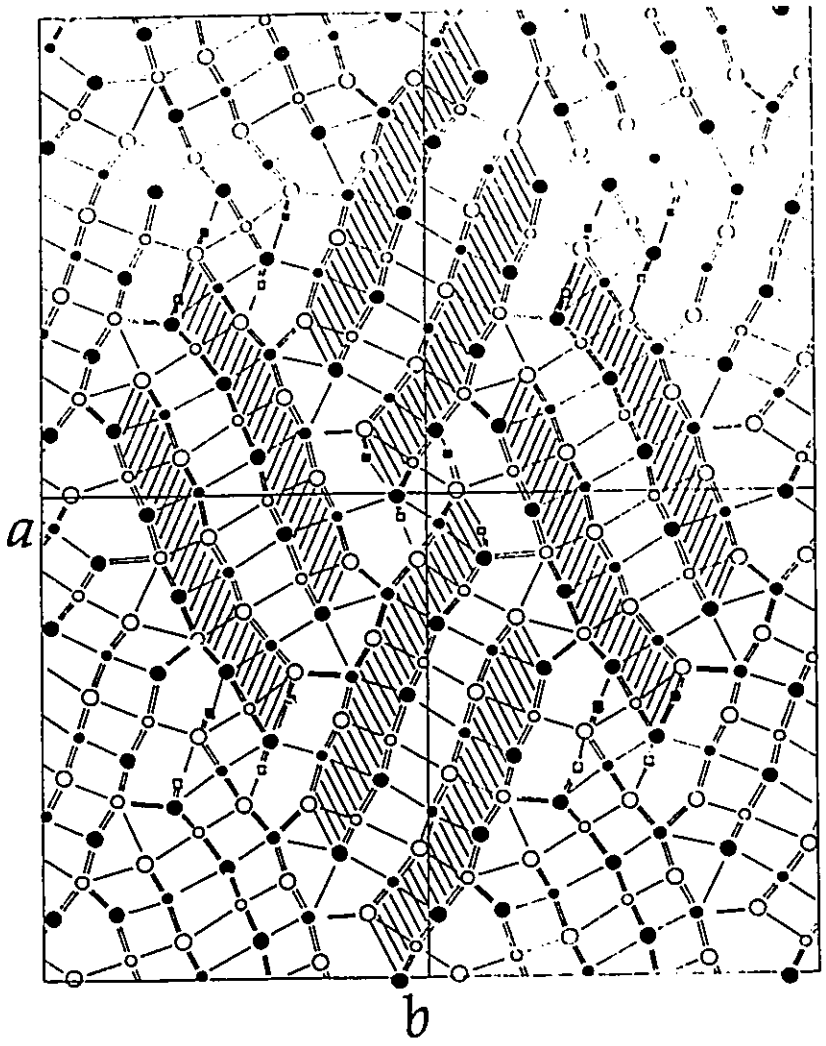

Fig. 1.15: The crystal structure of cosalite, $\cong Pb_2Bi_2S_5$ projected along [001]. The ribbons composing the distorted galena fragments are shaded and the tetrahedral sites occupied by Cu are indicated by □.

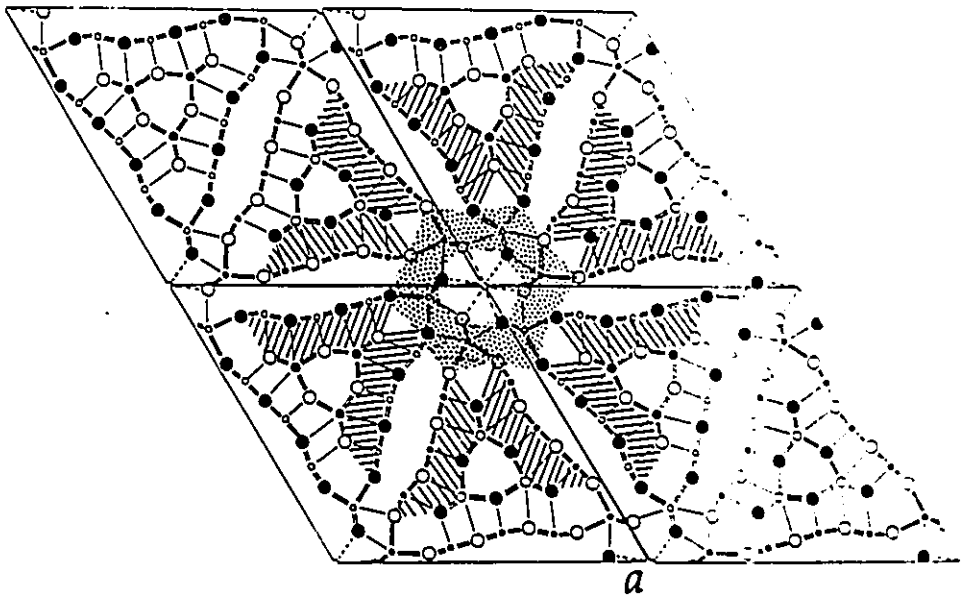

Fig. 1.16: The crystal structure of zinckenite, $\cong PbSb_2S_4$ projected along [001]. Circles in order of decreasing size indicate S, Pb and mixed sites or Sb. The hexagonal ring walls are shaded and the ribbons composing the fragments of distorted galena-like structure are ruled.

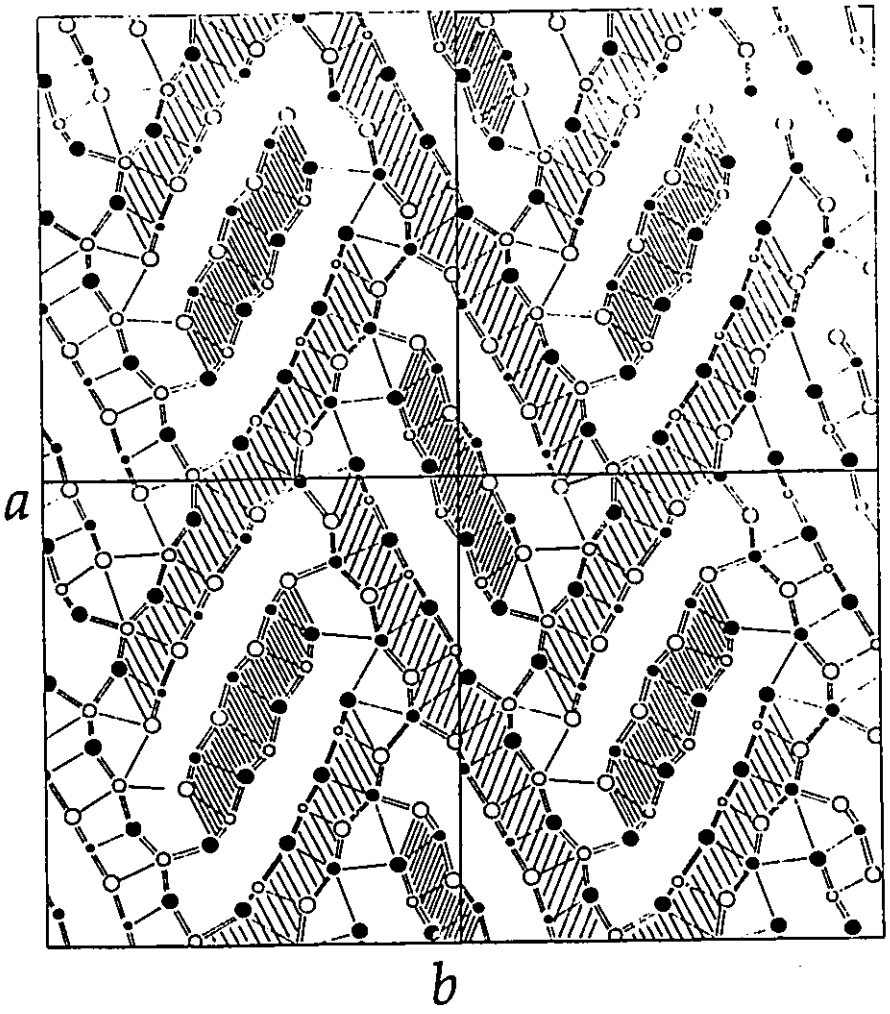

Fig. 1.17: The crystal structure of boulangerite, $Pb_5Sb_4S_{11}$, projected down [001]. In order of decreasing size, the circles denote S, Pb, mixed sites and Sb. Atoms at $z=\frac{1}{4}$ and $z=\frac{3}{4}$ are indicated by open and full circles respectively. The wide and narrow ribbons are indicated by coarse and fine ruling.

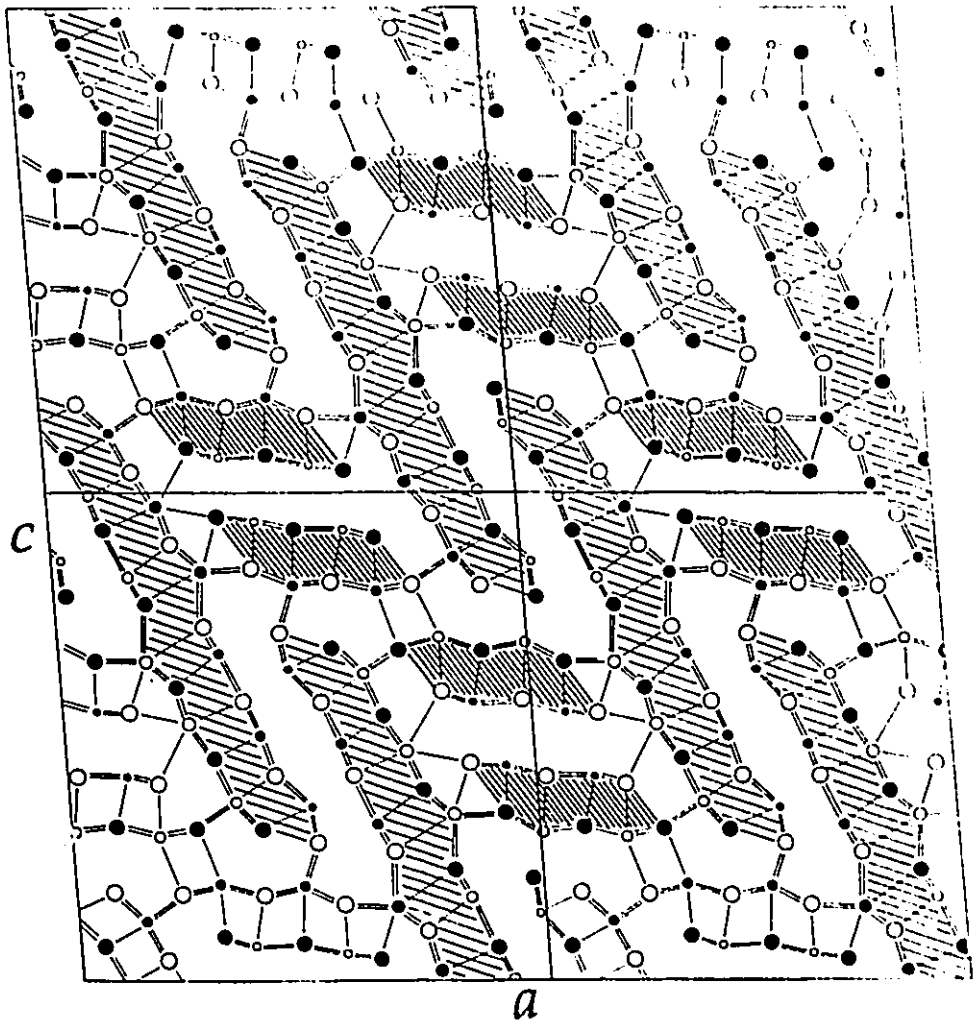

Fig. 1.18: The crystal structure of robinsonite, $Pb_4Sb_6S_{13}$, projected down [001]. In order of decreasing size, the circles denote S, Pb, mixed sites and Sb. Atoms at $z=\frac{1}{4}$ and $z=\frac{3}{4}$ are indicated by open and full circles respectively. The wide and narrow ribbons are indicated by coarse and fine ruling.

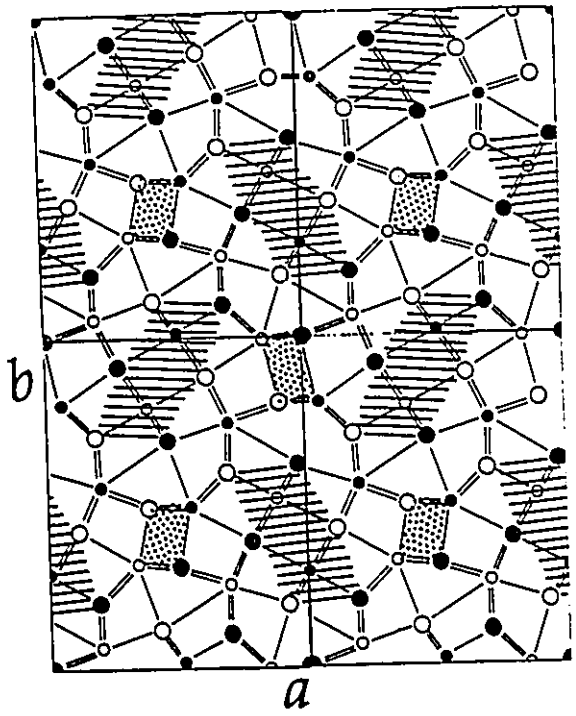

Fig. 1.19: The crystal structure of galenobismutite, $PbBi_2S_4$, projected along [001]. The circles in order of decreasing size: S, Pb, Bi. Atoms at $z=\frac{1}{4}$ and $z=\frac{3}{4}$ are indicated by open and full circles respectively. The structure can be seen as an example of a member of a homologous seres that combines the accretional and the variable-fit principles. The short H type layers, analogical to those in cannizzarite are ruled; the Q type layers are stippled.

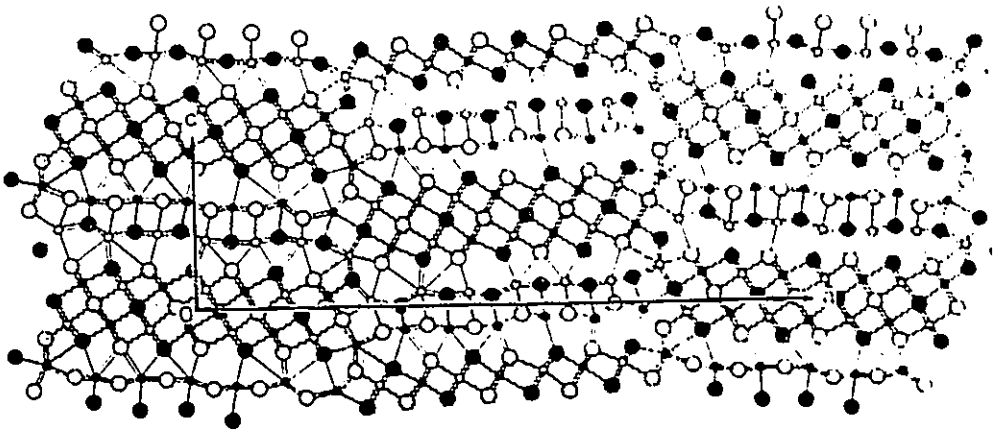

Fig. 1.20: The crystal structure of weibullite, $Ag_{0.33}Pb_{5.33}Bi_{8.33}(S,Se)_{18}$, projected along [001] and interpreted as a higher member of the galenobismutite homologous series. Small circles Me atoms, large circles S or Se atoms. Shading as in Fig. 1.19.

Table 1.1: Synthetic phases reported in the $PbS-Sb_2S_3$ system.

Phase	Composition	Stability range [°C]		Solubility of Sb_2S_3 [mole%]	Reference
galena	PbS		<1113 ∓5	3 at 637 ∓3	Salanci & Moh (1970)
				3 at 600	Garvin (1973)
				<2 at 400	Garvin (1973)
				2.9∓0.3 at 400-600	Craig et al. (1979)
	$76.5PbS \cdot 23.5Sb_2S_3$	617∓2<	<635∓2		Salanci (1979)
	$3PbS \cdot Sb_2S_3$	621∓3<	<637∓3		Salanci & Moh (1970)
		633∓2<	<640∓2		Salanci (1979)
Boulangerite	$5PbS \cdot 2Sb_2S_3$		<638∓2		Craig et al. (1973)
			<631∓3	2.5 at 505∓7	Salanci & Moh (1970)
			<634∓5	<1 at 580	Garvin (1973)
	$\approx 2PbS \cdot Sb_2S_3$(?)	505∓7<	<597∓3		Salanci & Moh (1970)
	$2PbS \cdot Sb_2S_3$(m)	506∓5<	<598∓3		Salanci (1979)
	(m)	425∓25<	<600∓5		Garvin (1973)
	(?)	450∓25<	<603∓5		Craig (1973)
	(m)	576<			Wang (1976)
	(o)	<576	<607		Wang (1976)
Robinsonite	$4PbS \cdot 3Sb_2S_3$		<582∓4	1 at 545∓3	Salanci & Moh (1970)
			<583∓3		Salanci (1979)
		300<	<582∓6	2 at 542	Garvin (1973)
			<582∓2		Craig et al. (1973)
	$5PbS \cdot 3Sb_2S_3$	510<	<592		Wang (1976)
	$6PbS \cdot 3Sb_2S_3$	602<	<605		Wang (1976)

Table 1.1 cont.

Phase	Composition	Stability range [°C]	Solubility of Sb_2S_3 [mole%]	Reference
Zinckenite	≈PbS·Sb_2S_3	<545∓3	1.5 at 521	Salanci & Moh (1970)
		<546∓3		Salanci (1979)
		<540∓5		Garvin (1973)
Stibnite	Sb_2S_3		<2 PbS at 520	Garvin (1973)

(m)- monoclinic

(o)- orthorombic

Table 1.2: Crystallographic parameters of the structures reported in the PbS-Sb_2S_3 system.

Name	Formula	Symbol	Space group	Lattice parameters (Å),(deg)	Reference
	$Pb_3Sb_2S_6$	S5,5	Pbnm	a=11.36 b=23.98 c=4.10	Wang (1977)
Boulangerite	$Pb_5Sb_4S_{11}$	B(3,6)(3,6)	Pbnm	a=21.14 b=23.46 c=4.035	Born and Hellner (1960)
			$Bb2_1m$	a=42.28 b=23.46 c=8.07	Born and Hellner (1960)
			Pbnm	a=21.30(2) b=23 c=4.04(7)	Petrova et al. (1978)
			Pbnm	a=21.24(1) b=23.51 c=4.036	Petrova et al. (1978)
	$Pb_2Sb_2S_5$	S4,4	Pbnm	a=19.80 b=11.40 c=4.04	Wang (1976)
			Pnma	a=19.808(5) b=4.042 c=11.353	Smith & Hyde (1983)
			monocl A-cent	a=20.81 b=50.52 c=4.03	Wang (1977)
	$Pb_6Sb_6S_{15}$(?)	R7(3,3)(?)	monocl A-cent	a=26.11 b=35.44 c=4.04 γ=128°30'	Wang (1976)
		after converting	monocl I-cent	a=28.25 b=4.04 c=26.11 β=98.7°	

Table 1.2:cont.

Name	Formula	Symbol	Space group	Lattice parameters (Å),(deg)	Reference
	$Pb_8Sb_6S_{14}$	R7(2,2)	monocl A-cent	a=21.98 b=35.12 c=4.02 γ=126°15'	Wang (1976)
		after converting	monocl I-cent	a=28.44 b=4.02 c=21.98 β=92	
Robinsonite	$Pb_4Sb_6S_{13}$	R6(2,2)	P1	a=16.51 b=17.62 c=3.97 α=96.01 β=96.37 γ=91.2	Berry et al. (1952)
			P1	a=16.56 b=17.69 c=3.982 α=91.09 β=96.46 γ=96.77	Petrova et al. (1978)
			monocl B-cent	a=32.85 b=23.64 c=3.97 γ=131.95	Wang (1977)
			reduced unit cell:	a=16.54 b=17.7 c=3.97 α=92.77 β=96.44 γ=96.89	
Zinckenite	$PbSb_2S_4$		$P6_3$	a=22.09 c=4.321	Takeda & Horiuchi (1971)
			$P6_3$	a=22.148(6) c=4.333(6)	Portheine & Nowacki (1975)
			$P6_3$	a=22.126 c=4.342	Tilley & Wright (1987)

Table 1.3: Reported minerals in the PbS-Sb_2S_3 system. Those labelled with * are structurally related and form the plagionite group.

Mineral name	Composition PbS:Sb_2S_3	Reference
Geocronite	5:1	Douglass et al. (1954)
Semseyite*	9:4	Kohatsu & Wuensch (1974)
Heteromorphite*	7:4	Jambor (1969)
Plagionite*	5:4	Cho & Wuensch (1970, 1974)
Fullopite*	3:4	Nuffield (1946)
Mineral QM	11:6	Hiller (1938)
Sterryite	12:5	Jambor (1967)
Madocite	17:8	Jambor (1967)
Veenite	2:1	Jambor (1967)
Playfairite	16:9	Jambor (1967)
Launayite	22:13	Jambor (1967)
Sorbyite	17:11	Jambor (1967)
Tintinaite	5:4	Harris et al. (1968)
Guettardite	9:8	Jambor (1967)
Twinnite	1:1	Jambor (1967)

Table 1.4: Phases reported in PbS-Bi_2S_3 system.

Phase	Composition [mole% PbS]	Stability range [^{0}C]		Solubility of Bi_2S_3 [mole%]	Reference
Heyrovskyite	82∓2	<325<	<829∓6		Craig (1967)
	82.5				Otto & Strunz (1968)
	80.0		<825±5		Salanci & Moh (1969)
Lillianite	73∓2	<200<	<816∓6	2∓1 at 750	Craig (1967)
	72.7				Otto & Strunz (1968)
	70.0		<805±5		Salanci & Moh (1969)
Galenobismutite	48.7∓0.5		<750∓6		Craig (1967)
	50.0		<755±5		Salanci & Moh (1969)
		<375			Chang & Hoda (1977)
V-phase	35∓0.5	<680	<730∓5		Craig (1967)
	44±0.6	<675±5	<736±2		Salanci & Moh (1969)

Table 1.5: Phases reported in the Ag_2S-PbS-Bi_2S_3 system.

Symbol	Composition	a α	b β	c [Å] γ [deg]	Space group	Reference
L4,4	$Pb_3Bi_2S_6$	13.522	20.608	4.112	Bbmm	Otto & Strunz (1968)
lillianite						
L4,4		13.535	20.451	4.104	Bbmm	Takagi & Takèuchi (1972)
(minor Ag)						
L4,4		13.47	20.75	4.13	orthor.	Hoda & Chang (1975)
gustavite	$PbBi_3AgS_6$	13.522	19.566	4.136	Bbmm	Charis & Chen (1975)
L7,7	$Pb_6Bi_2S_9$	13.715	31.210	4.131	Bbmm	Takèuchi & Takagi (1974)
heyrovskyite (minor Ag)						
L7,7		13.697	31.355	4.132	Bbmm	Otto & Strunz (1968)

Table 1.5: cont.

Symbol	Composition	a α	b β	c [Å] γ [deg]	Space group	Reference
L5,9	$Pb_{10}Bi_{15}Ag_7S_{36}$	13.459(5) 93.35	30.194(8)	4.100(5)	B2/m or Bm	Makovicky & Karup-Møller (1977)b
L4,7 vikingite	$Pb_8Bi_{13}Ag_5S_{30}$	13.603(6) 95.55	25.248(7)	4.112(4)	B2/m or Bm	Makovicky & Karup-Møller (1977)b
L4,8 treasurite	$Pb_6Bi_{15}Ag_7S_{32}$	13.349(10) 92.77(7)	26.538(20)	4.092(7)	B2/m or Bm	Makovicky & Karup-Møller (1977)b
L11,11 ourayite	$Pb_{15}Bi_{20.5}Ag_{12.5}S_{52}$	13.457(14)	44.042(40)	4.100(10)	Bbmm or $Bb2_1/m$	Makovicky & Karup-Møller (1977)b

Table 1.5: cont.

Symbol	Composition	a	b	c [Å]	Space	Reference
		α	β	γ [deg]	group	
schirmerite	sub-cell					
		4.089(4)	5.880(4)	4.106(4)	I2/m	Makovicky &
		91.13				Karup-Møller (1977)b
	full lattice contains non-integral satellites, c-axis becomes doubled					
P5	$AgBi_3S_5$	13.305	4.042	16.417	C2/m	Makovicky, Mumme
pavonite		94.02				Watts (1977)
galenobismutite	$PbBi_2S_4$	11.79	14.59	4.10	Pnam	Itaka & Nowacki (1962)

2 Introduction to theory of diffraction and bond-valence theory

This chapter starts with a brief account of the diffraction of X-rays and electrons by matter. Then it indicates how to interpret the diffraction patterns, and in the case of electrons, the images, to find crystal structures. The chapter finishes with a brief introduction to the bond-valence theory which is used in later chapters to analyse and model the structures.

2.1 General

Electrons and X-rays, although both can be treated as waves, interact with matter differently - their nature is different and so is the strength of the interaction. The X-ray electromagnetic wave weakly interacts with matter and consequently its scattering can be adequately treated in the kinematic approximation which describes diffraction as the simple sum of single scattering processes. The electron beam, which is a particle wave, interacts with matter strongly and the scattering of electrons has to be treated in the dynamical approximation i.e. with multiple interactions taken into account.

Another difference between the two radiations is that only the

electron beam can be focussed by electric and magnetic fields. There is no material which can be used as a lens for X-rays because of their small refractive index. Consequently, it is possible to produce magnified images of objects illuminated by electron beams but not by X-ray beams. With the latter only the "middle stage" of imaging process - the diffraction pattern - can be recorded.

The dynamical theory of electron scattering is complicated and approximations have to be used to establish the essential concepts of diffraction geometry and scattering amplitudes. One approximation, the weak-scattering kinematical approximation, developed for use in X-ray diffraction, is convenient for describing the geometry of electron diffraction patterns and images of crystals but it fails badly in describing the interactions between the electron beam and the crystal and hence cannot be used to calculate the expected appearance of high resolution electron microscope images because the dynamical-scattering effects are so strong. But it is because of the strong interaction that strong signals can be obtained from small numbers of atoms, making electron microscopy a powerful tool for investigating the structure of matter on an atomic scale. The complication of the image interpretation is an unavoidable adjunct of that capability.

Diffraction process

A specimen can be described by its transmission function, $q(\mathbf{r})$, (Cowley, 1975). Take a plane wave, $\psi_o(\mathbf{r}) = \psi \exp[-2\pi i\ (\nu t + \mathbf{r}\cdot\mathbf{k}_o)]$, with amplitude ψ, the wave vector $\mathbf{k}$ and frequency ν, illuminating the specimen. For elastic scattering this wave amplitude can be time averaged to give $\langle\psi_o(\mathbf{r})\rangle_t = \psi \exp[-2\pi i\ \mathbf{r}\cdot\mathbf{k}_o]$, the plane wave which will be considered thereafter. If the plane wave illuminates the sample the wave function at the exit surface of the specimen can be described as a function $\psi_1(\mathbf{r})$, represented as the product of the incident-wave amplitude $\psi_o(\mathbf{r})$ and the transmission function of the specimen $q(\mathbf{r})$. The exit wave has a phase and amplitude related to the specimen structure and is composed of a forward-scattered transmitted wave plus other scattered waves that proceed in directions inclined to it.

Kinematic scattering of waves observed at a distance large compared to the dimensions of the object defines Fraunhofer diffraction. The Fraunhofer diffraction is mathematically described by a Fourier-transform operation, denoted by $\mathcal{F}$, of the exit wave function $\psi_1(\mathbf{r}) = q(\mathbf{r})\psi_o(\mathbf{r})$ giving the Fraunhofer diffracted amplitudes $F(\mathbf{k})$, (Cowley, 1975):

$$\mathcal{F}[\psi_1(\mathbf{r})] \equiv F(\mathbf{k}) = \int_{-\infty}^{\infty} q(\mathbf{r})\exp(-2\pi i\mathbf{r}\cdot\mathbf{k}_o)\exp(2\pi i\mathbf{r}\cdot\mathbf{k}')d\mathbf{r} =$$

$$= \int_{-\infty}^{\infty} q(r)\exp[\ 2\pi i r\cdot(k'-k_o)\ ]dr$$

$$= \int_{-\infty}^{\infty} q(r)\exp(2\pi i r\cdot k)dr, \qquad k = k'-k_o \qquad (2.1)$$

Thus, the Fraunhofer diffracted amplitude, F(k), scattered in direction k', is obtained by applying the Fourier-transform operation on the transmission function of the specimen. Eq. (2.1) indicates that the diffracted amplitude, in general, will be a complex function.

Transmission function q(r) of a periodic object can be expressed by:

$$q(r) = \sum_S Q(s)\exp(-2\pi i s\cdot r) \qquad (2.2)$$

where $r = xa + yb + zc$, $s = ha^* + kb^* + lc^*$ and $a\cdot a^* = 1$, $a\cdot b^* = 0$ etc. and h, k, l are integers.

The diffracted amplitude, found by the Fourier transform of q(r), is:

$$F[q(r)] \equiv F(k) = \int_{-\infty}^{\infty} \sum_S Q(s)\exp(-2\pi i s\cdot r)\exp(2\pi i r\cdot k)dr =$$

$$= \sum_S Q(s) \int_{-\infty}^{\infty} \exp[\ 2\pi i r\cdot(k-s)\ ]dr = \sum_S Q(s)\ \delta(k-s) \qquad (2.3)$$

Hence the diffracted amplitude from an object with periodic transmission function q(r), is represented by a set of delta functions spaced with separation s in reciprocal space, each delta function having the weight Q(s) equal to the corresponding Fourier coefficient of q(r).

Eq. (2.3) expresses the Laue condition for diffraction. Since k represents the change of the wave vector on scattering (eq. 2.1) then the eq. 2.3 indicates that the diffraction occurs only if $\mathbf{k} = \mathbf{s}$, i.e. $\mathbf{k}$, the scattering vector, is also a reciprocal lattice vector and hence can be expressed as a function of the reciprocal lattice coordinates h,k,l giving k(h,k,l).

The above condition for diffraction can also be expressed by the Ewald construction of the sphere of reflection, shown in Fig. 2.1, where $\mathbf{k}_o$ and $\mathbf{k}'$ are the wave vectors of the incident and diffracted beams and $\mathbf{k} = \mathbf{s} = \mathbf{k}_o - \mathbf{k}'$ is the scattering vector. The reciprocal lattice of the object (crystal) has its origin at point O and diffraction occurs when a reciprocal lattice point, e.g. Q, lies on the sphere of radius $|\mathbf{k}'|$ centered on the crystal.

Imaging

The Fraunhofer diffraction pattern can be observed directly i.e.

without a lens, if viewed at a large enough distance and this is necessarily the way X-rays patterns must be viewed. The electron wave however, can be focused with an electromagnetic lens. The ideal thin lens brings the parallel transmitted wave to a focus on the axis in the back focal plane to give an image of the Fraunhofer diffraction pattern at the finite distance from the specimen. Then an image, either of the diffraction pattern or the crystal, can be produced at the image plane as shown in Fig. 2.2. For an ideally perfect lens, the image amplitude $\psi(x,y)$ would be an inverted, magnified reproduction of $\psi_1(x,y)$, the object. In propagation from the back focal plane to the image plane the interference process is inverted and the object wave function is re-created.

The interference of the waves generated at the object gives the Fraunhofer diffraction pattern in the back focal plane. Interference of the waves from the back focal plane re-creates the object wave function $\psi_1(x,y)$ in the image plane. The formation of the image is then described by two successive Fourier-transform operations, and apart from scaling factors, the equation is, (Buseck, Cowley, Eyring, 1988):

$$\psi(x,y) = F[F\psi_1(x,y)] = \psi_1(-x,-y) \qquad (2.4)$$

Transfer function of an instrument

Because of imperfections in the instruments with which the

diffraction patterns (and images) are obtained and recorded or because of the method of measurement, the intensities on the diffraction patterns (and thus the images produced from them) are changed from those which would be obtained by a perfect instrument. The influence of the instrument on the diffraction pattern can be generally described by a transfer function T. For X-ray experiment the recorded diffraction amplitudes (and thus intensities) are changed. For the electron scattering the diffraction amplitudes, their phases and the image are all changed since the transfer function of the lens multiplies the wave function $\psi(x, y)$ in the back focal plane, and thus modifies the wave amplitudes and phases of the Fraunhofer diffraction pattern of the object, preventing their proper interference needed to form an undistorted image. Including the transfer function, T, in eq (2.4) gives:

$$\psi(x,y) = F\left(T\, F\left(\psi_1(x,y)\right)\right) \qquad (2.5)$$

Structure determination

Both the recorded diffraction patterns and images can be used as the source of information about the crystal structure of the specimen. However, in the process of deducing the structure both cases present some difficulties: for X-rays only the diffraction pattern is available, for the electron wave an image of the

crystal structure can be formed but the dynamical interactions of the wave with the sample are complex and both these interactions and the lenses distort the image.

However, the approach taken in both cases is essentially the same. A model of the crystal structure, expressed by a model transmission function, is first proposed. The diffraction patterns and images of this model are then calculated by Fourier-transformation. For X-rays the calculated diffraction pattern (diffracted amplitudes) is compared with the observed diffraction pattern. In the case of the electrons the calculated images are compared with the observed images.

The methods available for proposing the models, and then refining them to fit the observations, are slightly different in both cases and will be discussed separately. The models themselves, however, have the same essential features which are introduced below.

The structure model

The model most commonly used by crystallographers in both X-ray diffraction and electron microscopy is the "Independent Atom Model" in which a crystal is made up by repetition in three dimensions of a unit cell containing one or more atoms (or ions). The atoms are assumed to be spherical and to perform harmonic

oscillations independently and anisotropically about their equilibrium positions. The aim of the structure determination is to find all the parameters of the model i.e. atoms positions (coordinates) in the unit cell and the parameters describing their anisotropic motion.

The next sections deal, separately, with the determination of crystal structure from X-ray and electron scattering experiments.

2.2 X-ray diffraction

Atomic X-rays scattering amplitude

The scattering of X-rays by matter is usually considered in terms of the scattering by a single electron, localized at the origin of coordinates and having some resonant frequency, ν_o, associated with it. A plane incident electromagnetic wave having an amplitude E_o and wave vector **k** can be described by the electric field displacement **E**:

$$\mathbf{E} = \mathbf{E}_o \exp(2\pi i \mathbf{k}\cdot\mathbf{r}) \qquad (2.6)$$

The Thompson scattering theory (Cowley, 1975) gives a radiated wave of amplitude:

$$E_s = -E_o \frac{e^2}{mc^2} r^{-1} \sin\alpha \exp(2\pi i \mathbf{k}\cdot\mathbf{r}) \qquad (2.7)$$

where r is the distance to the point of observation, α is the angle between the scattered beam and the direction of the electric vector, e-charge and m-mass of the electron.

It is customary to take $(e^2/mc^2)r^{-1}$ as the unit of scattering amplitude from one electron at the point of observation. We may define a distribution function of electron density for an electron, $\rho_e(r)$ such that the probability of finding the electron in volume dV, at the position r, is $\rho_e(r)dr$. Replacing $(e^2/mc^2)r^{-1}$ with $\int_{-\infty}^{\infty} \rho_e(r)dr$ in eq (2.7) gives:

$$E_s = -E_o \sin\alpha \int_{-\infty}^{\infty} \rho_e(r)\exp(2\pi i \mathbf{k}\cdot\mathbf{r})dr \qquad (2.8)$$

For the scattering of X-ray wave from an atom the the scattering from nucleus can be ignored relative to that of electrons as indicated by the mass in eq. (2.7). If $\rho_a(r)$ is the electron density in the atom then the eq. (2.8) becomes:

$$E_s = -E_o \sin\alpha \int_{-\infty}^{\infty} \rho_a(r)\exp(2\pi i \mathbf{k}\cdot\mathbf{r})dr \qquad (2.9)$$

The integral in the above equation defines the atomic X-ray scattering amplitude:

$$f(\mathbf{k}) \equiv \int_{-\infty}^{\infty} \rho_a(\mathbf{r}) \exp(2\pi i \mathbf{k}\cdot\mathbf{r}) d\mathbf{r} \qquad (2.10)$$

Values of $f(\mathbf{k})$ for free atoms are tabulated in the International Tables of X-ray Crystallography, Vols 3 and 4.

Although the above discussion has only concerned a single electron or a single atom, $\rho(\mathbf{r})$ generally can represent <u>any</u> electron density distribution including that in a crystal, $\rho_c(\mathbf{r})$ in which case $\rho_c(\mathbf{r})$ can be treated as the transmission function of the crystal.

Amplitudes of X-rays diffracted by a crystal

In order to calculate the amplitudes of X-rays diffracted by a crystal its full transmission function has first to be calculated. According to the "Independent Atom Model" an ideal crystal is made up by the repetiton in three dimensions of a unit cell containing one or more atoms. If $\rho_1(\mathbf{r})$ indicates the electron density associated with the atom centered at $\mathbf{r}=\mathbf{r}_1$ and '* ' represents the convolution operation defined as:

$$f(\mathbf{r}) * g(\mathbf{r}) = \int f(\mathbf{R}) g(\mathbf{r}-\mathbf{R}) d\mathbf{R} \qquad (2.11)$$

then the electron density, representing the transmission function of a unit cell containing n atoms, may be written as:

$$\rho(r) = \sum_{i=1}^{n} \rho_i(r) * \delta(r-r_i)$$

For the whole infinite crystal with periodicities a, b, and c the transmission function becomes:

$$\rho(r) = \sum_{j=-\infty}^{\infty} \sum_{i=1}^{n} \rho_i(r) * \delta[\, r-(r_i+T_j)\,]$$

where $T_j = va + wb + uc$ is the translation vector and v, w, u are integers.

For a finite crystal containing N^3 unit cells the transmission function is:

$$\rho(r) = \sum_{j=1}^{N^3} \sum_{i=1}^{n} \rho_i(r) * \delta[\, r-(r_i+T_j)\,] \qquad (2.12)$$

In crystals the atoms are assumed to vibrate thermally about their equilibrium positions with harmonic motion, so the time average of the electron density function $\langle\rho(r)\rangle_t$ around each lattice point is given by spreading the stationary electron density function $\rho_o(r)$ with a Gaussian function, G_i. For simplicity we treat the one dimensional case:

$$G_i(x) = [\, 2\pi(u_{ii})^2 \,]^{-1/2} \exp(\, -(x^2/2(u_{ii})^2 \,) \qquad (2.13)$$

where u_{i1} is the root mean-square displacement of an atom i from its lattice point in x direction. (in 1D $u_{i1} = u_i$).

The eq. (2.12) becomes:

$$\rho(x) = \sum_{j=1}^{N} \sum_{i=1}^{n} \rho_{oi}(x) * \delta[\, x-(x_i+v_j)\,] * [\, 2\pi(u_i)^2\,]^{-1/2} \exp(\, -(x^2/2(u_i)^2\,) \qquad (2.14)$$

where $\rho_{oi}(x)$ is the electron density of the i-th stationary atom in the unit cell and v_j is the component of the lattice translation vector T_j.

Eq. (2.14) introduces all the features of the Independent Atom Model into the transmission function of the crystal. However, real crystals usually deviate from this model in several ways:

1. In some crystals the assumed periodicity may be broken not only by the thermal motion of atoms but also by disorder. For example, some atoms may randomly occupy different positions in different unit cells (positional disorder) or different kinds of atoms may occupy the same position in different cells (substitutional disorder).
2. Unit cells may not be aligned exactly with respect to the neighbouring cells resulting in mosaic spread, stacking faults etc.

Thermal motion occurs in all crystals. The other kinds of

disorder may or may not occur to a significant extent depending on the crystal. Substitutional disorder was frequently found during this study and will be briefly discussed.

Assume the substitutional disorder occurs at a site i in the unit cell, i.e. a proportion, say p, of the available i sites are randomly occupied by atoms A and the rest, q=1-p, are occupied by atoms B. The average electron density at the i site, $\bar{\rho}_{oi}$, is then:

$$\bar{\rho}_{oi}(x) = p\ \rho_{oi}^{A}(x) + q\ \rho_{oi}^{B}(x) \qquad (2.15)$$

p and q are called atomic occupation numbers. Eq (2.15) substituted to eq (2.14) gives:

$$\rho(x) = \sum_{j=1}^{N} \sum_{i=1}^{n} \bar{\rho}_{oi}(x) * \delta[\ x-(x_i+v_j)\ ] * * [\ 2\pi(u_i)^2\ ]^{-1/2} \exp(\ -(x^2/2(u_i)^2\ ) \qquad (2.16)$$

The right hand side of the eq. (2.16) represents the transmission function of the crystal. The corresponding component $\bar{F}(h)$ of the diffracted amplitude F(k) is given by the Fourier transform of eq. (2.16) as:

$$F(k) = F\ [\ \rho(r)\ ]$$

$$F(h) = \sum_{j=1}^{N} \sum_{i=1}^{n} F(\bar{\rho}_{oi}(x)) \cdot F(\delta[\, x-(x_i+v_j)\,]) \cdot F(G_i(x)) =$$

$$= \sum_{i=1}^{n} \int_{-\infty}^{\infty} \bar{\rho}_{oi}(x)\exp(2\pi ihx)dx \sum_{j=1}^{N} \exp[\, 2\pi ih(x_i+v_j)\,] \exp[-2\pi^2h^2(u_i)^2] =$$

$$= \sum_{i=1}^{n} \bar{f}_i(h) \exp(2\pi ihx_i) \exp[\, -2\pi^2h^2(u_i)^2\,] \sum_{j=1}^{N} \exp(\, 2\pi ihv_j)$$

Since h and v_j are integers, then the last summation equals N, the number of the unit cells, and the above equation becomes:

$$F(h) = N \sum_{i=1}^{n} \bar{f}_i(h) \exp(2\pi ihx_i) \exp[\, -2\pi^2h^2(u_i)^2\,] \qquad (2.17)$$

where $\bar{f}_i(h)$ is the average scattering factor of atom i.

In three dimensions the eq. (2.17) has the form:

$$F(\mathbf{k}) = N^3 \sum_{i=1}^{n} \bar{f}_i(\mathbf{k}) \exp(2\pi i\mathbf{k}\cdot\mathbf{r}_i) \exp[\, -2\pi^2(\mathbf{k}\cdot\mathbf{u}_i)^2\,] \qquad (2.18)$$

The last exponential factor in eq.(2.18) is called atomic displacement parameter or Debye-Waller factor. Calculating $(\mathbf{k}\cdot\mathbf{u})^2$, where $\mathbf{k} = h\mathbf{a}^* + k\mathbf{b}^* + l\mathbf{c}^*$ and $\mathbf{u}(u_1, u_2, u_3)$, gives:

$$(\mathbf{k}\cdot\mathbf{u})^2 = (ha^*u_1 + kb^*u_2\ lc^*u_3)^2 =$$
$$= h^2a^{*2}u_1^2 + k^2b^{*2}u_2^2 + l^2c^{*2}u_3^2 +$$
$$+ 2hka^*b^*u_1u_2 + 2hla^*c^*u_1u_3 + 2klb^*c^*u_2u_3$$

The terms $u_m u_n$ can be treated as elements of a 3x3 symmetric matrix, $U_{mn} = u_m u_n$, and are called atomic displacement parameters. In general $U_{11} \neq U_{22} \neq U_{33}$ i.e. the thermal motion of an atom is anisotropic and U_{mn} are called anisotropic displacement parameters.

Eq. (2.18) is the equation used for calculating the diffraction amplitudes where $\bar{f}_l$, r_l and $U_{l,mn}$ are the parameters of the Independent Atom Model.

If the diffraction amplitudes, F(k), could be measured then the electron density $\rho(r)$ could be calculated from the equation:

$$\rho(r) = N^{-3} \sum_{k} F(k)\exp(-2\pi i k \cdot r) \qquad (2.19)$$

The above equation will, in general, yield a complex function for $\rho(r)$.

The intensity, I, of the diffracted radiation is proportional to $F(k)^* \cdot F(k) = |F(k)|^2$, where $F(k)^*$ is a complex conjugate of F(k). If the diffraction amplitudes could be measured, so that the phase as well as magnitude of F(k) could be derived, then the distribution of electron density $\rho(r)$ could be calculated using eq. (2.19). However, only the intensities (proportional to $|F(k)|^2$) can be recorded, thus information on the relative phases of the diffracted beams is lost and the function $\rho(r)$ cannot be

directly calculated from eq. (2.19).

Transfer function of the diffractometer

The intensity of the diffracted beams, proportional to $|F(k)|^2$, is changed by a transfer function, T, such that:

$$I_{measured} = |F(r)|^2 \cdot T \qquad (2.20)$$

where T = L p A. The three factors, L, p and A, are discussed below.

Lorentz effect (L)

Since the incident X-ray beam is never exactly collimated and the mosaic structure of the crystal introduces a certain width to the diffracted beam, the intensities are usually integrated over a volume in reciprocal space large enough to include deviations from the point at which the ideal diffracted peak occurs. To obtain the integrated intensities, the crystal is usually rotated about an axis perpendicular to the plane containing the incident and reflected beam, see Fig. 2.1, and the counter is rotated at twice the angular velocity, ($\theta/2\theta$ scan). The total intensity measured is proportional to the time, t, required for a particular point, Q, of the reciprocal lattice to pass through the sphere of reflection, thus the required correction L is also

proportional to t.

The time, t, is inversly proportional to the component of linear velocity of the reciprocal point normal to the sphere of reflection. The linear velocity with which the point Q moves is $\Omega|\mathbf{k}|$ where Ω is the angular velocity of the crystal (and of the reciprocal lattice) and $\mathbf{k}$ is the scattering vector. Since the angle between the velocity and the normal to the sphere is θ, then the angular velocity normal to the sphere is $\Omega|\mathbf{k}|\cos\theta$, which gives:

$$t = 1/\Omega|\mathbf{k}|\cos\theta \qquad (2.22)$$

Since $|\mathbf{k}| = 2|\mathbf{k}'|\sin\theta$, then eq. (2.22) yields:

$$t = 1/\Omega|\mathbf{k}'|\sin 2\theta$$

$|\mathbf{k}'|$ and Ω are constants in a given experiment so L, known as the Lorentz factor, depends only on the scattering angle 2θ:

$$L = (\sin 2\theta)^{-1} \qquad (2.23)$$

Polarization (p)

Equation (2.9) for the scattering amplitude by a single electron contains a number of physical constants, which are the same for

all scattering angles, and the trigonometric term, $\sin\alpha$, where α is the angle between the direction of the electric vector of the incident radiation and the direction of the scattered radiation. Non-polarized radiation is ordinarily used in X-ray crystallography, and it can be regarded as consisting of two components with their planes of polarization at right angles, one with the electric vector in the reflecting plane and the second with the electric vector perpendicular to this plane. For the first $\alpha = \pi/2-2\theta$, and for the second $\alpha = \pi/2$. This means that the component of the electric field parallel to the reflection plane reflects with 100% efficiency and the perpendicular component reflects with efficiency of $\cos 2\theta$ i.e.:

$$(E_{||})_{reflected} = (E_{||})_{incident} \qquad (2.24a)$$

$$(E_{\perp})_{reflected} = (E_{\perp})_{incident}\cos(2\theta) \qquad (2.24b)$$

Thus the polarization factor, p, that changes $|F(k)|^2$ is:

$$p = 1/2 + 1/2\cos^2 2\theta$$

If the initial beam is monochromated by a crystal with the Bragg angle θ_m, then it will be already partially polarized, and the two polarized incident beams will be of unequal intensity. The division of intensity between them depends on the angular relations between the original, pre-reflected and scattered

beams, but very commonly all three are coplanar. In such case the relative intensities of the two beams considered above will be $(1/2)\cos^2 2\theta_m$ and 1/2, instead 1/2 and 1/2. The final polarization factor is then:

$$p = \frac{1 + \cos^2 2\theta_m \cdot \cos^2 2\theta}{1 + \cos^2 2\theta_m} \qquad (2.25)$$

Absorption (A)

Crystals absorb X-ray radiation (more or less depending on elements present in them) to produce electronic excitations and release electrons from atoms. This effect can be taken into account by multiplying the transmission function of the crystal (eq. 2.16) by a factor $\exp(-\mu(r))$. However, this approach, although correct, is not practical since $\mu(r)$ will, in general, be a complicated function of the crystal size and orientation with respect to the incident and diffracted beams. The approach usually taken in practice is to treat absorption of the crystal as the transfer function of the crystal i.e. a factor which multiplies the intensity of the diffracted radiation by A, where A is the absorption function of the form:

$$A = 1/V \int_{\text{crystal}} \exp\,[-\mu(l+l')]\, dV \qquad (2.26)$$

where V-volume of the crystal and l and l' are path lengths

respectively of the incident and diffracted beam inside the crystal when the scattering takes place at volume element dV.

For a spherical crystal with a known radius, the values of A are tabulated in the International Tables for X-ray Crystallography (1959) vol II p.302, but for a crystal of arbitrary shape the values of A have to be calculated for each reflection by numerical evaluation of the integral (2.26). For favourable crystal shapes i.e. needle-like crystals mounted for rotation about the needle axis, a simpler approach can be taken. As shown by Furnas (1957) and later by North, Phillips and Mathews (1969) and by Kopfmann and Huber (1968, 1969) the absorption in the crystal can be evaluated by measuring the intensity of a Bragg reflection as the crystal is rotated about the normal to the corresponding reflection plane (so called Ψ axis). The observed variation of intensity for several reflections can be then converted into a correction expressed as a function of φ (angle of crystal rotation) and applied to all the reflections. This method (the Ψ scan method) was used in the present study.

The phase problem

As mentioned before only the intensities proportional to $|F(k)|^2$) can be recorded in X-ray diffraction experiment, thus information on the relative phases of the diffracted beams is lost. The

difficulty of overcoming this lack of the information constitutes the phase problem of crystal structure analysis. A great deal of ingenuity has been expended developing procedures to supply this missing information by using all the available knowledge about $\rho(\mathbf{r})$. This knowledge can be summed up in the following:

- $\rho(\mathbf{r})$ is a positive, real function having small near-constant value except for isolated peaks, weighted by the atomic numbers of the atoms, near the atom positions.
- The peaks are separated by a distance greater than some minimum value between 1 and 2Å.
- The number of atoms of each kind in the unit cell is known from the chemical analysis of the material, the unit cell dimensions (given by the geometry of the diffraction patterns) and the density of the crystal.
- The symmetry of $\rho(\mathbf{r})$ is known from the distribution of intensity in the diffracion pattern.
- In some cases, some a priori information about chemical structure may be known.

Structure determination methods

The main techniques which have been developed to assist in the determination of the phases of the scattering amplitudes $F(\mathbf{k})$ have been described in detail in a number of books (Lipson and

Cochran 1957, Stout and Jensen, 1989) and here will only be treated briefly.

The process of phase determination can be divided into three steps. The first step comprises development of a trial phase set sufficiently close to the correct one for further methods to be used. Such a model, a phasing model, is often incomplete i.e. only some of the phases are assigned. The rest have to be found in further steps of the structure determination. Only one method for developing the phasing model, the one which was used in this study, will be introduced here. This goes under the name of direct methods.

As pointed out earlier, the electron distribution in the crystal, $\rho(r)$, is a positive quantity at every point in the unit cell. The direct methods use this property as a constraint from which a set of trial phases can be assigned to a number of strong diffracted reflections. This assignment, based on inequality relationships between the magnitudes of the diffracted amplitudes (Harker and Kasper, 1948; Karle and Hauptman, 1950), is not unique and results in a number of trial sets of phases. Approximations to the electron density are then calculated using eq.(2.19) with the trial sets of phases. It is the role of a crystallographer to choose the electron density corresponding to the chemically most plausible trial arrangement of atoms, usually the heaviest atoms in the unit cell, and proceed to the second

step of the structure analysis.

In the second step the remaining, usually the lighter, atoms in the unit cell are located by <u>difference synthesis</u> (Cochran, 1951). The difference map is calculated using eq (2.29):

$$\Delta\rho(\mathbf{r}) = \frac{1}{V}\sum_{\mathbf{k}}\left(\,|\,F_o(\mathbf{k})\,|\,-\,|\,F_c(\mathbf{k})\,|\,\right)\exp(i\alpha_c)\,\exp(-2\pi i\mathbf{k}\cdot\mathbf{r}) \qquad (2.29)$$

where $F_c(\mathbf{k})$ is the diffraction amplitude calculated from the trial arrangement of atoms using eq. (2.18) and α_c is the phase of $F_c(\mathbf{k})$.

$\Delta\rho(\mathbf{r})$ corresponds to a point-by-point subtraction of an F_c-map (Fourier transform of $|F_c|\exp(-i\alpha_c)$) from the F_o-map (Fourier transform of $|F_o|\exp(-i\alpha_c)$) both calculated with the same phase α_c. Thus, the difference map has a positive peak everywhere the F_c model fails to provide the electron density implied by the measured diffraction amplitudes, $|F_o(\mathbf{k})|$, (when taken with the F_c phases) and a negative peak where it provides too much. As a first approximation, therefore, correctly placed atoms will not appear in the synthesis, incorrectly placed ones will be a complex mixture of positive and negative density, and missing ones will appear as positive peaks. Trial coordinates for all the atoms in the unit cell can usually be determined from a good starting model by successively applying this technique.

The last step in the structure analysis is the refinement. All the parameters of the model: coordinates of the displacement parameters of all the atoms and the occupation numbers of some atoms (depending on the crystal) are refined by the least squares to minimise the function:

$$\delta_{min} = \sum_{\substack{all \\ reflections}} w \left(|F_o| - k|F_c| \right)^2 \qquad (2.30)$$

where k is an overall scale factor necessary since the measured $|F_o|$ are on an arbitrary scale and w is the weight given to a reflection depending on its reliabity. Weights were calculated using eq. (2.31):

$$w = 1/(\sigma^2(F_o) + gF_o^2) \qquad (2.31)$$

where $\sigma(F_o)$ is the uncertainty in F_o derived from the counting statistics and g is a constant reflecting the error in the measurement of the diffracted intensity due to instabilities of the instrument (power supply etc.) and obtained in the process of the refinement.

Since F_c given by eq. (2.18) is not a linear function of the parameters of the model, a non-linear least-square method of refinement has to be used. Details of the underlying theory are

given in many books e.g. Stout and Jensen, (1989), and there are many computer programs developed for such refinements. SHELX76, (Sheldrick, 1976), was used in this study.

The functions:

$$R_w = \frac{\sum w\,(|F_o| - |F_c|)}{\sum w\,F_o} \qquad (2.32)$$

$$R = \frac{\sum (|F_o| - |F_c|)}{\sum F_o} \qquad (2.33)$$

are called residual indexes and are the indicators of the agreement between the observed structure and the assumed model. Correct structures generally have $R < 0.1$ and well refined structures have $R < 0.05$.

2.3 Electron diffraction and imaging

Atomic scattering amplitude for electrons

The property of matter which is of interest in calculations of elastic scattering of electrons is the electric potential distribution, $\varphi(r)$. The atomic scattering amplitude for electrons is defined (Cowley, 1975, 1988) as the Fourier

transform of the potential distribution for the atom, $F(\varphi(r))$:

$$f_e(k) \equiv \int_{-\infty}^{\infty} \varphi(r) \exp(2\pi i k \cdot r) dr \qquad (2.34)$$

Diffraction of electrons by a crystal

The refractive index for electrons, accelerated by the electric field E and passing through a medium with a potential field $\varphi(r)$, is (Cowley, 1975):

$$n = \frac{k/\omega}{(k/\omega)_o} = \frac{(E + \varphi(r))^{1/2}}{E^{1/2}} \cong 1 + \frac{\varphi(r)}{2E} \qquad (2.35)$$

where k and ω are the electron wave vector and frequency in the medium. The subscript o refers to k and ω in vacuum.

The phase difference for the wave passing through the potential field $\varphi(r)$ in z direction, relative to the wave in vacuum is then:

$$\frac{\pi}{\lambda E} \int_0^l \varphi(r) dz = \frac{\pi}{\lambda E} \varphi(x,y) = \sigma \varphi(x,y) \qquad (2.36)$$

where λ is the electron wavelength in vacuum, l is the thickness of the crystal, and $\sigma = \frac{\pi}{\lambda E}$ is an interaction constant. Thus, $\sigma \varphi(x,y)$ defines the strength of the interaction of electron waves with the medium.

For very thin specimens and fast electrons the following transmission function can be assumed (Cowley, 1975, 1988):

$$q_e(x,y) = \exp[\ -i\sigma\varphi(x,y)\ ] \qquad (2.37)$$

The above equation is called the phase-object approximation since this transmission function describes a change of phase but no change of amplitude of the electron wave passing through the object.

If $\sigma\varphi(x,y)$ is small then:

$$q_e(x,y) = \exp[\ -i\sigma\varphi(x,y)\ ] \cong 1 - i\sigma\varphi(x,y) \qquad (2.38)$$

which defines the weak phase-object approximation.
The corresponding scattered amplitude is:

$$F[q_e(x,y)] \equiv F(h,k) = \int_{-\infty}^{\infty} \exp(2\pi i\mathbf{k}\cdot\mathbf{r})d\mathbf{r} - \int_{-\infty}^{\infty} i\sigma\varphi(x,y)\exp(2\pi i\mathbf{k}\cdot\mathbf{r})d\mathbf{r} =$$
$$= \delta(h,k) - i\sigma f_e(h,k) \qquad (2.39)$$

where $\delta(h,k)$ represents the transmitted undiffracted beam and $f_e(h,k)$ the planar section of $f_e(\mathbf{k})$ defined in eq (2.34).

A perfect crystal gives only sharp diffracted reflections, but deviations from the perfect periodicity give rise to other types

of scattering. The defect scattering may take the form of a broadening or streaking of the sharp reflections, continuous sharp lines or broad lines, or general diffuse scattering in the background of the diffraction pattern. Electron diffraction is particularly well suited for the observation of defect scattering because, relative to X-ray or neutron scattering, the electron beams are intense and the samples have high-scattering cross sections and relatively weak diffuse-scattering effects can be observed.

Transfer function of a lens

A function describing the imperfections in the action of the lens system: the limitation of amplitudes by the aperture and the distortion of relative phases by the aberrations, is known as the transfer function of the lens.

In considering the distortion of the wave fronts by aberrations and the consequent loss of resolution, electron microscopy is fortunate that it is only necessary to deal with paraxial rays and small-angle scattering. It is usually possible to ignore the off-axis and higher-order aberrations that are important for light optics, and confine attention to the simplest axial aberrations: defocus, spherical aberration, astigmatism, and chromatic aberration. Astigmatism refers to differences in focal lengths of the magnetic field of the lens. This fault is common

in electron microscopes but can be corrected, with care, by stigmators that supply correcting fields. Defocus and spherical aberration are treated together as providing the most significant, cylindrically symmetrical perturbations of the phase change produced by a lens. Including the aperture, the total transfer function of the lens is:

$$T(k) = A(k)\ \exp(i\pi\Delta f\lambda k^2 + i\pi/2C_s\lambda^3k^4) \qquad (2.40)$$

where A(**k**) is the aperture function which cuts off some of the diffracted beams, and the first and the second term in the exponent represent the phase change due to defocus and spherical aberration, respectively.

The effect of the lens transfer function on images can be calculated by deriving the smearing function $s(xy) \equiv F(T(k))$. The best images obtainable with a lens of given spherical aberration coefficient C_s are found by choosing the defocus Δf such that s(xy) is as close as possible to a single, sharp peak with no subsidiary maxima. The optimum defocus was first calculated by Scherzer (1949) as: $\Delta f = -(1.33C_s\lambda)^{1/2}$. For this defocus the microscope transfer function is a slowly varying function of **k** for $|\mathbf{k}| < |\mathbf{k}_o| = 1.51C_s^{-1/4}\lambda^{-3/4}$. For higher values of **k** the signs of the transfer function reverse and oscillate rapidly so it is customary to insert an objective aperture to limit the diffraction pattern to $\mathbf{k}_o$. Alternatively, one may consider $\mathbf{k}_o$ as

determining the limit of the meaningful contributions to the image - that is, the resolution limit. On this assumption, the resolution limit, or in common parlance, the "resolution" is given by the inverse of k_o as: $\Delta x = 0.66 C_s^{1/4} \lambda^{3/4}$.

General dynamical scattering

"A simplified description of the dynamical interaction of electrons with a crystal is illustrated in Fig.2.3. The crystal is assumed to be made up of well-separated parallel planes of atoms. A plane wave passing through the first plane of atoms is modulated in phase because, in the phase-object approximation, the phase of the wave is changed in proportion to the projection of the potential distribution of the atoms. Hence, the plot of the phase of the wave as a function of lateral distance shows a periodic array of phase bumps. Next, the wave is propagated through space to the next plane of atoms. The propagation involves an interference effect, Fresnel diffraction, which complicates the phase distribution further, spreading out each of the phase bumps. Then, as the wave passes through the next layer of atoms, the phases are modified further, and so on. Gradually, the phase bump corresponding to any one row of atoms spreads out and overlaps with those from neighboring rows of atoms and interference effects occur, complicating the whole phase distribution. The wave leaving the crystal then has modulations very different from those for a single layer of atoms, although

the periodicity is the same. When the exit wave is imaged, the intensity distribution may be correspondingly complicated.", (Cowley, 1989).

In this quotation Cowley has oversimplified the description because the phase changes produced by passing through the potential field of a plane of atoms and the phase changes due to Fresnel diffraction actually occur simultaneously. The result remains, however, that unless the phase changes for the layers of atoms are very small and the crystal is very thin, we cannot assume that the effect on the wave will be simply proportional to the projected potential of the crystal.

There are a number of formal approaches to the dynamical transmission-scattering problem (Bethe, 1928; Hirsch et al., 1977; Cowley, 1985). One calculates the progressive modification of wave amplitudes or diffracted-beam amplitudes as the electron beam passes through the crystal. This is the basis of the multislice formulation of Cowley and Moodie (1957, 1958, 1959a, b) and Goodman and Moodie (1974) much used in calculations of the high resolution electron images (Skarnulis, 1976; Stedelmann, 1987).

Because of the complexity of the dynamical theory of the electron interaction with the sample and the influence of the lens system on the phases of the electron waves passing through it, a precise

calculation of the final phases of the diffracted amplitudes and using them to calculate the crystal structure of the specimen is very complex. As mentioned earlier, in this case, the experimental image is compared with a calculated image. For this purpose a model of the structure of the sample is needed. A technique capable of proposing such a trial model 'ab initio' analogous to, say, the direct methods developed for X-rays is not yet available for the electron diffraction. Thus, at present, the two diffraction techniques are complementary. X-ray diffraction provides precise average geometry but electron microscopy can image small regions revealing defects and disorder.

2.4 Bond-valence theory

Bond-valence theory has been developed by Brown (1981) as a means of describing the structural chemistry of inorganic solids. Each atom is assumed to possess a valence (V) which is a measure of its bonding power and which is characteristic of the atom. The valence can be thought of as the number of electrons taking part in chemical bonding. A molecule, crystal, or liquid consists of a network of atoms connected to each other by bonds and the number of bonds formed by an atom is called its coordination number (ν). The bonding graph is one in which all bonds have a Lewis acid (cation) at one end and a Lewis base (anion) at the

other.

Compounds with acid-base networks obey two empirical network rules:

1. The sum of bond valences at each atom is equal to the atomic valence:

$$\sum_j s_{ij} = V_i \qquad (2.41)$$

(valence sum rule)

2. The sum of bond valences around a loop is zero i.e.:

$$\sum_{\text{loop}} s_{ij} = 0 \qquad (2.42)$$

The above equations are similar to the Kirchhoff equations for electrical networks and they uniquely define the bond valences in cases where electronic effects, such as stereoactivity of electron lone pairs, are not important.

Correlations between the bond valence and the bond length have been found in such networks for many different types of bond by an examination of a large number of crystal structures (Brown and Shannon, 1973). A typical bond valence - bond length curve is shown in Fig. 2.4 and over the central part of its range it can be approximated by a logarithmic function:

$$s = \exp[(r_o - r)/B] \qquad (2.43)$$

where r is the bond length, r_o and B are fitted parameters. B can be chosen as 0.37Å for most bonds.

The Lewis acid strength of the cation, S_a is defined as:

$$(S_a) = V/\langle \nu \rangle \qquad (2.44)$$

where $\langle \nu \rangle$ is the average coordination number. S_a is a measure of cation's characteristic valence.

The Lewis base strength, S_b, of an anion or group can similarly be defined as the characteristic valence of a bond formed by the base.

The valence matching principle states that:

The most stable structures will be formed when the Lewis acid strength of the cation is most nearly equal to the Lewis base strength of the anion.

This principle stems from the fact that the actual valence of a bond formed by a cation is necessarily the same as the valence of the same bond at the anion. Since this value is expected to be close to both the acid strength of the cation and the base strength of the anion, these two strengths cannot be very diffferent from each other.

Because of their good correlation with bond length, bond valences have a number of practical applications in the analysis of crystal structures (Brown, 1978):

•Bond valences, calculated from the observed bond lengths, can be used through the valence sum rule, eq.(2.41), to calculate experimental atomic valences. Discrepancies between the experimental and theoretical valences may indicate that the structure has not been correctly determined or that it has not been correctly interpreted.

•The experimental atomic valences can be used to identify elements that cannot be distinguished by X-ray diffraction. Pb and Bi are difficult to tell apart since they have similar X-ray scattering powers and frequently occur in a similar environment in the same mineral. However, an atom can be identified as Bi if its atomic valence is found to be 3.0 and as Pb if it is found to be 2.0.

•The atomic valences can be used to calculate the occupation numbers of mixed occupancy sites in crystals as described below for lead-antimony sulphides.

Determination of occupation numbers by the bond-valence method

In structure determinations of the lead-antimony-sulphides, atomic occupation numbers of cations needed to be refined as partial occupation occurred in some sites. Although the atomic occupation numbers, p and q in eq. (2.15), of each such site could be refined, the program SHEXL76 did not provide a constraint to fix the total number of each kind of atom to a value that gives an electrically neutral formula. As a consequence the final formula, after the site occupancy refinement, was often not electrically neutral. To calculate the occupation numbers independently the bond-valence method was used.

To determine the site occupancies, the bond valences (s) are first calculated from the bond lengths (r) using the eq. (2.43). Valence sums around Pb atoms are expected to be 2, for Sb they should be 3, but for most cation sites the sums fall between 2 and 3 indicating mixed occupation. If p and q are the occupation numbers for Sb and Pb respectively, then the requirement that the sum of the bond valences at each site is equal to the oxidation number becomes:

$$p \sum s_{Sb} + q \sum s_{Pb} = pV_{Sb} + qV_{Pb} \qquad (2.47)$$

where s_{Sb} is the bond valence calculated with r_o(Sb-S) and s_{Pb} is the valence of the same bond calculated with r_o(Pb-S), V_{Sb}=3 and V_{Pb}=2. The values of p and q can be found recognizing that

$p + q = 1$ i.e. assuming that each site is fully occupied.

The chemical formula for the compounds calculated using these occupation numbers depends on the correct choice of r_o for the Sb-S and Pb-S bonds. Initially the values r_o(Pb-S)=2.541Å, r_o(Sb-S)=2.474Å and B=0.37, taken from Brown and Altermatt (1985), were used in the eq. (2.43) but in order to obtain electroneutral formula it was found necessary to change r_o(Sb-S) to slightly different values for each structure[1]. The value of B also had to be changed for the Sb-S bonds and the long Sb-S bonds (<3.6Å) had to be included to improve the valence sums at sulphur atoms. The bond valence parameters (r_o, B) obtained for all the structures were subsequently averaged and the following final set of parameters was used: r_o(Pb-S)=2.451Å, B(Pb-S)=0.37; r_o(Sb-S)=2.479Å, B(Sb-S)=0.42.

Because the occupation numbers derived from the bond-valences correspond to an electrically neutral crystal we consider them as more reliable and they were used as fixed parameters in the X-ray refinement with all positional and anisotropic atomic displacement

---

[1]An electrically neutral formula can be obtained either by decreasing the value of r_o(Pb-S) or increasing the value of r_o(Sb-S) or both. Decreasing r_o(Pb-S) leads to physically unreasonable occupation numbers for some sites (q<0). The best fit is reached by increasing the value of r_o(Sb-S)

parameters refined. Although, as expected[2] the residual indices, eqs 2.32 and 2.33, are slightly larger these refinements were used to generate the final atomic coordinates and the anisotropic atomic displacement parameters for each structure.

---

[2]The refinement with fixed occupation numbers has fewer parameters than the full refinement thus it will necessarily (Hamilton, 1965) yield larger agreement indexes.

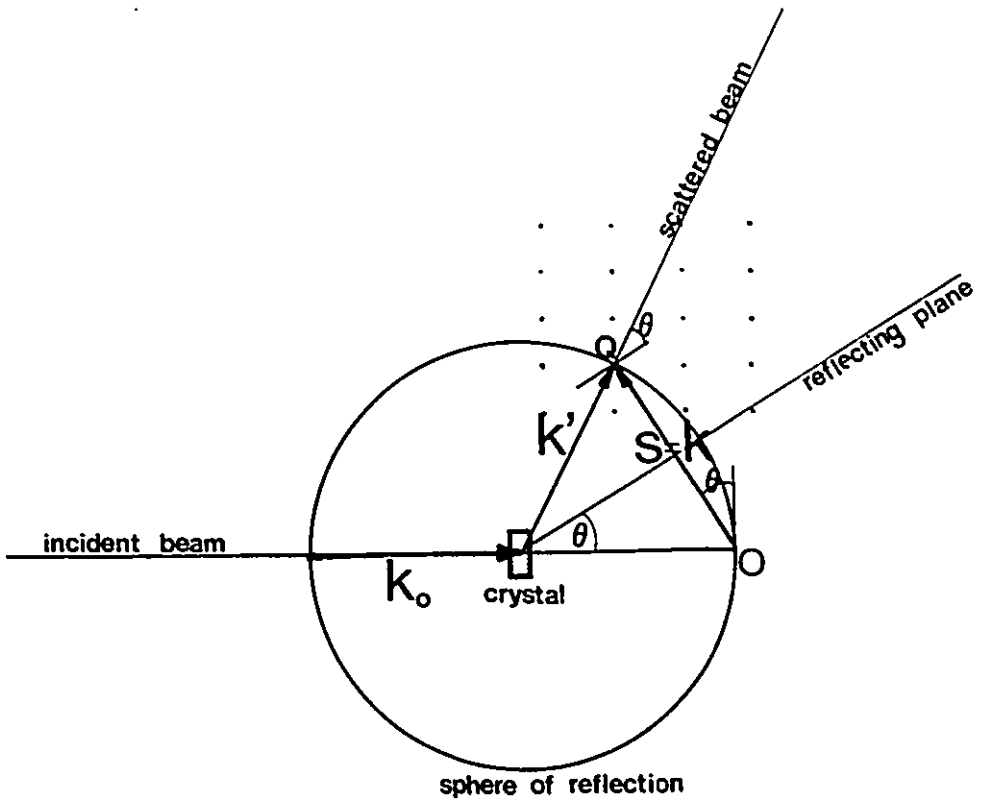

Fig. 2.1: The Ewald sphere of reflection. $\mathbf{k}_o$ and $\mathbf{k}'$ are the wave vectors of the incident and diffrated beams. $\mathbf{s}$ is the scattering vector.

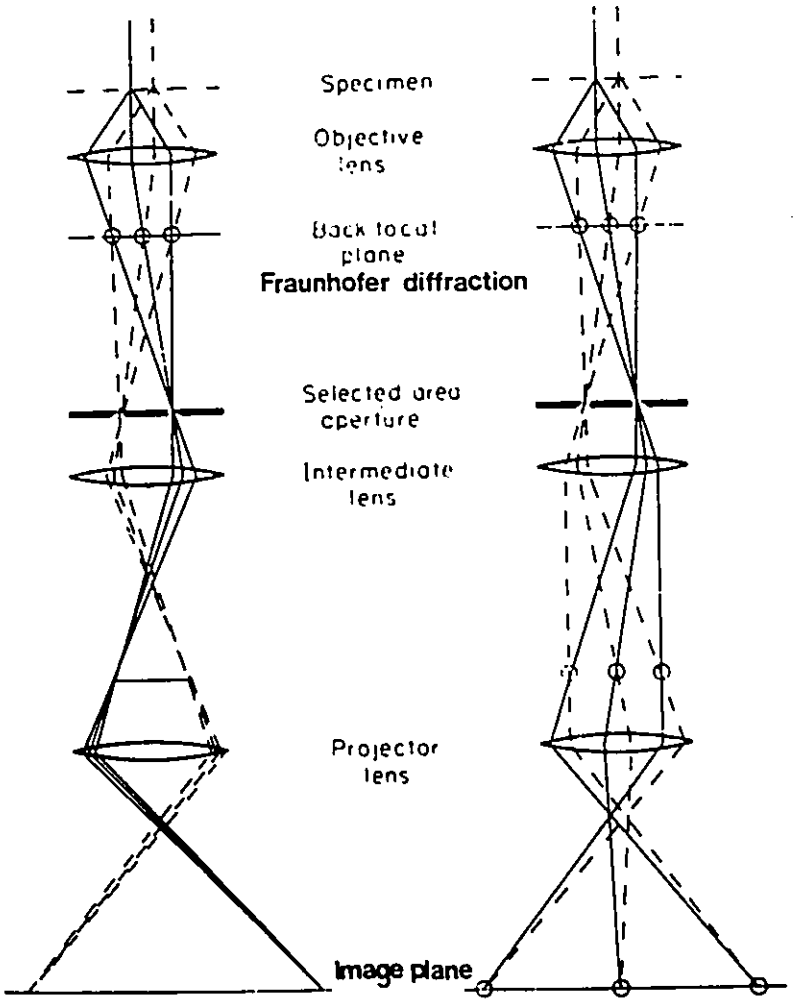

Fig. 2.2: The ray path in an electron microscope used (a) to produce a high magnification image and (b) to produce a diffraction pattern of a selected area of the specimen, (Cowley, 1975).

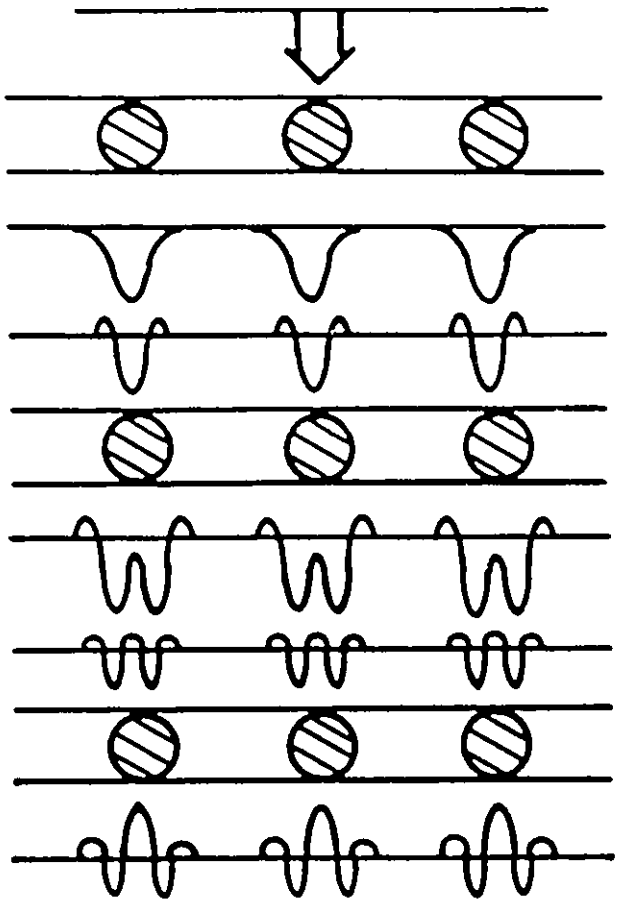

Fig. 2.3: Representation of the many-beam dynamical diffraction process in terms of the progressive modulation of an electron wave (Cowley, 1988).

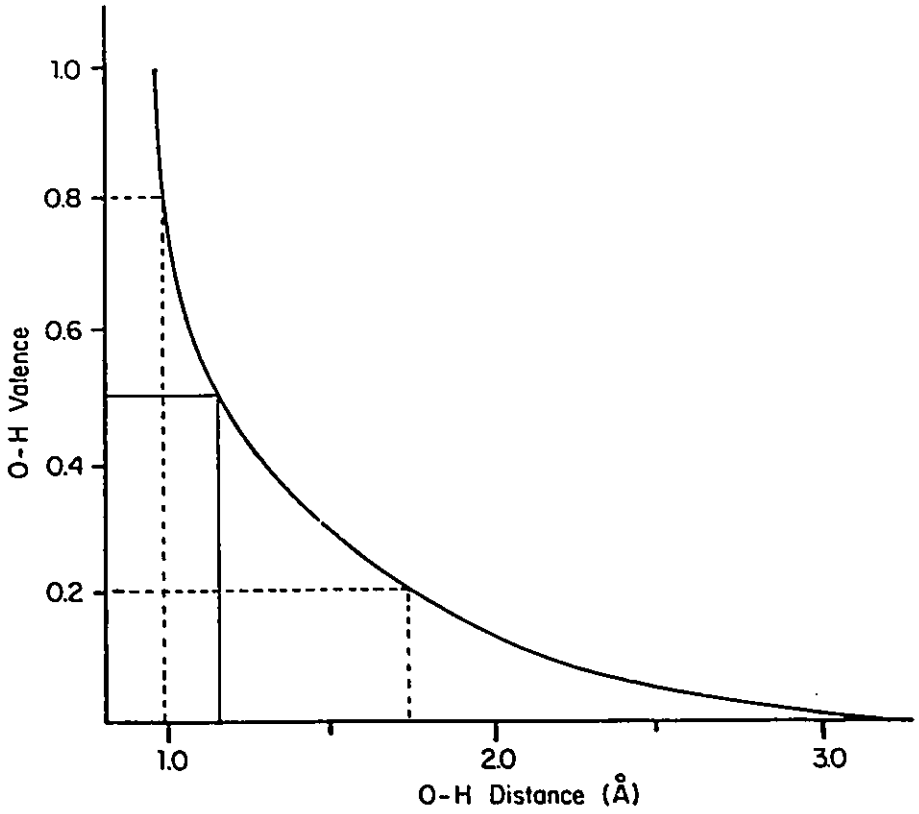

Fig. 2.4: Bond valence-bond length correlations for H-O bonds. The dotted lines indicate the valences and lengths found in normal asymmetric hydrogen bonds; the thin solid line indicates the valence and length found in symmetrical hydrogen bonds, (Brown, 1981).

3 Experiments

3.1 Materials and sample preparation technique

The samples were prepared from elemental lead, bismuth, silver, antimony and sulphur of 'Specpure' grade supplied by Johnson Matthey Ltd.. The total metallic impurity content of each chemical was stated by the manufacturer not to exceed 10 p.p.m. The lead, which was in the form of 7 mm diameter rods, was reduced to small pieces by paring with a fresh scalpel after initial removal of the tarnished outer surface. The bismuth and antimony were supplied in the form of lumps and were broken into fragments in a percussion mortar. The sulphur and the silver came as powders and were used without further treatment.

The starting materials were weighed in the proportions described in Appendix 1, into individual vials on a Mettler H15 balance to an accuracy of at least 0.001 gram. The total sample weight was approximately 1 gram. The materials were then transferred to clean silica tubes of 12.5 mm outside diameter with a 1.25 mm wall thickness. The sulphur was put in first followed by the metallic elements so as to prevent sulphur powder from being drawn up the tube during evacuation. During sealing, the reactants were cooled in a water bath to prevent evaporation.

The free space above the reactants in the sealed tube was kept to a minimum and this was usually at most 4 cm^3. The vacuum, measured with an ionisation gauge, had usually reached a pressure of 5 x 10^{-2} Pa after one hour of pumping. After sealing the samples were melted at approximately 1370K and then cooled as described in later sections.

3.2 Sample examination techniques

3.2.1 Powder X- ray diffraction

All samples were examined using X-ray powder diffraction. The materials were mixed with small amounts of KCl (a=6.2932Å at 298K) as an internal standard, and then ground in an agate mortar. The resulting powder was spread evenly over sellotape and mounted in an IRD Guinier-Hägg focusing camera of 50 mm radius, operated at 40kV and 20mA with monochromatic $CuK\alpha_1$ radiation at room temperature.

Interpretation of the X-ray powder patterns started with visual comparison with the ASTM library standards and other previously published powder patterns. Selected films were then measured using a monocular eyepiece. The measurement was performed relative to the printed scale on the film and the position of sharp, high angle edges of the reflections were recorded in this

way with an accuracy of 0.05 mm. The relative intensities of reflections were estimated visually. The lattice parameters were refined by the least squares method from the fit between the calculated and observed values of $\sin^2\theta$ using the program PARUM (Werner, 1969).

3.2.2. Single crystal X-ray diffraction

To identify the compound and ensure that the crystals were of good quality they were first examined on a precession camera. As all the studied compounds have a short, ≃ 4Å, axis parallel to the needle axis, the crystals were mounted with this axis parallel to the incident beam. In this way two long axes could be quickly aligned and identified. To find the crystal symmetry and the approximate unit cell dimensions, zero and first layer precession photographs were taken in two projections.

For intensity measurements the crystals were remounted with the needle axis along the goniometer axis and placed on a Syntex $P2_1$, a four-circle X-ray diffractometer. The unit cell parameters were refined from the Bragg angles of 15 well-centered reflections in the range $15^\circ < 2\theta < 30^\circ$ measured on the diffractometer using MoK_α radiation (λ=0.71069Å) monochromated with a high quality pyrolitic graphite crystal. The intensities were measured in the range $2\theta \leq 50^\circ$ with a $\theta/2\theta$ scan preceded and followed by a pair of background measurements. To monitor the crystal alignment and the stability of the X-ray source two

standard reflections were measured every 50 reflections. The absorption correction was based on Ψ-scans of several, usually 15-20, reflections and the intensities were corrected for Lorentz and polarization effects. Equivalent reflections were then averaged.

The initial atomic positions, found by direct methods using SHELXS, were refined using SHELX76 by full matrix least squares with anisotropic atomic displacement parameters for all the atoms and mixed Pb/Sb occupancies for the cation sites. Complex scattering factors for neutral atoms were taken from International Tables for X-ray Crystallography, (1974). If the Pb or Sb occupation numbers of some sites quickly refined to values close to 1.0 they were kept fixed at this value in the subsequent stages of the refinement.

3.2.3. Electron microscopy

To prepare the samples for electron microscopy the material was crushed (rather than ground in order to produce thin slices or wedge shaped fragments with thin edges) in an agate mortar under n-butanol. Because the liquid is both inert to the sample and of medium volatility, it was an ideal suspension medium. A drop of the suspension was allowed to dry on a holey carbon support film, the manufacture of which is described by Gannon and Tilley (1976).

Examination of the specimens was carried out on two instruments. A JEM 100B, operated at an accelerating voltage of 100kV and fitted with a top-entry, double-tilt goniometer stage (±30°), was used to conduct a statistical survey of each sample to record images from at least twenty fragments, if possible, and to provide a general picture of the microstructure of a given sample. However, the materials were very sensitive to the electron beam and the effective resolving power of 3.5Å for this instrument was insufficient to resolve the cation positions.

In order to obtain high resolution lattice images a JEOL 200CX electron microscope fitted with a high resolution objective lens pole piece (C_s=1.2 mm) and a top-entry, double-tilt goniometer stage, (±10°), operated at an accelerating voltage of 200kV was used. All the micrographs presented here were obtained using the JEOL 200CX since the materials were more stable in this instrument and it had higher resolution, 2.2Å, than JEM 100B.

First a suitable crystal fragment was sought; one with thin edges protruding over a hole in the carbon support film and oriented with its short crystallographic axis almost parallel to the electron beam. Since all the prepared materials were mechanically weak with cleavage planes parallel to the short axis such fragments were difficult to find. Next, the fragment was tilted until the short axis lay exactly in the direction of the beam. In order to decrease the effect of spherical aberration of

the objective lens and to remove scattered electrons, an objective aperture was inserted in the back focal plane of the objective lens. The image astigmatism and beam alignment were corrected by direct observation of perfection of the support film granularity at typical magnifications of x600,000 to x750,000. Images were recorded at a series of defocus steps near the Scherzer defocus [$\Delta f = -660$Å] to obtain optimum phase contrast. Exposure times were typically 4s at a magnification of x750,000.

Two major technical problems had to be overcome, viz. sample contamination and sample stability. To limit the contamination of the thin crystal edges with carbon from the support film, an anticontamination device, e.g. a cold finger, was placed close to the sample in the electron microscope chamber. Also, to limit both the contamination and heating of the sample in the beam the initial alignment was performed in a region a few microns away from the area of the final observation. The lowest possible illumination was used until the sample was well aligned and focusing of the beam was very gradual to avoid the sudden heating which was most damaging to the sample.

The recorded lattice images were compared with the theoretical electron micrographs obtained by computer simulation performed with a program system written by A.G. Skarnulis (1976) and Stadelmann (1987).

4 Structures in the PbS-Sb_2S_3 system

Six different phases were isolated with crystals large enough to be used for X-ray diffraction and as a result the structures of two compounds, $Pb_2Sb_2S_5$; S4,4 and $Pb_5Sb_6S_{14}$; R7,(2,2) were determined for the first time and the structures of two others, boulangerite; B(3,6)(3,6) and robinsonite; R6,(2,2) were refined. Additionally two more compounds, $Pb_3Sb_2S_6$; S5,5 and $Pb_7Sb_4S_{13}$; B(4,7)(4,7) were characterized by their lattice parameters measured on precession photographs and their structures proposed by an analogy with previously solved or refined structures.

The precise bond distances determined in the structures allowed the distortion of the metal polyhedra to be examined and an independent determination of the occupation numbers using the bond-valence method as described in chapter 2.

$Pb_5Sb_6S_{14}$ was found in our electron microscope study. High resolution electron micrographs suggested a model for the structure and indicated that the phase decomposed under electron irradiation to a galena-like structure. Models for the decomposition could be proposed on the basis of the high

resolution electron micrographs.

This chapter starts with a description of the sample preparation and the powder X-ray diffraction phase analysis. The results of the single crystal X-ray structure determinations are then presented, followed by the analysis of the coordination polyhedra. The results of the electron microscope study constitute the last part of this chapter. Most of the material presented in this chapter has been published in Skowron and Brown, (1990 a, b, c) and Skowron, Brown and Tilley (1990).

4.1 Sample preparation and phase analysis by powder X-ray diffraction

Thirty six samples with compositions 90-52 mole % of PbS were prepared in the PbS - Sb_2S_3 system by slow cooling from the melt to 723K, annealing for 3 weeks and then brine quenching. In some preparations phase separation occured and crystals grew on the bulk material or on the ampoule walls in a mass of tangled very thin needles.

The results of the phase analysis are summarized in Table 4.1. Five compounds could be unambiguously identified in the samples annealed at 723K: galena, boulangerite, robinsonite, zinckenite and a phase with the approximate composition and powder

diffraction pattern reported by Wang (1976) for $Pb_5Sb_6S_{14}$. The compounds found in these samples agree with those expected from the phase diagram at 723K, Fig. 1.1, except that $Pb_5Sb_6S_{14}$ was not found by Salanci, (1979). Wang, (1976), reported the lower stability limit for $Pb_5Sb_6S_{14}$ as 733K but the samples reported here were equilibrated at a slightly lower temperature (723K).

To grow single crystals, the melts with the corresponding compositions were brine quenched and the resulting ingots ground, pressed into approximately 1g pellets and, after addition of approximately 1 mg of I_2, annealed in a two zone horizontal furnace for three days. Each pellet was placed at the end of an approximately 20 cm long ampoule and held at temperatures close to those reported by Wang (1976) and listed in Table 1.1, with the other end kept at a temperature some 50K higher.

These preparations yielded three additional compounds: $Pb_2Sb_2S_5$, $Pb_3Sb_2S_6$ (both synthesized before by Wang, 1976, 1977) and a new compound: $Pb_7Sb_4S_{13}$.

4.2 Single crystal X-ray structure determinations

Six compounds gave crystals large enough for X-ray diffraction studies. Their crystallographic parameters are given in Table 4.2. The structures of four were determined using the procedure described in chapter 3 section 3.2.2, while the

structures of the other two were proposed on the basis of their diffraction patterns recorded on the precession photographs.

4.2.1 $Pb_2Sb_2S_5$-orthorhombic, S4,4

The experimental and computational parameters used in the structure determination are listed in Table 4.3. The systematic absences, 0kl: k=2n+1; h0l: h+l=2n+1, found on precession photographs, indicate the space groups Pbnm or $Pbn2_1$. The former was chosen and led to a satisfactory refinement. The Sb occupation number of site 1 quickly refined to value close to 1.0 and was kept fixed at this value in the subsequent stages of the refinement. The refinement converged to wR=0.058, R=0.067, goodness of fit s=1.40.

The refined occupation numbers, shown in column 2 of Table 4.4, result in the formula $Pb_{1.44}Sb_{2.56}S_5$ which is appreciably different from the expected electrically neutral formula $Pb_2Sb_2S_5$. An independent set of occupation numbers was determined using the bond-valence method as described in chapter 2. The valence analysis is presented in Table 4.5 and both the X-ray and valence occupation numbers are compared in Table 4.4. The sites M(1) and M(2) have similar occupations as determined by both methods but the valence sums for the M(3) and M(4) sites are close to 2.0 (2.08, 2.06) which suggests that the sites are richer in lead than the 70% indicated by the X-ray refinement.

The occupation numbers determined from the bond valences were used as fixed parameters and all positional and anisotropic atomic displacement parameters were refined yielding wR=0.063, R=0.071 and s=1.56. This refinement was used to generate the final atomic coordinates listed in Table 4.6 and the anisotropic atomic displacement parameters listed in Table 4.7. Interatomic distances are given in Table 4.8.

The structure of one unit cell of $Pb_2Sb_2S_5$, shown in Fig. 4.1, is the same as that proposed by Smith and Hyde, (1983). It consists of ribbons composed of square pyramidal $(Pb,Sb)S_5$ groups and according to the classification outlined in chapter 1 can be represented as S4,4. The antimony occupies the 5-coordinated sites on the side of the ribbon that faces a neighbouring ribbon. Lead occupies the 8- and 7-coordinated sites on the other side of the ribbon.

4.2.2. Boulangerite, B(3,6)(3,6)

The experimental and computational parameters used in the structure determination are listed in Table 4.9. The systematic absences, 0kl: k+l=2n+1; h0l:h=2n+1, found using precession photographs indicate the space groups as Pnam or $Pna2_1$. The first was chosen and led to a satisfactory refinement. The Pb occupation numbers of sites 13, 14 and 15 quickly refined to

values close to 1.0 and were kept fixed at this value in the subsequent stages of the refinement. The refinement converged to wR=0.066, R=0.075 and s=1.51.

The valence analysis is presented in Table 4.11 and both the X-ray and valence occupation numbers are compared in Table 4.10. The two sets of the occupation numbers are similar. Those determined by the bond-valence method give more Pb in all the mixed sites approximately uniformly.

The occupation numbers determined from the bond valences, corresponding to an electrically neutral crystal, were used as fixed parameters in SHELX76 and all positional and atomic displacement parameters were refined to obtain wR=0.068, R=0.077 and s=1.56. This refinement was used to generate the final atomic coordinates listed in Table 4.12 and the anisotropic atomic displacement parameters listed in Table 4.13. The interatomic distances are given in Table 4.14.

The unit cell of boulangerite is shown in Fig. 4.2 confirming the general features of the structures reported by Born and Hellner, (1960), and Petrova et al. (1978). The structure consists of two types of ribbon made of back to back square pyramidal $(Pb,Sb)S_5$ groups and according to the classification presented in chapter 2 can be symbolically described as B(3,6),(3,6). The cation sites where parallel ribbons face each other mostly contain

5-coordinated antimony. The cation sites on the faces that connect to the edges of other ribbons have higher coordination numbers and are occupied by lead. All the cation positions in the narrow ribbon have mixed occupancy, while there is only one such site in the wide ribbon.

There were two structure determinations of boulangerite prior to this study, Born and Hellner (1960), and Petrova et al. (1978). Born and Hellner measured the intensities on two layers of Weissenberg photographs and used only strong reflections in their refinement of the structure. Petrova et al. measured 936 independent reflections on a P1 Syntex diffractometer. In both structure refinements, isotropic atomic displacement parameters were used and the measured intensities were not corrected for absorption. In their determination, Born and Hellner (1960), split the Sb(11) atom in the xy plane. In the present study, the structure refined satisfactorily without such a splitting but a large atomic displacement parameter U_{11} (0.062Å^2) was found in this site. The agreement indexes obtained by Born and Hellner were 0.176 and by Petrova et al. 0.102, both considerably larger than those obtained here indicating that the present refinement should be much more accurate.

Born and Hellner (1960) used $\frac{1}{2}(f_{Pb}+f_{Sb})$ scattering factors for

M(2), M(3) and M(12) sites[3] while Petrova et al. refined the occupancies for M(1), M(2), M(3) and M(12) sites obtaining the occupation numbers shown in column 2 of Table 4.10. In the present study the occupation numbers determined using the bond valence method from the interatomic distances are more accurate then those obtained before and therefore more reliable.

4.2.3 Robinsonite, R6,(2,2)

The experimental and computational parameters used in the structure determination are listed in Table 4.15. The systematic absences, hkl: h+k+l=2n+1, and the symmetry of the intensities of the reflections observed on precession photographs, indicate I2/m, I2, or Im as possible space groups. The first was assumed and led to a satisfactory refinement. The Pb occupation numbers of sites 13 and 14 quickly refined to values close to 1.0 and were kept fixed at this value in the subsequent stages of the refinement. The refinement converged to wR=0.061, R=0.068 and s=2.2. The bond valence analysis is presented in Table 4.17 and both the X-ray and valence occupation numbers are compared in Table 4.16.

The occupation numbers determined from the bond valences were

[3]The chemical formula resulting from Born and Hellner assignment does not correspond to an electrically neutral crystal.

used as fixed parameters in SHELX76 and all positional and atomic displacement parameters were refined to obtain wR=0.064, R=0.071 and s=2.4. This refinement was used to generate the final atomic coordinates listed in Table 4.18 and the anisotropic atomic displacement parameters listed in Table 4.19. The interatomic distances are given in Table 4.20.

The unit cell of robinsonite is shown in Fig. 4.3. The structure consists of two types of ribbon made of back to back square pyramidal $(Pb,Sb)S_5$ groups and, according to the classification presented in chapter 2, can be symbolically described as R6,(2,2). Antimony favors the 5-coordinated metal sites found where one ribbon faces a parallel ribbon. The Pb atoms occupy positions of higher coordination number found at sites where the face of one ribbon meets the edge of a different ribbon.

Several crystallographic studies, summarized in Table 1.2 of chapter 1, have been devoted to both mineral and synthetic robinsonite. Our unit cell agrees with most previous results but only Petrova, Kaplunnik, Bortnikov, Pobedimskaya and Belov (1978) report the structure. The space group they use (P1) differs from that (B2/m) assigned by Wang (1977) and they also appear to have permuted the lattice angles. Jumas, Olivier-Fourcade, Phillipot and Maurin (1980) have reported a similar structure for $Sn_4Sb_6S_{13}$ in the same space group, I2/m used here (equivalent to Wang's B2/m). In their determination, Petrova et al. used isotropic

atomic displacement parameters, did not correct the intensities for absorption, and obtained an agreement index of 0.099.

Our determination confirms the general features of the structure reported by Petrova et al. (1978) but indicates that they missed the mirror plane and center of symmetry. By ignoring this higher symmetry they were able to refine a model without using sites of mixed occupancy. As a check on their determination, the interatomic distances obtained by Petrova et al. were used to calculate the bond valences and occupation numbers[4]. The resulting Pb/Sb distribution is presented in Table 4.21 with the pseudo-symmetry related positions listed together. Petrova et al. put different metal atoms in two of the positions that are related by centers of symmetry in I2/m (sites 1 and 15 using our notation). However, the bond-valence calculation indicate that both sites of each pair have mixed Pb/Sb occupancies. In site no. 1 especially, the pseudo-symmetry related positions are calculated to have very similar occupations. The average of the bond-valence occupancies found for the pseudo-symmetry related sites in Petrova's structure, shown in the last column of Table 4.21, and column 2 of Table 4.16 are very similar to the occupancies found in the present determination, column 4 of

---

[4]In the bond-valence analysis of the structure determination by Petrova's et al. r_o(Sb-S)=2.50Å and B=0.37Å was used to obtain an electroneutral formula.

Table 4.16.

In the diffraction patterns on the precession photographs obtained in this study there was no evidence of the loss of monoclinic symmetry implied by the space group P1 reported by Petrova et al. Further, the refined atomic displacement parameters, U_{33}, do not have large values and are consistent with all the atoms lying on mirror planes.

Jumas, Olivier-Fourcade, Philippot and Maurin, (1980), refined the structure of the homeotypic $Sn_4Sb_6S_{13}$ from single crystal X-ray diffraction measurements in the space group I2/m, but the difficulty in distinguishing Sn from Sb by X-rays made the assignment of the cation site occupancies impossible. They assigned antimony mostly to the wide ribbon and tin to the narrow but this results in unsatisfactory bond-valence sums. A bond-valence analysis on $Sn_4Sb_6S_{13}$ using r_o=2.437Å for Sn-S and r_o=2.52Å for Sb-S bonds gives the Sn/Sb distribution presented in Table 4.16 (shown together with the authors' original assignment). The distribution of Sb atoms is very similar in both the Sn and Pb analogues.

4.2.4. $Pb_5Sb_6S_{14}$, R7, (2,2)

The experimental and computational parameters used in the structure determination are listed in Table 4.22. The systematic

absences, hkl: h+k+l=2n+1, found on precession photographs, indicate I centering and the intensities showed a pseudo-mirror plane normal to b. The body centered space group reflects the pseudo-monoclinic cell better than the more usual $P\bar{1}$ setting .

Pb occupation numbers of sites 14 and 15 and Sb occupation numbers of sites 3, 4 and 10 quickly refined to values close to 1.0 and were kept fixed at this value in the subsequent stages of the refinement. Because of large positive peaks in the electron density difference maps and large thermal displacement parameters in the b direction of three mixed occupancy sites, M(11), M(12), M(13), and one antimony site, M(10), these positions were split in the b direction and, by trial and error, Pb was placed in sites denoted M(11)a, M(12)a and M(13)a and Sb in sites M(11)b, M(12)b, M(13)b keeping the total occupation of a site equal 1.0. The y coordinates of the split positions were heavily correlated in the refinement and they were also correlated with the thermal displacement parameters in this direction (correlation factors between 0.60-0.91). The antimony atoms in sites 3 and 4 also had high U_{22} atomic displacement parameters ($\cong 0.057\text{Å}^2$) but were left unsplit because the atomic displacement parameters were approximately $0.03\text{-}0.05\text{Å}^2$ smaller than those in sites 11-13 before introducing the splitting. The refinement converged to wR=0.087 R=0.099 and s=1.74. The valence analysis is presented in Table 4.24 and both the X-ray and valence occupation numbers are compared in Table 4.23.

The occupation numbers determined from the bond valences were used as fixed parameters in SHELX76 and refined all positional and atomic displacement parameters to obtain wR=0.100, R=0.088 and s=1.74. This refinement was used to generate the final atomic coordinates listed in Table 4.25 and the anisotropic atomic displacement parameters in Table 4.26. The interatomic distances are given in Table 4.27.

The unit cell of $Pb_5Sb_6S_{14}$ is shown in Fig. 4.4. The structure is closely related to robinsonite, R6,(2,2), and can be obtained from it by inserting an additional pair of back to back PbS_5 pyramids into the middle of the wide ribbon of robinsonite. $Pb_5Sb_6S_{14}$ can therefore be represented as R7,(2,2). Sb prefers the 5-coordinated sites which occur at the places where each ribbon faces a parallel ribbon while Pb favours the higher coordinated sites where the face of one ribbon meets the edge of a neighbour.

4.2.5 $Pb_7Sb_4S_{13}$, B(4,7)(4,7)

The diffraction pattern of $Pb_7Sb_4S_{13}$, obtained using the precession method[5], is shown in Fig. 4.5a and that of

[5]The crystals of $Pb_7Sb_4S_{13}$ were not suitable for the intensity measurement on the diffractometer due to twinning.

boulangerite, $Pb_5Sb_4S_{11}$, in Fig. 4.5b. The strong reflections, visible on both diffraction patterns, correspond to the reflections of the PbS-like sublattice in [011] projection and show that the orientation of the PbS-like sublattice with respect to the crystal lattices of both $Pb_7Sb_4S_{13}$ and $Pb_5Sb_4S_{11}$ is the same. These observations suggest that the structures of the two phases are closely related and are built of PbS-like fragments arranged in the same way. The a and c lattice parameters of $Pb_7Sb_4S_{13}$, measured on the precession photographs and shown in Table 4.2, are close to those in bouiangerite, while b is ≅ 4Å larger. The structure of $Pb_7Sb_4S_{13}$ can thus be derived from that of boulangerite, B(3,6)(3,6), by inserting an additional pair of back to back PbS_5 pyramids in both narrow and wide ribbons. This results in a B(4,7)(4,7) structure for $Pb_7Sb_4S_{13}$ with ≅ 4Å increase in b parameter. The proposed unit cell of $Pb_7Sb_4S_{13}$, is shown in Fig. 4.6.

4.2.6 $Pb_3Sb_2S_6$, S5,5

The intensity distribution in the diffraction patterns of $Pb_3Sb_2S_6$ and $Pb_2Sb_2S_5$ are, like those of $Pb_7Sb_4S_{13}$ and $Pb_5Sb_4S_{11}$, quite similar suggesting that the structures of $Pb_3Sb_2S_6$ and $Pb_2Sb_2S_5$ are closely related. The a and c lattice parameters of $Pb_3Sb_2S_6$, shown in Table 4.2, are close to those in $Pb_2Sb_2S_5$ while b is ≅ 4Å bigger. The structure of $Pb_3Sb_2S_6$ can thus be derived from that of $Pb_2Sb_2S_5$, S4,4, by inserting an additional

pair of back to back PbS_5 pyramids in the ribbon. This results in S5,5 structure for $Pb_3Sb_2S_6$ with increase in b parameter of ≅ 4Å. The proposed unit cell of $Pb_3Sb_2S_6$, S5,5, is isotypic with the structure of the copper free meneghenite shown in Fig. 1.14.

4.3 Discussion of the X-ray structure determinations

Although the chemical analysis was not performed on the single crystals grown in the presence of iodine, no crystallographic anomalies on the sulphur sites were observed suggesting that iodine was not incorporated into the structures but merely facilitated the chemical transport of the elements to give better crystal growth.

There has been some discussion in the literature on the existence of the mirror plane normal to the b axis in robinsonite. Wang (1977) found the space group B2/m for robinsonite but recognized that the apparent mirror plane symmetry might be caused, not by the true symmetry of the structure, but instead by an intimate twinning of domains in which the cations are displaced about the mirror plane in opposite directions. Because he had only the evidence of the precession photographs, and the results published prior to his work (Robinson, 1948a, Berry, 1952) indicated lower symmetry, he could not confidently decide what the true symmetry of the crystal was. The same reservations about the existance of the mirror plane were expressed by Makovicky (1981) who, after

the structure determination of Petrova et al. (1978), favoured the SnS type structure as the archetype for robinsonite and attributed the apparent symmetry to twinning. However, the present determination of the crystal structure, leaves no doubt that the mirror plane symmetry is preserved and that no twinning of domains occurs as there are no large atomic displacement parameters and no splitting of atom sites. The solution of the structure of $Pb_5Sb_6S_{14}$; R7(2,2) shows that a true lowering of the crystal symmetry can be readily detected if present. The two structure determinations suggest that there is no evidence of intimate twinning involved in either robinsonite or $Pb_5Sb_6S_{14}$. Instead, recalling that there is a broad phase transition of SnS from SnS type to TlI type structure, it is possible that in $Pb_5Sb_6S_{14}$ the SnS archetype occurs at an intermediate stage in a broad transformation towards TlI, while in robinsonite the structure has passed through the transition and assumed the higher symmetry TlI structure.

4.4 Structures interpretation

In chapter 1 it was shown that the structures in the PbS-Sb_2S_3 system could be classified into a number of homologous series based on boulangerite, robinsonite etc. The structure analysis of the six compounds in the PbS rich part of the system shows that the structures belong to three series (S, B and R), and robinsonite and boulangerite, which were thought to be single

examples of a type of structure, are in fact only the first members of two different series.

Cation distribution

The observed cation distribution in all the structures is such that antimony favours the 5-coordinated sites where the parallel parts of the ribbons face each other, while lead occupies the higher, 7- or 8-coordinated sites in places where the ribbons join. In all structures the cation sites at the edge of the wide ribbons are fully occupied by antimony.

Cation coordination polyhedra

The nearly square pyramids which compose the ribbons are distorted in two ways, in apical direction and in the base of the pyramids.

The first, apical distortion, is the more pronounced and corresponds to the apical bond of the pyramid being the shorter than the four equatorial bonds. In addition to the five bonds within the pyramid there are two weak bonds opposite to the apical, those connecting the parallel neighbouring ribbons, which are much longer (>3.4Å) than the bonds within the pyramids. Including these bonds in the coordination polyhedra gives (1+4+2) coordination. The substitution of Sb for Pb increases the distortion e.g. the short apical bonds become shorter and the two long ones, opposite to the apical bond, become longer. The

increasing distortion reflects the influence of the cation's lone electron pairs projecting from the surface of the ribbons.

The bond valences (s) of the apical bonds vary linearly with the atomic valence (V) according to eq.(4.1), Fig. 4.7:

$$s = 0.68\ V - 0.95 \qquad (4.1)$$

where s = bond valence and V = oxidation of a site, (goodness of fit 94%).

For the long bonds, a parabolic relationship between V and the sum of the valences of the two opposite long bonds, given by eq.(4.2), is shown in Fig. 4.7.

$$s = 0.31\ V^2 - 1.83\ V + 2.78 \qquad (4.2)$$

The goodness of fit is 90%. The mean valence of the apical bond for a fully antimony occupied site is 1.01 v.u. while for the lead occupied site it is only 0.46 v.u. The two long bonds, opposite to the apical, have their total bond valence close to 0.1v.u. for the antimony and 0.3v.u. for lead sites.

The long bonds are the bonds external to the ribbons so the segregation of lead into certain parts of the ribbon faces is related to the concentration of external bonding capability of

ribbons in certain regions.

The second distortion of the pyramids is smaller then the apical distortion and occurs within the bases of the pyramids in those parts of the ribbon which are occupied by antimony. The two symmetry distinct pairs of basal bonds are not equal, the antimony atoms are displaced in the mirror plane towards the edges of the ribbons, as shown in Fig. 4.8. This distortion has a natural explanation in the bond valence theory. The antimony atoms, having a higher valence than the sulphur atoms to which they are bonded, will want to form stronger bonds than sulphur. The S atoms bonded to an Sb in the middle of the ribbon will form weaker bonds to their other Sb neighbours, which in turn must form even stronger bonds to the next S atoms etc. The result will be a tendency for the Sb atoms to bond more strongly to the S atom near the edge than the S atom near the center of the ribbon.

Bond-valence analysis

In three of the four determined structures, S4,4, boulangerite and R7(2,2), the compositions obtained from the unconstrained X-ray refinements are Pb deficient as shown in Tables 4.4, 4.10, 4.16 and 4.23. In robinsonite the deviation from the stoichiometric formula per metal atom is about 3 times larger than that for boulangerite or R7(2,2) but the deviation has

opposite sense which could be an artifact of the unconstrained refinements.

The bond-valence analysis of the four structures, (Tables 4.5, 4.11, 4.17 and 4.24), indicates that the sulphur atoms which lie in the overlapping parts of the parallel ribbons (those labelled • in the tables) are systematically underbonded as indicated by their small valence sums. The sulphur atoms which lie in the parts where the ribbons join are overbonded. Underbonding can be caused by the neglect of certain bonds but in this case all the bonds out to a distance of 3.6Å have been included. Similar observations of certain atoms being consistently overbonded or underbonded in groups of related structures, is well known, (Wagner and O'Keeffe, 1988) and has been interpreted as the result of intrinsic internal strain compressive or tensile respectively. Similarly, there might be some residual tensile strain present in the structures investigated here, but more study is needed to elucidate this point.

4.5 Electron microscope study of decomposition of $Pb_5Sb_6S_{14}$, R7, (2,2)

Observations

Fig. 4.9a shows a high resolution electron micrograph of a thin

crystal fragment of $Pb_5Sb_6S_{14}$. The structure is projected down the short b axis and the contrast can be interpreted directly as projected charge density. The metal-metal distances in the ribbons are approximately 4.0Å (parallel to the face of ribbon) and 3.7Å (diagonally across the ribbon). These distances are resolved in the HREM image and the metal atoms appear as dark spots in the thinnest parts of the crystal. The wide ribbons are very clearly recognizable while the narrow ribbons are less well resolved. The lattice images were calculated using the EMS package of programs (Stadelmann, 1987) and the crystallographic data given in Tables 4.22-4.23. The calculated lattice images, presented in Fig. 4.9b, show the effect of variation of crystal thickness, defocus and objective aperture size. The best fit between the calculated images and those observed at the edges of the crystal is obtained for the conditions: 5 unit cells thickness, 700Å defocus and $100Å^{-1}$ objective aperture. The alternate grey and white strips visible in the thicker parts of the crystal are not mirrored exactly in the simulations, but the contrast in the 20 cell 700Å defocus image is close to that observed.

The samples were found to be very sensitive to the electron beam and during examination many crystal fragments decomposed. The process was usually rapid and occurred first at the edges of the crystal flakes. Figs. 4.10 and 4.11 show the micrographs of two regions in a $Pb_5Sb_6S_{14}$ crystal which has partly decomposed into

other structures.

The first of these structures, visible on both micrographs and labelled A, consists of ribbons, widened into sheets which follow the direction of the narrow ribbon in $Pb_5Sb_6S_{14}$. The sheets occur in groups of three, two of which grow straight out from parallel narrow ribbons and one of which starts from a truncated wide ribbon after a 120° change in direction. If we label the sheets extended from the narrow ribbons N, and the sheets joining the wide ribbons W, we can describe the structure seen in regions A as ...N N W N N W... The transformation advances in steps indicated by an arrow on Fig. 4.10. At the step the sequence of sheets changes to N N W W N N. There is a noticeable bending of the W type sheet where it advances deeper into the $Pb_5Sb_6S_{14}$ crystal.

In contrast to the pattern in region A, the structures seen in regions B and C, Fig. 4.11, have grown in the direction of the wide ribbons, but they differ in contrast. In region B, the dark contrast lines are wavy and they resemble the contrast lines characteristic of wide ribbons in $Pb_5Sb_6S_{14}$ suggesting that a set of sheets has been formed by extending the wide ribbons. The same type of fringe is seen at the edges of region C but in the middle of the region the fringes become straight and uniform with an approximate spacing, 3Å, which corresponds to the distance between (002) planes in PbS. We infer that in the region C, near

the interface, the transformation has started by extending the wide $Pb_5Sb_6S_{14}$ ribbons into sheets which in turn transformed into PbS structure by shearing in b direction.

Models.

All the observed transformations require severe atomic rearrangements and must occur by recrystallization and growth rather than by small atomic displacements. The transformations result in the formation of infinitely wide sheets which implies either the creation of cation vacancies or a change in stoichiometry to PbS. The latter is likely since Sb_2S_3 is more volatile than PbS and the required loss of antimony or antimony sulphide species can easily occur in the thin parts of the sample exposed to the electron beam. The resulting PbS rich material recrystallizes using the thicker untransformed parts of the crystal as a seed. Two possible structures (the stable galena structure and the TlI structure) could be formed by extending the ribbons of $Pb_5Sb_6S_{14}$. Hybrids of these two structures in which only some of the planes are sheared may also occur.

In region B the wide ribbons of $Pb_5Sb_6S_{14}$ become extended resulting in TlI type structure proceeding coherently from the crystal to produce a series of widened parallel ribbons as shown in Fig. 4.12. To model the decomposition in region C we start the transformation by first producing a series of widened TlI

type ribbons as in region B. To obtain the galena structure every other sheet is sheared in the b-direction by introducing the stacking faults indicated by circles in Fig. 4.13.

Fig. 4.14 shows a model of the decomposition seen in region A. Here, the narrow ribbons (N) extend coherently from the $Pb_5Sb_6S_{14}$ crystal as pairs of TlI type sheets. The space between them is filled with a single sheet (W) that connects with the truncated wide ribbon. This gives the sheet sequence ...N N W N N W.... Two models can be proposed for fitting the single, W, sheets between the pairs of N sheets. In the first, the W sheet is fitted without the shear and each Pb has a regular 6 coordination. This gives bands of galena structure separated by a single shear, indicated as ^, between the N sheets e.g. N^NWN^NWN^N. In the second model the W sheet is sheared with respect to both its N neighbours resulting in a uniform region of TlI type structure, N^N^N^W^N^N^W. The micrographs themselves do not indicate which model is correct and neither model is completely consistent with the observations. The contrast variation in every third sheet, seen in the region A (particularly in Fig. 4.11), suggests the first model, with the galena-type stacking of sheets between the shears but this should result in uniform contrast within the galena-like bands as observed in region C, Fig. 4.11. The second model, with the shears between all the sheets, presents difficulties at the step in the interface between the crystal and the region A, since

forming continuous TlI structure requires that an odd number of shears be introduced, which leads to ribbons that are out of phase with the parent structure. This could only be accomodated by leaving the two W slabs unsheared with respect to each other. Fig. 4.14 shows the arrangement of the ribbons according to the first (unsheared) N^NWN^N model. The bending required by the crystal is observed in the micrograph at the step in the interface between the crystal and the region A.

4.6 Summary

Three homologous series (two members each) were identified in the PbS rich part of the PbS-Sb_2S_3 system in the dry synthesis preparations. The members of the series have structures built of ribbons consisting of back-to-back square pyramids. Lead occupies sites at junction where the ribbons join edge-to-face. Antimony prefers sites on the faces of the parallel parts of the ribbons.

The coordination polyhedra of cations are not ideal square pyramids. The pyramids are distorted in two ways: in the apical direction and in the basal plane. Both distortions increase with increase of antimony content in a site. The faces of the ribbons have regions where strong and weak external bonding occurs. The external bonds between the ribbons are weaker for antimony (≅ 0.1v.u.) than for lead (≅ 0.3v.u.), indicating that the lone electron pair, which manifests itself in the distortion, is more

stereoactive for antimony than for lead.

The high resolution electron microscope study shows that three forms of PbS, of which only one is the normally stable galena (NaCl type), grow epitaxially on $Pb_5Sb_6S_{14}$ in the electron beam. The metastable forms are related to the TlI type structure and grow coherently from the parent crystal.

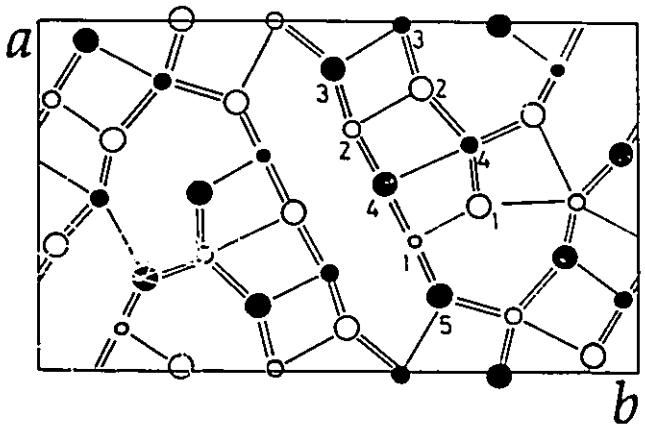

Fig. 4.1: The unit cell of S4,4, $Pb_2Sb_2S_5$, projected down [001]. In order of decreasing size, the circles denote S, Pb, mixed sites and Sb. Atoms at z=0.25 and z=0.75 are indicated by open and full circles respectively.

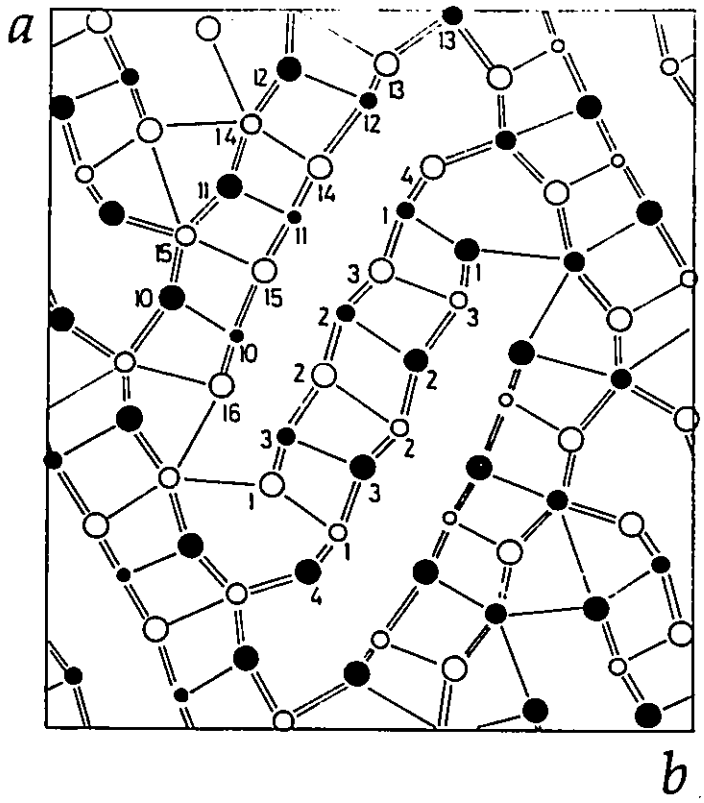

Fig. 4.2: The unit cell of B(3,6)(3,6), boulangerite, $Pb_5Sb_4S_{11}$ projected down [001]. Conventions for indicating atoms are the same as in Fig. 4.1.

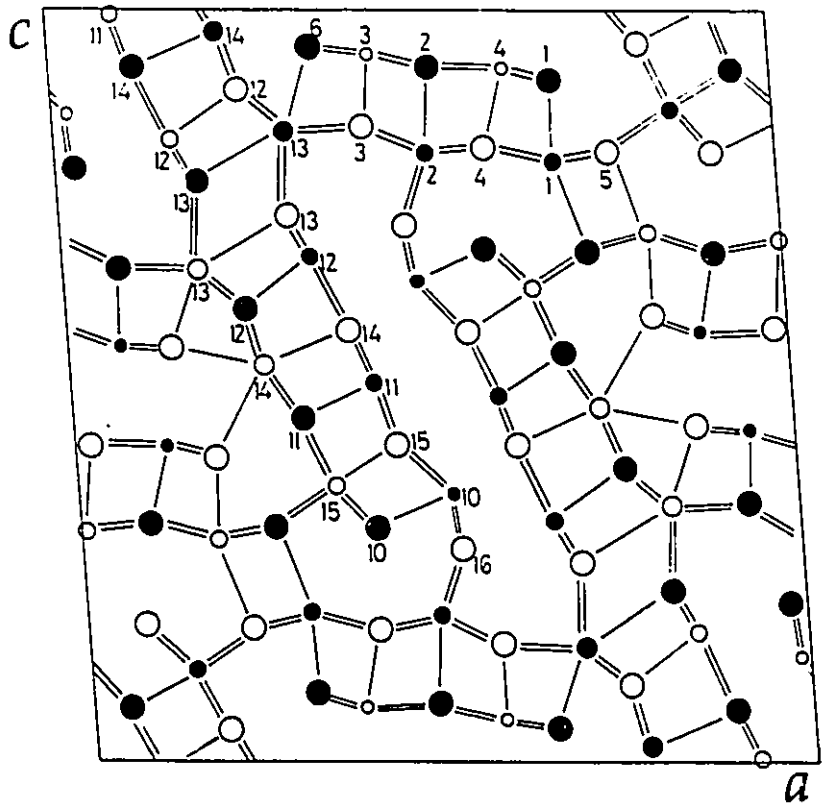

Fig. 4.3: The unit cell of R6,(2,2), robinsonite, $Pb_4Sb_6S_{13}$ projected down [010]. In order of decreasing size, the circles denote S, Pb, mixed sites and Sb. Atoms at z=0.25 and z=0.75 are indicated by open and full circles respectively.

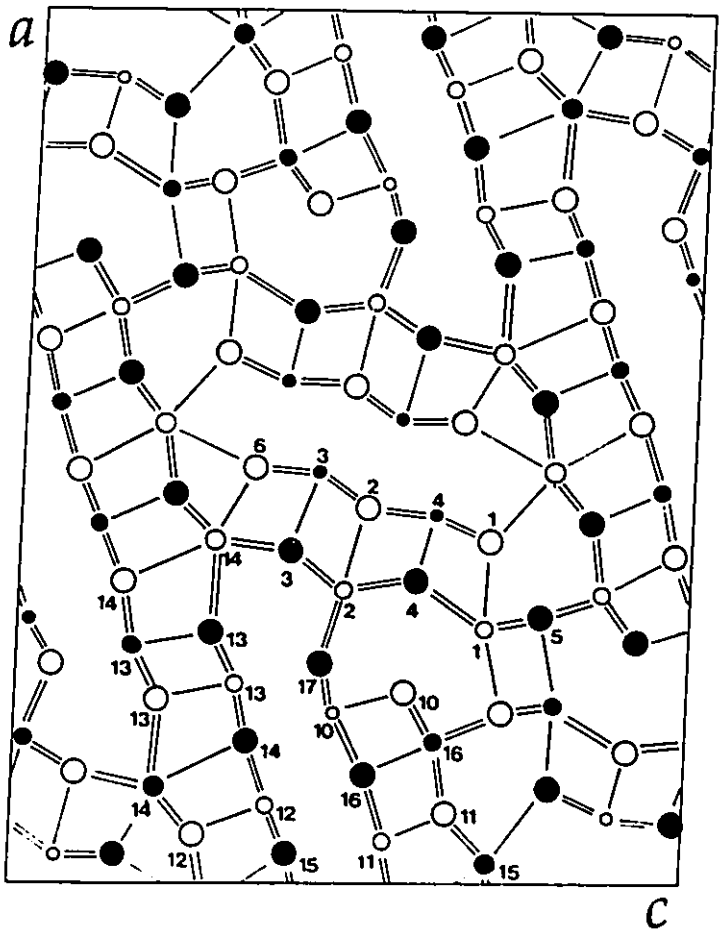

Fig. 4.4: The unit cell of R7,(2,2), $Pb_5Sb_6S_{14}$, projected down [010]. Conventions for indicating atoms are the same as in Fig. 4.1.

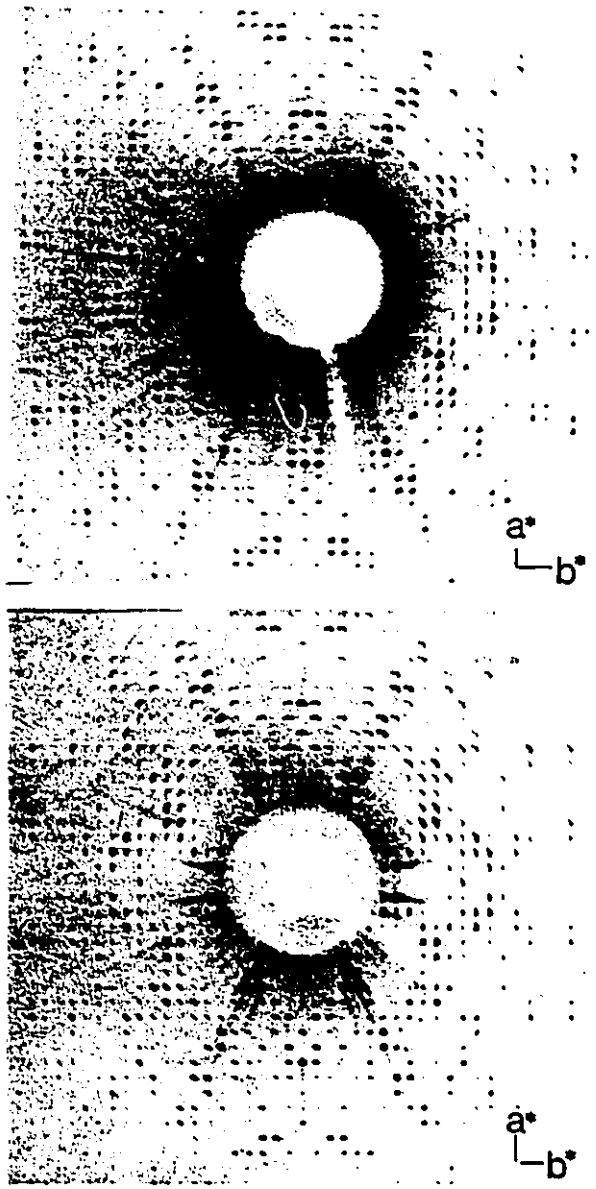

Fig. 4.5: The similar precession X-ray diffraction patterns of (a) $Pb_7Sb_4S_{13}$ and (b) boulangerite. The strong reflections, visible on both diffraction patterns, corrrespond with the reflections of the PbS-like sublattice in [011] projection. The orientation of the PbS-like sublattice with respect to the crystal lattices of both $Pb_7Sb_4S_{13}$ and boulangerite is the same. The a and c lattice parameters are close in both phases while b is ≅ 4Å bigger in (a) then in (b).

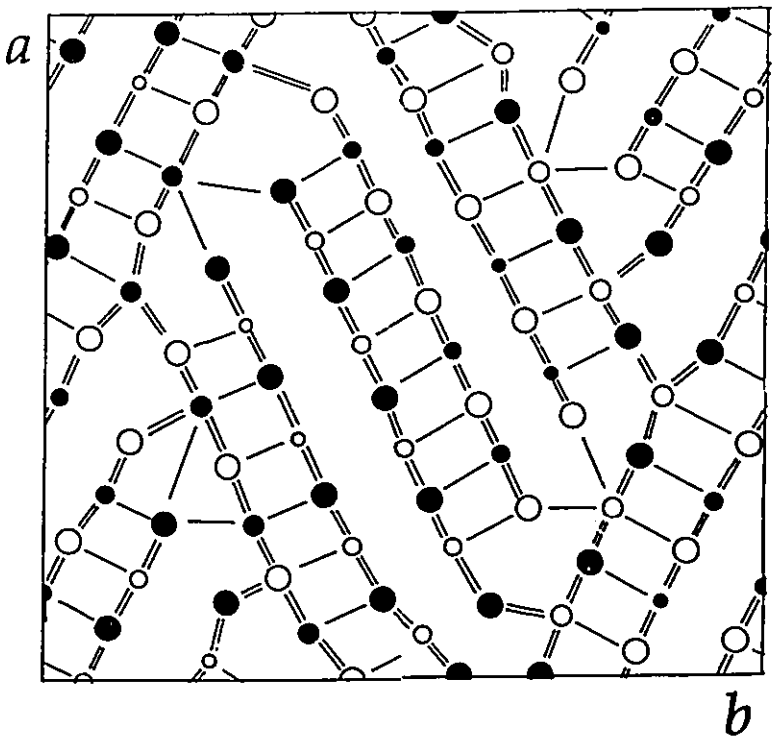

Fig. 4.6: The proposed unit cell of B(4,7)(4,7), $Pb_7Sb_4S_{13}$, projected down [001]. Conventions for indicating atoms are the same as in Fig. 4.1.

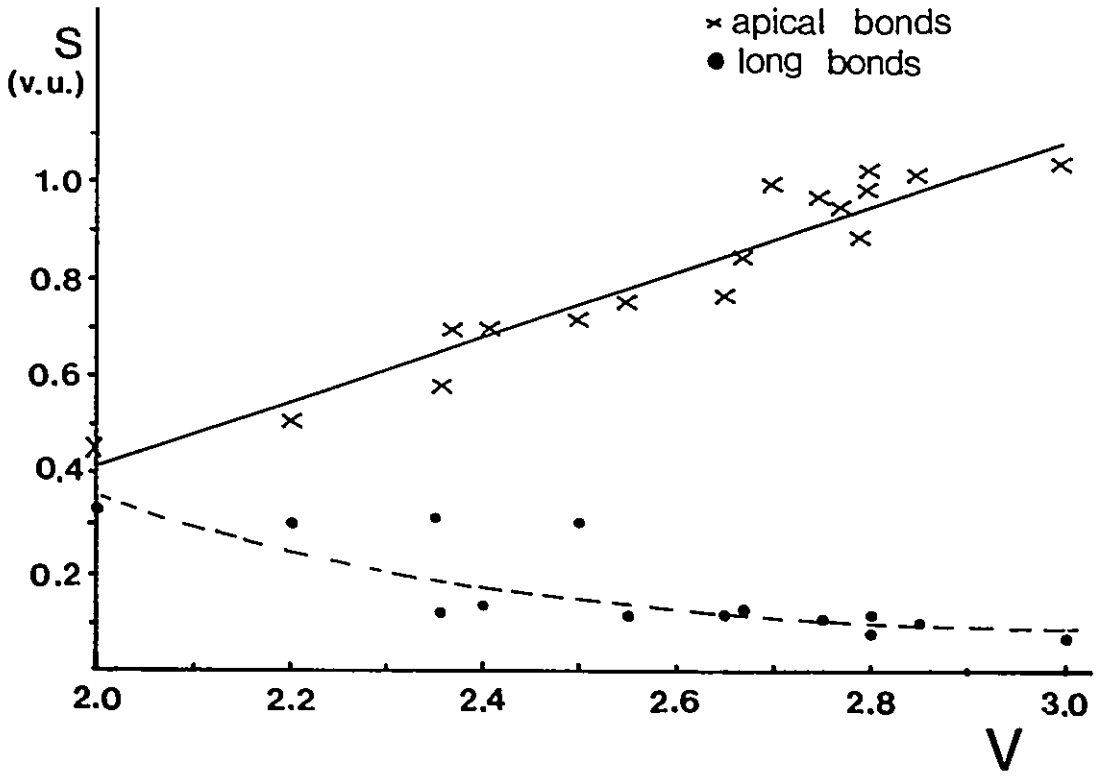

Fig. 4.7: The observed bond valences (s) versus the oxidation (V) of the apical bonds (crosses) and the long bonds opposite to the apical (dots) in 7-coordinated sites in the lead-antimony sulphides. The solid line represents eq. (4.1), the broken line represents eq. (4.2).

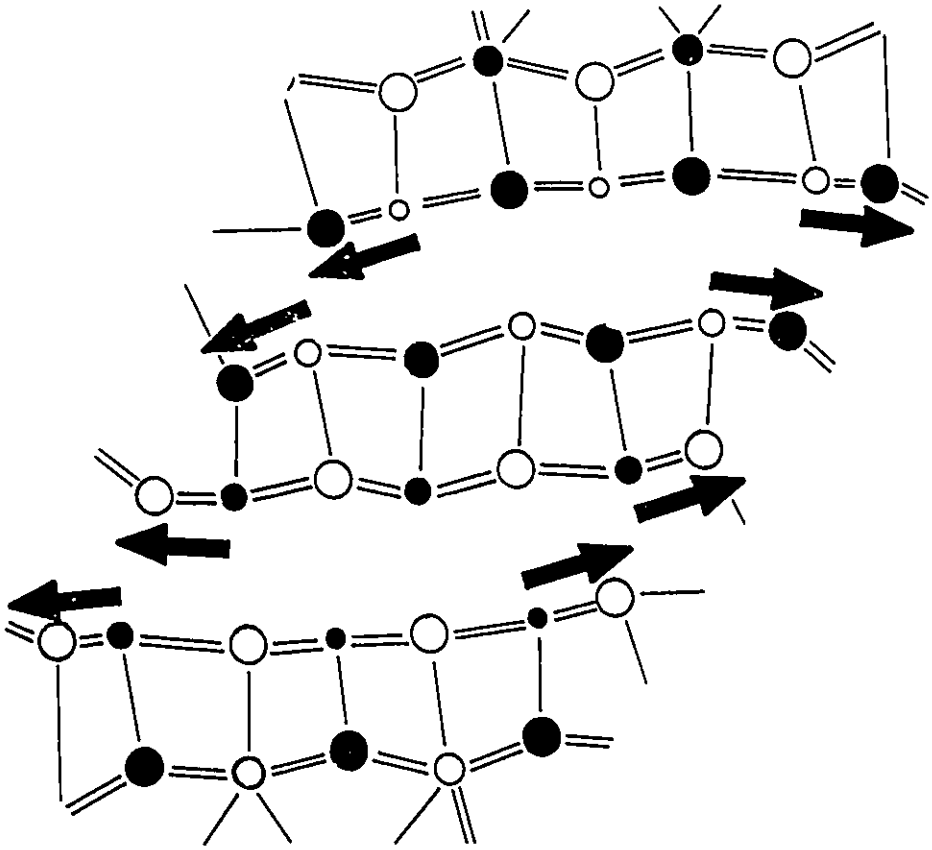

Fig. 4.8: The distortion occuring in the base of the pyramids. The two pairs of the basal bonds are not equal, the antimony atoms are displaced in the plane away from the middle of the region betweeen the parallel parts of the ribbons, as indicated by the arrows.

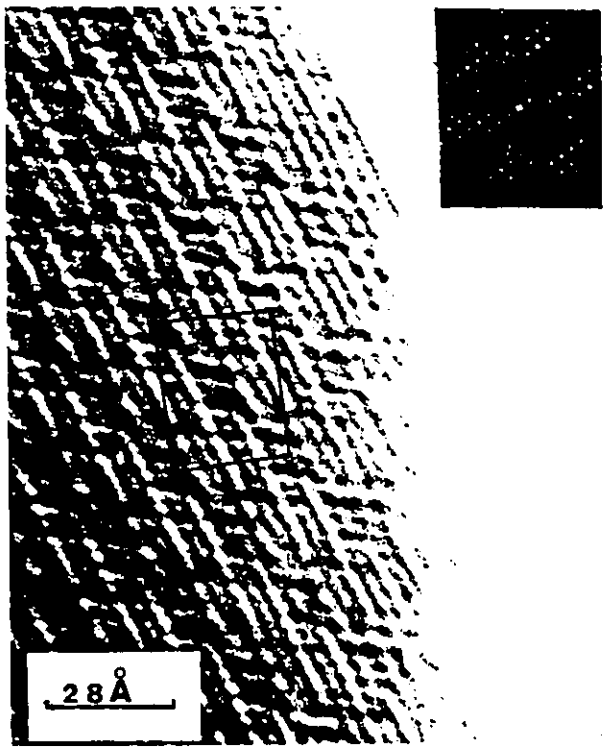

Fig. 4.9(a): High resolution electron micrograph of a thin crystal fragment of $Pb_5Sb_6S_{14}$. The structure is projected along [010] and the unit cell is outlined. By comparison with Fig. 4.4 it can be seen that both wide and narrow ribbons are resolved.

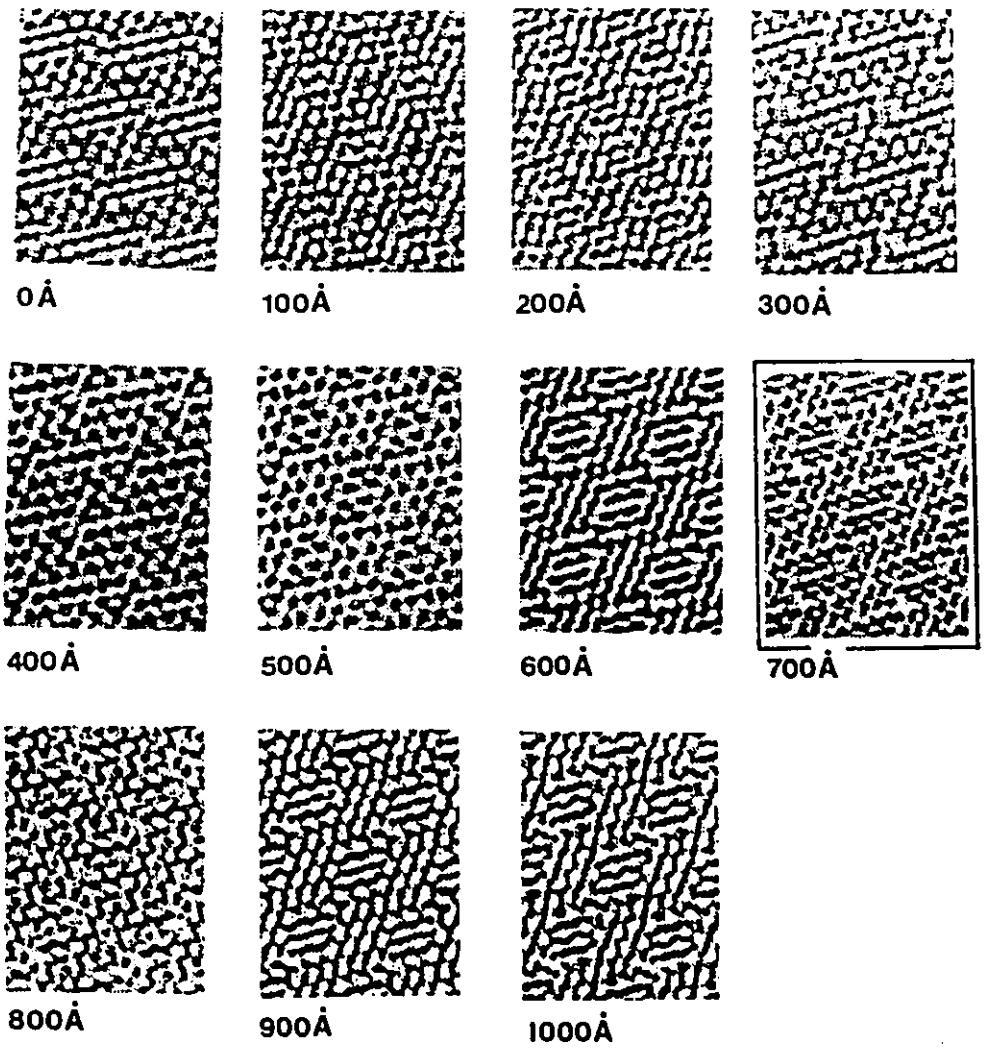

Fig. 4.9(b): The calculated images of $Pb_5Sb_6S_{14}$ for the crystal thickness of 5 unit cells, the objective aperture $10nm^{-1}$ and various defocus as indicated. The best fit between the calculated images and those observed at the edges of the crystal is obtained for the defocuss of 700 Å.

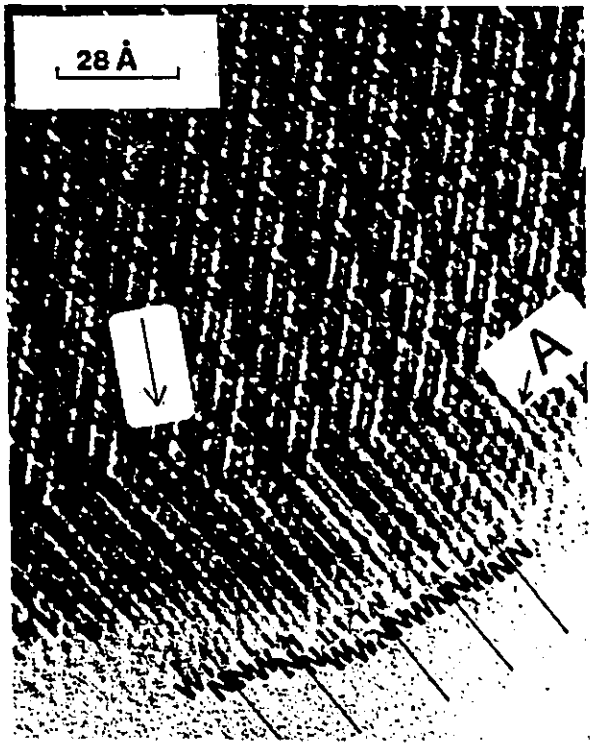

Fig. 4.10: Electron micrograph of a $Pb_5Sb_6S_{14}$ crystal fragment which has partly decomposed into widened sheets in region indicated by A. The sheets extended from the narrow ribbon are labelled N and the sheets joining the wide ribbon W. The step in the interface between transformed and untransformed part of the crystal is indicated by an arrow.

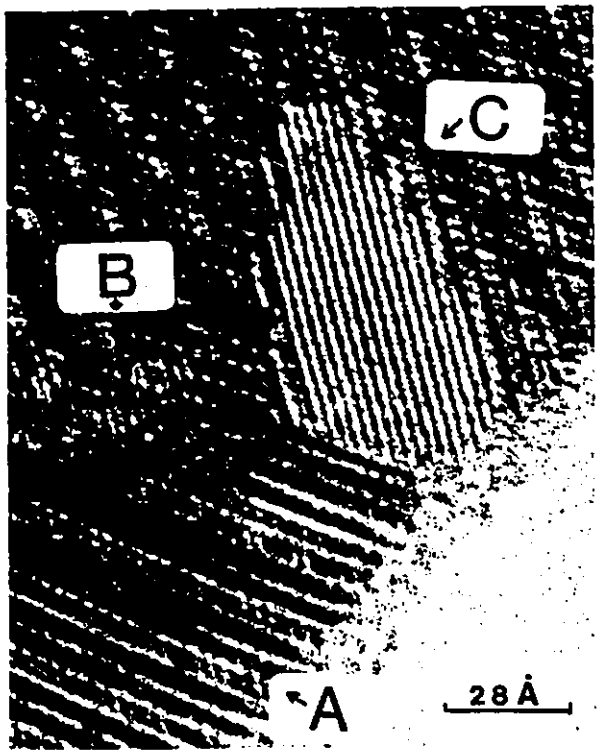

Fig. 4.11: Electron micrograph of a $Pb_5Sb_6S_{14}$ crystal fragment which has partly decomposed into three structures seen in regions labelled A, B and C. Region A is formed by the extension of the narrow ribbons of $Pb_5Sb_6S_{14}$, as in Figure 4.10. Regions B and C are formed by extension of the wide ribbons.

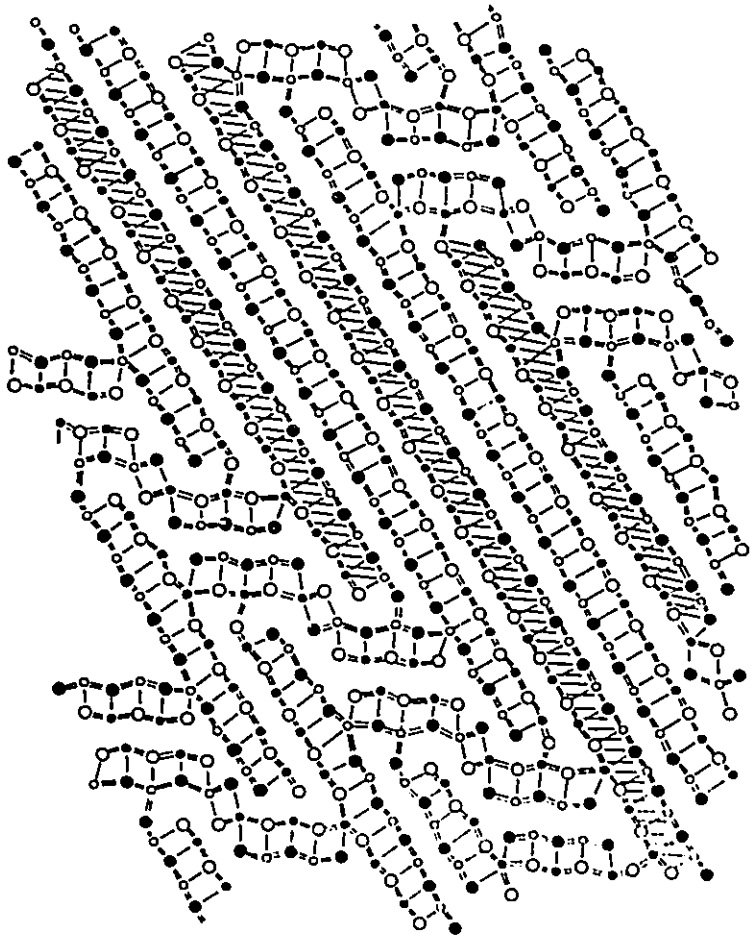

Fig. 4.12: A model of the decomposition in region B using the conventions of Fig. 4.1. The wide ribbons of $Pb_5Sb_6S_{14}$ become extended into sheets and proceed coherently from the crystal.

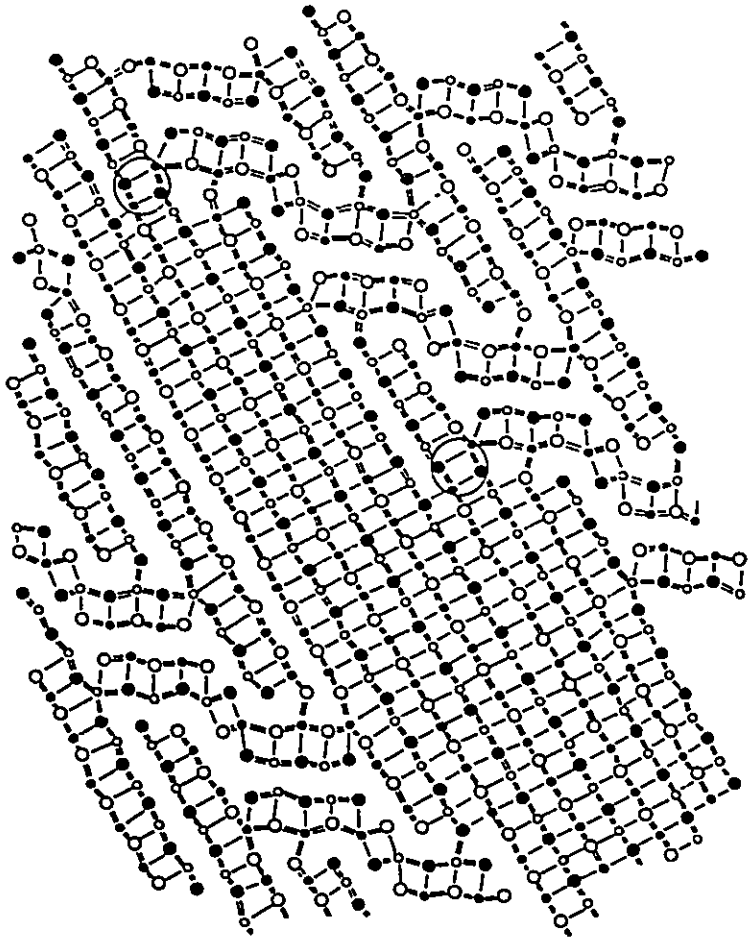

Fig. 4.13: A model of the decomposition in region C. Every other sheet extending from the wide ribbon of $Pb_5Sb_6S_{14}$ is sheared in b direction (perpendicular to page) and galena structure is produced. The resulting stacking faults are indicated by circles.

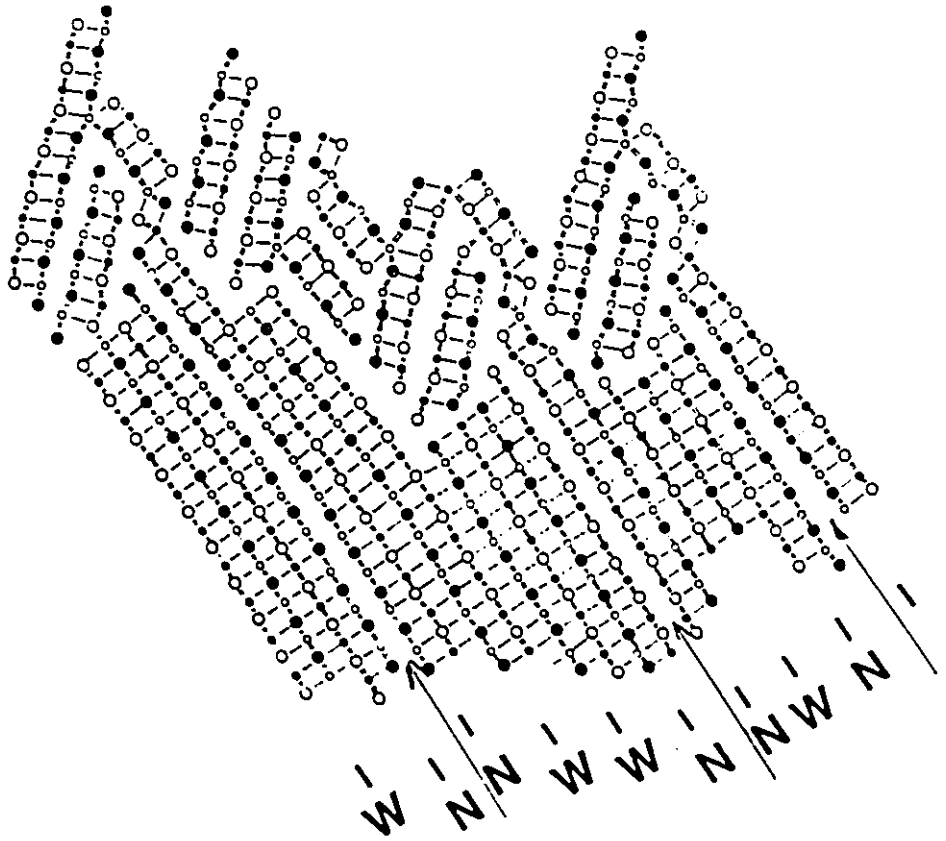

Fig. 4.14 A model of the decomposition in region A. The narrow ribbons of $Pb_5Sb_6S_{14}$ are extended into sheets. Only the representation with the bands of galena structure separated by a single shear is drawn. The sheets are bent at the step in the interface between the transformed and untransformed part of the crystal (compare with Fig. 4.10).

Table 4.1: Powder X-ray phase analysis in the PbS-Sb_2S_3 system.

Composition (% PbS)	Phases present	Composition (% PbS)	Phases present
90	PbS, boul	70	boul
89	PbS, boul	69	boul
88	PbS, boul^{s}	68	boul
87	PbS, boul	67	boul, $Pb_5Sb_6S_{14}$(tr)
86	PbS, boul	66	boul^{s}, $Pb_5Sb_6S_{14}$(tr)
85	PbS, boul	65	boul
84	boul, PbS	64	boul, $Pb_5Sb_6S_{14}$(tr)
83	boul, PbS	62	$Pb_5Sb_6S_{14}$, boul(tr)^{b}
82	boul, PbS	61	$Pb_5Sb_6S_{14}^{s}$, boul
81	boul^{s}, PbS	60	$Pb_5Sb_6S_{14}$, rob(tr)
80	boul, PbS	58	rob
79	boul, PbS	56	rob^{s}, zink^{b}
78	boul, PbS	55	rob, $Pb_5Sb_6S_{14}^{s}$
77	boul, PbS	54	zink^{b}, rob
76	boul, tr(?)	53	rob, zink(tr)
75	boul, PbS	52	zink
74	boul, PbS(tr)		
73	boul, PbS(tr)		
72	boul		
71	boul		

^{s}-phase separation

^{b}-broad lines

^{tr}-trace

PbS-galena

boul-boulangerite, B(3,6)(3,6)

rob-robinsonite, R6,(2,2)

$Pb_5Sb_6S_{11}$- R7,(2,2)

zink-zinckenite

Table 4.2: Crystallographic parameters of the structures in the PbS-Sb_2S_3 system reported in this study.

Name	Formula	Symbol	Space group	Lattice parameters (Å) (deg)	Status of structure determination
-	$Pb_7Sb_4S_{13}$	B(4,7)(4,7)	Pnam	a=23.7 b=25.6 c=4.0	proposed
-	$Pb_3Sb_2S_6$	S5,5	Pbnm	a=11.0 b=23.3 c=4.0	proposed
Boulangerite	$Pb_5Sb_4S_{11}$	B(3,6)(3,6)	Pbnm	a=23.490(5) b=21.245(5) c=4.020(1)	refined
-	$Pb_2Sb_2S_5$	S4,4	Pbnm	a=11.355(4) b=19.783(8) c=4.042(1)	determined and refined
Robinsonite	$Pb_4Sb_6S_{13}$	R6(2,2)	I2/m	a=23.698(8) b=3.980(8) c=24.466(8) β=93.9(3)	refined
-	$Pb_5Sb_6S_{14}$	R7(2,2)	$I\bar{1}$	a=28.367(8) b=4.024(1) c=22.044(7) α=89.59(2) β=92.28(3) γ=89.93(2)	determined and refined

Table 4.3: Structure determination of $Pb_2Sb_2S_5$, S4,4.

Composition	$Pb_2Sb_2S_5$
Space group	Pbnm
Lattice parameters (Å)	
	a=11.355(4)
	b=19.783(8)
	c= 4.042(1)
Volume ($Å^3$)	907.98
Calculated density (g/cm^3)	5.95
Reflections used to determine a and b	$20.25°<2\theta<46.5°$
Standard reflections	3 1 0, -2 3 1
e.s.d. of standard reflections (%)	1.7, 1.6
No. of standard reflection measurements	37, 37
Range of measured reflections	0<h<13
	0<k<23
	-4<l<4
No. of reflections measured	1750
No. of unique reflections	931
Linear absorption coefficient μ (mm^{-1})	42.13
No. of reflections used in psi-scan	11
Maximum absorption correction; reflection	1.65; 0 8 2
Internal agreement factor R_{int} before the absorption correction	0.037
Internal agreement factor R_{int} after the absorption correction	0.031
Weighting parameters: k; g	1.35; 0.0006
Final R; R_w	0.071; 0.063
Shift/error in final cycle: maximum	0.07
average	0.02
Number of variables refined	58
Residual electron density: maximum ($eÅ^{-3}$)	3.4
minimum	-3.3

Table 4.4. Percentage of Sb on cation sites in $Pb_2Sb_2S_5$, S4,4.

	Hyde & Smith (1983)	X-ray	Bond-valence
M(1)	100	100	100
M(2)	100	90	82
M(3)	0	32	10
M(4)	0	34	8
Formula	$Pb_2Sb_2S_5$	$Pb_{1.44}Sb_{2.56}S_5$	$Pb_2Sb_2S_5$

Table 4.5: Bond valences, Σs, in $Pb_2Sb_2S_5$, S4,4, weighted according to X-ray occupation number. V is the atomic valence weighted using these occupancies.

	M(1)	M(2)	M(3)	M(4)	Σs
%Sb	100	90	32	34	
S(1)	1.01	-	0.12	0.41x2+0.03	-1.98
S(2)	-	0.97	0.33x2	0.24x2	-2.11
S(3)	0.08	0.35x2	0.49+0.32x2	-	-1.91
S(4)	0.21x2	0.51x2+0.06	-	0.43	-1.93
S(5)	0.71x2	0.03	0.17	0.15x2	-1.92
Σs	2.93	2.78	2.08	2.06	
V	3.00	2.90	2.32	2.34	

Table 4.6: Atomic coordinates for $Pb_2Sb_2S_5$, S4,4.

	x	y	z
M(1)	0.3757(2)	0.3715(1)	0.25
M(2)	0.7022(2)	0.4758(1)	0.25
M(3)	0.9983(1)	0.4008(1)	0.75
M(4)	0.6678(1)	0.2914(1)	0.75
S(1)	0.4950(6)	0.2670(4)	0.25
S(2)	0.8183(7)	0.3685(4)	0.25
S(3)	0.8690(6)	0.5212(4)	0.75
S(4)	0.5659(7)	0.4221(4)	0.75
S(5)	0.2495(7)	0.3288(4)	0.75

Table 4.7: Anisotropic atomic displacement parameters ($Å^2$) for $Pb_2Sb_2S_5$, S4,4. $U_{13} = U_{23} = 0$.

	U_{11}	U_{22}	U_{33}	U_{12}
M(1)	0.0190(10)	0.0165(11)	0.0188(10)	-0.043(8)
M(2)	0.0383(12)	0.0321(12)	0.0274(11)	0.042(10)
M(3)	0.0285(7)	0.0341(8)	0.0237(7)	-0.012(6)
M(4)	0.0407(8)	0.0216(7)	0.0272(7)	0.051(6)
S(1)	0.0178(36)	0.0169(39)	0.0229(40)	0.033(31)
S(2)	0.0223(40)	0.0112(36)	0.0227(37)	0.021(30)
S(3)	0.0141(35)	0.0201(36)	0.0291(42)	0.075(31)
S(4)	0.0218(42)	0.0185(40)	0.0353(50)	-0.057(34)
S(5)	0.0168(37)	0.0220(43)	0.0522(54)	-0.020(34)

Table 4.8: Interatomic distances (Å) less than 3.6Å in $Pb_2Sb_2S_5$, S4,4.

M(1) -	S(1)	2.475(7)
	S(5) x 2	2.621(5)
	S(4) x 2	3.124(5)
	S(3)	3.499(7)
M(2) -	S(2)	2.497(7)
	S(4) x 2	2.757(5)
	S(3) x 2	2.915(5)
M(3) -	S(3)	2.795(7)
	S(2) x 2	2.947(5)
	S(3) x 2	2.952(5)
	S(5)	3.183(8)
M(4) -	S(4)	2.836(7)
	S(1) x 2	2.858(5)
	S(2) x 2	3.052(5)
	S(5) x 2	3.253(6)

Table 4.9: Structure determination of boulangerite, B(3,6)(3,6).

Composition	$Pb_5Sb_4S_{11}$
Space group	Pnam
Lattice parameters (Å)	
	a=23.490(5)
	b=21.245(5)
	c= 4.020(1)
Volume ($Å^3$)	2006
Calculated density (g/cm^3)	6.21
Reflections used to determine a and b	$19^\circ<2\theta<26^\circ$
Standard reflections	-9 6 1, 10 4 0
e.s.d. of standard reflections (%)	1.3, 1.4
No. of standard reflection measurements	79, 79
Range of measured reflections	0<h<27
	0<k<25
	-4<l<4
No. of reflections measured	3700
No. of unique reflections	2035
Linear absorption coefficient μ (mm^{-1})	46.28
No. of reflections used in psi-scan	20
Absorption correction: maximum; reflection	1.67; 15 0 4
Internal agreement factor R_{int} before the absorption correction	0.037
Internal agreement factor R_{int} after the absorption correction	0.035
Weighting parameters k; g	1.97; 0.0006
Final R; R_w	0.077; 0.068
Shift/error in final cycle: maximum	0.053
average	0.014
Number of variables refined	142
Residual electron density: maximum ($eÅ^{-3}$)	3.5
minimum	-3.9

Table 4.10: Percentage of Sb on cation sites in boulangerite, B(3,6)(3,6).

	Born & Hellner	Petrova	X-ray	Bond valence
M(1)	100	50	76	70
M(2)	50	55	50	36
M(3)	50	40	41	38
M(10)	100	100	100	100
M(11)	100	100	100	100
M(12)	50	55	68	56
M(13)	0	0	0	0
M(14)	0	0	0	0
M(15)	0	0	0	0
Formula	$Pb_{4.5}Sb_{4.5}S_{11}$	$Pb_5Sb_4S_{11}$	$Pb_{4.65}Sb_{4.35}S_{11}$	$Pb_5Sb_4S_{11}$

Table 4.11: Bond valences, Σs, in boulangerite, B(3,6)(3,6), weigthed according to X-ray occupation number. V is the atomic valence weigthed using these occupancies.

	M(1)	M(2)	M(3)	M(10)	M(11)	M(12)	M(13)	M(14)	M(15)	Σs
XSb	76	50	41	100	100	68	0	0	0	
S(1)	0.77		0.56x2					0.15		-2.04
S(2)		0.69+0.39x2	0.25x2	0.04x2						-2.05
S(3)	0.23x2	0.40x2	0.71		0.04x2					-2.05
S(4)	0.66x2					0.07x2				-1.82
S(10)				1.12			0.18x2		0.32x2	-2.12
S(11)					1.03			0.33x2	0.26x2	-2.21
S(12)						0.76	0.36x2	0.31x2		-2.10
S(13)						0.68x2	0.2+0.13x2			-2.02
S(14)	0.06x2				0.44x2	0.16x2		0.57		-1.89*
S(15)		0.06x2		0.24x2	0.35x2				0.40	-1.70*
S(16)			0.07x2	0.64x2			0.32	0.12		-1.86*
Σs	2.67	2.39	2.47	2.96	2.69	2.51	1.86	2.12	1.92	
V	2.76	2.5	2.41	3.00	3.00	2.68	2.00	2.00	2.00	

Table 4.12: Atomic coordinates for boulangerite, B(3,6)(3,6).

	x	y	z
M(1)	0.2675(1)	0.5505(1)	0.75
M(2)	0.4325(1)	0.4580(1)	0.75
M(3)	0.5975(1)	0.3688(1)	0.75
M(10)	0.4625(1)	0.2889(1)	0.75
M(11)	0.2953(1)	0.3820(1)	0.75
M(12)	0.1290(1)	0.4855(1)	0.75
M(13)	0.0021(1)	0.6179(1)	0.75
M(14)	0.1602(1)	0.3062(1)	0.25
M(15)	0.3229(1)	0.2080(1)	0.25
S(1)	0.6743(3)	0.3454(4)	0.25
S(2)	0.5166(4)	0.4304(4)	0.25
S(3)	0.3620(3)	0.5147(4)	0.25
S(4)	0.2057(4)	0.5962(4)	0.25
S(10)	0.4137(3)	0.1876(3)	0.75
S(11)	0.2486(3)	0.2780(3)	0.75
S(12)	0.0878(3)	0.3717(3)	0.75
S(13)	0.0593(4)	0.5126(4)	0.25
S(14)	0.2180(4)	0.4187(4)	0.25
S(15)	0.3725(4)	0.3319(4)	0.25
S(16)	0.5293(4)	0.2531(4)	0.25

Table 4.13: Anisotropic atomic displacement parameters ($Å^2$) for boulangerite, B(3,6)(3,6). $U_{13} = U_{23} = 0$

	U_{11}	U_{22}	U_{33}	U_{12}
M(1)	0.0182(10)	0.0469(13)	0.0399(12)	-0.0058(9)
M(2)	0.0286(9)	0.0419(11)	0.0390(10)	0.0065(8)
M(3)	0.0336(10)	0.0275(9)	0.0310(9)	-0.0050(7)
M(10)	0.0335(14)	0.0181(12)	0.0414(1[illegible])	-0.0099(10)
M(11)	0.0624(19)	0.0309(15)	0.0345(15)	-0.0270(13)
M(12)	0.0322(10)	0.0264(10)	0.0365(11)	0.0036(8)
M(13)	0.0196(7)	0.0525(10)	0.0245(8)	0.0053(6)
M(14)	0.0204(7)	0.0199(7)	0.0230(7)	-0.0016(5)
M(15)	0.0236(7)	0.0193(7)	0.0238(7)	0.0011(5)
S(1)	0.0197(44)	0.0114(38)	0.0352(50)	0.0044(31)
S(2)	0.0265(44)	0.0127(39)	0.0276(47)	0.0028(33)
S(3)	0.0209(42)	0.0117(38)	0.0306(47)	0.0022(31)
S(4)	0.0236(46)	0.0159(42)	0.0605(67)	-0.0063(36)
S(10)	0.0136(39)	0.0143(38)	0.0239(42)	-0.0052(30)
S(11)	0.0147(39)	0.0107(35).	0.0179(39)	-0.0025(30)
S(12)	0.0147(39)	0.0150(38)	0.0167(39)	0.0051(30)
S(13)	0.0177(44)	0.0228(46)	0.0595(65)	0.0006(36)
S(14)	0.0209(44)	0.0098(38)	0.0432(54)	-0.0001(32)
S(15)	0.0343(53)	0.0247(46)	0.0318(51)	-0.0100(39)
S(16)	0.0183(42)	0.0168(39)	0.0346(50)	-0.0025(32)

Table 4.14: Interatomic distances (Å) less than 3.6Å in boulangerite, B(3,6)(3,6).

Narrow Ribbon			Wide Ribbon		
M(1) -	S(1)	2.602(8)	M(10) -	S(10)	2.432(7)
	S(4)X2	2.662(6)		S(16)X2	2.661(5)
	S(3)X2	3.090(6)		S(15)X2	3.058(2)
M(2) -	S(2)	2.659(8)	M(11) -	S(11)	2.468(8)
	S(3)X2	2.869(6)		S(14)X2	2.817(6)
	S(2)X2	2.880(6)		S(15)X2	2.907(7)
M(3) -	S(3)	2.651(8)	M(12) -	S(12)	2.609(7)
	S(1)X2	2.744(5)		S(13)X2	2.656(6)
	S(2)X2	3.059(6)		S(14)X2	3.230(6)
				S(4)X2	3.583(7)
			M(13) -	S(13)	3.130(9)
				S(12)X2	2.920(5)
				S(16)	2.965(8)
				S(10)X2	3.186(6)
				S(13)X2	3.293(7)
			M(14) -	S(14)	2.749(8)
				S(11)X2	2.954(5)
				S(12)X2	2.979(5)
				S(1)	3.236(7)
				S(16)	3.322(8)
			M(15) -	S(15)	2.877(9)
				S(10)X2	2.964(5)
				S(11)X2	3.046(5)
				S(4)X2	3.182(7)

Table 4.15: Structure determination of robinsonite, R6,(2,2).

Composition	$Pb_4Sb_6S_{13}$
Space group	I2/m
Lattice parameters (Å)	
	a=23.698(8)
	b= 3.980(8)
	c=24.466(8)
	β=93.9(3)°
Volume (Å^3)	2302
Calculated density (g/cm^3)	5.7
Reflections used to determine a and b	10°<2θ<24°
Standard reflections	6 1 -3, -1 0 -9
e.s.d. of standard reflections (%)	3.1, 3.1
No. of standard reflection measurements	92, 92
Range of measured reflections	-30<h<30
	-29<k<29
	0<l<5
No. of reflections measured	4075
No. of unique reflections	2361
Linear absorption coefficient μ (mm^{-1})	35.64
No. of reflections used in psi-scan	21
Absorption correction: maximum; reflection	3.15; 303
Internal agreement factor R_{int} before the absorption correction	0.032
Internal agreement factor R_{int} after the absorption correction	0.029
Weighting parameters k; g	0.34; 0.0002
Final R; R_w	0.068; 0.061
Shift/error in final cycle: maximum	0.68
average	0.12
Number of variables refined	156
Residual electron density: maximum (eÅ^{-3})	3.7
minimum	-5.2

Table 4.16: Percentage of Sb on cation sites in robinsonite, R6,(2,2) and $Sn_4Sb_6S_{13}$.

	Robinsonite				$Sn_4Sb_6S_{13}$	
	Petrova et al. (1978)		this work		Jumas et al. (1980)	
	(average, Table 4.21 col 3)	bond val	X-ray	bond val	as given	bond val[6]
M(1)	50	74	59	80	0	100
M(2)	0	17	15	18	100	0
M(3)	100	95	92	100	0	100
M(4)	100	94	84	100	0	100
M(10)	100	100	84	100	0	100
M(11)	100	93	76	88	100	48
M(12)	100	71	73	78	100	100
M(13)	0	0	0	0	100	0
M(14)	0	0	0	0	100	0
M(15)	50	53	12	36	100	35
Formula	$Pb_4Sb_6S_{13}$ ↓ $Pb_{5.04}Sb_{4.96}S_{13}$		$Pb_4Sb_6Sb_{13}$ ↓ $Sn_4Sb_6S_{13}$		$Sn_{4.17}Sb_{5.83}S_{13}$	

[6] r_o(Sb-S)=2.52Å and r_o(Sn-S)=2.437Å were used.

Table 4.17: Bond valences, Σs, in robinsonite, R7,(2,2), weighted according to X-ray occupation number. V is the atomic valence weighted using these occupancies.

	H(1)	H(2)	H(3)	H(4)	H(10)	H(11)	H(12)	H(13)	H(14)	H(15)	Σs
%Sb	59	15	92	84	84	76	73	0	0	12	
S(1)	0.61			0.59x2					0.16		-1.95
S(2)		0.51	0.30x2+0.04x2	0.32x2							-1.87
S(3)		0.30x2	1.12					0.22x2			-2.16
S(4)	0.21x2	0.39x2		1.09							-2.29
S(5)	0.71x2+0.27									0.16x2	-2.01
S(6)			0.65x2	0.05x2				0.38	0.14		-1.92
S(10)	0.10	0.04			1.03					0.48x2	-2.13
S(11)						1.05			0.35x2	0.26x2	-2.25
S(12)							0.90	0.35x2	0.28x2		-2.16
S(13)							0.71x2	0.15+0.12x2			-1.96
S(14)					0.05x2	0.49x2	0.176x2		0.47		-1.89*
S(15)					0.20x2	0.38x2+0.05x2				0.58	-1.84*
S(16)		0.14x2			0.72x2		0.06x2				-1.84*
Σs	2.82	2.21	3.26	3.01	2.97	2.89	2.78	1.91	2.03	2.38	
V	2.59	2.15	2.95	2.84	2.84	2.53	2.73	2.00	2.00	2.12	

Table 4.18: Atomic coordinates for robinsonite, R6,(2,2).

	x	y	z
M(1)	0.6901(1)	0.5	0.7983(1)
M(2)	0.5053(1)	0.5	0.8117(1)
M(3)	0.4365(1)	0.0	0.9438(1)
M(4)	0.6172(1)	0.0	0.9228(1)
M(10)	0.5068(1)	0.5	0.3527(1)
M(11)	0.4206(1)	0.5	0.5114(1)
M(12)	0.3431(1)	0.5	0.6706(1)
M(13)	0.1811(1)	0.0	0.6627(1)
M(14)	0.2698(1)	0.0	0.5216(1)
M(15)	0.3559(1)	0.0	0.3694(1)
S(1)	0.6921(3)	0.5	0.9088(3)
S(2)	0.5258(3)	0.5	0.9251(3)
S(3)	0.4199(3)	0.0	0.8444(3)
S(4)	0.5934(3)	0.0	0.8235(3)
S(5)	0.7627(3)	0.0	0.8132(3)
S(6)	0.3629(3)	0.5	0.9507(3)
S(10)	0.4090(3)	0.5	0.3101(3)
S(11)	0.3279(3)	0.5	0.4579(3)
S(12)	0.2509(3)	0.5	0.6108(3)
S(13)	0.3046(3)	0.0	0.7281(3)
S(14)	0.3782(3)	0.0	0.5766(3)
S(15)	0.4545(3)	0.0	0.4347(3)
S(16)	0.5335(3)	0.0	0.2896(3)

Table 4.19: Anisotropic atomic displacement parameters ($Å^2$) for robinsonite, R6,(2,2). $U_{12} = U_{23} = 0$.

	U_{11}	U_{22}	U_{33}	U_{13}
M(1)	0.0184(10)	0.0096(9)	0.0348(11)	0.0078(8)
M(2)	0.0217(8)	0.0190(8)	0.0424(9)	0.0019(7)
M(3)	0.0283(1)	0.0378(10)	0.0134(10)	-0.0026(9)
M(4)	0.00358(14)	0.0417(15)	0.0145(12)	-0.0006(10)
M(10)	0.0191(12)	0.0390(14)	0.020(12)	-0.0003(9)
M(11)	0.0240(12)	0.0333(14)	0.0292(13)	-0.00894(10)
M(12)	0.0235(11)	0.0311(12)	0.0141(10)	0.0002(9)
M(13)	0.0379(8)	0.00198(7)	0.0357(8)	0.0172(7)
M(14)	0.0219(7)	0.0179(7)	0.0253(7)	0.0017(5)
M(15)	0.0585(10)	0.0258(8)	0.0316(8)	-0.0052(7)
S(1)	0.0144(37)	0.0263(43)	0.0051(34)	-0.0009(29)
S(2)	0.0235(42)	0.0235(42)	0.0108(37)	0.0013(32)
S(3)	0.0173(37)	0.0143(36)	0.0069(33)	0.0029(28)
S(4)	0.0149(37)	0.0182(39)	0.0130(36)	-0.0014(30)
S(5)	0.0117(37)	0.0358(49)	0.0145(38)	-0.0034(30)
S(6)	0.0071(35)	0.0302(45)	0.0148(38)	-0.0016(30)
S(10)	0.0105(36)	0.0267(43)	0.0177(40)	-0.0059(31)
S(11)	0.0130(36)	0.0216(41)	0.0140(37)	-0.0030(30)
S(12)	0.0140(36)	0.0167(38)	0.0107(36)	-0.0028(29)
S(13)	0.0087(37)	0.0522(58)	0.0179(41)	-0.0032(31)
S(14)	0.0135(37)	0.0235(44)	0.0220(42)	-0.0063(32)
S(15)	0.0152(40)	0.0299(50)	0.0298(47)	-0.0099(35)
S(16)	0.0208(44)	0.0607(65)	0.0145(41)	-0.0025(35)

Table 4.20: Bond distances (less than 3.6Å) in robinsonite, R6,(2,2).

Narrow Ribbon			Wide Ribbon		
M(1) -	S(1)	2.701(6)	M(10) -	S(10)	2.478(7)
	S(5)X2	2.640(6)		S(16)X2	2.622(5)
	S(5)	3.016(7)		S(15)X2	3.141(6)
	S(4)X2	3.128(5)			
	S(10)	3.420(7)			
M(2) -	S(2)	2.783(6)	M(11) -	S(11)	2.477(7)
	S(4)X2	2.885(5)		S(14)X2	2.779(5)
	S(3)X2	2.986(5)		S(15)X2	2.885(6)
	S(16)X2	3.258(6)			
M(3) -	S(3)	2.437(6)	M(12) -	S(12)	2.538(6)
	S(6)X2	2.657(4)		S(13)X2	2.633(5)
	S(2)X2	2.963(5)		S(14)X2	3.196(6)
M(4) -	S(4)	2.455(7)	M(13) -	S(6)	2.900(7)
	S(1)X2	2.702(5)		S(12)X2	2.933(5)
	S(2)X2	2.946(5)		S(3)X2	3.109(5)
				S(13)	3.236(7)
				S(13)X2	3.334(6)
			M(14) -	S(14)	2.828(7)
				S(11)X2	2.932(5)
				S(12)X2	3.010(5)
				S(1)	3.210(6)
				S(6)	3.262(6)
			M(15) -	S(15)	2.739(7)
				S(10)X2	2.808(5)
				S(11)X2	3.045(5)
				S(5)X2	3.211(5)

Table 4.21: Cation occupations in robinsonite, R6,(2,2) according to results of Petrova et al. (1978).

metal position (this study)	metal position (Petrova et al.)	Occupation		
		Petrova et al.	bond valence method	average
1	8, 12	Pb, Sb	0.32Pb+0.68Sb,	0.19Pb+0.81Sb	0.26Pb+0.74Sb
2	6, 7	Pb, Pb	Pb,	0.65Pb+0.35Sb	0.83Pb+0.17Sb
3	14, 19	Sb, Sb	0.10Pb+0.90Sb,	Sb	0.05Pb+0.95Sb
4	15, 20	Sb, Sb	Sb,	0.11Pb+0.89Sb	0.06Pb+0.94Sb
10	16, 18	Sb, Sb	Sb,	Sb	Sb
11	17, 13	Sb, Sb	0.14Pb+0.86Sb,	Sb	0.07Pb+0.93Sb
12	10, 11	Sb, Sb	0.26Pb+0.74Sb,	0.32Pb+0.68Sb	0.29Pb+0.71Sb
13	4, 5	Pb, Pb	Pb,	Pb	Pb
14	1, 2	Pb, Pb	Pb,	Pb	Pb
15	3, 9	Pb, Sb	0.69Pb+0.3iSb,	0.25Pb+0.75Sb	0.47Pb+0.53Sb
Formula		$Pb_8Sb_{12}S_{26}$	$Pb_{8.03}Sb_{11.97}S_{26}$		

Table 4.22: Structure determination of $Pb_5Sb_6S_{14}$, R7, (2,2).

Space group		$I\bar{1}$
Lattice parameters (Å)		
	a=28.367(8)	α=89.59(2)
	b= 4.024(1)	β=92.28(3)
	c=22.044(7)	γ=89.93(2)
Volume ($Å^3$)		2514
Calculated density (g/cm^3)		5.86
Reflections used to determine a and b		$19^\circ<2\theta<24^\circ$
Standard reflections		13 0 3, -13 1 -2
e.s.d. of standard reflections (%)		3.0, 3.0
No. of standard reflection measurements		95, 95
Range of measured reflections		-33≤h≤32
		-4≤k≤4
		0≤l≤26
No. of reflections measured		4444
No. of unique reflections		4444
Linear absorption coefficient μ (mm^{-1})		39.1
No. of reflections used in psi-scan		21
Absorption correction: maximum; reflection		4.10; 1 2 1
Weighting parameters k; g		1.07; 0.0006
Final R; R_w		0.088; 0.100
Shift/error in final cycle: maximum		0.011
average		0.002
Number of variables refined		245
Residual electron density: maximum ($eÅ^{-3}$)		4.3
minimum		-3.4

Table 4.23: Percentage of Sb on cation sites in $Pb_5Sb_6S_{14}$, R7, (2,2).

Site	X-ray	Bond valence
M(1)	66	55 (70)[145]
M(2)	21	10
M(3)	100	100
M(4)	100	100
M(10)	100	100
M(11)b[146]	82	80
M(12)b	75	70
M(13)b	65	65 (50)
M(14)	0	0
M(15)	0	0
M(16)	23	20
Formula	$Pb_{4.68}Sb_{6.32}S_{14}$	$Pb_5Sb_6S_{14}$

[145]The values in brackets were obtained from the bond valence analysis but lower residuals (R) were obtained in SHELX76 refinement for values not in brackets.

[146]Lead occupies sites M(11)a, M(12)a and M(13)a.

Table 4.24: Bond valences, Σs, in $Pb_5Sb_6S_{14}$, R7,(2,2) weighted according to X-ray occupation number.
V is the atomic valence weighted using these occupancies.

	M(1)	M(2)	M(3)	M(4)	M(10)	M(11)	M(12)	M(13)	M(14)	M(15)	M(16)	Σs
%Sb	66	21	100	100	100	82	75	65	0	0	23	
S(1)	0.57			0.59+0.53						0.17	0.02	-1.88
S(2)		0.5	0.62+0.07	0.61								-1.80
S(3)		0.27+0.28	1.10						0.45			-2.10
S(4)	0.20+0.20	0.41+0.38		1.08								-2.27
S(5)	0.67+0.93										0.19+0.17	-1.96
S(6)			0.63+0.59	0.10					0.41	0.16		-1.89
S(10)	0.12	0.03			1.09						0.47+0.42	-2.13
S(11)						0.98				0.69	0.25+0.25	-2.17
S(12)							0.85		0.66	0.60		-2.11
S(13)								0.74+1.02	0.25			-2.01
S(14)					0.05		0.39+0.79	0.18+0.32	0.15			-1.88*
S(15)						0.28+0.54	0.19+0.34			0.39		-1.74*
S(16)					0.33+0.14	0.26+0.57	0.06+0.03				0.44	-1.83*
S(17)		0.14+0.13			1.09+0.40			0.07+0.12				-1.95*
Σs	2.69	2.14	3.01	2.91	3.10	2.63	2.65	2.45	1.92	2.01	2.21	
V	2.66	2.21	3.00	3.00	3.00	2.82	2.75	2.65	2.00	2.00	2.23	

Table 4.25: Atomic coordinates for $Pb_5Sb_6S_{14}$, R7, (2,2).

	x	y	z
M(1)	0.7005(1)	0.0005(4)	0.6880(1)
M(2)	0.6628(1)	0.0069(3)	0.4937(1)
M(3)	0.5396(1)	0.5129(6)	0.4293(1)
M(4)	0.5829(1)	0.5076(6)	0.6199(1)
M(10)a	0.8038(1)	0.9726(26)	0.4761(1)
M(10)b	0.8038(1)	0.0823(18)	0.4761(1)
M(11)a	0.9500(1)	0.9521(32)	0.5485(1)
M(11)b	0.9500(1)	0.0602(8)	0.5485(1)
M(12)a	0.9067(1)	0.0277(35)	0.3792(1)
M(12)b	0.9067(1)	0.9347(25)	0.3792(1)
M(13)a	0.7667(1)	0.0258(55)	0.3265(1)
M(13)b	0.7667(1)	0.9440(45)	0.3265(1)
M(14)	0.8864(1)	0.4943(3)	0.2026(1)
M(15)	0.9813(1)	0.5088(3)	0.7122(1)
M(16)	0.8397(1)	0.5110(3)	0.6346(1)
S(1)	0 6052(2)	0.9995(19)	0.6989(4)
S(2)	0.5678(2)	0.0023(19)	0.5223(4)
S(3)	0.6225(2)	0.5074(16)	0.4038(3)
S(4)	0.6643(2)	0.5020(18)	0.5873(3)
S(5)	0.6981(2)	0.4988(21)	0.7670(3)
S(6)	0.5230(2)	0.0083(19)	0.3507(3)
S(10)	0.7811(2)	0.0188(19)	0.5813(4)
S(11)	0.9199(2)	0.0104(18)	0.6532(3)
S(12)	0.9411(2)	0.9908(17)	0.2738(4)
S(13)	0.7942(3)	0.9977(21)	0.2128(4)
S(14)	0.8475(3)	0.4950(20)	0.3384(4)
S(15)	0.9836(3)	0.4902(19)	0.4093(4)
S(16)	0.8812(3)	0.5149(19)	0.5195(4)
S(17)	0.7462(3)	0.5151(24)	0.4495(4)

Table 4.26: Anisotropic thermal displacement parameters ($Å^2$) for $Pb_5Sb_6S_{14}$, R7,(2,2).

	U_{11}	U_{22}	U_{33}	U_{12}	U_{13}	U_{23}
M(1)	0.045(1)	0.029(1)	0.040(1)	0.0001(7)	-0.0076(8)	0.0009(7)
M(2)	0.043(1)	0.032(1)	0.031(1)	0.0011(5)	0.0032(6)	0.0001(6)
M(3)	0.022(1)	0.057(1)	0.045(1)	-0.0069(3)	0.0098(9)	0.0022(11)
M(4)	0.023(1)	0.056(1)	0.047(2)	-0.0005(1)	0.0099(10)	0.0016(12)
M(10)	0.036(1)	0.035(6)	0.028(1)	0.0061(8)	0.0091(10)	0.0028(9)
M(11)	0.039(1)	0.037(3)	0.040(1)	0.0061(8)	0.0101(10)	0.0028(9)
M(12)	0.032(1)	0.030(5)	0.044(1)	-0.0066(9)	0.0076(9)	-0.0035(12)
M(13)	0.029(1)	0.057(9)	0.055(1)	-0.0059(9)	-0.0017(9)	-0.0064(2)
M(14)	0.030(1)	0.030(1)	0.039(1)	-0.0006(5)	-0.0059(5)	0.0014(6)
M(15)	0.028(1)	0.029(1)	0.031(7)	0.0000(5)	0.0016(5)	-0.0001(5)
M(16)	0.027(1)	0.031(1)	0.044(1)	-0.0004(5)	0.0099(6)	-0.0007(6)
S(1)	0.017(3)	0.041(4)	0.025(4)	0.0017(28)	0.0082(29)	0.0005(34)
S(2)	0.016(3)	0.036(4)	0.034(5)	-0.0051(27)	0.0075(30)	0.0025(36)
S(3)	0.017(3)	0.018(3)	0.026(4)	-0.0002(24)	0.0041(27)	0.0013(29)
S(4)	0.013(3)	0.033(4)	0.021(4)	-0.0004(25)	0.0005(25)	-0.0019(30)
S(5)	0.027(4)	0.051(5)	0.018(4)	-0.0005(33)	0.0038(30)	0.0025(35)
S(6)	0.018(3)	0.042(4)	0.018(4)	-0.0009(28)	0.0009(27)	-0.0030(32)
S(10)	0.026(4)	0.035(4)	0.027(4)	0.0033(30)	0.0063(30)	0.0026(34)
S(11)	0.022(3)	0.031(4)	0.024(4)	0.0015(28)	0.0008(29)	0.0008(32)
S(12)	0.015(3)	0.026(3)	0.038(5)	-0.0014(26)	-0.0018(30)	-0.0011(33)
S(13)	0.028(4)	0.050(5)	0.023(4)	-0.0029(33)	0.0050(31)	0.0035(37)
S(14)	0.034(4)	0.037(4)	0.030(5)	-0.0021(32)	0.0117(34)	-0.0014(36)
S(15)	0.045(4)	0.024(4)	0.029(4)	-0.0030(31)	0.0087(35)	0.0074(33)
S(16)	0.040(4)	0.030(4)	0.030(4)	0.0044(32)	0.0119(34)	0.0033(34)
S(17)	0.028(4)	0.064(6)	0.037(5)	0.0024(37)	0.0103(36)	0.0124(45)

Table 4.27: Bond distances (Å), less than 3.6Å in $Pb_5Sb_6S_{14}$, R7,(2,2).

Narrow ribbon			Wide ribbon		
M(1) -	S(5)	2.660(8)	M(10)a -	S(10)	2.437(09)
	S(5)	2.669(8)		S(17)	2.516(12)
	S(1)	2.725(7)		S(17)	2.776(12)
	S(5)	3.006(7)		S(16)	2.994(10)
	S(4)	3.134(7)		S(16)	3.214(11)
	S(4)	3.143(7)			
	S(10)	3.345(8)			
M(2) -	S(2)	2.792(7)	M(10)b -	S(10)	2.444(9)
	S(4)	2.868(7)		S(17)	2.444(10)
	S(4)	2.895(7)		S(17)	2.854(11)
	S(3)	3.015(7)		S(16)	2.932(9)
	S(3)	3.018(7)		S(16)	3.284(9)
	S(17)	3.263(9)			
	S(17)	3.304(9)			
M(3) -	S(3)	2.441(6)	M(11)a -	S(11)	2.504(8)
	S(6)	2.670(8)		S(16)	2.686(11)
	S(6)	2.699(8)		S(15)	2.729(11)
	S(2)	2.929(8)		S(16)	3.040(12)
	S(2)	2.988(8)		S(15)	3.051(12)
M(4) -	S(4)	2.446(7)	M(11)b -	S(11)	2.501(8)
	S(1)	2.694(8)		S(16)	2.733(8)
	S(1)	2.743(8)		S(15)	2.748(8)
	S(2)	2.951(8)		S(16)	2.988(8)
	S(2)	2.900(8)		S(15)	3.030(8)
			M(12)a -	S(12)	2.560(8)
				S(14)	2.635(11)
				S(14)	2.867(12)
				S(15)	2.905(11)
				S(15)	3.143(11)
			M(12)b -	S(12)	2.564(8)
				S(14)	2.577(9)
				S(15)	2.877(9)
				S(14)	2.931(9)
				S(15)	3.174(9)

Table 4.27 cont.

M(13)a	- S(13)	2.658(9)
	S(13)	2.700(19)
	S(13)	2.835(19)
	S(14)	2.974(17)
	S(14)	3.136(18)
	S(17)	3.421(17)
	S(17)	3.469(17)
M(13)b	- S(13)	2.603(17)
	S(13)	2.664(9)
	S(14)	2.924(15)
	S(13)	2.940(18)
	S(14)	3.191(17)
	S(17)	3.287(15)
	S(17)	3.618(17)
M(14)	- S(6)	2.868(7)
	S(12)	2.945(7)
	S(12)	2.963(7)
	S(3)	3.087(7)
	S(3)	3.096(7)
	S(14)	3.234(8)
	S(13)	3.308(8)
	S(13)	3.324(8)
M(15)	- S(15)	2.894(9)
	S(11)	2.928(7)
	S(11)	2.937(7)
	S(12)	2.988(7)
	S(12)	2.990(7)
	S(1)	3.199(7)
	S(6)	3.231(7)
M(16)	- S(10)	2.814(8)
	S(16)	2.839(9)
	S(10)	2.858(8)
	S(11)	3.050(7)
	S(11)	3.053(7)
	S(5)	3.149(8)
	S(5)	3.200(8)

5 Structures in the Ag_2S-PbS-Bi_2S_3 system

This chapter presents the results of the study of the Ag_2S-PbS-Bi_2S_3 system. The phases present at different compositions after different annealing treatments have been examined by electron diffraction and microscopy and X-ray diffraction. These results are presented first followed by the discussion of decomposion of the phases into galena. These results have been published in Skowron and Tilley (1986 a, b, 1989, 1990).

As discussed in chapter 1, the known phases occuring in the PbS rich part of the PbS-Bi_2S_3 and Ag_2S-PbS-Bi_2S_3 systems have structures which can be obtained by "twinning" galena along (311) planes which become mirror planes in the structure. The structures belong to the lillianite series and can be denoted by the LN_1,N_2 symbols indicating the width of galena slabs between the mirror planes. In the discussion below, these structures will be referred to as twinned structures, following common terminology, and indicated by their symbols.

5.1 Sample preparation

The samples in PbS-Bi_2S_3 and Ag_2S-PbS-Bi_2S_3 systems were prepared by weighing the elements in proportions corresponding to compositions indicated in Fig. 5.1 and listed in Appendix 1. The samples were melted first and then cooled in one of three ways viz, (1) Slow cooling to 773K, annealing for three weeks and then brine quenching, (2) Slow cooling to 973K, annealing for one week and then brine quenching, (3) Brine quenching from the melt.

5.2 Electron diffraction

Fig. 5.2a shows a [001] zone oriented diffraction pattern of L4,4 and Fig. 5.2b shows a drawing of the reflections expected from galena twinned along (311). The reflections corresponding to the galena sub-cell are strong in the diffraction pattern of L4,4 and can be indexed as $(0\ 12\ 0)_{L4,4}$ indicating that $d_{010(L4,4)} = 12d_{311(PbS)}$. Since each twin plane has width of $4d_{311(PbS)}$, as indicated in Fig. 5.3, then the total number of octahedra N_1+N_2 in two adjacent slabs equals 12-4=8. Measurements on the [001] zone oriented electron diffraction pattern give $\underline{a}$, $\underline{b}$ and γ which together with N_1+N_2 allows one to determine N_1 and N_2 from geometric considerations outlined in Appendix 2.

5.3 Phase analysis by electron microscopy

Only a few of the crystal fragments examined in the electron microscope were suitably aligned and thin enough to allow the high resolution lattice imaging. Most of the fragments could be imaged only with medium or low resolution. Contrast bands related to the appearance of the 0k0, k-odd, forbidden reflections were present for most aligned crystal fragments of all phases[9]. However, it was possible to interpret favourable micrographs by careful measurements on the plates. As the (111) galena planes were often well resolved, a measurement of spacing of these planes gives a scale which allows the twin plane separation to be accurately determined. In some cases, however, it was necessary to determine the structure of a phase from its diffraction pattern alone following the method described in Appendix 2. Where both the image and the diffraction pattern were available, the diffraction pattern measurements agreed with those from the direct image.

Samples annealed at 773K

The compositions of the samples annealed at 773K and the phases present are shown in Fig. 5.4. Nine phases were found, six of

[9]The 0k0, k-odd, reflections are forbidden in both kinematical and dynamical diffraction, provided the beam enters almost exactly in specified directions (Gjonnes and Moodie, 1965). Convergence of the beam or bending of crystal can result in observing the forbidden reflections and corresponding contrast features as discussed by Moodie and Whitfield (1984).

which were previously known: galena, galenobismutite, L4,4, L7,7, L4,7 and L4,8 and three of which are new: L8,8, L7,8, and L4,5. Figs 5.5, 5.6, 5.7 and 5.8 show L7,7 and L4,7 imaged at high resolution and L7,8 and L8,8 at iow resolution. For L4,8 and L4,5 only the electron diffraction patterns are available and these are shown in Fig. 5.9.

In addition to these phases, which were found frequently, one or two crystal fragments were encountered which contained the structures L5,7 and L5,8. In spite of searching for L5,9 and L11,11, which are known to occur in nature (Makovicky and Karup-Møller, 1977b) we could not find them even in samples prepared according to their reported stoichiometry. Apart from in L4,5, galena slabs 5 octahedra wide were rarely found.

Samples annealed at 973K

The compositions of the samples annealed at 973K and the phases found are shown in Fig. 5.10. The crystals that separated from the bulk during annealing were found to be mostly L4,4. L4,7 seems to cover the same narrow field at both 773K and 973K.

Samples quenched from the melt

The compositions of the samples quenched from the melt and the phases found are shown in Fig. 5.11. No new phases were found. A summary of the phase analysis obtained by the electron

microscopy is given in Fig. 5.12.

5.4 Phase analysis by powder X-ray diffraction

Samples annealed at 773K for three weeks

The compositions of the samples annealed at 773K and the phases present are shown in Fig. 5.13. In these preparations L7,7 and galena occurred in the region close to PbS, while in the series of samples 21-29, galenobismutite, L4,4, L4,7, and L8,8 were identified. In samples No.37 and 39 L8,8 and an unidentified phase or phases were present resulting in diffuse diffraction patterns. Diffraction patterns from samples No.24, 25, and 32 were also diffuse.

Samples annealed at 973K for one week

The compositions of the samples annealed at 973K and the phases found are shown in Fig. 5.14. In many of these preparations a separation of phases occurred in the silica tubes. Needle-like crystals frequently grew from the bulk during annealing. Most often they were identified as L4,4, although L4,7 also separated in this way. L4,4 coexisted with other phases, either in the bulk or as needles, over a wide range of compositions. For the series of samples No.21-29 five phases could be recognized: galenobismutite, L4,4, L4,7, L8,8, and galena. L4,7 predominated in only one sample and occurred in three others in traces. Galena coexisted with L7,7 for PbS rich and with L8,8 for PbS

poorer compositions.

Samples quenched from the melt

The compositions of the samples quenched from the melt and the results of phase analysis obtained by the X-ray powder are shown schematically in Fig. 5.15. X-ray diffraction of many samples showed broad lines consistent with a break down in the long-range crystalline order. This made precise phase analysis difficult. Despite this limitation L4,4 was identified in most of the samples, and other phases also unmistakably identified were PbS, L7,7 and galenobismutite. It was not possible to determine which phases were present in samples 31 and 32 because the lines were very broad. A summary of the phase analysis found by powder X-ray diffraction is given in Fig. 5.16. The regions in which L7,7 L4,4, L4,7 and L8,8 exist are delineated.

Lattice dimensions

Galena

Decrease of the a lattice parameter of cubic galena was observed as compositions changed from PbS to $AgBiS_2$. In the preparations off the PbS-$AgBiS_2$ line the galena lattice parameter decreased slightly as the samples became richer in L7,7 or L8,8.

L4,4

The lattice parameters of silver free L4,4, annealed at 773K for

three weeks, were refined first to provide a standard against which silver containing samples could be compared. They agreed with the results of Takéuchi and Takagi (1972) and Otto and Strunz (1969) on silver free L4,4 shown in Table 1.5. The lattice parameters of a number of samples with diffraction patterns similar to that of Ag free L4,4 but taken from preparations containing Ag were refined. The results are presented in Table 5.1. The lattice parameters are smaller in the Ag containing samples, with b changing more than a and c. There were no apparent changes in the relative intensities of reflections as the lattice parameters changed.

L4,7

The monoclinic unit cells refined from the two powder diffraction patterns of samples 23 and 24 are shown in Table 5.1 and they agree with the unit cell reported by Makovicky and Karup-Møller, (1977b), shown in Table 1.5. The space groups B2/m and Bm are both allowed by the systematic extinctions h,k,l: h+l=2n. Because the full powder X-ray pattern has not been published before, it is given in Appendix 3 (sample 24). L4,7 was found over a narrow range of compositions, as marked on Figs 5.13 and 5.14 and only small lattice parameter differences were observed for the material in the two samples.

L7,7

The unit cell parameters refined from the X-ray diffraction

pattern of silver free L7,7 agreed with the study of Otto and Strunz (1967) rather than with the results of Takéuchi and Takagi (1974a), who report a larger value for a as shown in Table 1.5. The unit cells observed in the Ag containing L7,7 are shown in Table 5.1. The smallest parameters were obtained for the sample no.32 which contained the largest amount of Ag.

L8,8

This new phase was found in the samples marked with a half filled circles on Figs 5.13 and 5.14. The unit cell parameters that index the powder pattern are given in Table 5.1. The space group allowed by the systematic extinctions: hkl: h+l = 2n; 0kl: k = 2n, is Bbmm and the indexed diffraction pattern is presented in Appendix 4.

5.5 Electron microscope study of intergrowths

In the PbS rich part of the system galena, L4,4 and L7,7 coexisted but did not intergrow. The large number of PbS crystal flakes examined in the electron microscope revealed mostly contrast characteristic of stoichiometric material with occasional contrast features typical of stacking faults, dislocations or other lattice defects. Irregularly spaced twin planes, similar to those shown in Fig. 5.17, were found but only rarely.

Although the twinned phases did not seem to intergrow easily for PbS rich compositions, a region in the PbS poorer part of the diagram, marked with a line AB on Fig. 5.12, was found where the phases had a strong tendency to intergrow. Of the five twinned phases that were found in this region, two, L4,7 and L4,4, intergrew especially easily. L7,7 and L8,8 also readily intergrew and Fig. 5.18 shows a micrograph of a crystal fragment of their irregular intergrowth. Similar intergrowths of L4,8 and L4,4 were found only occasionally. The tendency of L8,8 and L4,8 to intergrow was even poorer.

The degree of irregularity in the intergrowing material varied. Some fragments possessed highly differing widths of galena slabs and their diffraction patterns showed streaks instead of separate reflections as shown in Fig. 5.19. In other cases galena slabs with only two or three widths were intergrown with a varying regularity. An example of rather regularly intergrown material is shown in Fig. 5.20. Spacing of the lattice fringes, Fig. 5.20(a), indicate that L4,4 and L4,7 are present. On the diffraction pattern, Fig. 5.20(b), the strong 0k0 reflections corresponding to $(311)_{PbS}$ can be indexed as 0,12,0 as in L4,4 indicating that of the two phases L4,4 is predominant. The micrograph of the most regularly intergrowing material encountered is shown in Fig. 5.21(a). A tendency to form sequences of ABB and ABBB type, where A = L4,7 and B = L4,4, is visible. The approximate repeat distance measured from the

weaker superstructure reflections on the diffraction pattern, Fig. 5.21(b), is close to 66Å and corresponds with the dimension of the ABB type intergrowth calculated from the b parameters of L4,7 and L4,4.

5.6 Discussion

Phase analysis

The powder X-ray and the electron microscope phase analyses are in agreement, compare Figs 5.12 and 5.16. However, because even small crystal fragments could be identified in the electron microscope more phases were found by electron microscopy than by powder X-ray diffraction.

Galena slabs with four widths: 8, 7, 5 and 4 octahedra have been found. No phase with slabs six octahedra wide was found nor were the phases L5,9 and L11,11 both of which were reported by Makovicky and Karup-Møller, 1977b. The newly found phases, L8,8, L7,8, L4,5, L5,7 and L5,8[10] together with the previously reported L4,4, L4,7 L4,8 and L7,7 form structures with all possible combinations of the galena slabs with the widths of 4, 5, 7 and 8 except for L5,5.

[10]The last two phases were found only in two instances.

In the compositional region indicated by the line AB in Fig. 5.12 the twinned phases have a tendency to intergrow. The intergrowths of L4,4 and L4,7 form a distinct group among other intergrowing phases. The complexity of the intergrowth structure revealed in the electron microscope study explains the difficulties in the phase identification encountered during the X-ray powder examination.

Makovicky and Karup-Møller, (1977b), defined a "remarkable mineral species" schirmerite. They state: "The crystal structure of schirmerite is strongly disordered. Its reciprocal lattice contains three sets of reflections: a sharp, a slightly diffuse and a diffuse set. They densely populate the reciprocal lattice rows parallel to the lillianite b^* direction. (...) The sharp reflections represent nodes of (galena) sublattice. (...) The partly diffuse reflections, flanking the sharp reflections in both positive and negative directions parallel to b^*, represent non-integral satellites. Their intensities are very variable. (...). The diffuse spots flank symmetrically not only the sharp integral reflections but also their non-integral semi-sharp satellites." The features of the diffraction pattern of schirmerite they describe resemble the features of the diffraction patterns from the semi-regular intergrowths of L4,4 and L4,7, as seen in Fig. 5.21, suggesting that schirmerite is an intergrowth of phases rather than a single phase.

Slabs six octahedra wide are not observed. Fig. 5.12 suggests that L6,6 disproportionates into a mixture of L4,4 and L7,7 in the Ag-poor region and into mixtures or intergrowths of L8,8, L4,8 and L4,7 in the Ag-rich region. Clearly, silver facilitates both the formation of slabs other than 4 or 7 octahedra wide and the formation of LN_1,N_2 homologs and their intergrowths.

Currently there is no explanation why the phases with slabs 4 and 7 octahedra wide are the only ones found in the PbS-Bi_2S_3 system. Aizawa, Iguchi and Tilley, (1983), calculated the elastic strain energy in lillianite homologs but could not explain the observed higher stability of L4,4 and L7,7 over other LN_1,N_2 homologs. However, the accumulated observations on the formation of LN_1,N_2 phases in both PbS-Bi_2S_3 and Ag_2S-PbS-Bi_2S_3 systems, allow a qualitative description of the slabs stability. The slabs 4 octahedra wide are the most stable, with or without silver, and the slabs 6 octahedra wide are not stable at all. Weights, f(N), representing stability can be assigned to slabs N octahedra wide. By setting $f(N)=\cos^2[50N-200]^\circ$ one obtains: f(4)=1.0, f(5)=0.41, f(6)=0.003, f(7)=0.75, f(8)=0.88, f(9)=0.12, f(10)=0.25, f(11)=0.97. The stabilities of phases with combinations of slabs can now be calculated by multiplying respective $f(N_1)f(N_2)$. The resulting weights are shown in Table 5.2 in decreasing order. They describe fairly well the frequency of occurance of LN_1,N_2 phases. Although slabs six octahedra wide are not observed there are four stable phases, L4,8, L4,7, L5,8 and L5,7, for which the

mean slab width is close to six. So, whatever the reason for instability of the six octahedra slabs, their composition can be approximated by the formation of one or more of the other four phases. One could then expect an instability region for the compositions close to the missing L6,6 where the other phases would form instead and intergrow.

Ourayite, L11,11, and eskimoite, L5,9, are known as minerals but were not found in this study. L11,11 is predicted to be stable while L5,9 not. Figs 5.13-5.15 suggest that L4,4 is stable at higher temperatures and the phases with wide galena slabs like L7,7 and L8,8, grow better at lower temperatures. It may be that L11,11 was not observed in this study because the temperatures used in the syntheses were too high.

Lattice dimensions

The unit cell measured for samples prepared with silver tended to be smaller than for those prepared without silver. There is substantial data concerning compositions of mineral lillianites containing silver. For those cases where both the composition and unit cell dimensions were available a graph of change in b with the degree of $Ag + Bi \Leftrightarrow 2Pb$ substitution (gustavite substitution described in chapter 1) was obtained for L4,4 and L7,7 by Makovicky and Karup-Møller, (1977b), and by Karup-Møller

and Makovicky, (1981), and this is shown in Fig. 5.22. Silver incorporated into the lattice by the gustavite substitution results in a 5% contraction in the b lattice parameter. Although the b in all those structures decreases with increasing Ag content the corresponding changes in a and c are less pronounced though they also tend to decrease. If the graphs hold for the present samples, it follows, that in our samples the L4,4 richest in Ag (sample no 23) has approximately 33%, and L7,7 (sample no 32) 54% substitution.

The reduction in the size of the unit cells of L4,4 and L7,7 as silver is incorporated is expected from the smaller size of the Ag atom. Calculations of the bond lengths using the published fractional coordinates of L4,4 and L7,7 (Takagi and Takèuchi, 1972, and Takèuchi and Takagi, 1974a) but with the lattice parameters changed to those observed in silver containing L4,4 and L7,7 indicate that the bonds in (110) plane of both L4,4 and L7,7 are shortened the most by silver incorporation.

The incorporation of silver stabilizes new structures in the system. For example, L4,7 forms only in presence of silver even though both L7,7 and L4,4 are stable without it. Comparison of the unit cells suggests that silver does get incorporated into the lattice of L4,7. The separation of the twin planes that delineate the unit cell of L4,7, $d = 25.661 \times \cos(\gamma - 90^{\circ}) = 25.52$Å, is smaller than the mean twin plane separation of silver

free L4,4 and L7,7, 26.01Å, suggesting that the widths of both 4 and 7 octahedra slabs are smaller in L4,7 than those in the silver free L4,4 and L7,7 which is indicative of silver intake. However, more precise information about the structure and cation occupancies in L4,7 and silver containing L4,4 and L7,7 is needed to elucidate the role of silver in stabilizing L4,7 and other LN_1,N_2 phases.

5.7 Transformations of twinned phases to galena

Observations

Decomposition of crystal fragments of all the twinned phases to galena frequently occurred during examination in the electron microscope. Changes in structure and in contrast often took place abruptly under the electron beam making the high resolution observations very difficult. Frequently the decomposition process had to be recorded by imaging different crystal flakes in various stages of transformation.

Sometimes the reaction was slow and early stages could be recorded showing a partially detwinned crystal fragment as that in Fig. 5.23. The twin planes have been lost in pairs starting from the edges of the crystal and they have arrow headed terminations lying on $\{111\}_{PbS}$ planes. An example of a twinned structure reverting to galena imaged at high resolution is shown

in Fig. 5.24. An edge dislocations in the regions of the termination tips can be seen by viewing the micrographs along the indicated arrows.

When the electron beam was suddenly focussed on a crystal the reaction took place rapidly leaving the crystal fragment transformed in the way shown in Fig. 5.25. During such rapid reactions the twin planes started to disappear both from the edge and the middle of the crystal. As in Fig. 5.23 the shapes of terminating galena slabs are arrow-like but the galena slabs are thicker. The diffraction patterns taken before and during the decomposition are shown in Fig. 5.26.

Although the vast majority of twin planes were disappearing in pairs, the occurrence of a single, jogged, twin plane between two thick galena slabs, is shown in Fig. 5.27. A similar jog, imaged at higher resolution, is shown in Fig. 5.28.

While the reaction sequence represented by the above figures was the commonest pathway by which crystals reverted to galena, a second way of decomposition was also noted. Its early stages are represented by patches of ill defined contrast as that visible at the bottom of Fig. 5.23. Patches of galena matrix about 80-100Å in diameter developed on the otherwise regular array of twin planes. A more advanced stage of such decomposition is shown in Fig. 5.29. Lattice fringes continuous with the twinned matrix

are visible in the oval galena regions, indicating that no melting occurred and that the solid state reaction was taking place.

Discussion

The diffraction patterns and the micrographs indicate that the twinned phases transform into galena via a solid state pathway. The reaction takes place under the influence of the electron beam and it is presumed that the heating effect of the electron beam and the surrounding vacuum are responsible for the process rather than the chemical effect of the incident electrons on the solid. Since galena structure is produced the beam must be causing either the creation of cation vacancies or a change of stoichiometry to PbS. The latter is likely since Bi_2S_3 is more volatile than PbS and the required loss of bismuth or bismuth sulphide species can easily occur in the thin parts of the sample exposed to the electron beam.

In attempting to clarify the mechanism of the reaction one should bear in mind its rapidness and the fact that it is topotactic. A model of the reaction based on these two findings was proposed by Tilley and Wright, (1982), in which atoms in a lath of L4,4, for example, were rearranging into galena structure by only small atomic displacements reducing the number of twin boundaries in

the crystal. The model accounts for the fact that twin planes disappeared in pairs but did not concern itself with the movement of the tip of the twin plane pairs during transformation. The present observations are at a high enough resolution to derive a model for this aspect of the transformation.

Initially, it is useful to consider the relative sizes of the cation octahedra in L4,4 and in galena. A measurement on the diffraction pattern on Fig. 5.26 shows that $d\ (0\ 12\ 0)_{L4,4} < d\ (311)_{PbS}$ hence, there is an expansion of the structure on transforming from L4,4 to galena of $|20.451 - 12 \times 1.7898| = 1.027$Å per pair of lost twin planes and galena occupies a greater volume than the twinned matrix. This is equivalent to a considerable change in volume at the tip of the contracting twin plane pair, and, as the product occupies a greater volume than the reactant, a strain energy will be present which will undoubtedly cause the reaction to proceed rapidly, once initiated.

The resolution obtained in the micrographs was not always sufficient to reveal the positions of atoms at the tip of the twin planes terminations but it is adequate to propose a model for these terminations, such as that shown in Fig. 5.30. The principal structural feature of the tip, apart from the (111) plane at the termination, is an edge dislocation as seen in Fig. 5.24. Detwinning would be facilitated by movement of this

dislocation as the reaction takes place. As in the case of glide in metals, the dislocation movement decreases enormously the number of chemical bonds that have to be broken to allow the structural change to occur and makes it an energetically feasible process.

Although detwinning takes place by the elimination of pairs of twin planes, occasionally a single twin plane can also be eliminated when one galena region expands at the expense of another twin-related area, as shown in Figs 5.27 and 5.28. A drawing of the terminating region, shown in Fig. 5.31, reveals that a dislocation is associated with the junction. Once again, therefore, the physical process of detwinning is made easier by passage of a dislocation through the crystal.

This type of dislocation movement mechanism, is, however, not the only process by which twin planes can be removed. The patches shown in Fig. 5.29 indicate another route. At an early stage of the reaction, the patches are revealed by complex contrast which may be due to Moiré effects. At the end of the reaction, the oval regions of galena structure sometimes show a complex contrast along the edges which may be due to a strain field of dislocation net lying at the interface.

In order to discuss this feature in more detail it is necessary to have some information about the material lost in the reaction.

If it is Bi_2S_3, then perfect galena would form. In such a case, the volume of the galena produced would be larger than that of the twinned matrix, and misfit dislocations would be required at some of the boundaries. If, on the other hand, only Bi atoms are lost, the resulting galena would be sulphur rich, and contain, at least to a first approximation, a large number of cation vacancies. It is likely, in fact, that both Bi and S species are lost.

5.8 Summary

Only two twinned phases, L4,4 and L7,7, exist in the $PbS-Bi_2S_3$ system but addition of silver stabilizes galena slabs 5 and 8 octahedra wide and facilitates the intergrowths of slabs so formation of a variety of structures becomes possible. Slabs 6 octahedra wide have not been observed and appear to be unstable. In the Ag-poor region the composition of L6,6 is approximated by mixture of L4,4 and L7,7 and in the Ag- rich region by mixture or intergrowths of L8,8, L4,8 and L4,7. The relative stability of the silver containing slabs depends on their width and can be described by a function $f(N)=\cos^2[50N-200]^\circ$. Wider slabs appear to be more stable at lower temperatures. The unit cell parameters of L4,4 and L7,7 decrease with the silver incorporation into their crystal lattices.

All the twinned phases in the $Ag_2S-PbS-Bi_2S_3$ system were

decomposing to PbS by twin elimination during observation in the electron microscope. The tips of the shrinking twins were arrow-headed and terminated by (111) planes. Contraction of the twin tip in a reacting twinned phase involved edge dislocations.

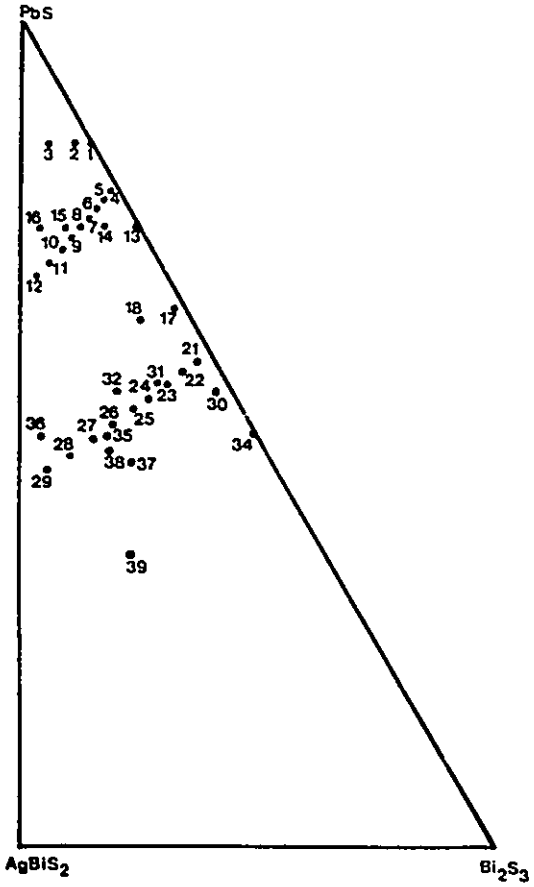

Fig. 5.1: Diagrammatic representation of the studied compositions. The numbers correspond to the compositions detailed in Appendix 1.

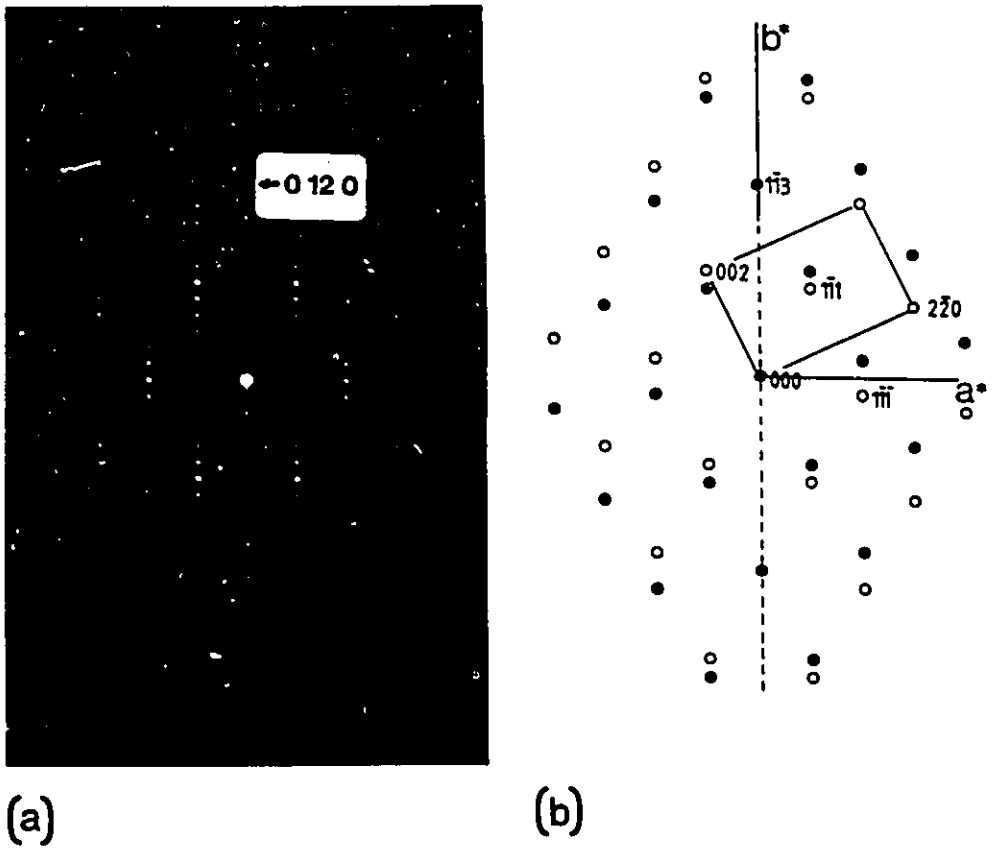

Fig. 5.2. a)[001] zone oriented diffraction pattern of L4,4. b) A drawing of the reflections expected from galena twinned along (311). The untwinned matrix reflections are drawn as open circles and are indexed on the PbS cell. The twin reflections are drawn as filled circles.

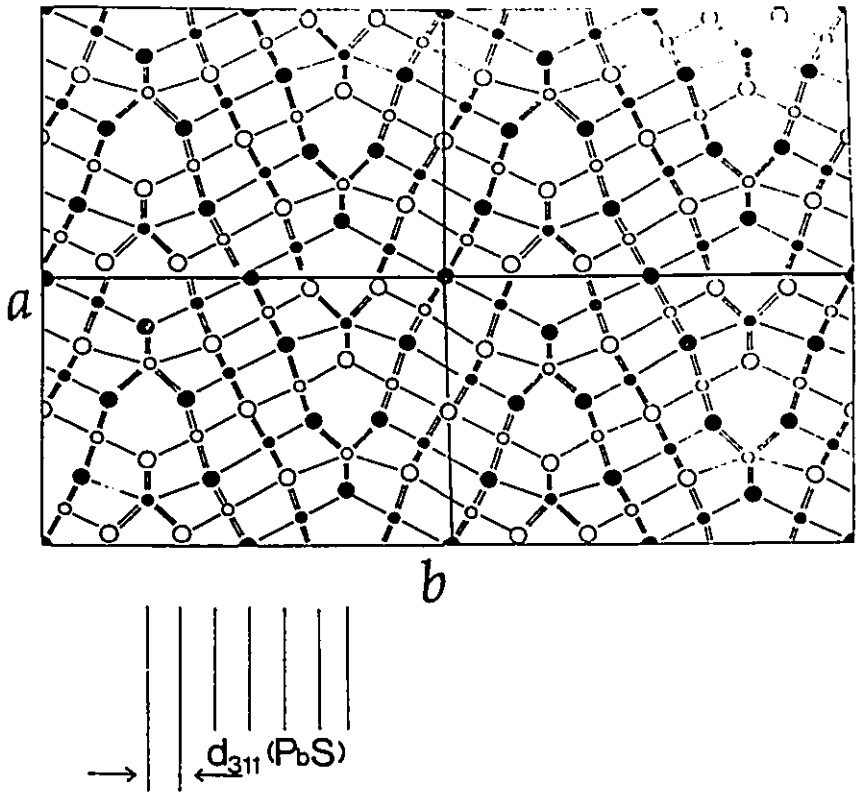

Fig. 5.3: The structure of L4,4. The spacing between the $(311)_{PbS}$ planes is indicated. The trigonal prismatic twin planes have width of $4d_{(311)PbS}$.

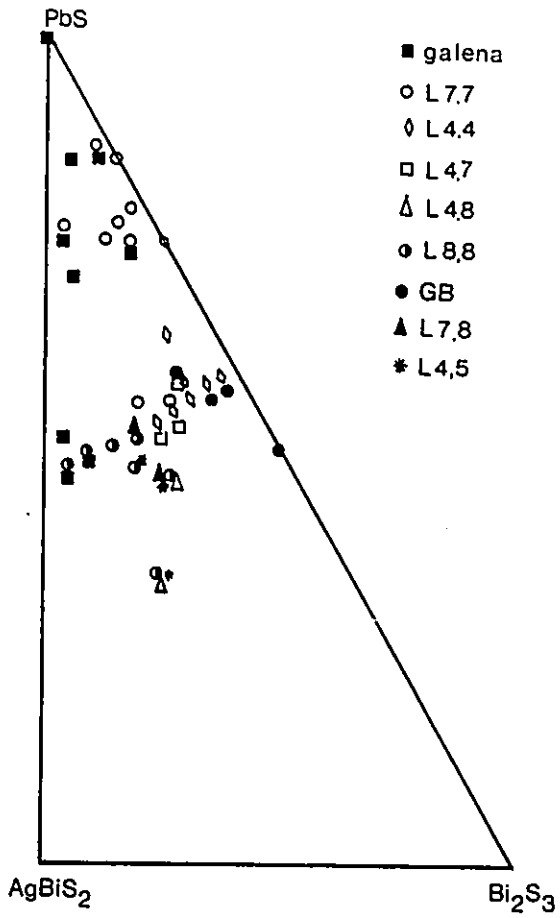

Fig. 5.4: Diagrammatic representation of the results of the electron microscope phase analysis for samples annealed at 773K.

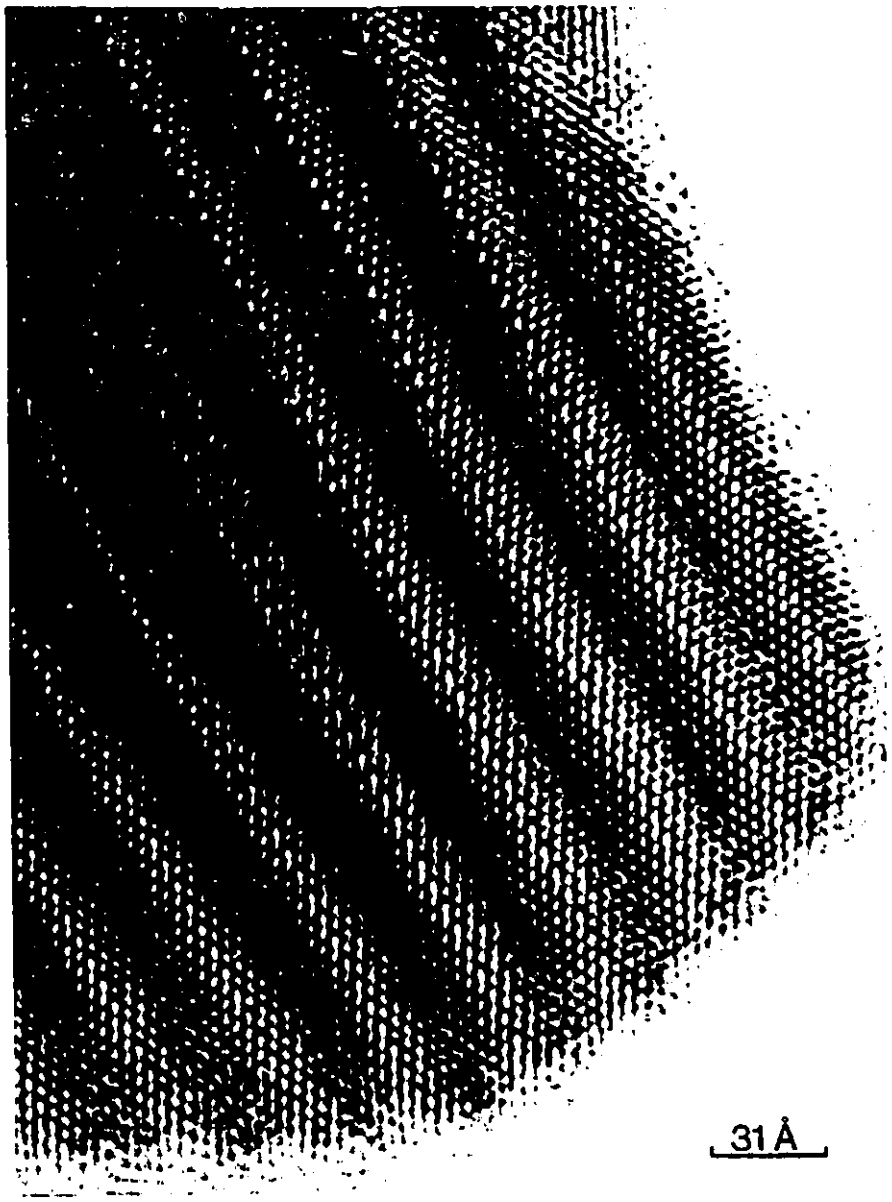

Fig. 5.5(a): High resolution electron micrograph of a crystal fragment of L7,7 viewed in [001] projection. Seven metal sites are revealed as dark contrast, running diagonally across the galena slabs.

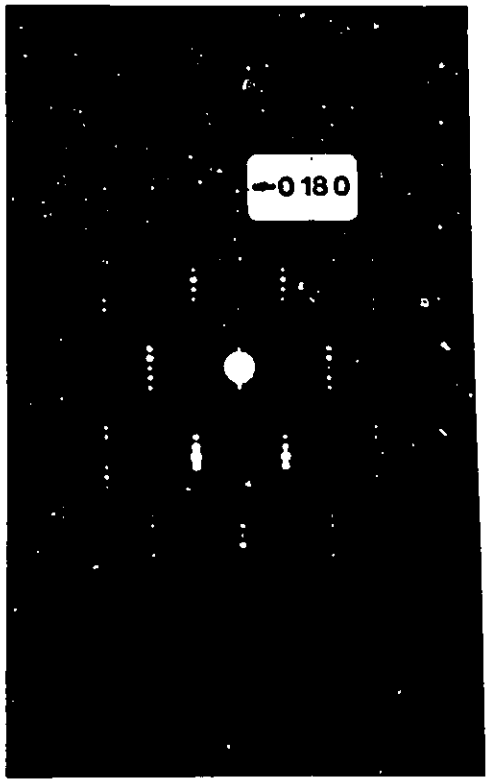

Fig. 5.5(b): [001] zone oriented diffraction pattern from L7,7.

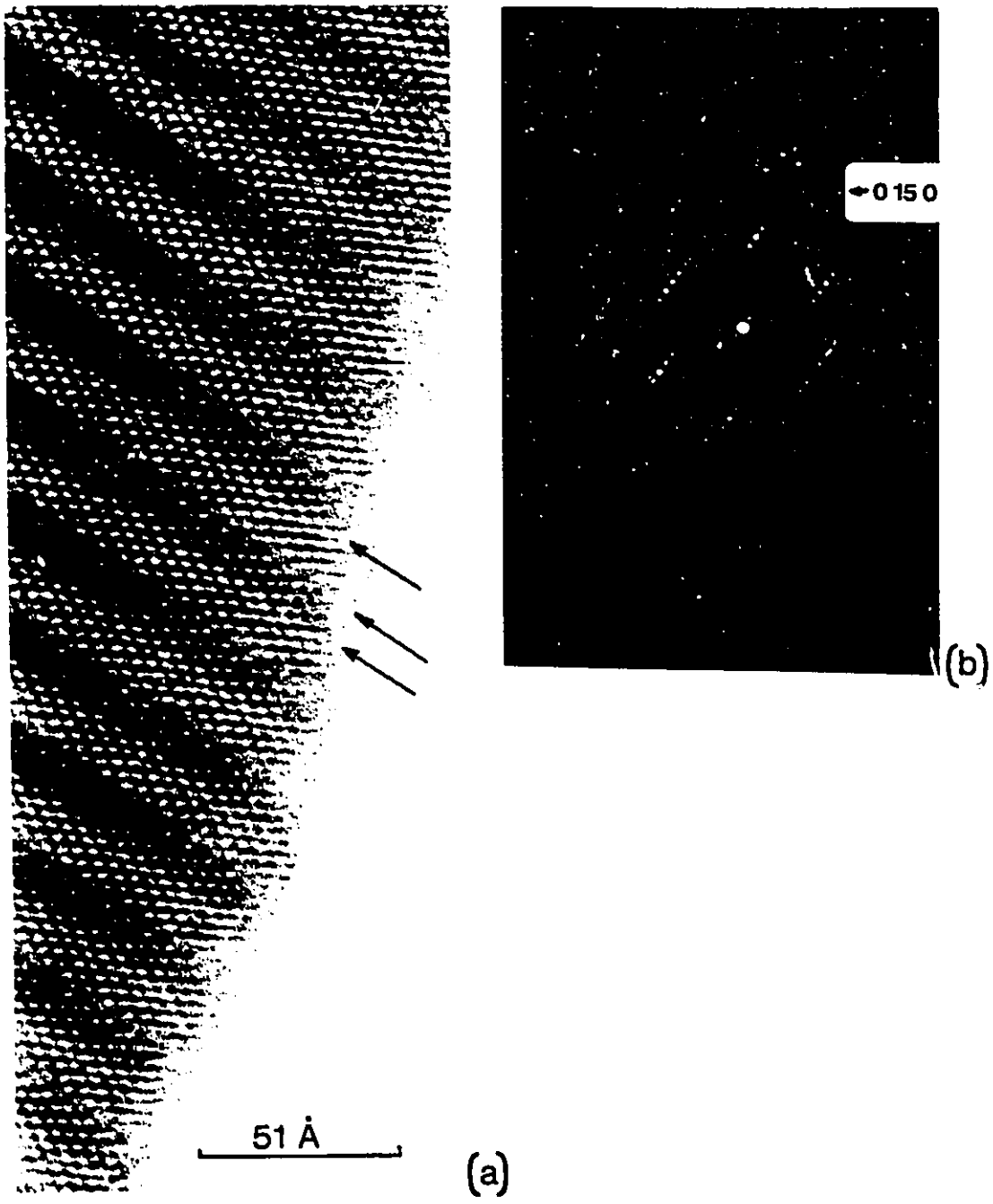

Fig. 5.6: (a) High resolution electron micrograph of L4,7 viewed in [001] projection. The twin planes are denoted by arrows. (b) The electron diffraction pattern of L4,7. The 0 15 0 reflections correspond to the 311_{PbS}.

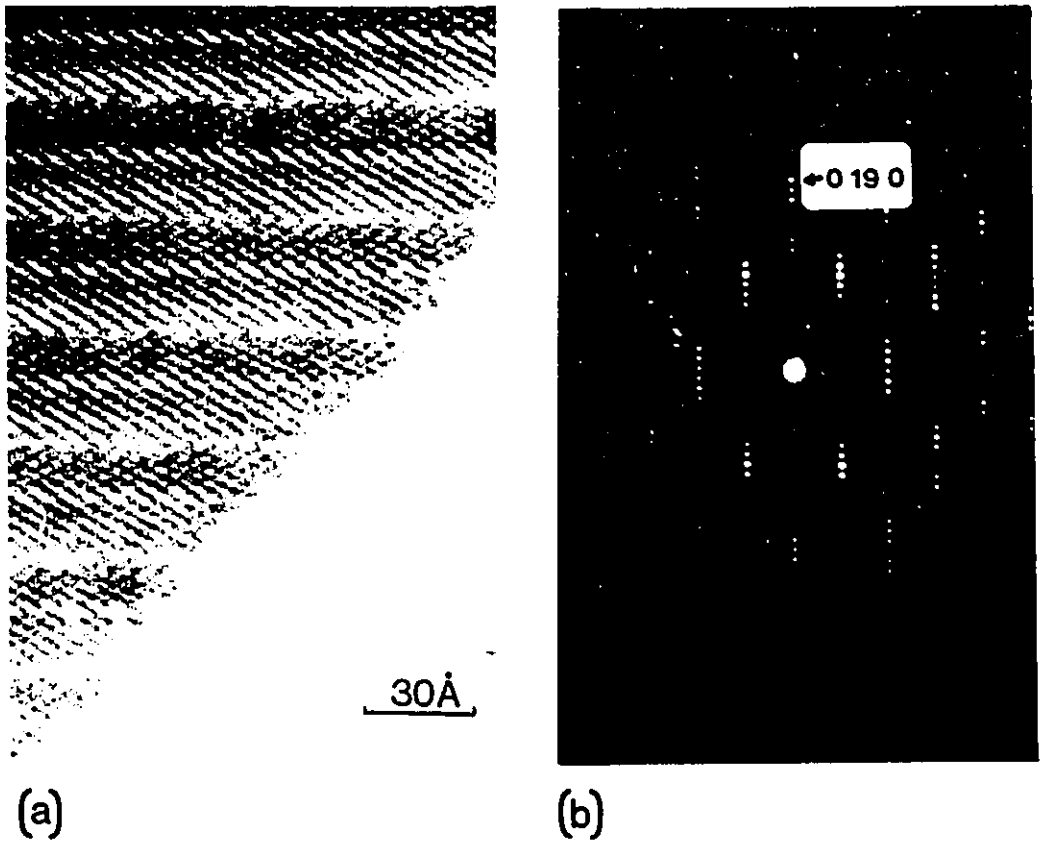

Fig. 5.7: (a) Medium resolution electron micrograph and (b) diffraction pattern of a crystal fragment of L7,8 in [001] projection. On the diffraction pattern the 0 19 0 reflections correspond to the 311_{PbS}.

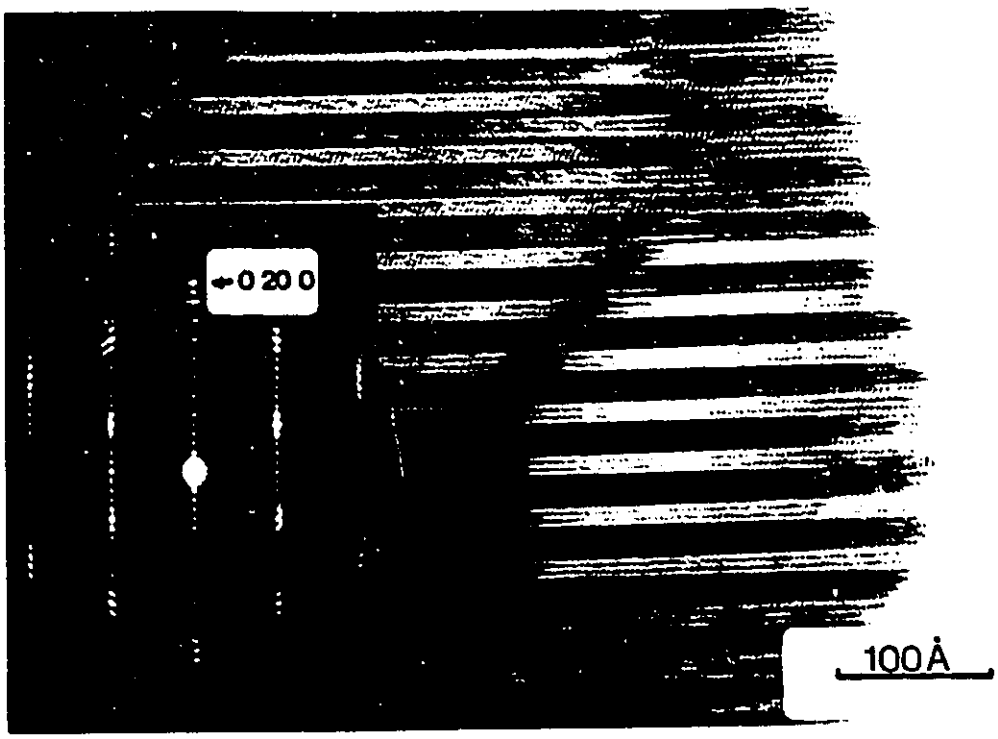

Fig. 5.8: Low resolution electron micrograph and the diffraction pattern of L8,8. The 0 20 0 reflections correspond to the 311_{PbS}.

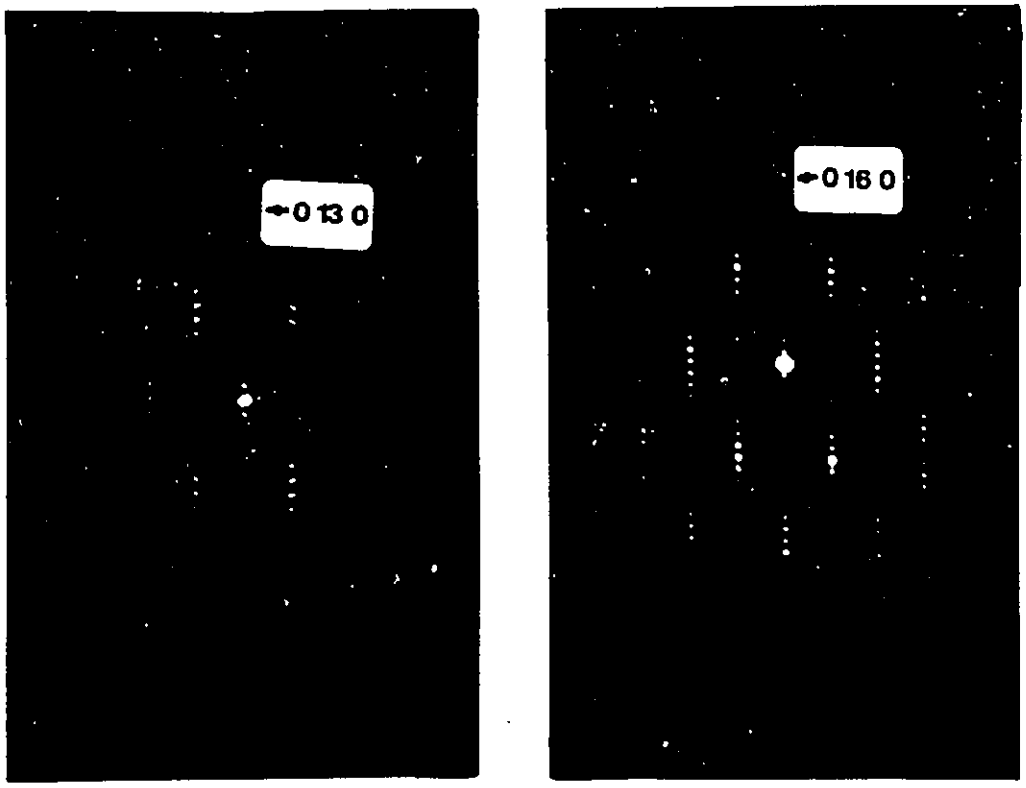

Fig. 5.9: Diffraction patterns of (a) L4,5 and (b) L4,8 in [001] projection. The reflections corresponding to 311_{PbS} are indexed as 0 13 0 for L4,5 and as 0 16 0 for L4,8.

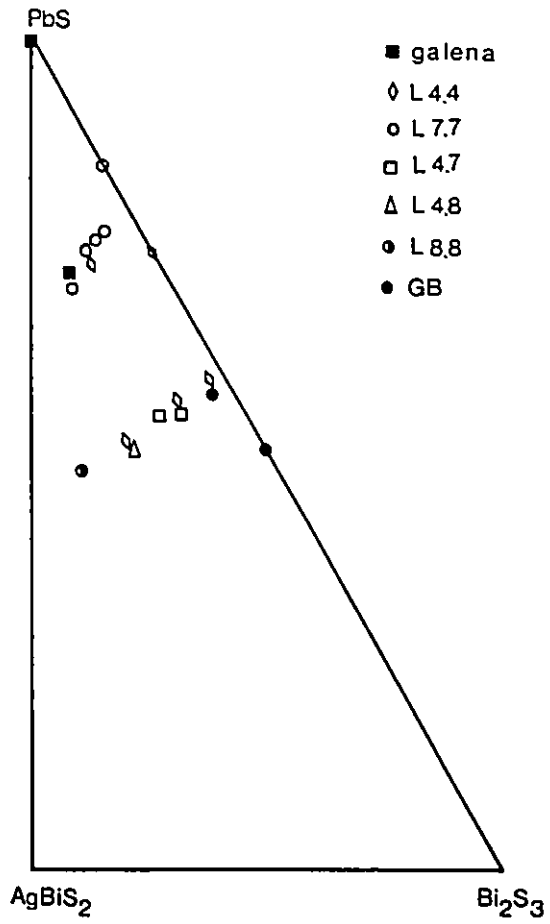

Fig. 5.10: Diagrammatic representation of the results of the electron microscope phase analysis for samples annealed at 973K.

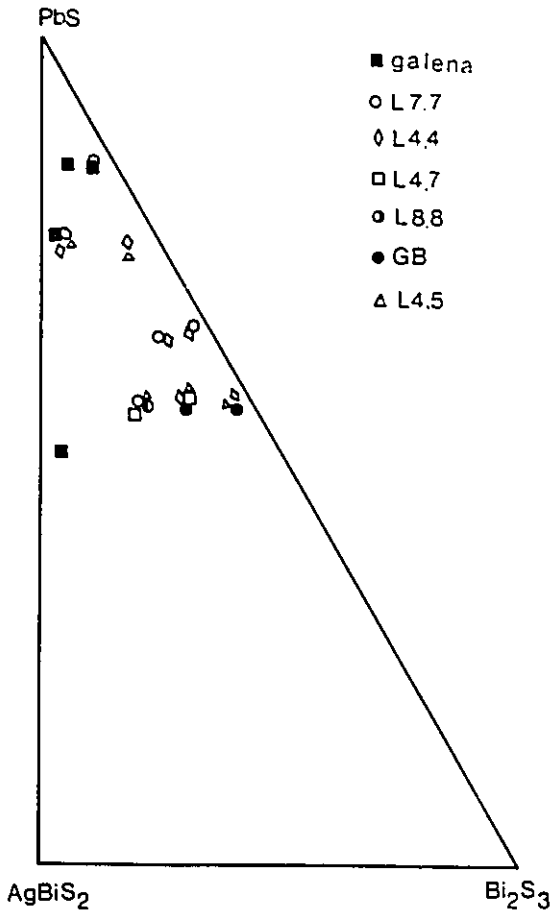

Fig. 5.11: Diagrammatic representation of the results of the electron microscope phase analysis for samples quenched from the melt.

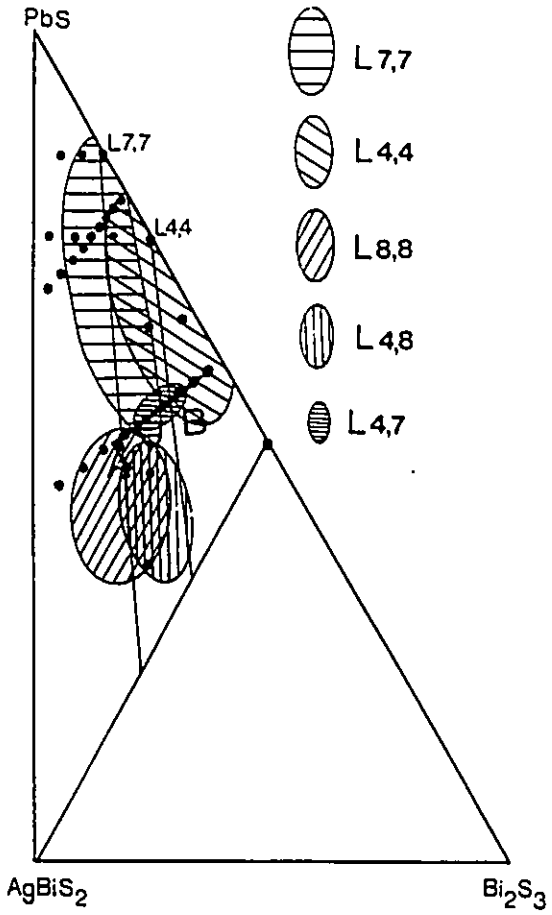

Fig. 5.12: Tentative existence diagram of the twinned phases in the Ag_2S-PbS-Bi_2S_3 system obtained by electron microscopy. The compositions of the samples studied are marked with dots and the shaded areas delineate the regions where L8,8, L7,7, L4,7, L4,8 and L4,4 exist. The almost vertical lines show the compositions of the solid solutions betweeen L4,4 and gustavite and between L7,7 and $PbAg_{2.5}Bi_{4.5}S_9$.

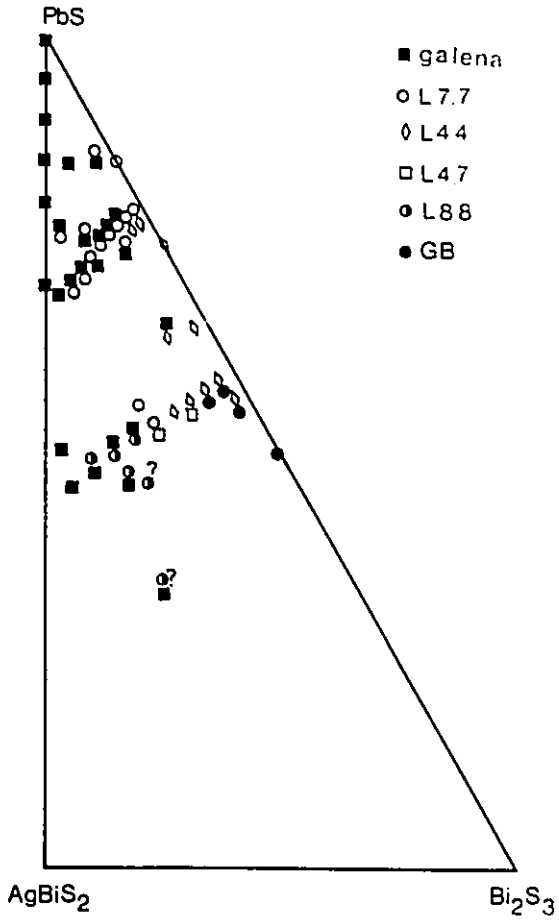

Fig. 5.13: Diagramatic representation of the results of powder X-ray phase analysis of samples annealed at 773K. Question marks for samples no 37 and 39 signify that apart from the phases that could be identified for those samples, there were also traces of phases present that could not be recognized.

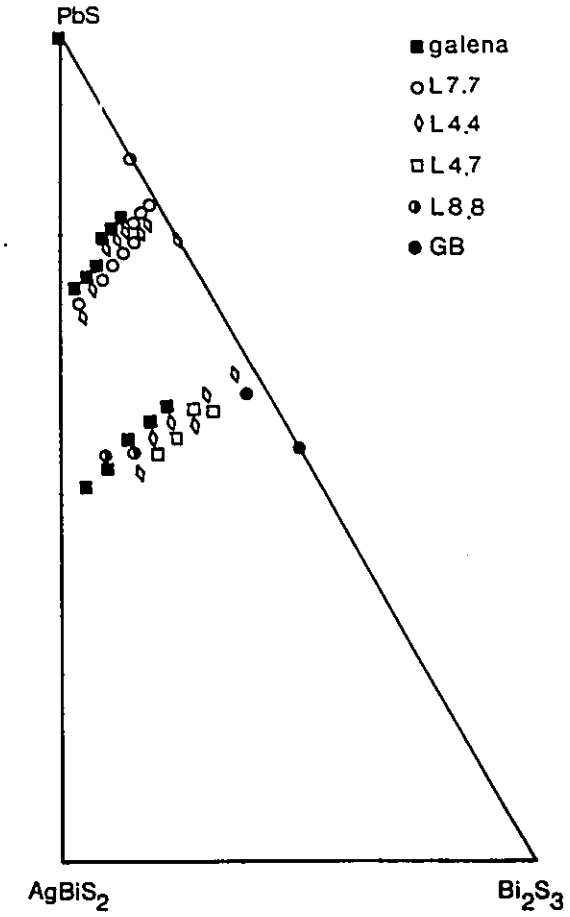

Fig. 5.14: Diagrammatic representation of the results of powder X-ray phase analysis of samples annealed at 973K.

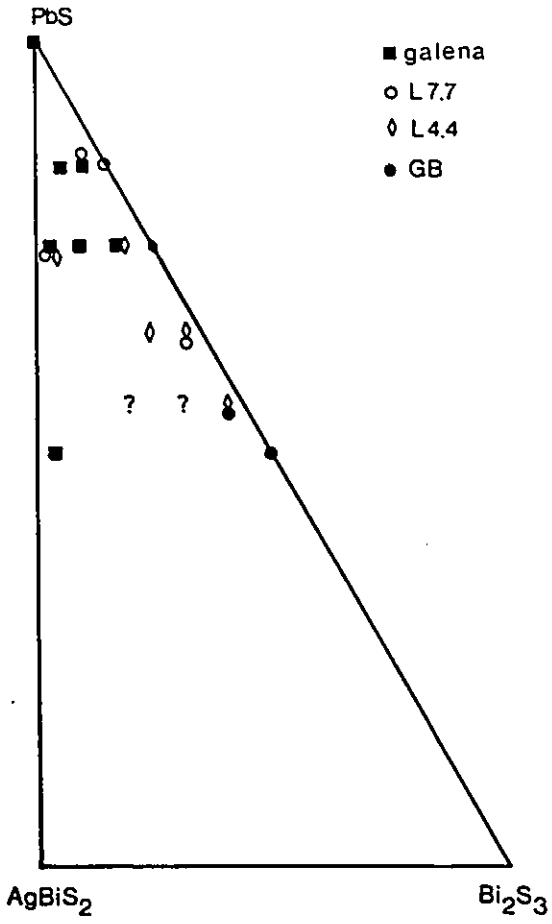

Fig. 5.15: Diagrammatic representation of the results of powder X-ray phase analysis of samples quenched from the melt. GB denotes galenobismutite. Question marks in places of samples no 31 and 32 signify that the phases present could not be identified.

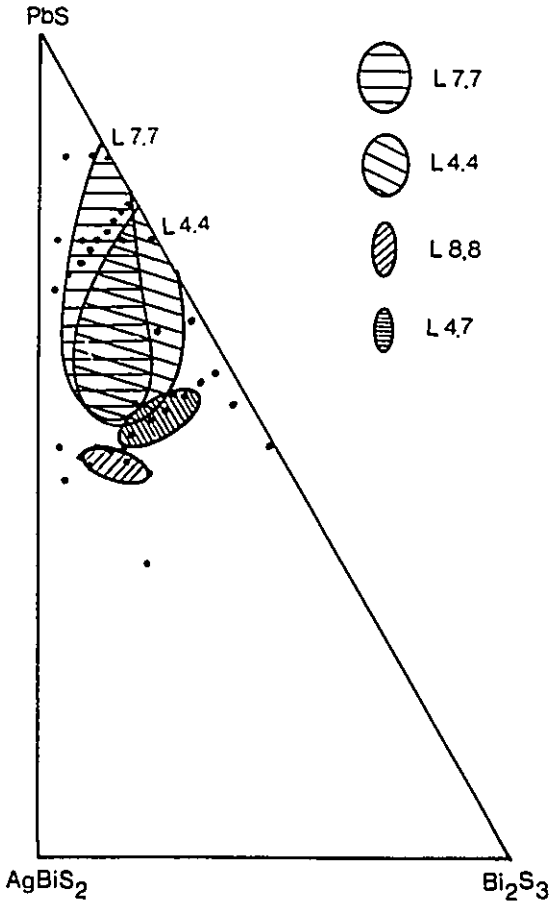

Fig. 5.16: Approximate existence diagram of the twinned phases in the Ag_2S-PbS-Bi_2S_3 system obtained by the powder X-ray analysis.

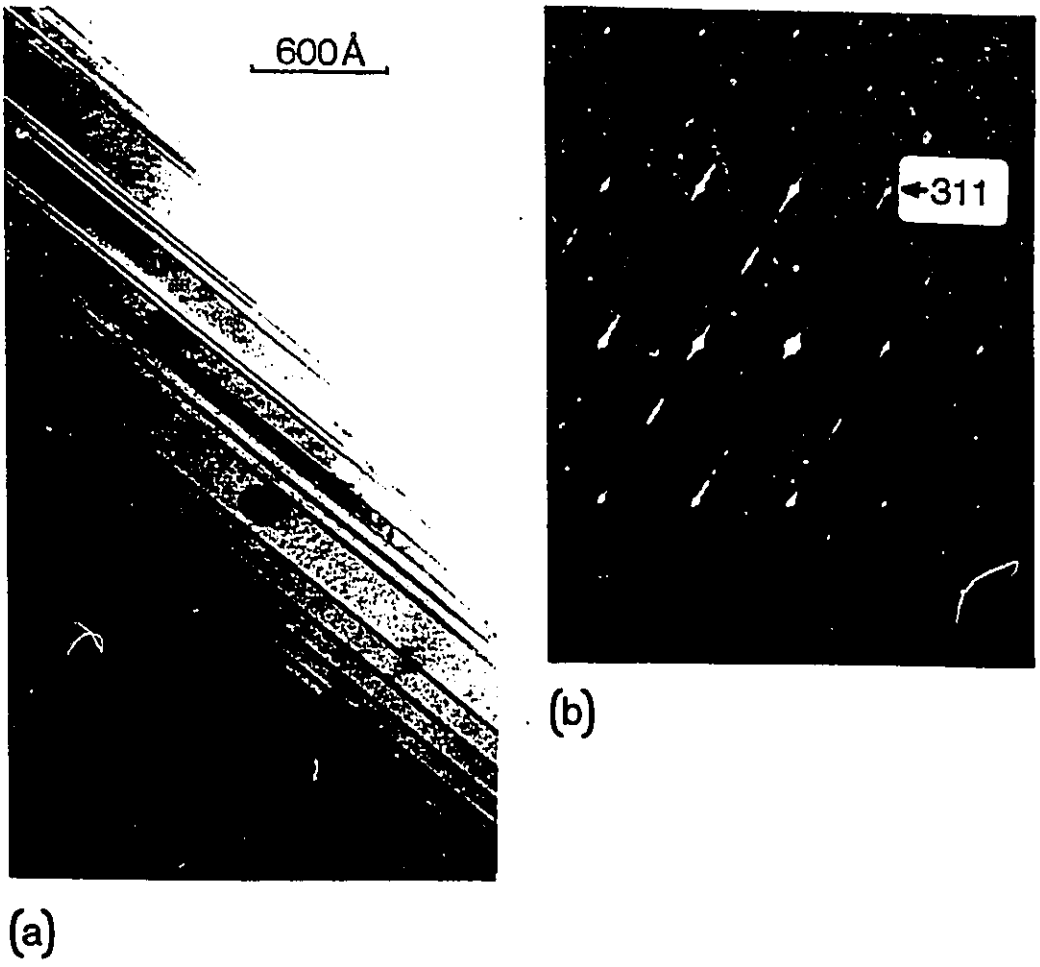

Fig. 5.17: (a) Irregularly spaced (311) twin planes in the PbS matrix. (b) Corresponding electron diffraction pattern showing streaking between the 0k0 reflection.

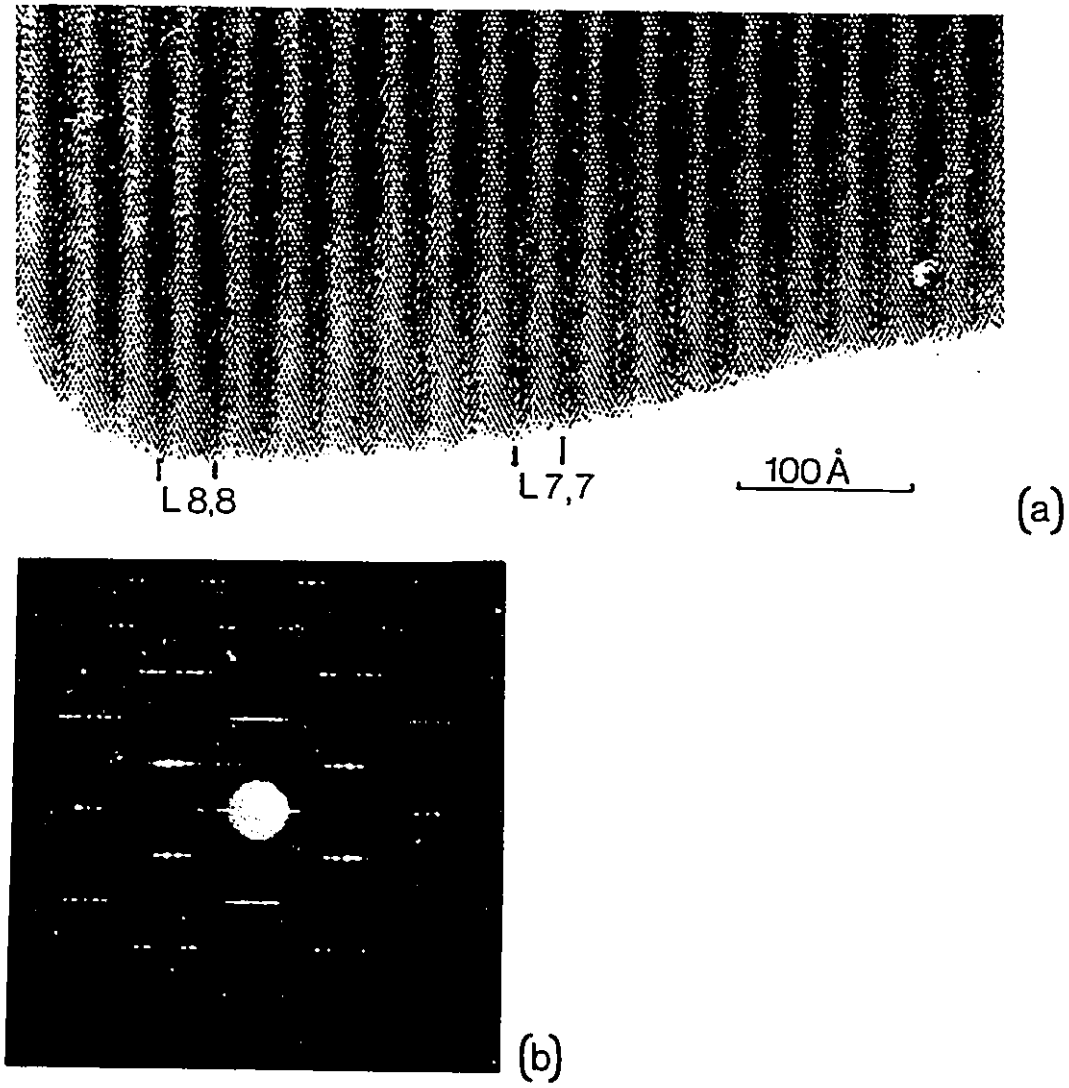

Fig. 5.18: (a) High resolution electron micrograph of an intergrowth of L7,7 and L8,8. The twin planes, imaged alternately in light and dark contrast, are indicated. The (111) planes of PbS are clearly resolved which introduces an internal standard for precise measurements of twin planes separation. (b) Diffraction pattern of (a). Two sets of superimposed reflections corresponding to L7,7 and L8,8 diffraction patterns can be distinguished.

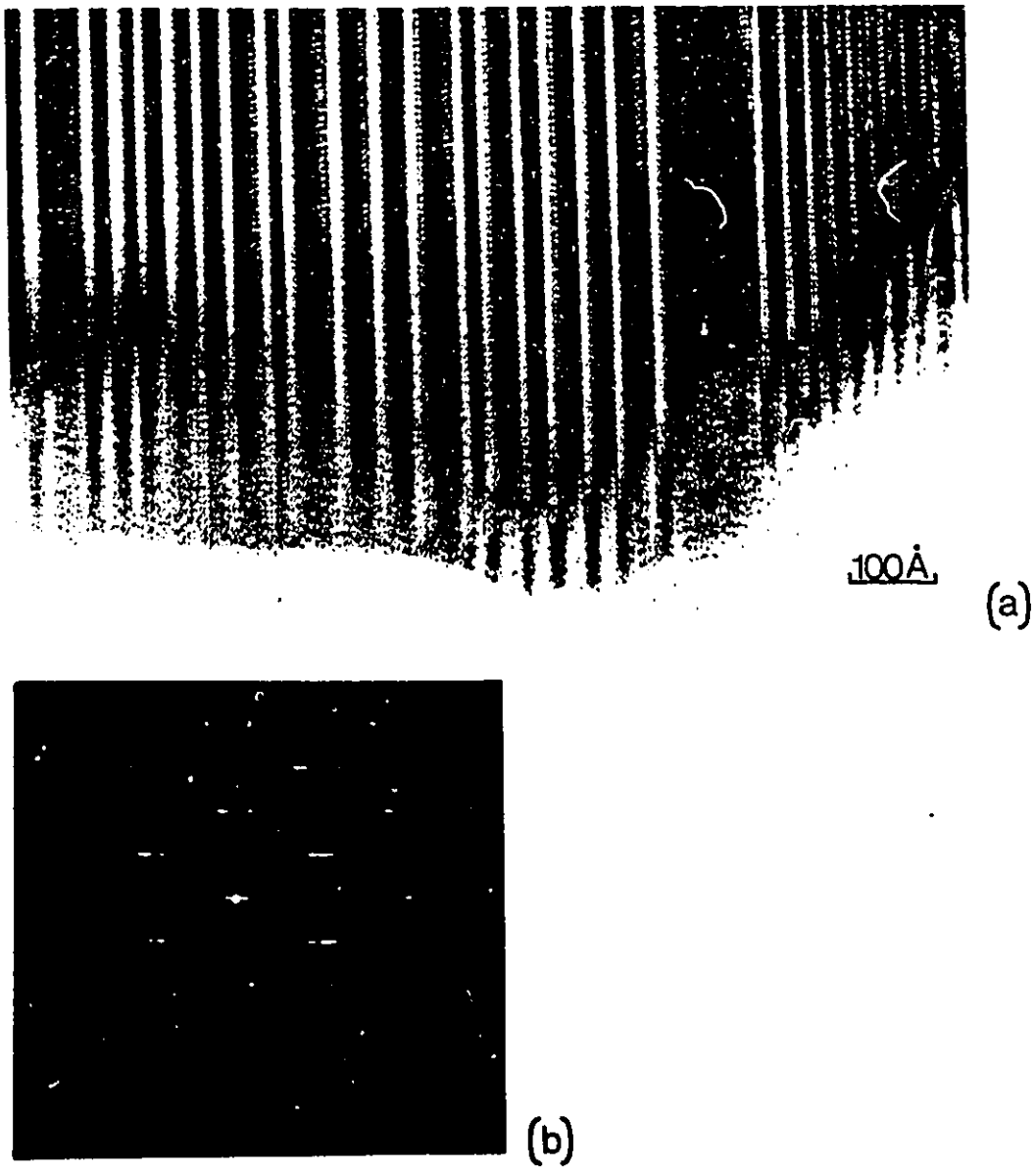

Fig. 5.19: (a) Low resolution image of a crystal fragment showing an irregular intergrowth of differently wide galena slabs. (b) The electron diffraction pattern from (a).

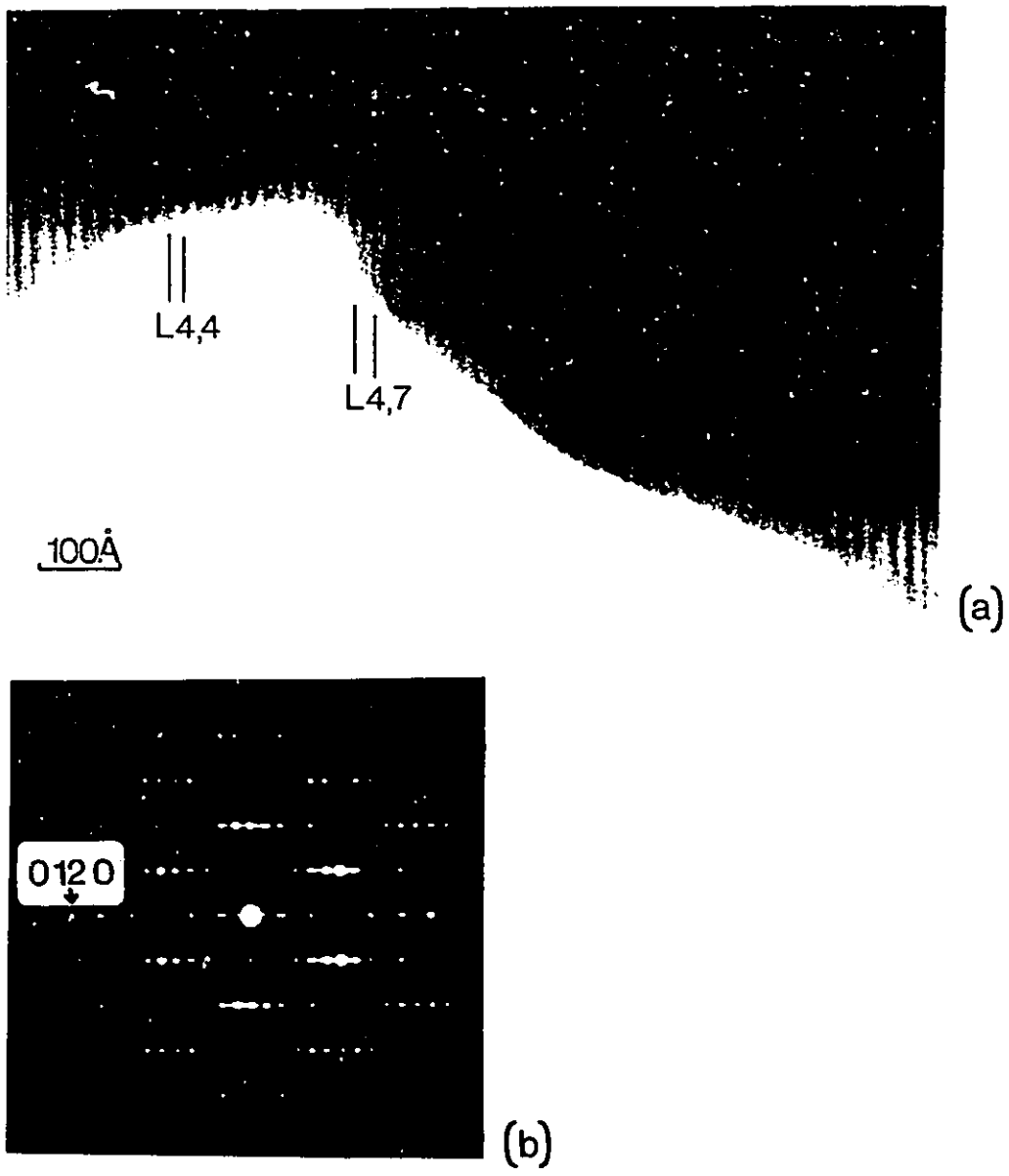

Fig. 5.20: (a) Low resolution image of a crystal fragment showing an irregular intergrowth of L4,4 and L7,7. (b) Electron diffraction pattern of (a). The 0 12 0 reflections correspond to the 311_{PbS} showing that L4,4 is predominant.

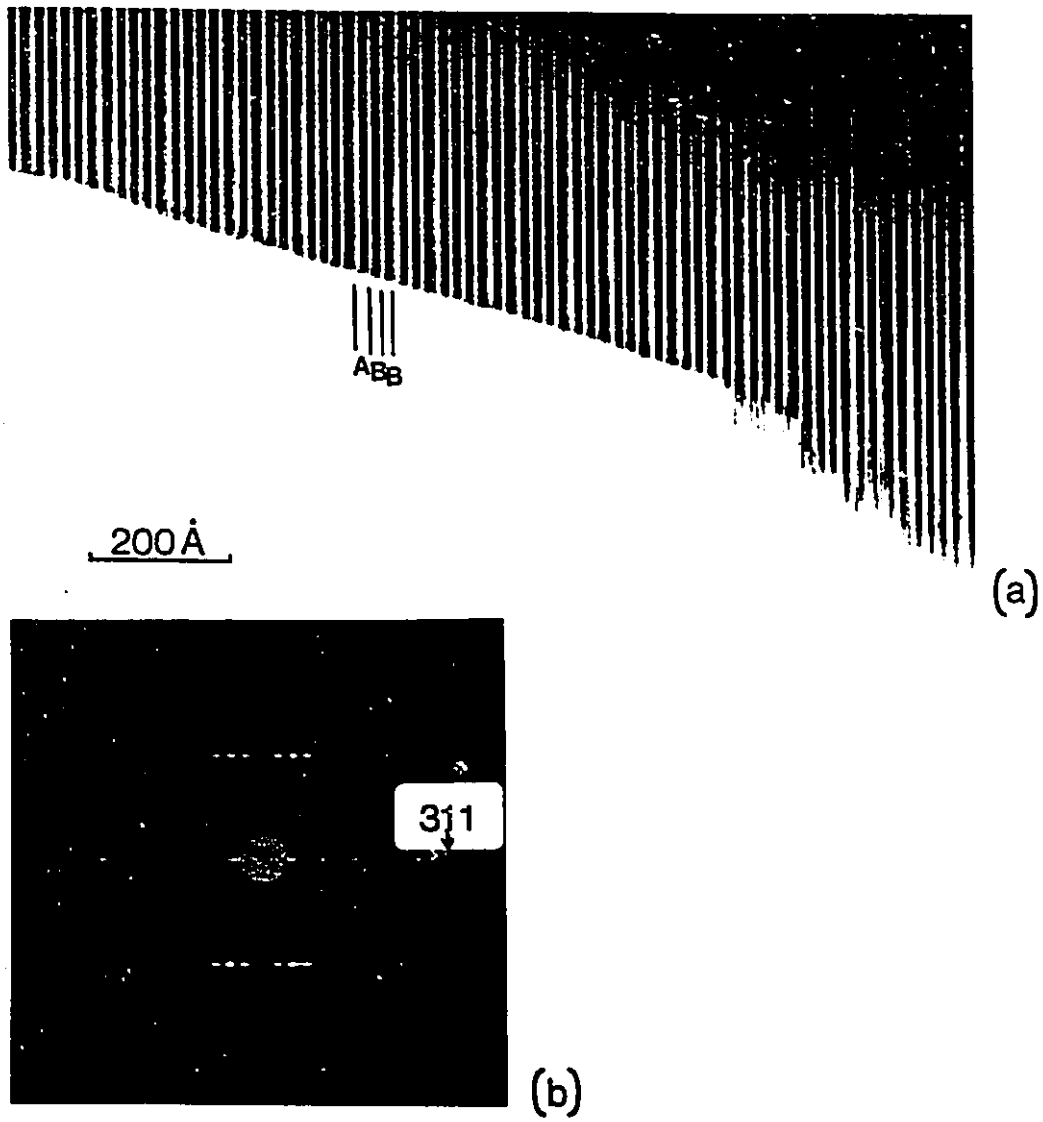

Fig. 5.21: (a) Low resolution image of a crystal fragment showing partial ordering of galena slabs. The spacing of the lattice fringes corresponds to sequences: ABB and ABBB where A ≅ 25Å and corresponds with b dimension of L4,7 and B ≅ 20Å and agrees with that of L4,4. (b) The electron diffraction pattern from (a). The more intense reflections correspond to superimposed L4,4 and L4,7 reflections and weaker, closely spaced reflections correspond to a superstructure formed by the partial ordering of L4,4 and L4,7 with a repeat distance ≅ 66Å.

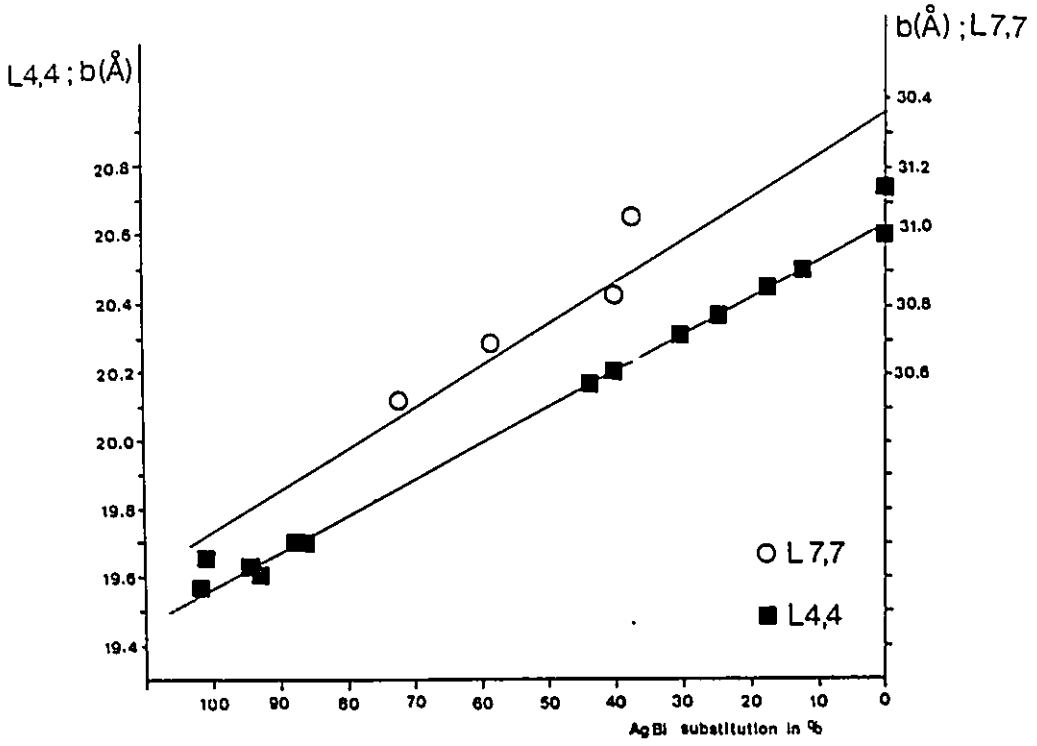

Fig. 5.22: The values of the lattice parameters b of the members of the lillianite-gustavite and heyrovskyite- solid solutions series plotted versus their Ag + Bi ⇔ 2Pb substitution percentages, after Makovicky and Karup-Møller, (1977b) and Karup-Møller and Makovicky, (1981).

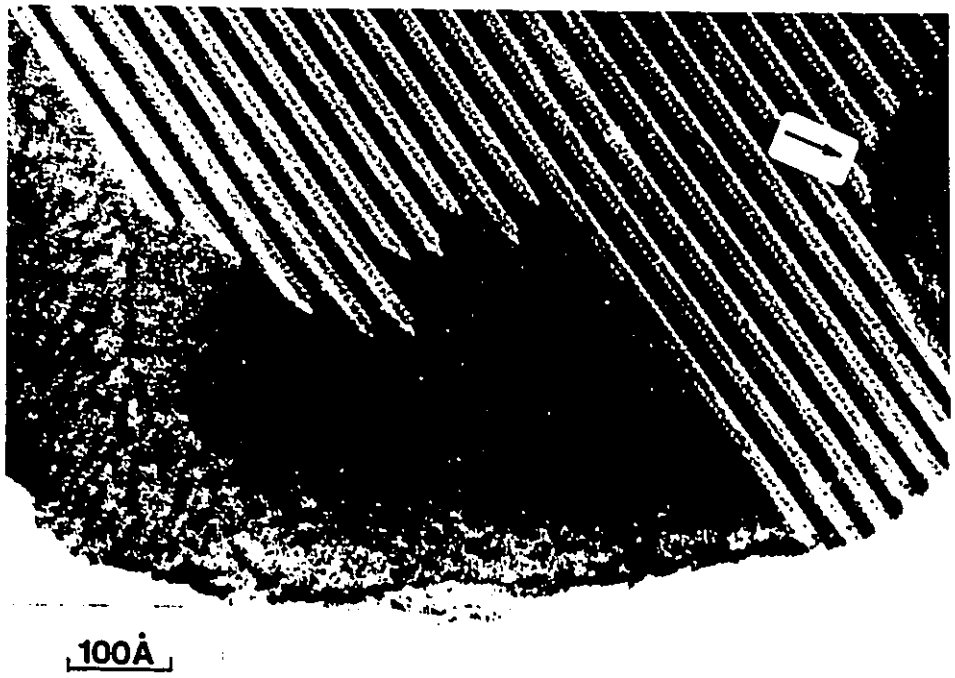

Fig. 5.23: Crystal fragment of a twinned crystal which has partially detwinned. The twin planes have been lost in pairs and their arrow headed terminations lie along (111) planes with respect to galena seen in the lower left part of the figure. The (111) planes are resolved in this region. To the right of the figure the ill-defined patch which is arrowed, represents an alternative mode of decomposition.

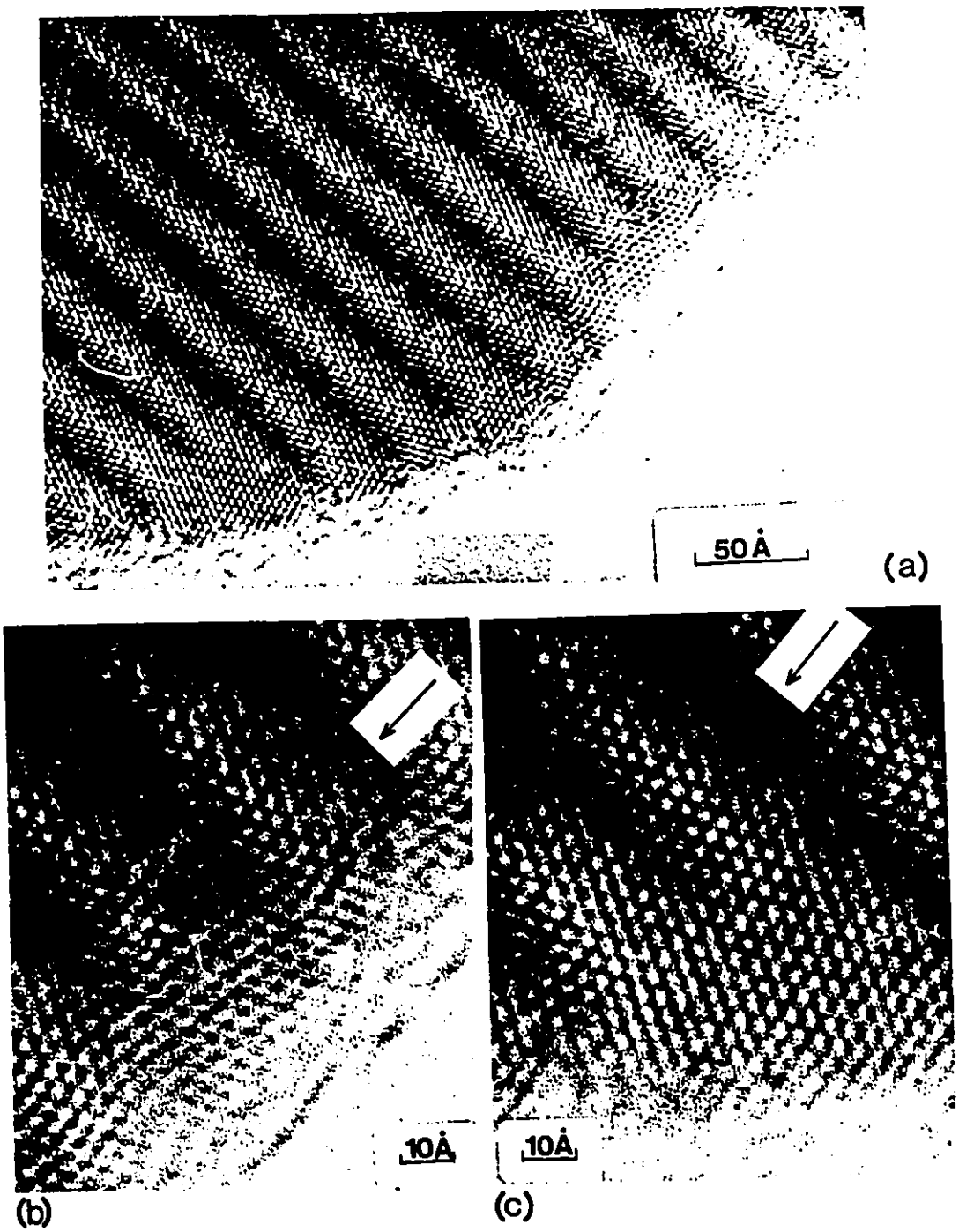

Fig. 5.24 Termination of two detwinned regions imaged at high resolution. (a) shows the general area of the crystal. (b) and (c) are enlargements of the twin tip. By viewing along the direction arrowed, the edge dislocations can be seen.

Fig. 5.25: Crystal fragment of L4,4 decomposed by an intense electron beam. The galena slabs have arrow-like terminations.

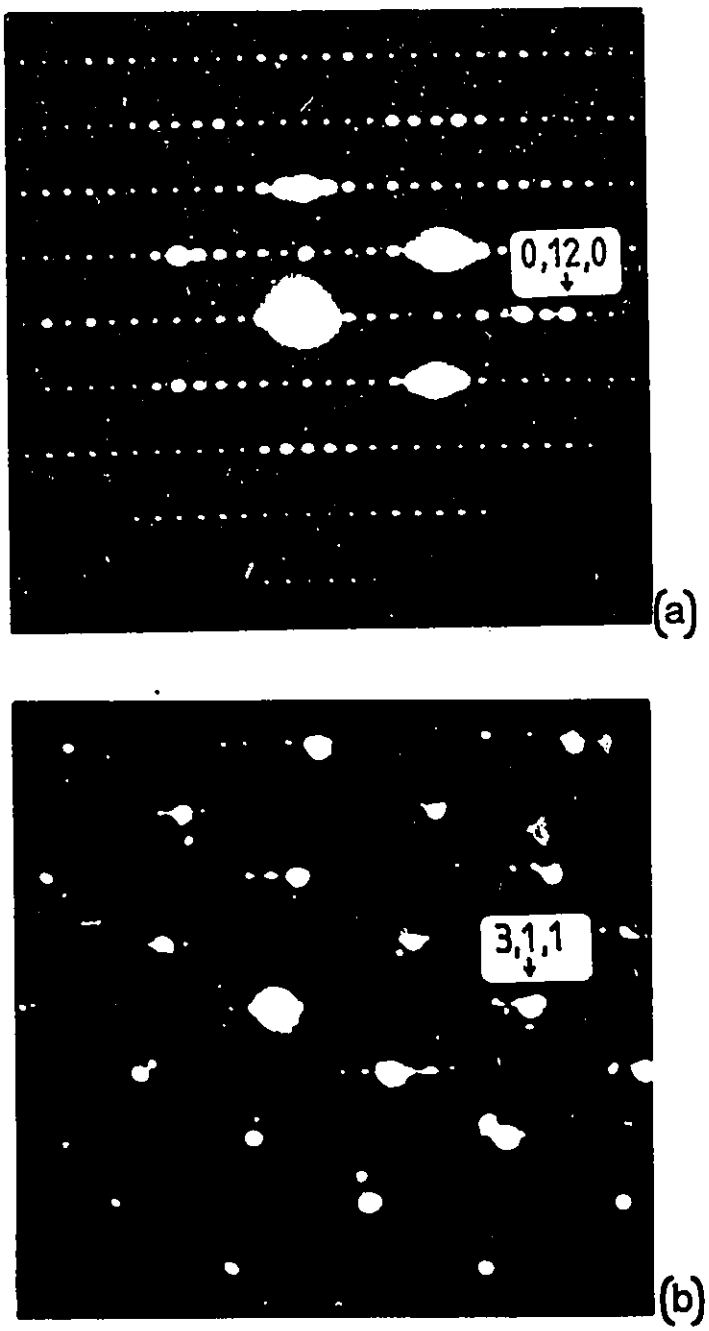

Fig. 5.26: Diffraction patterns of (a) L4,4 at the onset of observation and (b) after partial decomposition to galena. In (b) the large spots are due to the freshly formed galena matrix. Fig. 5.26(b) is from the crystal shown in Fig. 5.25.

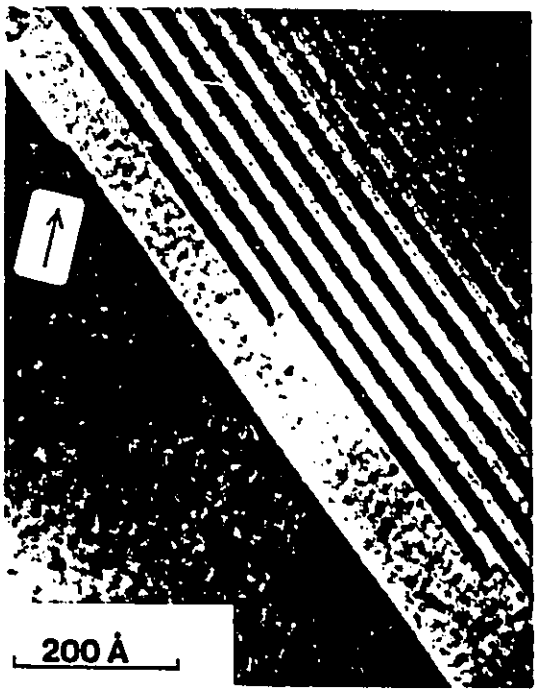

Fig. 5.27: Crystal of partly transformed twinned phase. Although twin planes have been lost in pairs in the main part of the crystal, the jog arrowed represents the loss of a single twin plane at the twin boundary between two wider galena slabs.

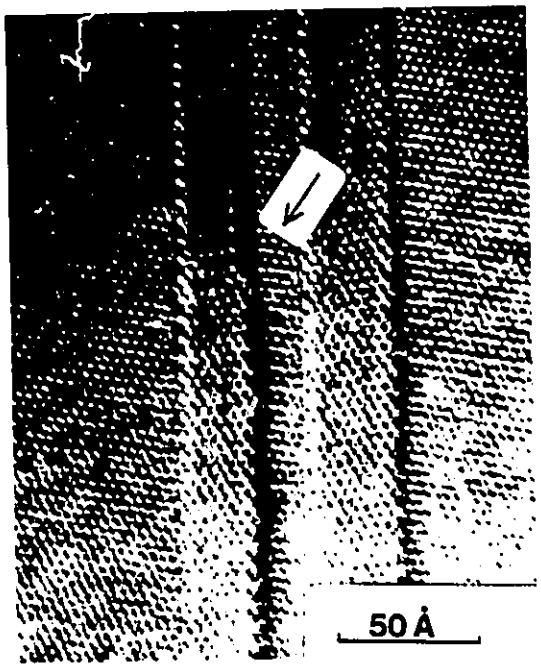

Fig. 5.28: High resolution image of twin boundaries between galena-like regions in a partly transformed crystal. The contrast arrowed represents a jog in the twin plane equivalent to three MS_6 octahedra in width.

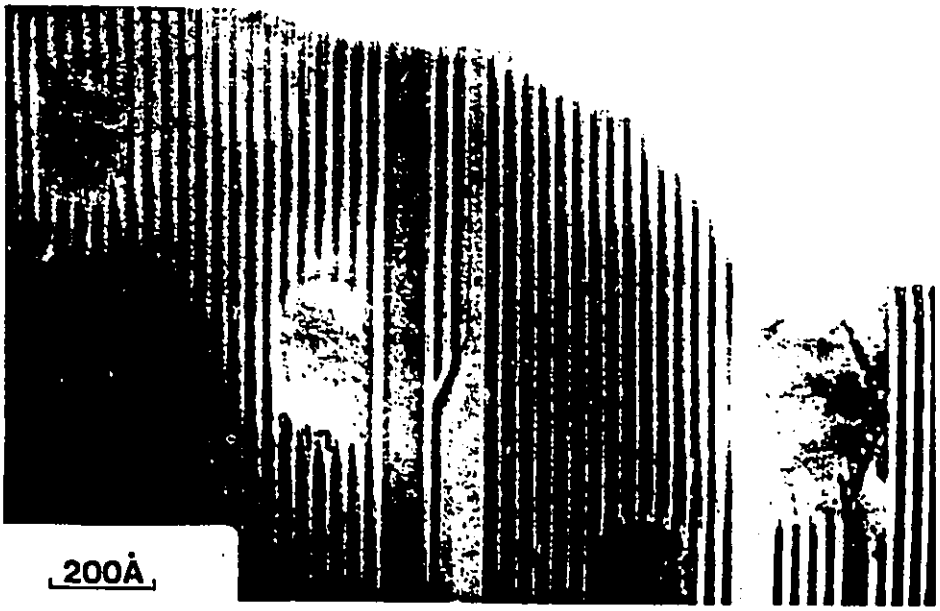

Fig. 5.29: Crystal fragment showing decomposition to the galena structure in discrete patches. Early stages of the decomposition are shown at the bottom of the micrograph as regions of hatched contrast. Complete reaction has occurred in the oval shaped patches nearer the edge of the crystal.

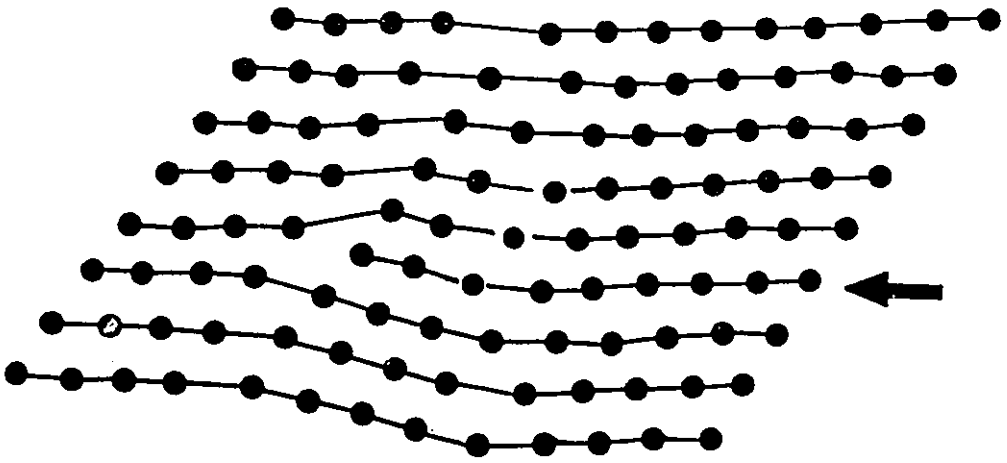

Fig. 5.30: Drawing of the metal atom positions at the termination of a pair of twin planes. The edge dislocation is clearly revealed in this representation, which can be compared with the experimental situation shown in Fig. 5.24.

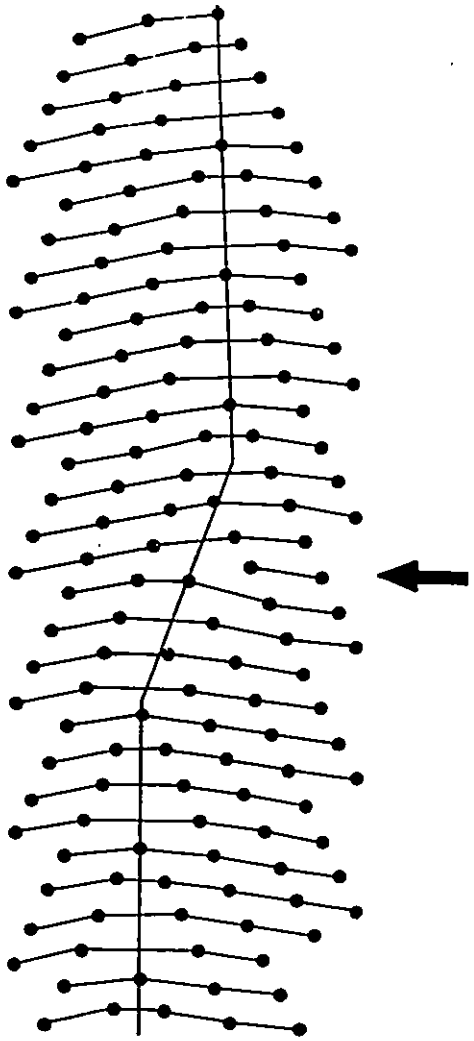

Fig. 5.31: Drawing of the metal atom positions at the jog on a twin plane. The structure is that shown in Fig. 5.28.

Table 5.1: Lattice parameters for the silver containing twinned phases found in this study. Only the samples no 13 and 1 do not contain silver.

Phase	Sample number	Temp (K)	Lattice parameters (Å) a	b	c	(deg) γ
L4,4	13	773	13.540(4)	20.654(4)	4.111(1)	
L4,4	21	773	13.499(4)	20.545(4)	4.123(1)	
L4,4	17	773	13.511(4)	20.499(4)	4.114(1)	
L4,4	31	773	13.462(4)	20.397(6)	4.098(2)	
L4,4	23	973	13.480(4)	20.312(5)	4.117(1)	
L4,4	22	773	13.471(2)	20.304(4)	4.112(1)	
L4,4	23	773	13.478(4)	20.255(4)	4.101(1)	
L4,7	24	973	13.461(3)	25.664(4)	4.105(1)	95.57(2)
L4,7	23	973	13.514(9)	25.590(1)	4.102(3)	95.59(5)
L7,7	1	773	13.670(9)	31.368(6)	4.143(1)	
L7,7	7	773	13.621(2)	31.081(6)	4.133(1)	
L7,7	8	773	13.623(2)	31.000(4)	4.119(1)	
L7,7	32	773	13.494(4)	30.679(5)	4.105(1)	
L8,8	26	773	13.565(4)	33.046(7)	4.102(2)	

Table 5.2: Weights representing relative stability of lillianite homologs with their average slab width $\bar{N}$.

Phase	Weight	$\bar{N}$
L4,4	1.00	4
L11,11	0.94	11
L4,8	0.88	6
L8,8	0.77	8
L4,7	0.75	5.5
L7,8	0.66	7.5
L7,7	0.56	7
L4,5	0.41	4.5
L5,8	0.36	6.5
L5,7	0.31	6
L5,5	0.17	5
L10,10	0.06	10
L5,9	0.05	7
L9,9	0.01	9
L6,x	<0.003	

6 Structure of $Pb_4Sb_4Se_{10}$

This chapter presents the structure of $Pb_4Sb_4Se_{10}$, determined by single crystal X-ray diffraction, and comments on the crystal chemical implications of its formation (Skowron and Brown, 1990 d).

Since PbSe and Sb_2Se_3 are isotypic with the corresponding sulphides (Earley, 1950; Tideswell et al., 1957) it was expected that the ternary selenides might also be isotypic with the ternary sulphides. A short study was undertaken to probe if good quality single crystals, isotypic with those in the PbS-Sb_2S_3 system, could be grown using selenides. The aim was to use selenides instead of sulphides for the structure determination since, initially, it was difficult to obtain single crystals of sulphides suitable for measurement of the diffraction intensities. However, it turned out that a selenide that easily formed in the system, $Pb_4Sb_4Se_{10}$, had structure isotypic with a lead-bismuth sulphide rather then with a lead-antimony sulphide. Consequently no further attempts were made to synthesize more lead-antimony selenides but the structure of $Pb_4Sb_4Se_{10}$ was determined and is presented here, providing a crystal chemical

link between the two systems already discussed.

6.1 Sample preparation

Single crystals of $Pb_4Sb_4Se_{10}$ were prepared from elemental lead, antimony and selenium of "Specpure" grade, supplied by Johnson Matthey Ltd. Six samples were prepared by weighing the elements in the proportions corresponding to 50-75 mole percent of PbSe. The samples were then sealed in evacuated silica tubes, melted at 1073K and subsequently slowly cooled over a period of two weeks to 823K. Extensive phase separation into regions of acicular crystals was observed in all the ampoules. A needle shaped crystal, 0.1mm x 0.2mm x 0.5mm, which was chosen from the ampoule with the initial composition 55 mole percent PbSe, was mounted with the needle axis along the goniometer axis for the X-ray study.

6.2 Structure determination of $Pb_4Sb_4Se_{10}$

The experimental and computational parameters used in the structure determination and refinement are listed in Table 6.1. The systematic absences, 0kl:k+l=2n+1; h0l:h=2n+1, found using precession photographs indicate space group Pnam or $Pna2_1$. The former was chosen and led to a satisfactory refinement. The Pb occupation numbers of sites 1 and 3 quickly refined to values close to 1.0 and were kept fixed at this value in the subsequent stages of the refinement. The refinement converged to wR=0.057,

R=0.062 and s=1.50.

The program did not permit a constraint to be put on the total number of Pb or Sb atoms in the unit cell and the refined occupation numbers, shown in column 1 of Table 6.2, result in a formula of $Pb_{3.58}Sb_{4.42}Se_{10}$ which is different from the expected electrically neutral formula $Pb_4Sb_4Se_{10}$. An independent set of occupation numbers was determined using the bond-valence method described in chapter 2. r_o was determined for Sb-Se (2.598Å) and Pb-Se (2.679Å) bonds using the published crystal structures of compounds which contained these bonds but which contained neither Se-Se, metal-metal bonds nor any kind of disorder. Table 6.3 summarizes the chemical compositions and references of these structures. The occupation numbers obtained correspond to the nearly correct formula $Pb_{4.07}Sb_{3.93}Se_{10}$. An exactly electroneutral formula was obtained by changing r_o(Sb-Se) to 2.602Å. The valence analysis using this value of r_o is presented in Table 6.4 and the occupation numbers inferred from this analysis in column 2 of Table 6.2.

Because the occupation numbers determined from the bond valences correspond to an electrically neutral crystal we consider these values to be more reliable. We used them as fixed parameters in SHELX76 and refined all positional and atomic displacement parameters to obtain wR = 0.059, R = 0.064 and s = 1.58. This refinement was used to generate the final atomic coordinates

listed in Table 6.5 and the anisotropic atomic displacement parameters listed in Table 6.6. The interatomic distances are given in Table 6.7.

Description of the structure

$Pb_4Sb_4Se_{10}$, shown in Fig. 6.1, is isotypic with cosalite, (Srikrishnan, Nowacki, 1974, Macicek, 1988) shown in Fig. 1.15 and traditionally given the idealized formula $Pb_4Bi_4S_{10}$.

Two parallel ribbons combine to form a ribbon pair in which metal atoms on the facing sides of the ribbons are 6-coordinated. On the other sides of the ribbons two sites are 8-coordinated and the other two 6-coordinated. The Sb atoms are only found on the 6-coordinated sites. As the result, each ribbon pair is rich in lead on the outside and rich in antimony on the inside. All cation sites show the distortions expected from stereoactive lone electron pairs.

Although both cosalite and $Pb_4Sb_4Se_{10}$ have the same geometrical framework, cosalite contains additional Cu atoms in sites near the edges of the ribbons. It also differs from $Pb_4Sb_4Se_{10}$ in the details of the metal occupancies (Macicek, 1988), see column 3 of Table 6.2. The two 8-coordinated cation sites are fully occupied by lead in both structures. In the selenide, mixed occupancies are found in the remaining six sites, four of which contain mostly

antimony.

6.3 Discussion

Armbruster and Hummel (1987) have examined the environments of lead, bismuth and antimony in a number of sulphides to study the distortion of the cation coordination polyhedra caused by the influence of the lone electron pair. To measure this distortion and to compare the sizes of the environments around the cations they plot the mean of the three shortest interatomic distances against the mean of the two next shortest.

We have constructed a similar diagram for lead, antimomy and bismuth in selenides, Fig. 6.2, using only the sites in the compounds listed in Table 6.3 that have coordination numbers greater than four. We used three structures with Bi (6 Bi sites) and five structures with Pb (7 Pb sites). The only suitable compound containing Sb in higher than four coordination was Sb_2Se_3 (2 Sb sites). In Fig. 6.2 we compare our results with those of Armbruster and Hummel after adjusting the distances for the difference in size of the Se and S atoms ($r_{Se} - r_S = 0.13$Å).

Good agreement between the sulphide and selenide distortion fields can be reached if the Armbruster and Hummel region of Sb is extended to include regular coordination (the dashed lines in Fig. 6.2). The octahedral sites in cosalite (Macicek, 1988) and

in $Pb_4Sb_4Se_{10}$ lie in the same part of the diagram, a part which corresponds short Bi-S and long Sb-Se distances with comparable distortion.

Macicek (1988) points out that copper and silver play an important role in stabilizing cosalite as the phase cannot be synthesized in the Pb-Bi-S system without their presence. Chang, Walia and Knowles (1980), on the other hand, reported the synthesis of a phase with composition $Pb_2(Bi_{0.8}Sb_{0.2})_2S_5$ which they identified as cosalite from its powder diffraction pattern. However, the cosalite analog grows readily in the undoped Pb-Sb-Se system. The tolerance on the size of metals that can be incorporated into cosalite is apparently not very large. It seems that the "ideal" cation to form the structure is one that prefers a weakly distorted environment and that is bigger than antimony but smaller than bismuth. In this respect, antimony in the selenide has an advantage over bismuth in sulphide, since it can, by partial occupation with lead, adapt to the necessary metal size. Bismuth however needs substitution by a smaller cation to reduce its average size. As a result stabilizers, like copper or silver, or substitution by antimony are necessary in the sulphide. In the structure obtained by Macicek Bi(1) is replaced on half the sites by either Ag or one or two Cu atoms at nearby interstitial positions.

Conclusion

The $PbSe-Sb_2Se_3$ system invites further study to establish if other types of structures form and if so, whether they are isotypic with the twinned lead-bismuth sulphides. As there has been no previous investigation in the $PbSe-Sb_2Se_3$ system such a study will certainly be valuable.

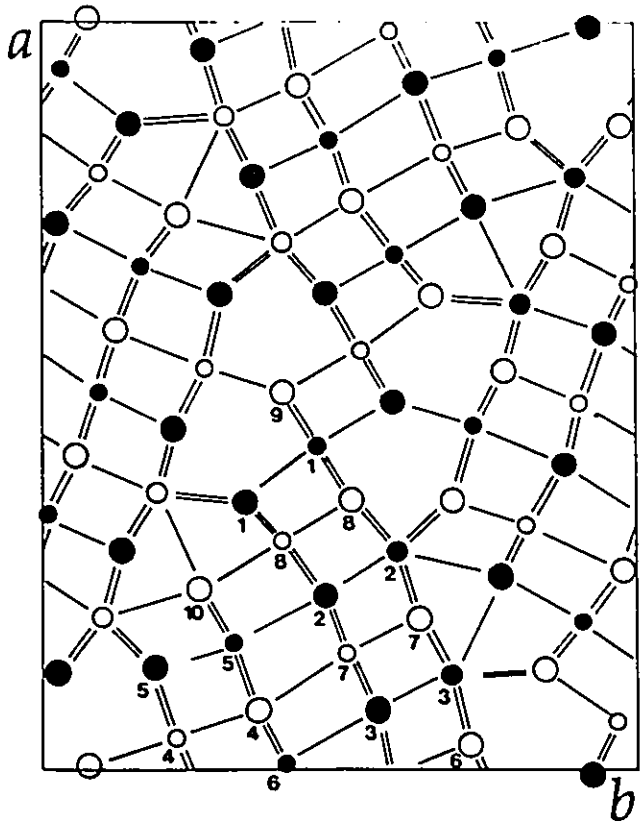

Fig. 6.1: The unit cell of $Pb_4Sb_4Se_{10}$ projected down [001]. In order of decreasing size, the circles denote Se, Pb and mixed sites. Atoms at z=0.25 and z=0.75 are indicated by open and filled circles respectively. The general view of the isotypic structure of cosalite is shown in Fig. 1.15.

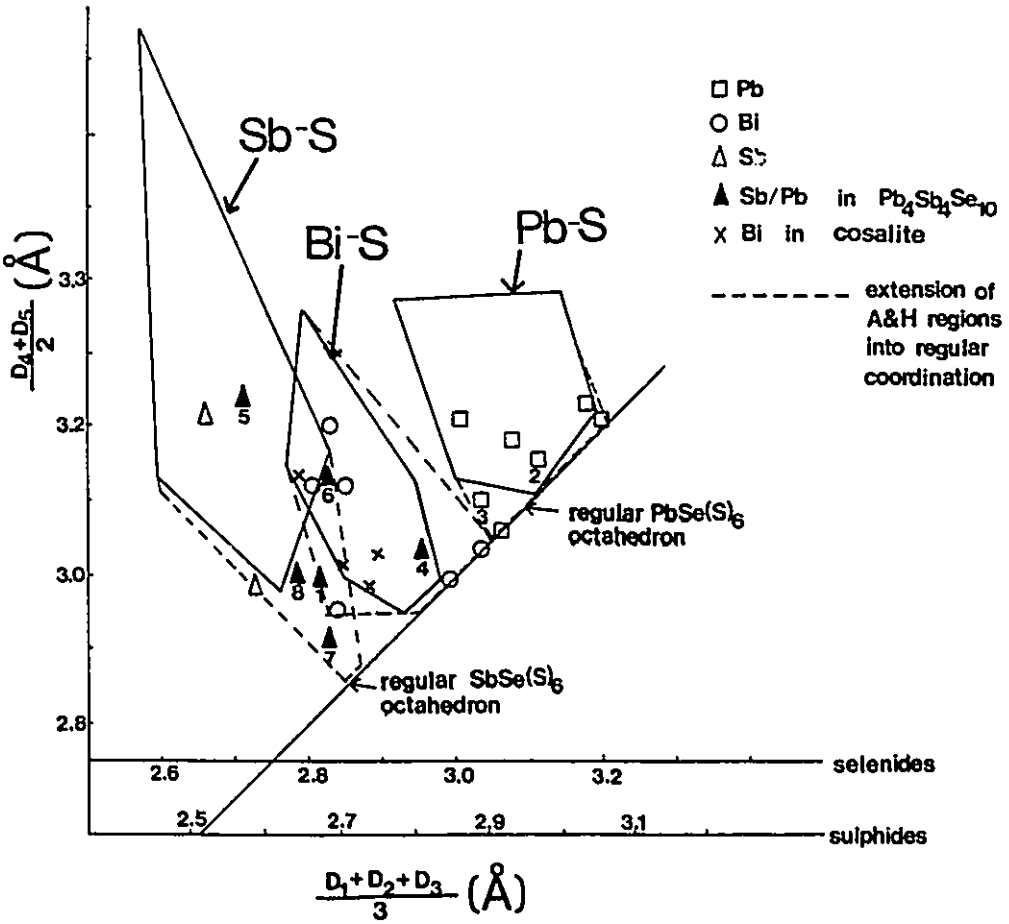

Fig. 6.2: The mean value of the three shortest Me-Se distances vs. the mean value of the next two shortest. The distances are obtained from the published structures of compounds labelled with • in the Table 6.3. The distortion fields for Pb, Sb and Bi coordination polyhedra in sulphides are indicated with solid line (after Armbruster and Hummel, 1987). The distortion fields for Me-Se bonds are drawn in broken line.

Table 6.1: Structure determination of $Pb_4Sb_4Se_{10}$.

Space group	Pnam
Lattice parameters (Å)	
	a=24.591(8)
	b=19.757(8)
	c= 4.166(8)
Volume ($Å^3$)	2024
Calculated density (g/cm^3)	6.91
Reflections used to determine a and b	$15° < 2\theta < 30°$
Standard reflections	6 2 -1, 10 -4 -2
e.s.d. of standard reflections (%)	2.1, 2.1
Range of measured reflections	$0 \le h \le 26$
	$-20 \le k \le 20$
	$-4 \le l \le 4$
No. of reflections measured	5308
No. of unique reflections	1562
Linear absorption coefficient μ (mm^{-1})	54.39
No. of reflections used in psi-scan	13
Absorption correction: maximum; reflection	6.29; 1 -2 2
Internal agreement factor R_{int} before the absorption correction	0.159
Internal agreement factor R_{int} after the absorption correction	0.049
Weighting parameters k; g	6.5; 0.0006
Final R; R_w	0.064; 0.059
Shift/error in final cycle: maximum	0.072
average	0.017
Number of variables refined	117
Residual electron density: maximum ($eÅ^{-3}$)	2.81
minimum	-3.11

Table 6.2: Percentage of Sb (or Bi) on cation sites in $Pb_4Sb_4Se_{10}$ and cosalite.

Site	X-ray refinement	Bond-valence[11] method	Macicek (1988)[12]
	$Pb_4Sb_4Se_{10}$	$Pb_4Sb_4Se_{10}$	cosalite
M(1)	82	80	54 Bi + 12 Ag[13]
M(2)	0	0	0
M(3)	0	0	0
M(4)	32	33	23
M(5)	88	75	100
M(6)	60	46	23
M(7)	88	80	100
M(8)	92	86	100
M(9)	-	-	30 Cu[14]
M(10)	-	-	24 Cu[15]
Formula	$Pb_{3.58}Sb_{4.42}Se_{10}$	$Pb_4Sb_4Se_{10}$	$Ag_{0.12}Cu_{0.54}Pb_{3.54}Bi_4S_{10}$

[11]To obtain the electoneutral formula r_o(Sb-Se)=2.602Å and r_o(Pb-Se)=2.679Å.

[12]Determined by bond valence method.

[13]This site does not contain lead (it is 34% vacant).

[14]A mixture of Cu^{2+}(52%) and Cu^{1+}(48%) is assumed to occupy this site.

[15]Only Cu^{+} is assumed on this site.

Table 6.3. Crystal structures selected for the calculation of r_o for Sb-Se, Pb-Se bonds. The structures used in Fig. 6.2, are labelled with *.

Compound	No. of positions	r (Å)[16]	Reference
*$BaBiSe_3$	2		Volk et al. (1980)
*Bi_2Se_3	2		Atabaeva et al. (1973)
*$AgBiSe_2$	2		Geller & Wernick (1959)
*$PbAl_2Se_4$	1	2.697	Klee & Schäfer (1980)
*$PbGa_2Se_4$	3	2.708, 2.708, 2.650	Klee & Schäfer (1980)
*$Pb_xMo_3Se_4$	1	2.664	Guillevic et al. (1967)
*PbU_2Se_5	1	2.663	Potel et al. (1975)
*PbSe	1	2.661	Earley (1950)
*Sb_2Se_3	2	2.583, 2.577	Tideswell et al. (1957)
$KSbSe_2$	2	2.577, 2.578	Dittmar & Schäfer (1977)
$BaSb_2Se_4$	4	2.589, 2.610	
		2.625, 2.623	Cordier & Schäfer (1979)
$CsSbSe_2$	2	2.529[17], 2.616	Kanishcheva et al. (1980)

[16]Values of r_o were those that gave valence sums of 2 at Pb or 3 at Sb using equations (2.43) and (2.41). The values of r_o used in valence analysis of $Pb_4Sb_4Se_{10}$ were the averages of those listed.

[17]rejected from the calculation of the mean value of r_o.

Table 6.4. Bond valences, Σs, in $Pb_4Sb_4S_{10}$, weigthed according to X-ray occupation number. V is the atomic valence weigthed using these occupancies.

	M(1)	M(2)	M(3)	M(4)	M(5)	M(6)	M(7)	M(8)	Σs
%Sb	82	0	0	32	88	60	88	92	
Se(1)	0.49		0.10x2					0.55x2	-1.79
Se(2)		0.28					0.43x2	0.33x2	-1.80
Se(3)			0.43			0.26x2	0.45x2		-1.85
Se(4)				0.38	0.18x2	0.51x2	0.14		-1.90
Se(5)		0.18x2		0.43x2	0.88				-2.12
Se(6)			0.35x2	0.34x2		0.78			-2.16
Se(7)		0.31x2	0.32x2				0.84		-2.10
Se(8)	0.33x2	0.28x2						0.79	-2.01
Se(9)	0.38+0.62x2			0.43					-2.05
Se(10)		0.18	0.09		0.69x2			0.25	-1.90
Σs	2.77	2.00	2.06	2.35	2.62	2.32	2.61	2.80	
V	2.82	2.00	2.00	2.32	2.88	2.60	2.88	2.92	

Table 6.5: Atomic coordinates for $Pb_4Sb_4Se_{10}$.

	x	y	z
M(1)	0.4359(1)	0.5389(1)	0.75
M(2)	0.2954(1)	0.3910(1)	0.75
M(3)	0.1273(1)	0.2976(1)	0.75
M(4)	0.0434(1)	0.7710(1)	0.25
M(5)	0.1741(1)	0.6872(1)	0.75
M(6)	0.0099(1)	0.5912(1)	0.75
M(7)	0.1560(1)	0.4841(1)	0.25
M(8)	0.3034(1)	0.5929(1)	0.25
Se(1)	0.3641(1)	0.6548(2)	0.75
Se(2)	0.2310(1)	0.5296(2)	0.75
Se(3)	0.0821(1)	0.4380(2)	0.75
Se(4)	0.0855(1)	0.6275(2)	0.25
Se(5)	0.1249(1)	0.8069(2)	0.75
Se(6)	0.0346(1)	0.2833(2)	0.25
Se(7)	0.2043(1)	0.3628(2)	0.25
Se(8)	0.3614(1)	0.4774(2)	0.25
Se(9)	0.5002(2)	0.5886(2)	0.25
Se(10)	0.2390(1)	0.7289(2)	0.25

Table 6.6: Anisotropic thermal displacememt parameters ($Å^2$) for $Pb_4Sb_4Se_{10}$. $U_{13}=U_{23}=0$.

	U_{11}	U_{22}	U_{33}	U_{12}
M(1)	0.0245(11)	0.0317(14)	0.00250(12)	-0.0004(10)
M(2)	0.0292(8)	0.0389(10)	0.0258(9)	0.0006(7)
M(3)	0.0352(9)	0.0273(9)	0.0275(9)	0.0017(7)
M(4)	0.0215(8)	0.0165(9)	0.0211(9)	0.0012(7)
M(5)	0.0286(11)	0.0276(13)	0.0271(12)	-0.0012(9)
M(6)	0.0387(11)	0.0316(12)	0.0285(11)	0.0013(9)
M(7)	0.0296(12)	0.0229(13)	0.0275(13)	-0.0007(9)
M(8)	0.0228(11)	0.0224(13)	0.0280(13)	0.0017(9)
Se(1)	0.0303(20)	0.01860(21)	0.0492(26)	0.0034(16)
Se(2)	0.0235(18)	0.0215(20)	0.0283(21)	0.0020(15)
Se(3)	0.0270(19)	0.0194(20)	0.0295(21)	0.0024(15)
Se(4)	0.0299(19)	0.0210(21)	0.0313(22)	0.0052(16)
Se(5)	0.0228(18)	0.0165(19)	0.0282(21)	0.0007(14)
Se(6)	0.0180(18)	0.0210(20)	0.0211(19)	0.0030(15)
Se(7)	0.0203(17)	0.0150(18)	0.0162(18)	0.0007(14)
Se(8)	0.0253(18)	0.0161(19)	0.0212(19)	-0.0004(15)
Se(9)	0.0368(21)	0.0214(21)	0.00454(26)	-0.0078(17)
Se(10)	0.0207(18)	0.0207(20)	0.03312(21)	-0.0003(15)

Table 6.7: Interatomic distances (Å) less than 3.6Å in $Pb_4Sb_4Se_{10}$.

M(1) -	Se(9)	x 2	2.793(3)	M(5) - Se(5)	2.656(4)
	Se(1)		2.879(4)	Se(10) x 2	2.750(4)
	Se(9)		2.970(4)	Se(4) x 2	3.236(3)
	Se(8)	x 2	3.028(3)	Se(2)	3.415(4)
M(2) -	Se(7)	x 2	3.109(2)	M(6) - Se(6)	2.728(4)
	Se(8)	x 2	3.146(3)	Se(4) x 2	2.883(3)
	Se(2)		3.163(4)	Se(3) x 2	3.131(3)
	Se(5)	x 2	3.308(3)	Se(3)	3.509(4)
	Se(10)		3.313(4)		
M(3) -	Se(3)		2.989(4)	M(7) - Se(7)	2.673(4)
	Se(6)	x 2	3.069(2)	Se(3) x 2	2.908(3)
	Se(7)	x 2	3.096(2)	Se(2) x 2	2.923(3)
	Se(1)	x 2	3.528(3)	Se(4)	3.324(4)
	Se(10)		3.557(3)		
M(4) -	Se(9)		2.969(4)	M(8) - Se(8)	2.692(4)
	Se(5)	x 2	2.976(2)	Se(1) x 2	2.830(3)
	Se(4)		3.019(5)	Se(2) x 2	3.011(3)
	Se(6)	x 2	3.055(2)	Se(10)	3.118(4)

7 Modelling the structures in the $PbS-Sb_2S_3$ system

In this chapter the ribbon structures in the $PbS-Sb_2S_3$ system are modelled. First the chemical properties of the ribbon are described. Next the packing of ribbons is analyzed and the topologically possible arrangements are identified. Models of possible structures and stability limits of their homologs are then derived from bond-valence considerations. Lastly, the predicted and observed structures are compared.

7.1 The acid and base strengths of the ribbons

A section through a single ribbon is shown in Fig. 7.1. The sulphur atoms within the body of the ribbon bond to five metal atoms but of those at the edge S(4) bond to only three metal atoms in the ribbon and S(5) to only two metal atoms in the ribbon. Consequently, to satisfy their atomic valence, these sulphur atoms need to form external bonds. They constitute the Lewis base function, (strength b), of the ribbon.

If the ribbon edges are Lewis bases (b) and if the ribbons are to bond to each other, their faces must be the Lewis acid function (strength a). This function must appear in the external bonding

of the Sb and Pb atoms.

Since Sb forms weaker external bonds than Pb, it therefore forms stronger internal bonds, particularly as it has a higher charge. Since S(5) only forms two bonds to metal atoms (M(4)) these bonds must be strong making it probable that M(4) will be occupied by Sb.

As indicated in summary of the chapter 4 the observed distortions of cation sites in the structures of the PbS-Sb_2S_3 system are markedly larger for Sb than for Pb sites reflecting more stereoactive character of the lone electron pair for Sb than for Pb. The difference in the stereoactivity of Pb and Sb results in ribbons having faces with regions of weak and strong external bonding at the cation sites. We assume that both Pb and Sb <u>are</u> stereoactive i.e. have distorted coordination environments, but Sb to a larger degree than Pb.

7.2 Structure of junctions between the ribbons

Two types of ribbons, A and B, are typically found in the observed structures. They are distinguished by lying at an angle of about 60° to each other. They need not to have the same width but if they do they are usually related by a crystallographic glide plane. Even when they do not have the same width there is a local glide relationship between them at the point where they

meet.

Because the edges of ribbons are basic and the faces acidic, the ribbons bond edge to face. Consider the structure of a joint between the ribbons. Three possibile arrangements for joining the ribbons are shown in Figs 7(a-c). In the arrangement shown in Fig. 7.2(a) the metal at the join is 6-coordinated which is not a favourable environment for Pb or Sb with stereoactive lone pairs. A non-stereoactive metal atom would be more suitable for this site. Consequently, this arrangement (which is found in $FeSb_2S_4$, Buerger and Hahn, 1955) will not be considered further in connection with Pb-Sb-S system. The arrangements shown in Figs 2(b) and 2(c) give rise to distorted 6- and 7-coordinations and are suitable for Pb but the latter arrangement requires adjustments in the shape of the ribbon to avoid short S-S distances. Both joints will be used in different ways in building structure models. The joint shown in Fig. 2(b) will be used to join the edge of a B-type ribbon to the first metal site, M(1), on the face of a A-type ribbon. It will be called a "single junction".

The arrangement shown in Fig. 7.2(c) can be used in conjunction with the single junction to attach a second B type ribbon at the third metal site, M(3) on the face of an A type ribbon. By this process an A ribbon is joined to two B ribbons (Fig. 7.3) and is referred to as a "double junction". In this junction bonding

occurs at three cation sites on the face of the A ribbon. Two of these sites are 7- and one is 8-coordinated. The double junction results in a shear between the parallel faces of the two B ribbons, shaded in Fig. 7.3, leading to weak or no bonding between the parallel B ribbons.

Since the acid strength of a ribbon is related to the strength of its external bonds, the metal sites on the A ribbons at the junctions are the regions where the Lewis acid strength is expressed. The metal sites that are not at the junctions should form only very weak external bonds and consequently should exhibit weak or no acid strength. The shear found between parallel B-type ribbons, such as those shown in Fig. 7.3, is consistent with this expectation.

7.3 Packing of the ribbons

This section explores the packing of ribbons and proposes four packings consistent with three conditions for acceptable topologies:

1. the packing of the ribbons must fill space, i.e. no voids should be left between ribbons.
2. the acid functions must be concentrated on the faces at the junction.
3. the facing parts of parallel ribbons must be sheared to keep the bonding between the ribbons weak at the non-junction

metal sites.

1a. In the first packing, denoted 1A:1B, each A type ribbon is attached to one B type ribbon and each B is attached to one A type ribbon joined to it by a single junction (Fig. 7.2b). For a 4-ribbon[18] there are four possibilities, shown in Figs 7.4(a-d), corresponding to the ribbons joined at first (a), second (b), third (c), and fourth (d), metal sites. Only the case 1A:1B(a) results in a space filling arrangement, the other three, (b-d), are not space filling and are excluded by condition 1 above.

When the width of the ribbons is decreased (or increased) and the same procedure repeated no new possibilities occur for 2-, 3- and 5-ribbons but for the 6-ribbons there is the possibility of forming a structure with the 1A:1B(c) arrangement. The cavities between the ribbons have become big enough to accommodate a 3-ribbon as shown in Fig. 7.5. The two B ribbons, the narrow and the wide one, can be attached to the wide A ribbon by the double junction, Fig. 7.3. The same arrangement provides acceptable packing for 7- and 4-ribbons, 8- and 5-ribbons etc.

In the 1A:1B(a) packings, Fig. 7.4(a) the edge-to-face bonding occurs at a single junction involving two 7-coordinated metal

---

[18]A ribbon n pyramids wide will be refered to as an n-ribbon.

sites on the faces of the ribbons. This packing results in parallel ribbons that are not sheared along the direction of projection but in the direction lying in the plane of projection. Consequently, the metal coordination polyhedra can be described as distorted octahedra. 1A:1B(a) can be identified with the topology observed in the stibnite series.

In the 1A:1B(c) arrangement the double junction, Fig. 7.3, results in ribbons sheared along the plane of projection between the narrow and each of its two neighbouring wide ribbons as indicated in Fig 7.5. The 1A:1B(c) arrangement is identical with that present in the boulangerite series.

2. In the second packing (1A:2B) two B type ribbons join one A type ribbon but only one A type ribbon joins each B type ribbon. This will be called the 1A:2B type arrangement. From an analysis similar to that shown in Fig. 7.4, a space filling arrangement requires that the two B ribbons join to the A ribbon at a double junction as shown in Fig. 7.6.

Most of the neighbouring parallel ribbons are related by shears in the direction of projection but between one pair of B ribbons (in a region indicated with an arrow in Fig. 7.6) there is no shear resulting in a rather unfavourable octahedral coordination for the metal atoms. This region can be minimized if the ribbons have different widths with A-type wider and B-type narrower. The

arrrangement is identical with that present in the robinsonite series.

3. In a third packing (2A:2B) two A type ribbons join one B type ribbon and two B type ribbons join one A type ribbon, as shown in Fig. 7.7. This will be called a 2A:2B arrangement. As before the double junction is used resulting in the bonding of the two edges to three metal sites on the faces of all ribbons and the shear between parallel ribbons in the direction of the projection as indicated by shading in Fig. 7.7. The 4-ribbon is the narrowest that can be fitted into this arrangement. This type of topology has not been found in any of the structures in the Pb-Sb-S system.

Further models can be constructed with similar rules by increasing the number of the A and B ribbons joining to each other. Such arrangements require increasingly wider ribbons which are shown below to be unstable so these arrangements will not be further considered.

Summary

Four types of space filling packing, shown in Figs 7.4(a) and 7.5-7.7, can be constructed from the ribbons. In the 1A:1B(a) (stibnite) arrangement the ribbons are joined with single junction and the edge-to-face bonding creates two 7-coordinated

metal sites. In structures where the ribbons are joined by double junctions the bonding occurs at three metal sites on the ribbon faces of which one site is 8- and two 7-coordinated. In the 1A:1B(c) (boulangerite) arrangement, the narrow ribbon has the minimum width of 3 pyramids and no ribbon bonds to its face. In the 1A:2B (robinsonite) arrangement, some face-to-face bonding without the shear between the two B ribbons necessarily occurs, so it is beneficial to minimize their overlap i.e. to use the 2-ribbons.

7.4 Chemical constraints in the structures

There are six chemical conditions which must be satisfied by the structures and which severely limit the number of stable homologs in each series. The first three of the following rules must be obeyed exactly, the three last need only be obeyed approximately.

1. The charge of a ribbon is determined by its composition

An electrically neutral stoichiometric ribbon with total of N_T metal sites per crystallographic repeat on each face, has composition: $(N_T-2)PbS + Sb_2S_3$. This means that a neutral ribbon has only two Sb atoms regardless of its width i.e. increasing the width of a neutral ribbon involves only the addition of lead atoms. However, a ribbon need not be electrically neutral as long as there are oppositely charged ribbons present to provide charge neutrality.

The net charge (c) carried by a ribbon having total N_T metal sites per face, of which N_{Pb} contain lead, can be expressed as:

$$c = 2N_{Pb} + 3N_{Sb} - 2(N_T+1) = 2N_{Pb} + 3(N_T-N_{Pb}) - 2(N_T+1)$$

which, recognizing that $N_{Pb} + N_{Sb} = N_T$, gives:

$$c = N_T - N_{Pb} - 2 = N_{Sb}-2 \qquad (7.1)$$

2. Lewis acid strength + Lewis base strength of a ribbon = charge on a ribbon

For charge conservation in the structure the sum of the acid (a) and the base (b) strengths of a ribbon equals the net charge of the ribbon (c):

$$a + b = c \qquad (7.2)$$

3. With 2 types of ribbon present the actual acid strength of one ribbon equals actual base strength of the other

Since the acid portions of the A ribbons must bond to the base portions of the B ribbons and vice versa the valence matching principle introduced in chapter 2 has to be exactly obeyed i.e.:

$$a_A = b_B \qquad (7.3a)$$

$$a_B = b_A \qquad (7.3b)$$

4. the acid strength of a ribbon is given approximately by its Pb content

We assume that only the Pb atoms provide sites of acid function because of the extremely weak bonding that occurs on the lone pair side of Sb atoms. This means that all the external bonding betweeen the ribbons occurs at lead atoms i.e. lead atoms occupy the 7- and 8-coordinated sites at the junctions. To estimate the total acid strength (a) of the ribbon as a function of N_{Pb}, in first approximation assume that each 7-coordinated Pb atom contributes 0.3v.u. to the acid strength of the ribbon (see Fig. 4.7) and the Sb atoms do not contribute. The acid strength of a Pb atom on an 8-coordinated site can be estimated (assuming that the coordination polyhedron is essentially regular) as: 2.0 x 3/8 = 0.75v.u. Then, the Lewis acid strength of a ribbon containing N_{Pb} lead atoms per face, all of which are 7-coordinated, is: $a_S=0.3N_{Pb}$. The Lewis acid strength of a ribbon in which one Pb site is 8-coordinated and the remaining $N_{Pb}-1$ sites are 7-coordinated is: $a_D = 0.3(N_{Pb}-1)+0.75$.

Substituting the above values of a_S, a_D and c (from eq. 7.1) to the eq.7.2 yields eq.7.4 and 7.5 for a_S and a_D as functions

of N_T and b:

$$a_S = 0.23N_T - 0.23b - 0.460 \quad (7.4)$$

$$a_D = 0.23N_T - 0.23b - 0.114 \quad (7.5)$$

Since the metal sites in the single junction are 7-coordinated the eq.(7.4) describes the acid strength of the N_T-ribbons which bond via single junction. Likewise eq.(7.5) describes the acid strength of the N_T-ribbons to which two ribbons are bonded by the double junction.

Substitution of eq. (7.4) and (7.5), respectively, into eq. (7.2) gives the corresponding net charges on the ribbons:

$$c_S = 0.23N_T + 0.77b - 0.460 \quad (7.6)$$

$$c_D = 0.23N_T + 0.77b - 0.114 \quad (7.7)$$

The relationships (eqs 7.4 and 7.5) between the acid strengths, a_S and a_D and the width of the ribbons, N_T, are shown in Fig. 7.8(a) for two values of b. The values of c_S are shown in Fig. 7.8(b).

The graph in Fig. 7.8(b) shows that in order to bond in one of the packings described above, the ribbons will normally be charged. The wide ribbons are charged positively i.e. they have excess of antimony, and the narrow ribbons are charged

negatively, i.e. they have excess of lead. Except, therefore, for ribbons with a width of about 4 (electrically neutral) we expect one ribbon to have a width less then 4 (negative charge) and one greater (positive charge).

5. There is a limit to the total acid strength of a ribbon

Since the acid strength of a ribbon is related to the strength of its external bonds, the acid function i.e. the lead atoms, will concentrate on the cation sites which lie in the junctions between the ribbons. Once these sites are filled further addition of Pb cannot add to the acid strength at the junctions.

The maximum number of lead atoms accomodated in the single and double junctions, shown in Figs 7.2(b) and 7.3, is 2 for the single junctions and 3 for the double junctions regardless of the width of the ribbons. Thus each type of junction has a maximum acid strength, a^{max}. For single junction: $a_S^{max} = 2x0.3$ v.u = 0.6 v.u. and for double junction: $a_D^{max} = 2x0.3$ v.u. + 0.75 v.u. = 1.35 v.u. .

6. The non-junction sites may contain up to 50% Pb which does not contribute to the acid strength at the junctions

Increasing ribbon width while keeping the charge constant,

requires that the lead content of the ribbon also increases. Eventually the number of lead atoms in the ribbon becomes larger than the number needed to fill the sites at the junctions, and a_S and a_D calculated from eqs (7.4) and (7.5) will exceed a_S^{max} and a_D^{max} respectively. Further increase in the width of ribbon forces the lead atoms into the non-junction sites, those that face a parallel ribbon and which are expected to form only weak inter-ribbon bonds. For the stability of the ribbons the lead atoms in these weakly bonding regions should not behave as Lewis acid so the lead concentration in these sites must be small. We assume that not more than 50% Pb can be accomodated in these sites before a structure becomes unstable, therefore:

$$a - a^{max} < 0.15\ N_m \qquad (7.8)$$

where N_m is the number of the non-junction sites available to lead and 0.15 is the acid strength of a site with 50% Pb.

7.5 Cations distribution in the ribbons

The cations distribution in the ribbons can now be predicted: lead preferentially occupies the sites at the junctions since it provides the acid strength needed for bonding to the sulphur on edges of the other ribbons. The metal sites of the type M(4) (see Fig. 7.1) are occupied by antimony since the M(4)-S(5) type bonds have to be strong. The rest of the metal sites have to be

non-bonding (non-acid) and so should be rich in antimony though they can accomodate some lead. Consequently, the N_m in eq.(7.8) is: $N_m = N_T-2-1 = N_T - 3$ for ribbons with a single junctions on their faces and $N_m = N_T-3-1 = N_T - 4$ for the ribbons with the double junctions.

7.6 Solutions to the constraints

We now separately consider each of the four structure series and establish stability limits for the ribbons widths using the six criteria presented above.

Stibnite series [1A:1B(a)]

In this series the ribbons are joined by the single junction, (Fig. 7.2b) and their acidity is described by eq.(7.4). Consider two cases, in the first all the ribbons have the same width, in the second the B ribbons are wider than the A ribbons.

In the first case, (A=B), recognizing that both the A and B ribbons have the same acid ($a=a_s$) and base (b) strengths, eqs (7.4) and (7.3) become:

$$\begin{cases} a = 0.23N_T - 0.23b - 0.460 & (7.9a) \\ a = -b & (7.9b) \end{cases}$$

These equations can be solved for a and b as a function of N_T (Fig. 7.9). The line $a' = a-0.15N_m$ indicates the acid strength of the ribbons if the non-junction sites are half filled with Pb according to the assumption (6) and $a_S^{max} = 0.6$v.u.. For structure stability $a' \leq a^{max}$ and the accesible regions are shown shaded. The observed structures are shown as squares. The graph indicates that only those ribbons that have widths between 3 and 5 pyramids can exist in this structure. In the 3-ribbons the bonding will be weaker than in the 4- and 5-ribbons. According to the assumption that antimony will not occur at a junction the structure with 2-ribbons, where only antimony is present, is not predicted to occur in spite of the fact that it is the well known mineral, stibnite.

In the second case the A and B ribbons have different widths, with B taken as wider than A. The equations (7.3a,b) and (7.4) become:

$$\begin{cases} a_A = 0.23N_{T(A)} - 0.23b_A - 0.46 & (7.10a) \\ a_B = 0.23N_{T(B)} - 0.23b_B - 0.46 & (7.10a) \\ a_A = -b_B & (7.10c) \\ a_B = -b_A & (7.10d) \end{cases}$$

The lines indicated as a and b in Fig. 7.10(a) are the solution of the set of eqs 7.10(a-d) where A is a 3-ribbon and the lines

in Fig. 7.10(b) the solutions where A is a 4-ribbon. Longer ribbons give rise to graphs with no shaded region and they therefore are not expected to occur.

The shaded regions indicate that the following combinations of ribbons are possible: A=3, B=3, 4, 5, 6 and A=4, B=3, 4, 5.

Boulangerite series [1A:1B(c)]

In this configuration a narrow and a wide ribbon are joined to a wide ribbon by the double junction shown in Fig. 7.3. The minimum possible width of the pair of ribbons is 6 and 3 and packing requires that both widths increase simulaneously in the higher homologs giving widths of N_T and N_T-3 as the widths of the wider and narrower ribbons respectively. The narrower ribbon does not bond on its face, thus $a^{max}_{narrow} = 0$. The two first necessary conditions for this configuration, (eqs 7.11a,b) are derived from eqs 7.5 and 7.3a. The third equation, 7.11(c), is given by combining eqs (7.1), (7.3b) and the condition of electroneutrality of the structure which requires that $c_{wide} = -c_{narrow}$

$$\begin{cases} a_{wide} = 0.23\ N_T - 0.23\ b_{wide} - 0.114 & (7.11a) \\ a_{wide} = -b_{wide} - b_{narrow} & (7.11b) \\ a_{narrow} = 0.3N_T - 1.5 + 0.3(a_{wide} + b_{wide}) & (7.11c) \end{cases}$$

where $N_T = 6,7,8...$

There are four unknowns (a_{wide}, a_{narrow}, b_{wide} and b_{narrow}) in these three equations so one of them, b_{wide}, is treated as a parameter and the set is solved for a number of values of b_{wide}. The resulting lines (a_{wide}, a_{narrow} and b_{narrow}) are shown in Fig. 7.11 for $b_{wide} = -1.1$.

Given that $a^{max}_{narrow} = 0$, the condition for stability of the narrow ribbon, eq (7.8), yields eq. (7.12):

$$a_{narrow} < 0.15N_m \qquad (7.12)$$

The broken line in Fig. 7.11 indicates $a' = a_{narrow} - 0.15N_m$ where $N_m = N_{T(narrow)} - 1$, i.e. one site in the narrow ribbon is occupied by antimony and the rest by 50% lead. However, for such cation distribution there is more than 50% lead in the mixed sites in the 3-ribbon even in the first homolog in the series. If, however all the metal sites in the narrow ribbon have some lead, then the concentration of lead per site is lower and, as indicated by the line $a'' = a_{narrow} - 0.15N_{T(narow)}$ in Fig. 7.11, the structure consisting of 3-ribbons and 6-ribbons is stable provided the wide ribbon has high base strength, say close to -1.1v.u.. The next homolog has 4- and 7-ribbons and the lead content in the narrow ribbon must be slightly higher than 50% if b=-1.1v.u. This structure, if it forms, will be marginally stable. All higher homologs will be unstable.

Robinsonite series [1A:2B]

As shown in section 7.3, the B ribbons should be as narrow as possible in order to minimize the unfavourable region where the metal atom will have regular octahedral coordination.

The smallest that the B ribbon can be is a 2-ribbon but we should also consider the case when it is a 3-ribbon. The two B ribbons are attached to the A ribbons by the double junction and the A to B by the single junction. The acidity of the wider A ribbon is expressed by eq. (7.5) while the acidity of the two narrrow B ribbons, treated as a single unit, is expresssed by eq. (7.4):

$$\begin{cases} a_A = 0.23N_{T(A)} - 0.23b_A - 0.114 & (7.13a) \\ a_B = 0.23N_{T(B)} - 0.23b_B - 0.460 & (7.13b) \end{cases}$$

To satisfy the valence matching principle the acid strength of the A ribbon has to equal the total base strength of the two B ribbons and vice versa, which gives the equations below:

$$\begin{cases} a_A = -b_B & (7.13c) \\ a_B = -b_A & (7.13d) \end{cases}$$

This set of the four equations can be solved exactly and the resulting pairs of a_A and b_A are plotted in Figs 7.12 and 7.13 as

functions of $N_{T(A)}$ for $N_{T(B)}$= 2 and 3, respectively. b_A slowly decreases as the width of the A ribbon increases while a_A increases sharply. The line a_A^{max} = 1.35v.u. for the double junction on the face of the A ribbons is also plotted in both figures.

Consider first the case with $N_{T(B)}$= 2. If $N_{T(A)}$= 4, 5, 6 then $a_A \leq a_A^{max}$. If, as before, we use eq.(7.8) as the criterion, then the 9-ribbon is the widest stable ribbon in the 1A:2B ($N_{T(B)}$=2) series. When the A is a 6-ribbon, the junction sites contain only lead and the non-junction sites contain no Pb. The structure with A=6 and B=2 should therefore be the most stable.

Consider the A 4- and 5-ribbons, the smallest of the series for $N_{T(B)}$=2. From the solution of the sets of the equations 7.13a-d the following a_{wide} and b_{wide} are obtained:

$$\begin{cases} a_4=-b_2=0.85\text{v.u.} & (7.14a) \\ a_2=-b_4=0.20\text{v.u} & (7.14b) \end{cases}$$

$$\begin{cases} a_5=-b_2=1.11\text{v.u.} & (7.15a) \\ a_2=-b_5=0.25\text{v.u} & (7.15b) \end{cases}$$

Since both a_4 and a_5 are smaller then a_A^{max} (=1.35v.u.) the sites

at the double junctions are not fully occupied by lead and the occupation number of lead in the junction can be calculated from the above values. Since for each ribbon a+b=c then c_4=+0.65 and c_5=+0.86 which, from eq (7.1), gives $N_{Pb(4)}$=1.35 and $N_{Pb(5)}$=2.16. If x and y are the occupation numbers respectively in the two 7- and one 8-coordinated sites in the junction, then:

$$\begin{cases} 0.6x + 0.75y = a_i & (7.16a) \\ 2x + y = N_{Pb(1)} & (7.16b) \end{cases}$$

Solving the equations 7.16a,b leads to 0.18Pb and 0.99Pb in the 7- and 8-coordinated sites respectively of the 4-ribbon and 0.57Pb and 1.0Pb in the 5-ribbon. The lead content in the 7-coordinated sites of the double junction in the 4-ribbon is very low (0.18Pb) suggesting that the structure is likely to be less stable. The 5-ribbon however, is likely to occur.

For $N_T(B)$=3 the solution of the set of the four equations (7.13a-d) results in the relationships shown in Fig. 7.13. According to the criterion given by eq.(7.8) the A ribbons can have widths from 4 to 13 pyramids. However, 4 and 5 are unlikely since they have strong deficit of lead in the sites located in the junctions. The 7-ribbon is the ideal arrangement so A=7, B=3 is the structure most likely to occur.

2A:2B

The 4-ribbons are the narrowest that, topologically, can be arranged in this way. Consider the case, in which all the ribbons have the same width. The ribbons are joined by the double junction so their acidity is described by eq. (7.5). Equations 7.3a,b describe the valence matching principle. Recognizing that both A and B ribbons have the same acid ($a=a_D$) and base (b) strengths:

$$\begin{cases} a = 0.23N_T - 0.23b - 0.114 & (7.17a) \\ a = -b & (7.17b) \end{cases}$$

The set can be solved for various N_T and the resulting values of $a(N_T)$ and $b(N_T)$ for $N_T \geq 4$ are shown in Fig. 7.14. In this arrangement $a_D^{max} = 1.35/2$v.u. $= 0.675$v.u. (per face of a ribbon) is shown in Fig. 7.14 together with $a' = a(N_T)-0.15N_m$. Since for all $N_T \geq 4$, a^{max} is less than a', no structure is possible in this arrangement.

7.7 Comparison between the predicted and the observed structures

Table 7.1 compares the predicted and observed structures.

Widths of the ribbons and their bonding strengths

Stibnite series (1A:1B(a))

In all the observed structures A=B and the ribbons widths, N_T, are: N_T= 2, 3, 4, 5, the predicted values of N_T= 3, 4, 5. The model does not predict the existence of stibnite, S(2,2), since no acid strength is attributed to antimony in the model. In reality antimony does display some acidity which allows the formation of a structure composed of weakly bonded 2-ribbons. The acid and base stengths observed in S(2,2) and S(4,4) are indicated with squares in Fig. 7.9. No precise interatomic distances are known for S(3,3) and S(5,5) as their structures have not been well determined. The observed values of a_4 and b_4 have the expected values. The observed a_2 is smaller then the observed a_4. No structures with A≠B have been observed.

Boulangerite series (1A:1B(c))

Two members of the series are known: the well characterized boulangerite itself, [B(3,6)(3,6)], and $Pb_7Sb_4S_{13}$ [B(4,7)(4,7)] reported in this study.

The prediction of the possible ribbon widths in this series is more complex than for the other series since the set of the equations 7.11(a,b,c) cannot be solved uniquely without treating one of the unknowns as a parameter. With the assumptions discussed in the previous section the two observed structures are those predicted to occur: B(3,6)(3,6) and B(4,7(4,7). The acid and base strengths on the wide and the narrow ribbons in boulangerite are indicated with squares in Fig. 7.11. The

observed a_6=1.28v.u. and b_6=-0.8v.u. do not satisfy the eq.(7.5). The a_6(observed) is less than predicted by the equation, an adaptation by which the charges on both ribbons get smaller, so that less lead is needed in the narrow ribbon for charge compensation. This is beneficial in keeping the narrow ribbon without face-to-face bonding with the wide ribbons.

Robinsonite series (1A:2B)

Two members of the series are known with certainty: robinsonite itself R6(2,2) and R7(2,2) reported in this study. The unit cell parameters of a phase reported by Wang (1976) as 'a new phase' and the reported similarity of its diffraction pattern to that of robinsonite suggest that this phase may also possibly belong to the series as a third member with the symbol R7(3,3).

The members of the series predicted by the model are listed in Table 7.1. Those expected to be the most stable (underlined) correspond to the observed members of the series. The observed acid and base strengths on the wider ribbon in R6(2,2) and R7(2,2) (indicated with squares in Fig. 7.12) agree with those predicted by the model. The model predicts a deficit of Pb in the junction and a weak bonding between the ribbons in R5(2,2) and R6(3,3) consistent with the fact that these structures have not been observed.

2A:2B arrangement

The model predicts that no Pb-Sb-S structure should be stable in this series and indeed none has yet been observed.

Cations distribution in the ribbons

The predicted cation distributions resulting from the model are shown in Table 7.2. In the stibnite and robinsonite series antimony is placed in the site closest to the edge of the ribbon [M(4) type site, seen in Fig. 7.1.], lead occupies the sites in the junctions and the rest of the sites have uniform, mixed occupancies such that the ribbons in the stibnite series are electrically neutral (for cases A=B) and in the robinsonite series they are charged to ±0.95v.u.

In case of the boulangerite series the wider ribbons are predicted to have a charge of +0.35v.u. and the narrow ribbon -0.35v.u.. However, the cation distribution in the narrow ribbon has to be different if the mixed sites are not to contain more than 50% lead. Even for the lowest homolog, boulangerite, B(3,6)(3,6), the concentration of lead in the small ribbon is more than 50% as shown in the column labelled 'unmodified' in Table 7.2. Under such circumstances some lead is to be expected in the M(4) site, the site nearest to the terminal S normally fully occupied by Sb. Accordingly, we propose a distribution which is an average between that adopted in all the other kinds of ribbons and a totally uniform one. This modified distribution

is shown in column labelled 'modified' in Table 7.2.

The correlation between the observed and the predicted lead distributions is shown in Fig. 7.15. The predicted and the observed values agree within experimental error.

Conclusion

The model predicts existence of three homologous series of structures built of ribbons. Only a few members in each series are predicted to be stable and (except for stibnite) the most stable are the ones observed. The model further correctly predicts the cation distribution in those members whose structures have been reported.

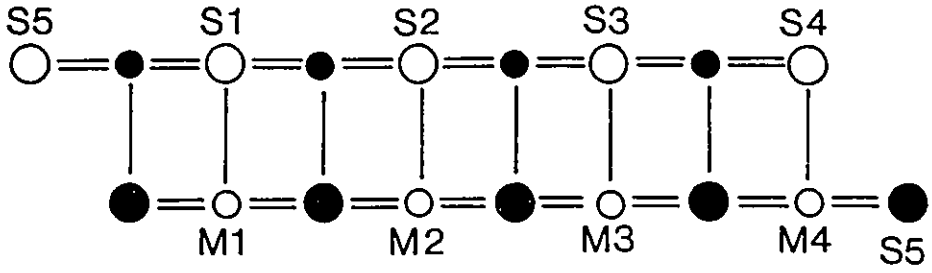

Fig. 7.1: A section through a single ribbon that extends infinitely perpendicular to the page. Open circles indicate atoms at one level, filled circles atoms half a unit cell above and below. Each edge of the ribbon is formed from two types of sulphur atoms of which one, S(4), bonds to three metal atoms and the other, S(5), to only two metal atoms in the ribbon. The M(4)-S(5) bonds are therefore expected to be strong.

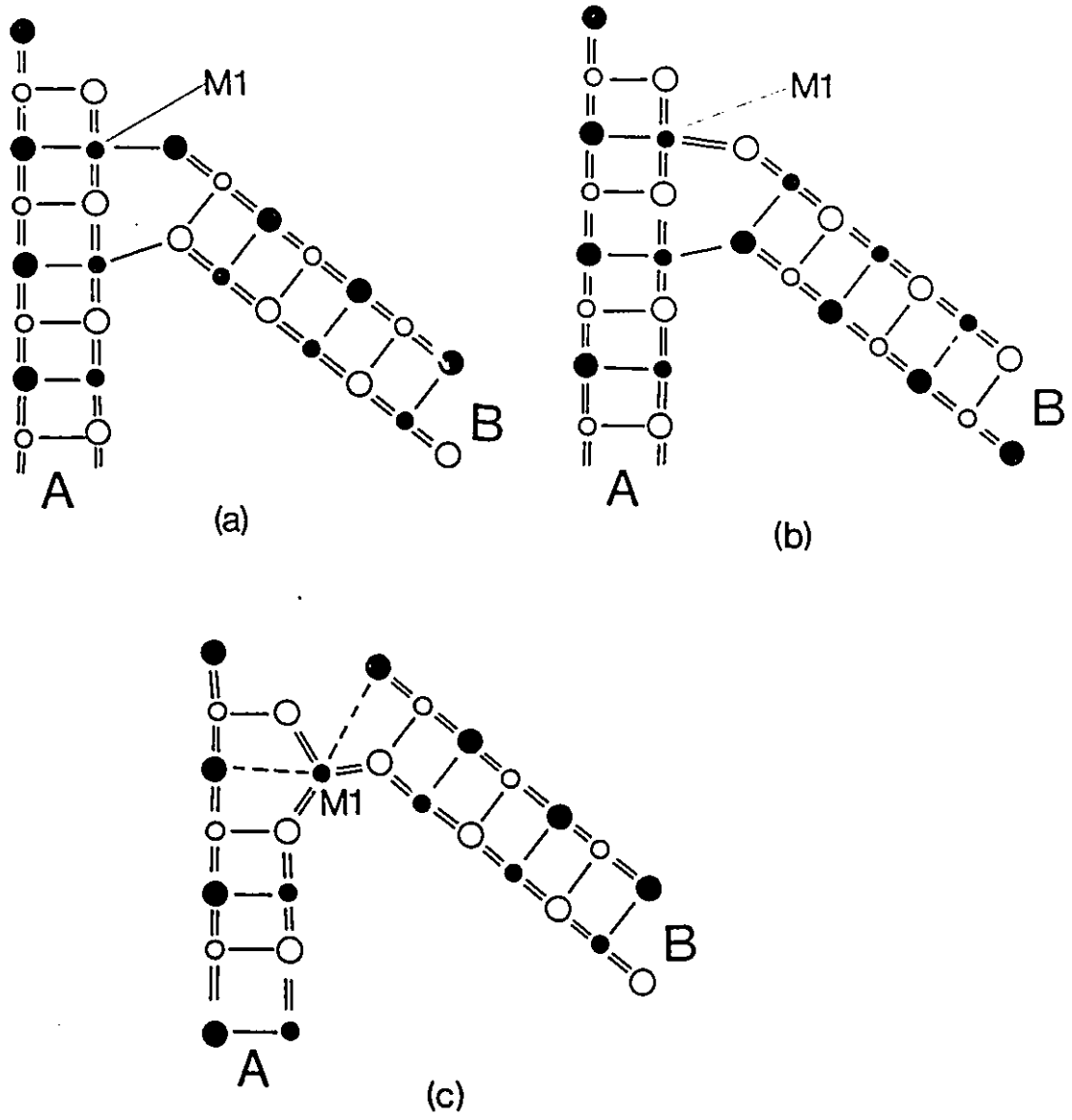

Fig. 7.2: Three ways of joining the ribbons, edge to face. In (a) the metal at the joint, M(1), is 6-coordinated and in (b) 7-coordinated. In the arrangement shown in (c) a change in the ribbon shape is required to avoid short S-S distances. The junction (b) will be used in further modelling and refered to as a single junction.

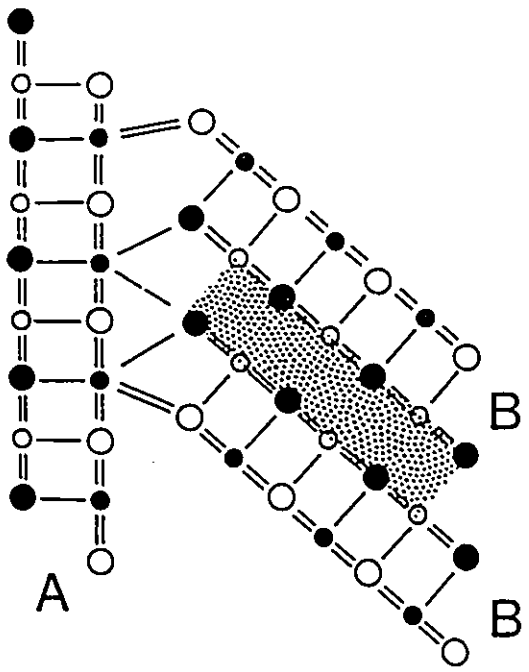

Fig. 7.3: The double junction where two paralell B type ribbons join with their edges to the face of an A type ribbon. The bonding occurs at three cation sites on the face of the A ribbon. Two of these sites are seven- and one eight-coordinated. This junction results in a favourable shear in the direction of the projection between the parallel parts of B-type ribbons, indicated with shading.

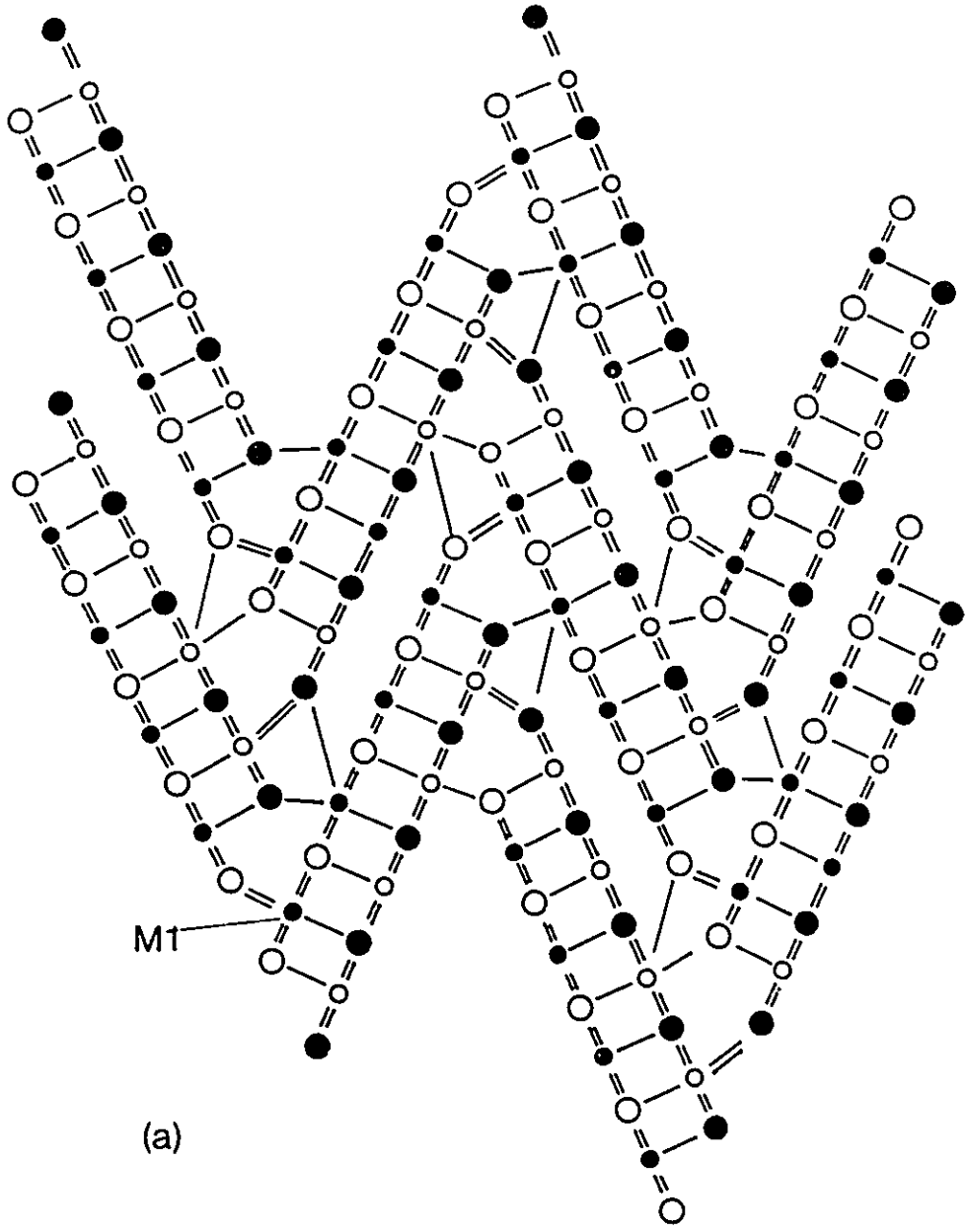

Fig. 7.4: The 1A:1B type arrangement of ribbons. They are joined by the junction shown in Fig. 7.2(b) in first (a), second (b), third (c) and fourth (d) metal sites, respectively. Only the arrangement shown in (a) is space filling. In this arrangement, 1A:1B(a), the packing results in the ribbons being sheared in the direction lying in the plane of projection and in distorted octahedral coordination for the metals.

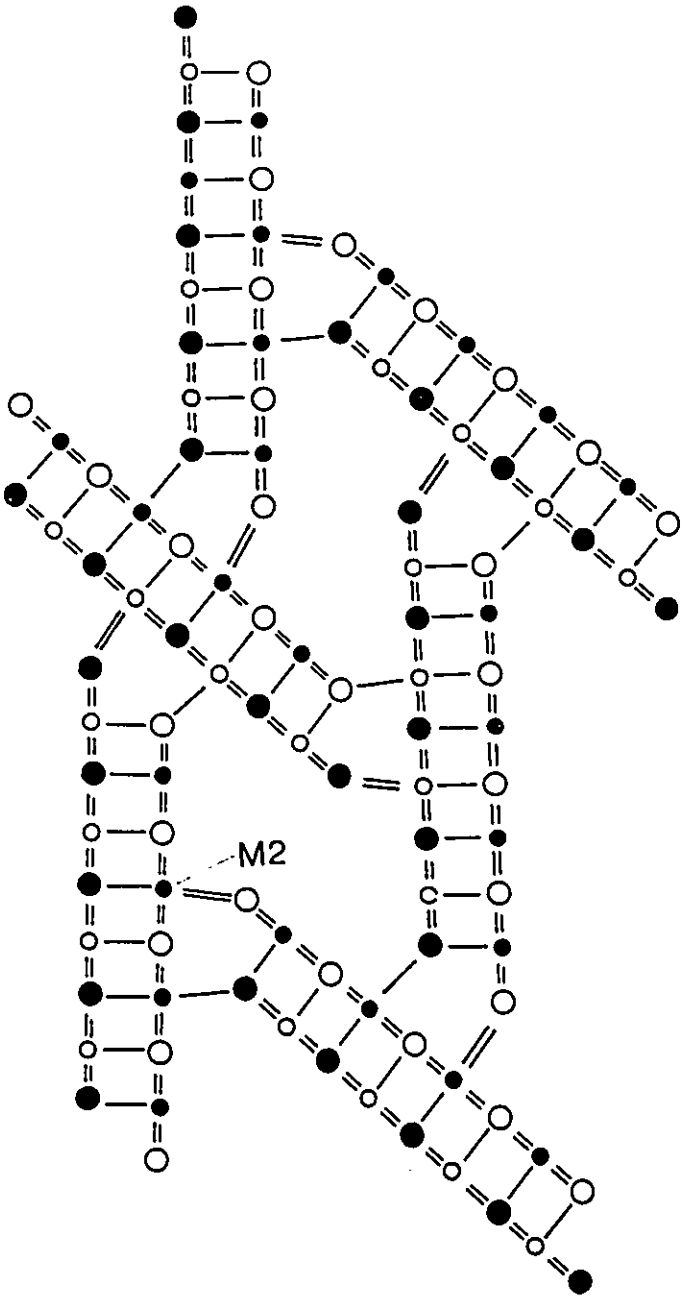

Fig. 7.4(b)

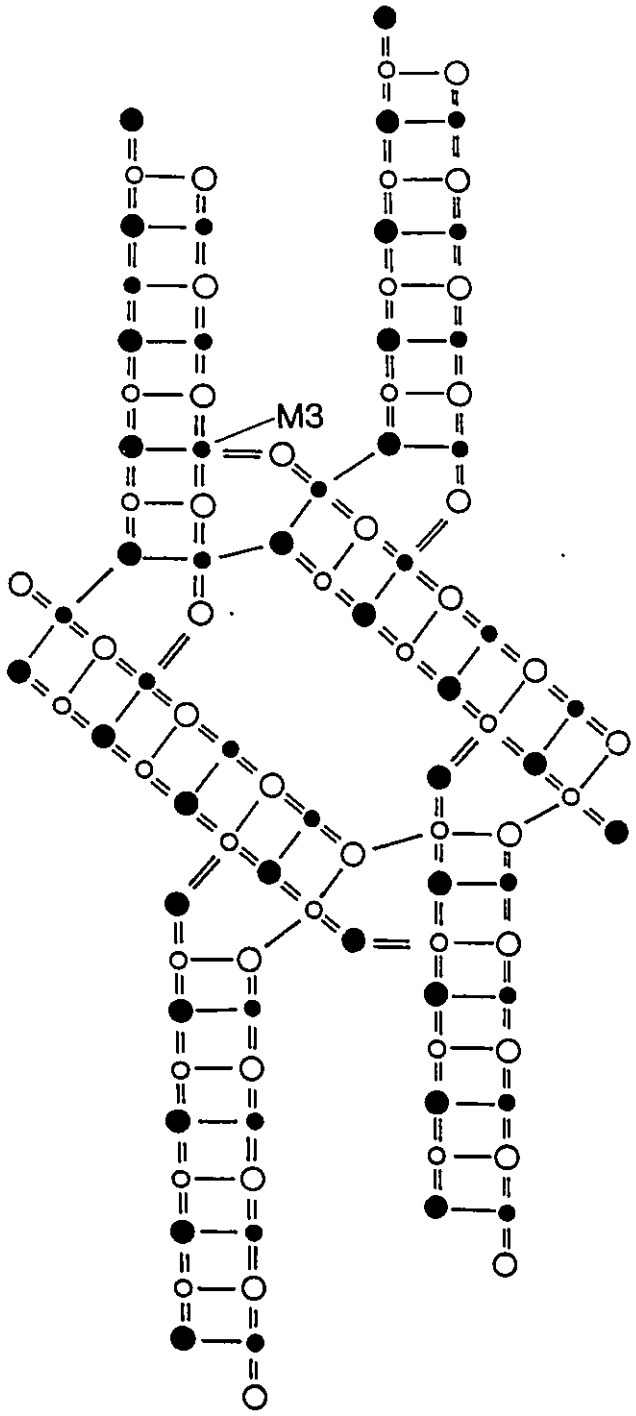

Fig 7.4(c)

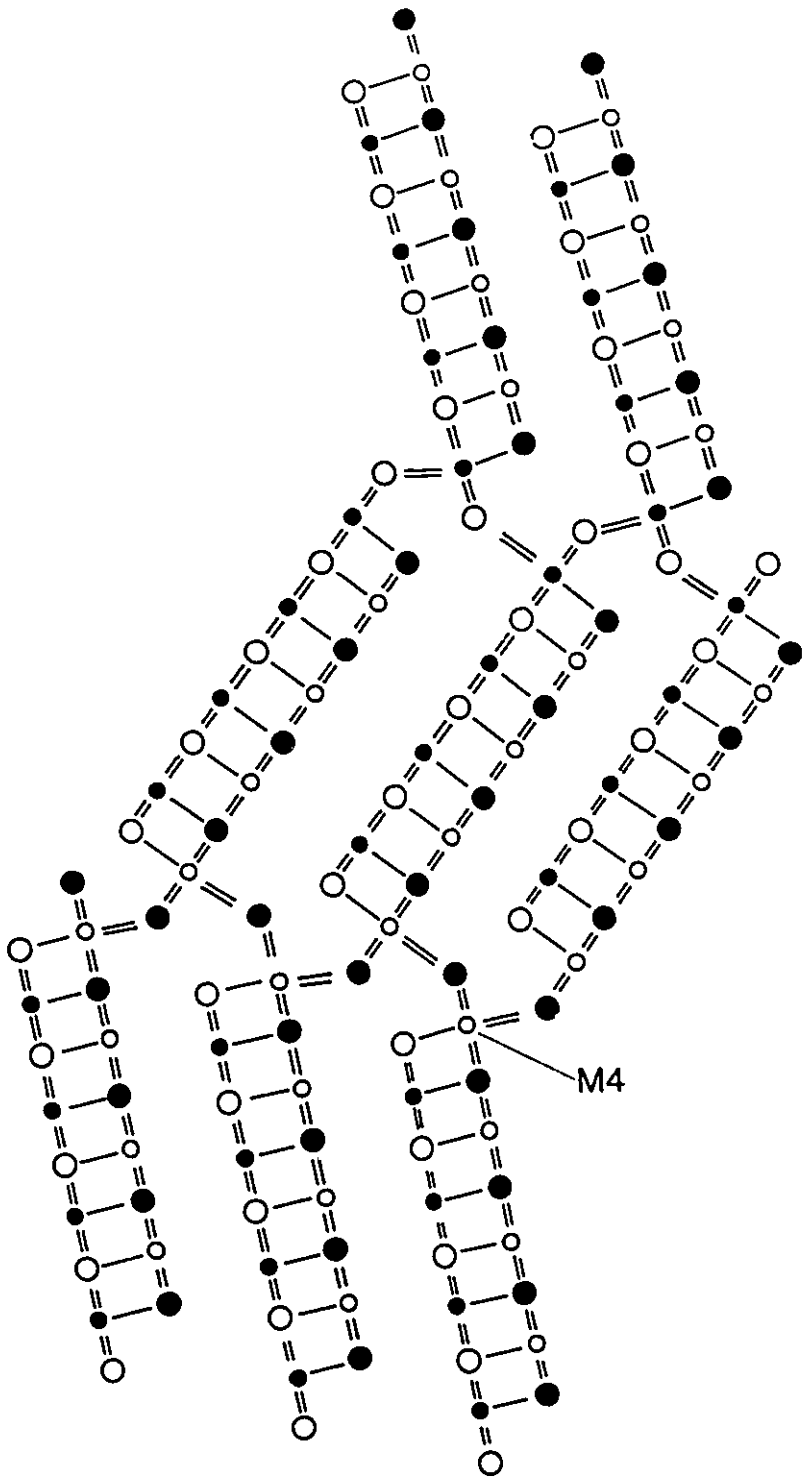

Fig. 7.4(d)

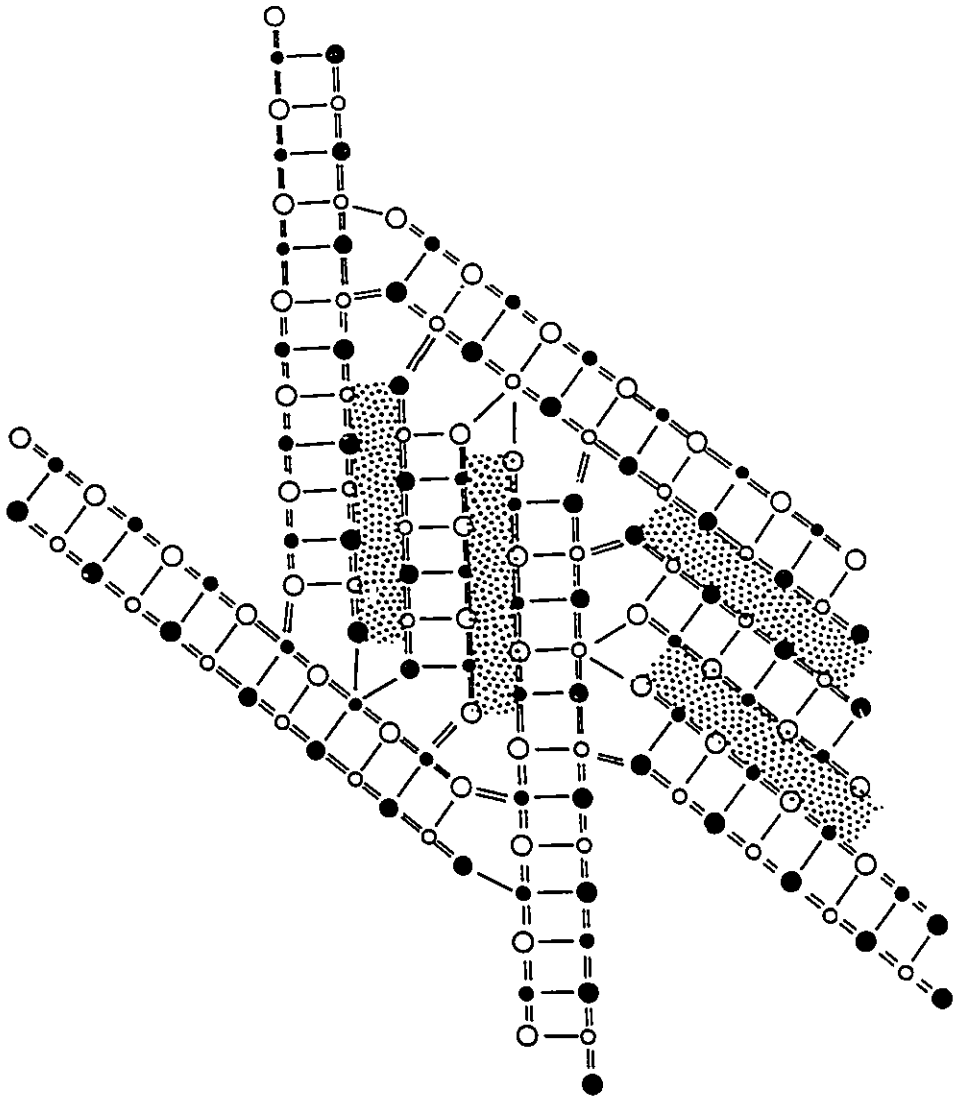

Fig. 7.5: The six pyramids wide ribbons in the 1A:1B(c) arrangement, shown in Fig. 7.4(c). The cavities between the ribbons have become big enough to accommodate a three pyramids wide ribbon. Two ribbons, a narrow and a wide one, are attached to the wide ribbon by the double junction (Fig. 7.3). This results in the ribbons sheared along the plane of projection between the narrow and each of the two neighbouring wide ones as indicated by shading.

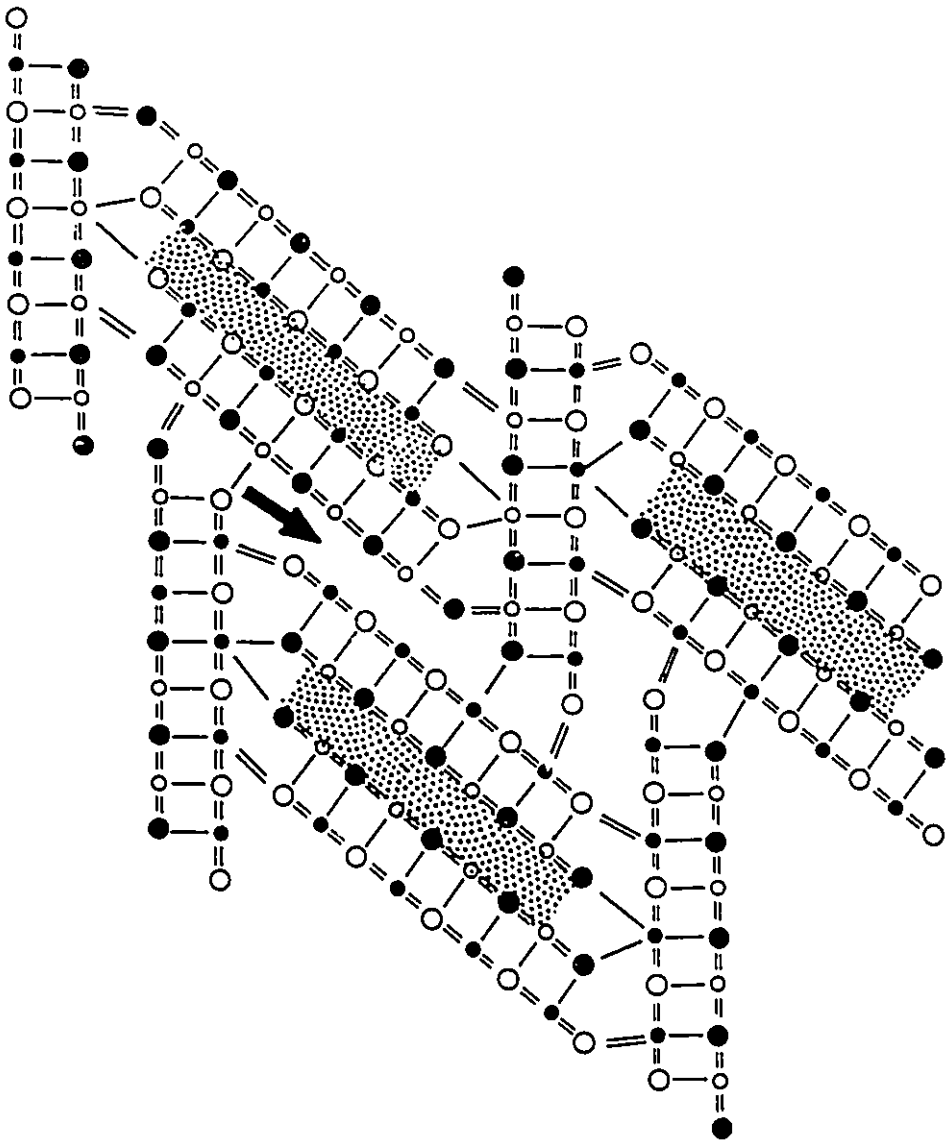

Fig. 7.6: The space filling 1A:2B arrangement of the ribbons. Both double and single junctions are used and in the resulting structure the most pairs of B ribbons are related by shears in the direction of projection, indicated by shading, but between the pairs indicated with an arrow there is no shear and the metals have the unfavourable regular octahedral coordination.

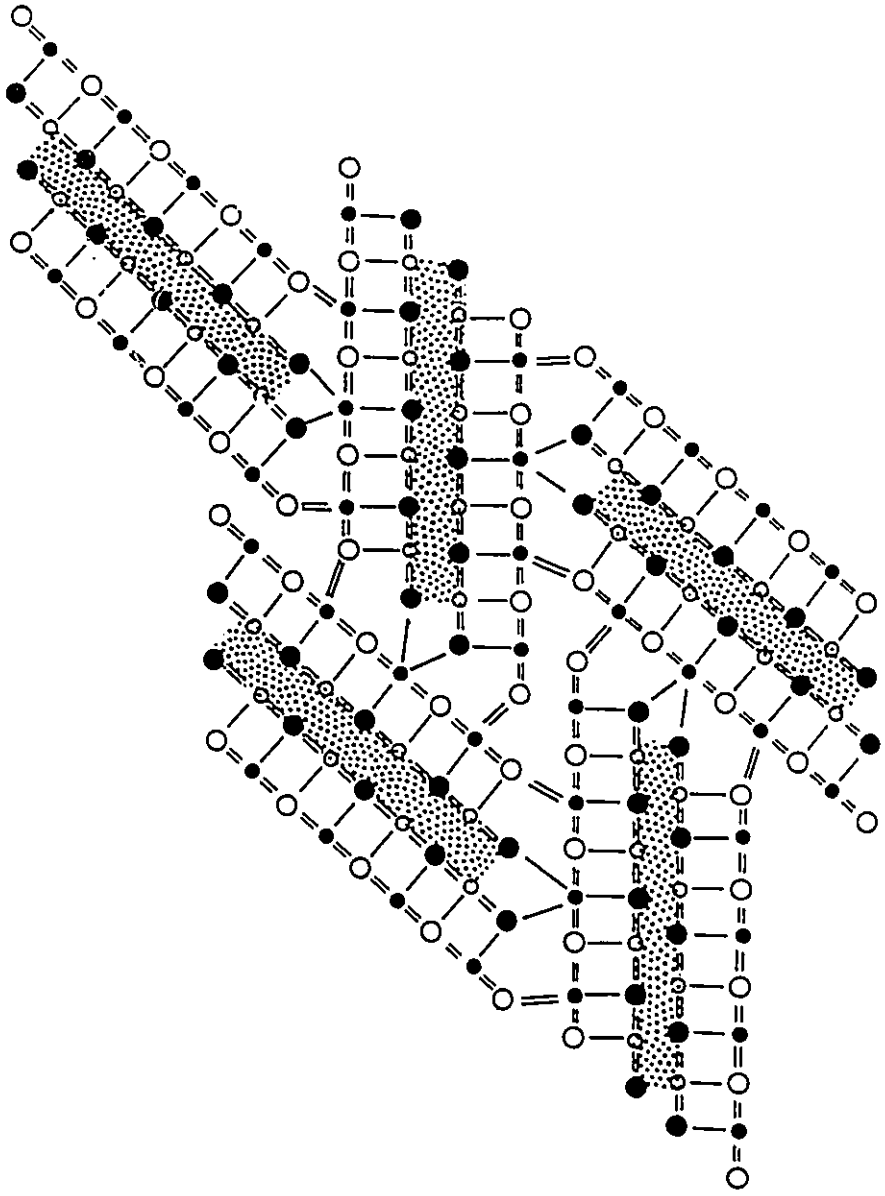

Fig. 7.7: The space filling 2A:2B arrangement of the ribbons. The four pyramids ribbon is the narrowest that can be fitted into it and the double junction is used resulting in the edge-to-face bonding at three metal sites on ribbons faces and the shear in the direction of the projection indicated by shading.

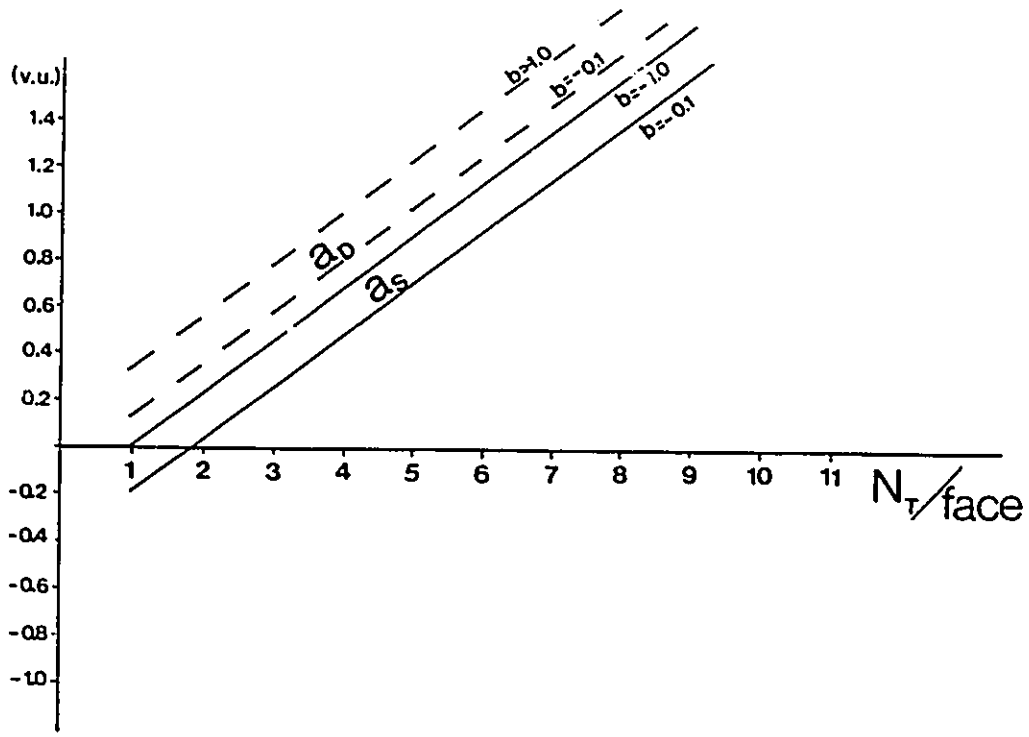

Fig. 7.8(a): Acid strength of ribbons bonded with single junctions (the solid lines indicated with a_S) and with double junctions (the broken lines indicated with a_D), for two values of the base strength (b), as functions of the total number of metal sites per face of a ribbon, N_T.

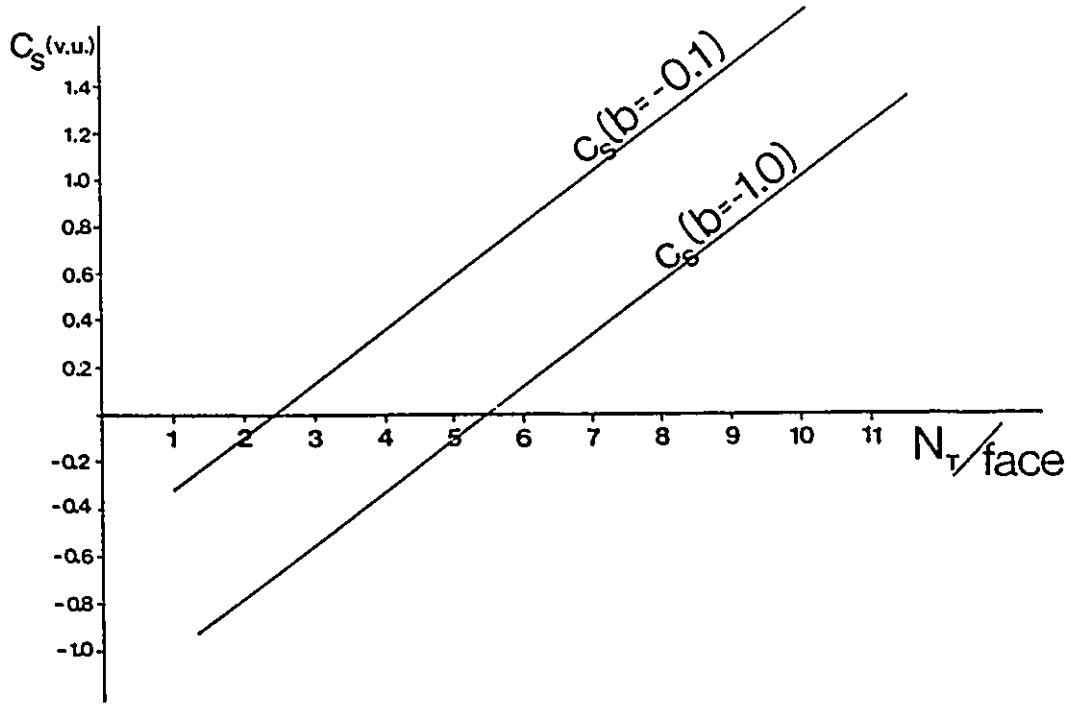

Fig. 7.8(b): The net charge on the ribbons joined with the single junctions (c_s) for a few values of base strength (b) as functions of N_T, the total number of metal sites per face of a ribbon. The narrow ribbons are charged negatively (have excess of lead) and the wide ribbons are charged positively (have excess of antimony).

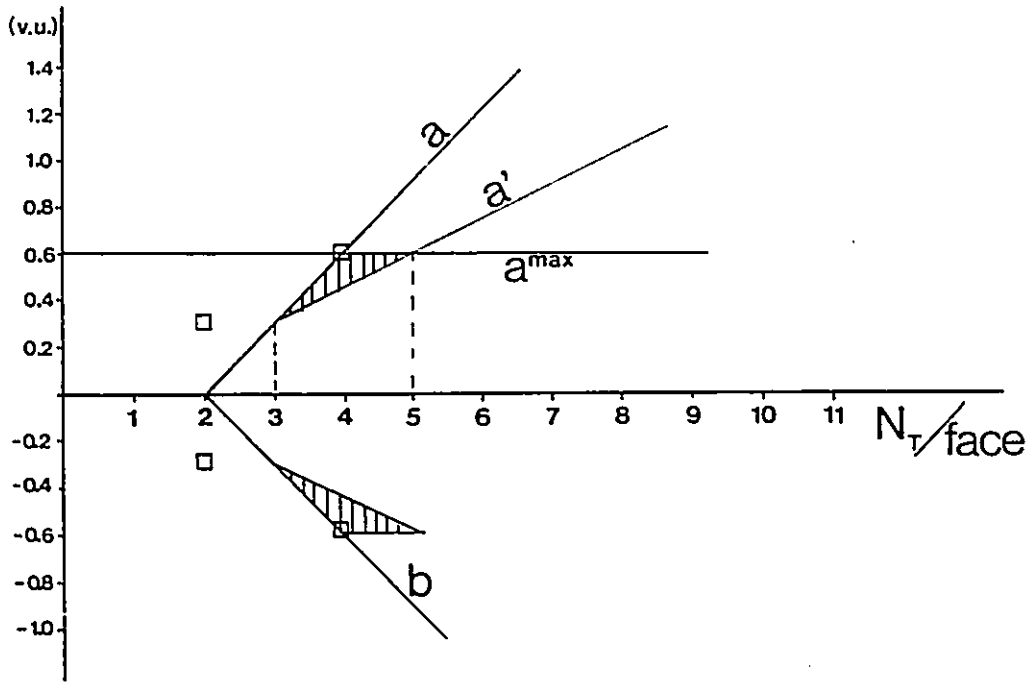

Fig. 7.9: The acid (a) and base (b) strengths of ribbons as functions of N_T, the total number of metal sites per face of a ribbon in stibnite arrangement with A and B ribbons of equal width (eqs (7.9a,b). The line a'(=a-0.15N_m) shows the acid strength of the ribbons if all the non-bonded sites are half filled with Pb. a^{max}= 0.6v.u. is indicated. For the structure stability a'≤a^{max} and the accesible regions are shown shaded e.g. The ribbons with N_T = 3, 4 and 5 are stable. The a and b in the observed structures are shown as squares.

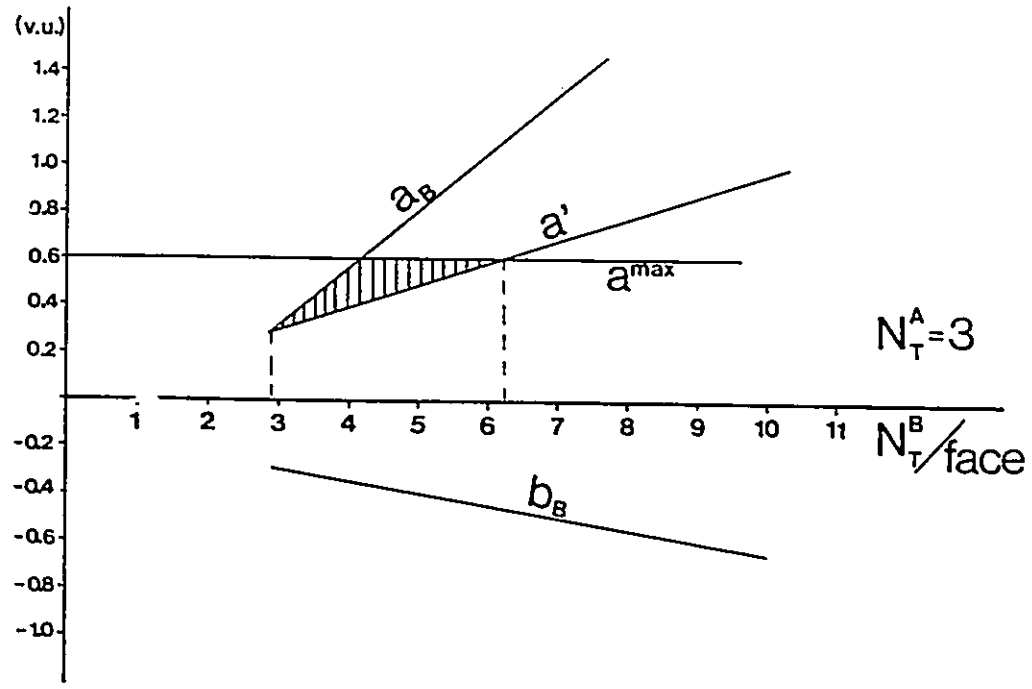

Fig. 7.10(a): The acid (a) and base (b) strengths of B ribbons as functions of N_T, the total number of metal sites per face of a ribbon, in stibnite arrangement for A=3 and B≥3 (the solutions of the set of equations (7.10a-d)). The line $a'=a-0.15N_m$ shows the acid strength of the ribbons if all the non-bonded sites are half filled with Pb and a^{max}= 0.6v.u. is indicated. The ribbons with A = 3 and B = 3, 4, 5 and 6 are in the accessible, shaded region and are predicted to be stable.

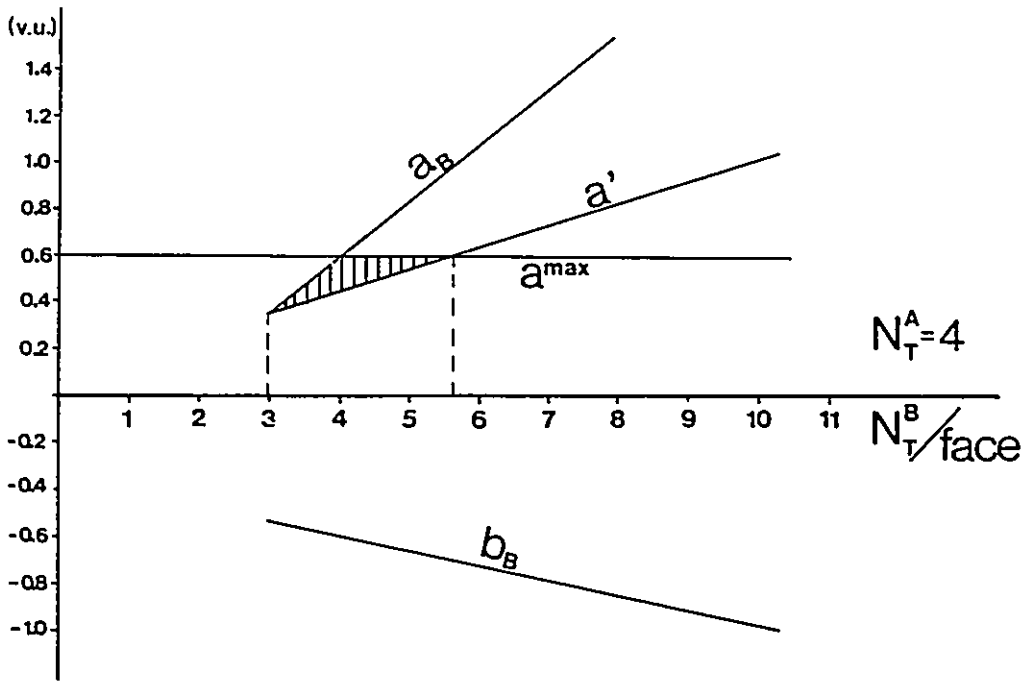

Fig. 7.10(b): The acid (a) and base (b) strengths of ribbons as functions of N_T, the total number of metal sites per face of a ribbon, in stibnite arrangement for A=4 and B≥3 (the solutions of the set of equations (7.10a-d)). The line $a'=a-0.15N_m$ shows the acid strength of the ribbons if all the non-bonded sites are half filled with Pb and a^{max}= 0.6v.u. is indicated. The ribbons with A = 4 and B = 3, 4, and 5 are in the accessible, shaded region and are predicted to be stable.

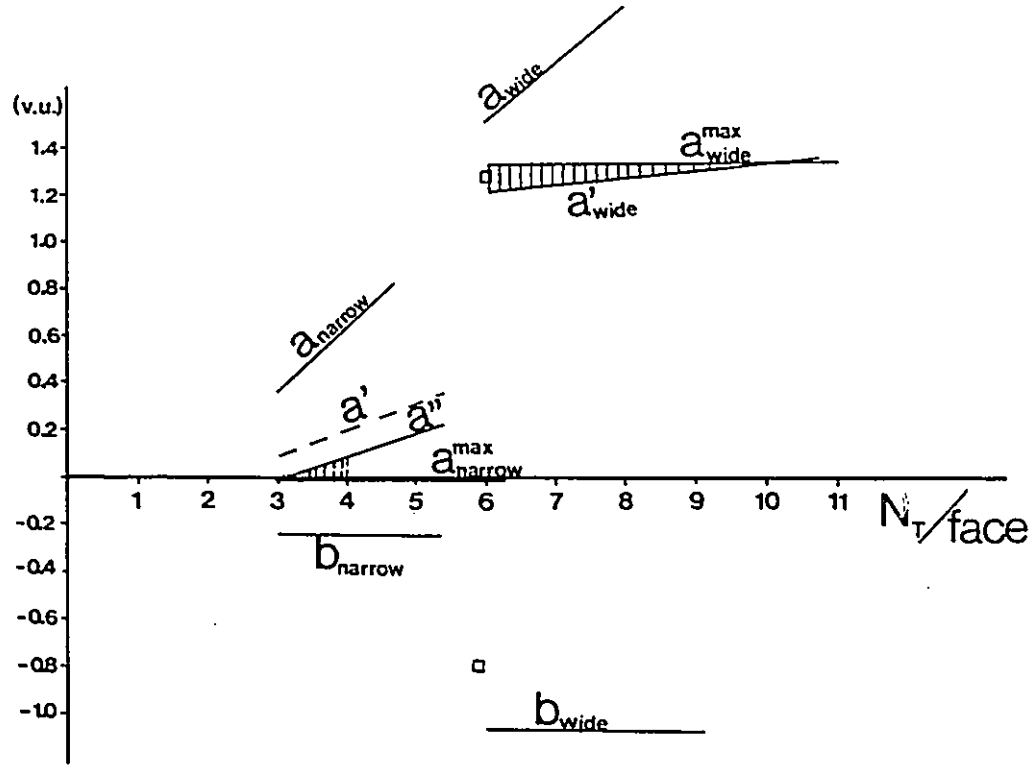

Fig. 7.11: The acid (a) and base (b) strengths of wide and narrow ribbons as functions of N_T, the total number of metal sites per face, in boulangerite arrangement (the solutions of the set of equations (7.11a-c). The lines a' and a'' correspond to the narrow ribbon with all but one (a') and one (a'') siteshalf filled with lead. The 3- and 6-ribbons are in the accessible (shaded) regions. 4-ribbon is only marginally stable.

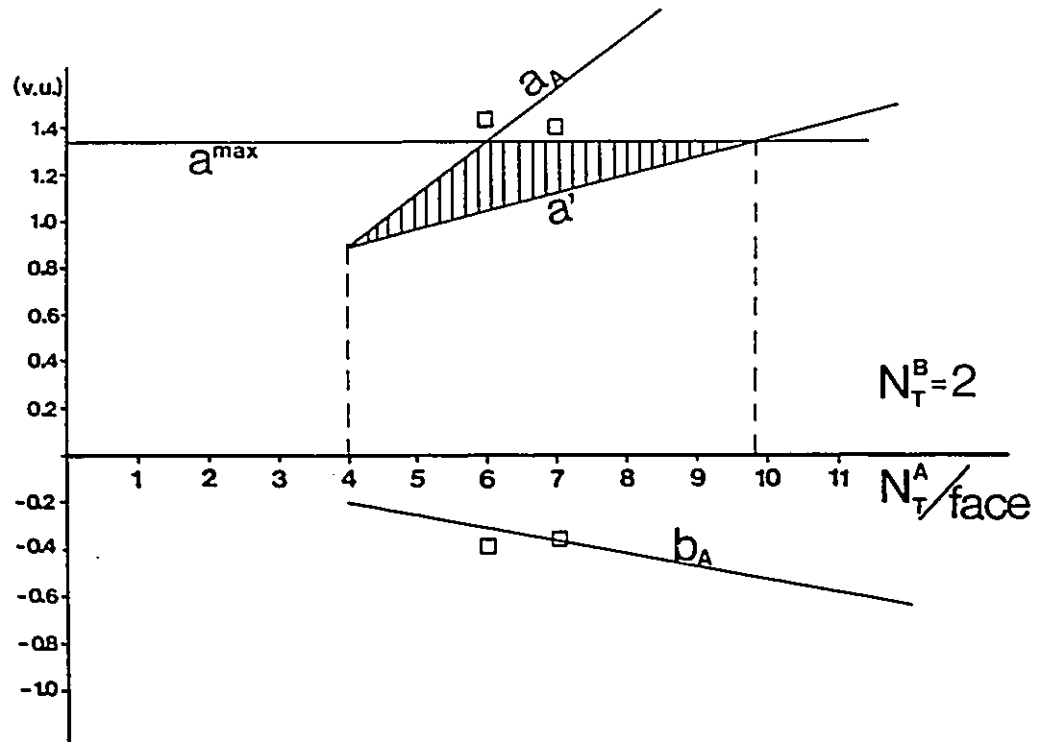

Fig. 7.12: The acid (a) and base (b) strength of wide ribbons in the robinsonite arrangement where B is a 2-ribbon, N_T=2, as functions of the total number of metal sites per face of the wide ribbon, (equations 7.13a-d). The line a'=a-0.15N_m shows the acid strength of the ribbons if all the non-bonded sites are half filled with Pb, a^{max}= 1.35v.u. is also indicated. The A ribbons with N_T(B) = 4 - 9 are in the accessible region (shaded) and are predicted to be stable.

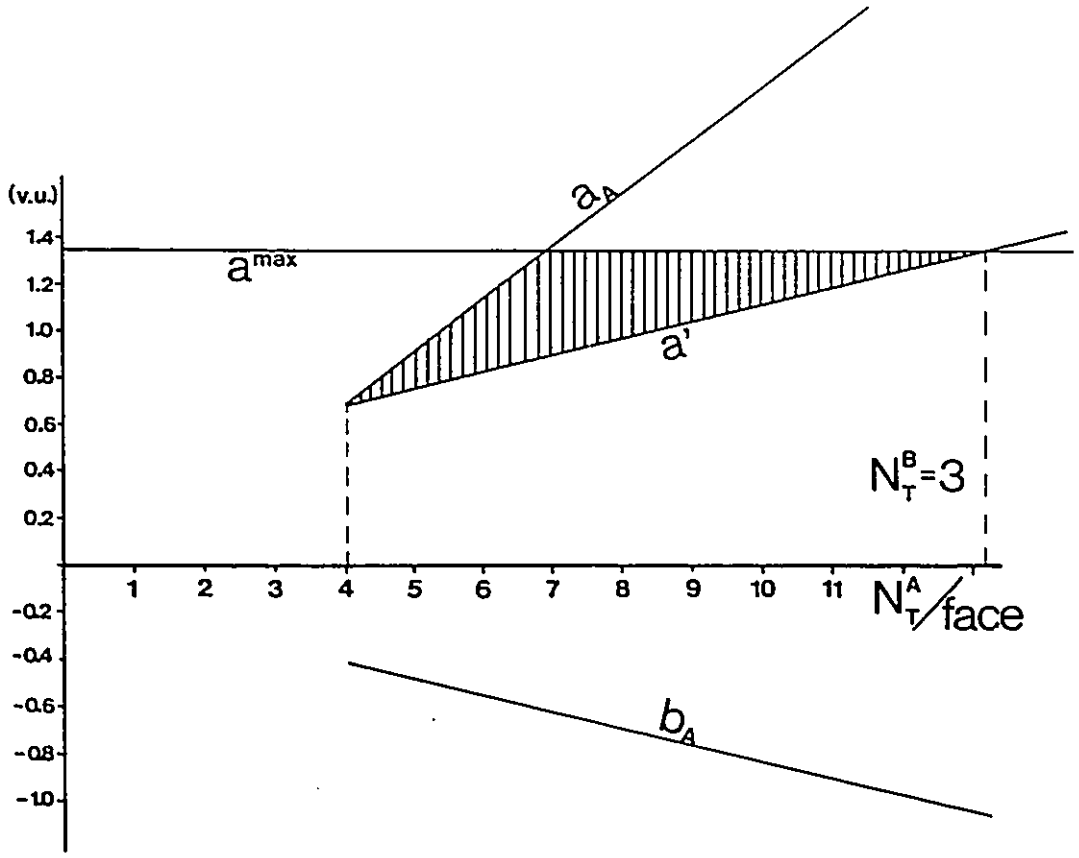

Fig. 7.13: The acid (a) and base (b) strength of A ribbons in robinsonite arrangement where B is a 3-ribbon, N_T=3, as functions of the total number of metal sites per face of A ribbon, (equations 7.13a-d). The line $a'=a-0.15N_m$ shows the acid strength of the ribbons if all the non-bonded sites are half filled with Pb, a^{max}= 1.35v.u. is indicated. The A ribbons with $N_T(B)$ = 4 - 13 are in the accessible, region (shaded) and are predicted to be stable.

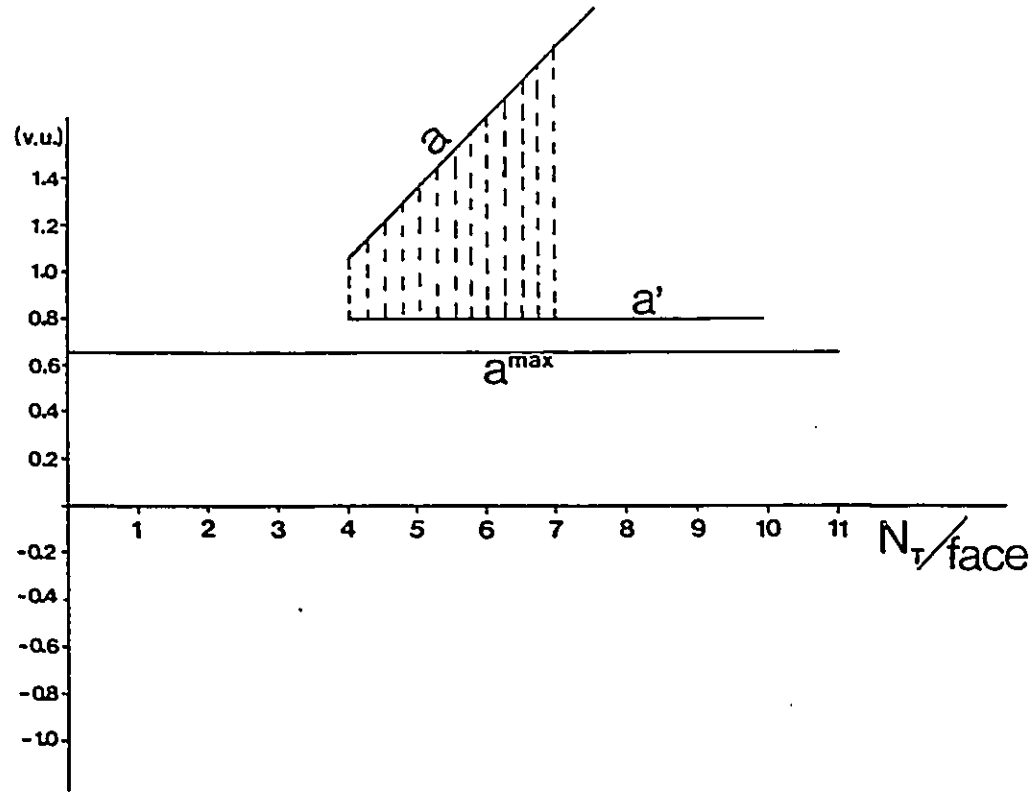

Fig. 7.14: The acid (a) and base (b) strength of ribbons in the 2A:2B arrangement, A=B, as functions of the total number of metal sites per face of a ribbon, e.g. the solutions of the set of equations 7.17(a,b). For all $N_T > 4$ (only $N_T > 4$ are topologically possible) $a^{max} < a - 0.15N_m$ which means that no structure is possible in the 2A:2B arrangement.

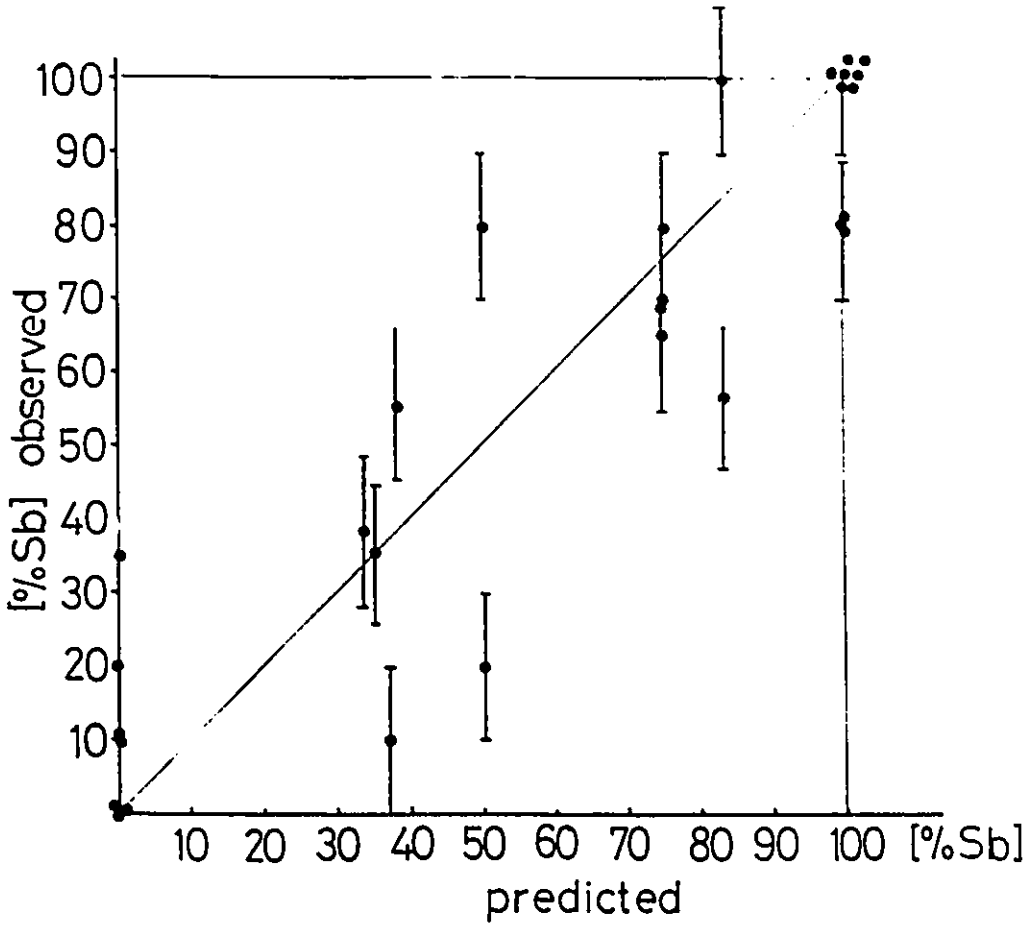

Fig. 7.15: Predicted vs. observed occupations in the structures with stibnite, boulangerite and robinsonite arrangements.

Table 7.1: Predicted and observed structures in the $PbS-Sb_2S_3$ system. The structures predicted to be the most stable are underlined.

Topology	Series, symbol	Predicted homologs	Observed homologs
1A:1B(a)	Stibnite		S(2,2)
	$S(N_1,N_2)$	S(3,3)	S(3,3)
		<u>S(4,4)</u>	S(4,4)
		S(5,5)	S(5,5)
		<u>S(3,4)</u>	
		S(3,5)	
		S(3,6)	
		S(4,5)	
1A:2B(c)	Boulangerite	B(3,6)	B(3,6)
	$B(N_1,N_2)$	B(4,7)	B(4,7)
1A:2B	Robinsonite	R5(2,2)	
	$RN_1(N_2,N_2)$	<u>R6(2,2)</u>	R6(2,2)
		R7(2,2)	R7(2,2)
		R8(2,2)	
		R9(2,2)	
		R6(3,3)	
		<u>R7(3,3)</u>	R7(3,3)?
		.....	
		R13(3,3)	
2A:2B	Sheared Cosalite	none	none

Table 7.2: Predicted and observed cation distribution (%Sb) in the phases which were reported to exist in the three homologous series of the $PbS-Sb_2S_3$ system.

Composition	Symbol		Predicted occupations (% Sb)	Observed occupations (% Sb)
$Pb_4Sb_6S_{13}$	R6(2,2)	M(1)	50	80
		M(2)	50	18
		M(3)	100	100
		M(4)	100	100
		M(10)	100	100
		M(11)	100	80
		M(12)	100	78
		M(13)	0	0
		M(14)	0	0
		M(15)	0	36
$Pb_5Sb_6S_{14}$	R7(2,2)	M(1)	38	55
		M(2)	38	10
		M(3)	100	100
		M(4)	100	100
		M(10)	100	100
		M(11)	75	80
		M(12)	75	70
		M(13)	75	65
		M(14)	0	0
		M(15)	0	0
		M(16)	0	20

Table 7.2: cont.

Composition	Symbol		Predicted occupations (% Sb)		Observed occupations (% Sb)
			unmod	mod	
$Pb_5Sb_4S_{11}$	B(3,6)(3,6)	M(1)	100	78	70
		M(2)	33	44	36
		M(3)	33	44	38
		M(10)	100		100
		M(11)	67		100
		M(12)	67		56
		M(13)	0		0
		M(14)	0		0
		M(15)	0		0
			unmod	mod	
$Pb_7Sb_4S_{13}$	B(4,7)(4,7)	M(1)	100	71	not known
		M(2)	22	32	
		M(3)	22	32	
		M(4)	22	32	
		M(10)	100		
		M(11)	44		
		M(12)	44		
		M(13)	44		
		M(14)	0		
		M(15)	0		
		M(16)	0		

Table 7.2: cont.

Composition	Symbol	Predicted occupations (% Sb)		Observed occupations (% Sb)
Sb_2S_3	S(2,2)	M(1)		100
		M(2)		100
$PbSb_2S_4$	S(3,3)	M(1)	50	not known
		M(2)	50	
		M(3)	100	
		M(10)	100	
$Pb_2Sb_2S_5$	S(4,4)	M(1)	100	100
		M(2)	100	82
		M(3)	0	10
		M(4)	0	8
$Pb_3Sb_2S_6$	S(5,5)	M(1)	100	not known
		M(2)	50	
		M(3)	50	
		M(4)	0	
		M(5)	0	

8 Conclusion

The aim of this thesis has been to study the crystal chemistry of systems in which main group elements occur in their lower oxidation state and display stereoactive lone electron pairs. The existing structures were studied in considerable detail in anticipation that understanding the observed chemistry and crystallography will allow the modelling, and ultimately the prediction, of first these and then other structures with similar electronic effects.

In cases where cation coordination polyhedra are not distorted by electronic effects, such as the stereoactivity of lone electron pairs, the two network equations, (2.41) and (2.42), uniquely define the bond valences and hence the bond lengths in the crystal structure using only the bonding topology and the atomic valences of the atoms. The coordinates of the atoms can then be predicted by fitting them to these predicted bond lengths. Although this method has been quite sucessful in those cases where electronic effects are not important it fails otherwise i.e. cannot predict the electronically induced distortions.

To solve this problem one must understand both the chemical and

topological properties of those structures which can exist. The classification of the Pb-Bi-S, and especially the Pb-Sb-S, systems presented in this thesis, although it draws on the ideas developed before by others, captures both those aspects of the structures. In this respect it is superior to the exhaustive classification of E. Makovicky (1985, 1989), where the emphasis is put only on the topology and the structural chemistry is left unexplored.

The choice of the structure building fragment is crucial to an understanding of the chemistry. Breaking a structure into fragments is always an arbitrary process but it can be justified if dictated by the chemistry. The most natural fragment is the most strongly bonded unit in the structure and is chosen by ignoring the weak bonds in the distorted coordination polyhedra around Sb, Bi and Pb. For the structures in the Pb-Sb-S system, the resulting fragment is the ribbon used in the classification presented here. In this respect the larger lozenge shaped units introduced by E. Makovicky, for example, do not reflect the chemistry of the structures.

It is this choice of the structure building units that leads to a fruitful modelling of the structures. The analysis of ribbon packing, and the consideraton of their composition and bonding strength, allow one to correctly predict the bonding topologies, the cation distributions and the limits of the homolgous series

in the system, as shown in the previous chapter. The achievement of this approach lies, not in the absolute precision with which it predicts the number of stable homologs and cations distribution in each series, but rather in showing that the chemical constraints severely limit the number of possible structures. The approach should be equally succesful when applied to other systems where chemistry dictates the choice of the building fragment that bonds in the space filling arrangements.

The study presented in this thesis uses the observed distortion of the coordination polyhedra not only as a guide to structure fragmentation, it also quantifies these distortions for antimony and lead in sulphides, as shown in Fig. 4.7. The propensity for distortion is shown to be stronger for smaller and more highly charged cations but weaker when selenium rather then sulphur is the anion. From these studies one can obtain all the necessary information to predict the structures namely the topology of the bonding network, the cation distributions and the distortion of the coordination polyhedra. A chemical, as well as topological approach to these systems serves not only to classify them, but to predict their bonding network and, ultimately, the lengths of their bonds and the coordinates of their atoms.

9 References

Aizawa, K., Iguchi, E. and Tilley, R. J. D. (1983). J. Solid State Chem. **48**, 284-294.

Andersson, S. and Hyde. B. G. (1974). J. Solid State Chem. 9, 92-101.

Armbruster, T. and H:mmel, W. (1987). Am. Mineral. 72, S21-831.

Atabaeva,E. Ya., Mashkov, S. A., and Popova, S.V. (1973). Kristallografiya. 8, 173-174.

Basset, W. A., Takahashi, T. and Stook, P. W. (1967). Rev. Sci. Instr. 38, 37-42.

Bayliss, P. and Nowacki, W. (1972). Z. Kristall. 135, 308-315.

Berry, L. G., Fahey, J. J. and Bailey, E. H. (1952). Am. Mineral. 37, 438-446

Bethe, H. A. (1928). Ann. Phys. (Leipzig) 87, 55.

Born, L. and Hellner, E., (1960). Am. Mineral. **45**, 1266-1271.

Bortnikov, N. S., Nekrasov, I. Ya., Mozgova, N. N. and Tsepin, A. I. (1981). N. Jh. Mineral. Abh. **143**, 37-60.

Buerger, M. T. and Hahn, T. (1955). Am. Mineral. **40**, 226-238.

Brown, I. D., In Structure and Bonding in Crystals, vol II, O'Keeffe, M., Navrotsky, A., Eds.; Academic Press: New York, (1981) pp 1-30.

Brown, I. D. (1978). Chem. Soc. Rev. 7, 359-376.

Brown, I. D. and Altermatt, D. (1985). Acta Cryst. B41, 244-247.

Brown, I. D. and Shannon, R. D. (1973). Acta Cryst. A29, 266-282.

Chang, L. L. Y. and Hoda, S. H. (1977). Am. Mineral. 62, 346-350.

Chang, L.L.Y., Walia, D.S. and Knowles, C.R. (1980). Econ. Geol. 75, 317-328.

Cho, S. A. and Wuensch, B. J. (1970). Nature, Lond. 225, 444-445.

Cho, S. A. and Wuensch, B. J. (1974). Z. Kristallogr. 139, 351-378.

Cochran, W., (1951). Acta Cryst. 4, 408.

Colaïtis, D., van Dyck, D. and Amelinckx, S. (1981). phys. stat. sol.(a) 68, 419-438.

Cordier, G. and Schäfer, H. (1979). Z. Naturforsch. 34b, 1053-1056.

Cowley, J. M., Diffraction Physics, North-Holland Publishing Company, Amsterdam, Oxford, (1975).

Cowley, J.M., In High Resolution Transmission Electron Microscopy and Associated Techniques, Eds: Buseck, P.R., Cowley, J. M. and Eyring, L., (1988).

Cowley, J.M. and Moodie, A.F. (1957). Acta Cryst. 10, 609.

Cowley, J.M. and Moodie, A.F. (1958). Proc. Phys. Soc., London, 71, 533.

Cowley, J.M. and Moodie, A.F. (1959a). Acta Cryst. 12, 353.

Cowley, J.M. and Moodie, A.F. (1959b). Acta Cryst. 12, 360.

Craig, J. R. (1967). Mineral. Deposita, 1, 278-306.

Craig, J. R., Chang, L. L. Y. and Lees, W. R. (1973). Can. Mineral. 12, 199-206.

Del Bacchia, S., Jumas, J.C., Maurin, M. (1980). Acta Cryst. B37, 1903-1905.

Dittmar, G. and Schäfer, H. (1977). Z. Naturforsch. 32b, 1346-1348.

Douglass, R.M., Murphy, M.J. and Pabst, A., (1954). Am. Miner. 39, 908-928.

Earley, J.W. (1950). Am. Mineral. 35, 338-350.

Euler, R. and Hellner, E. (1960). Z. Kristall. 113, 345-372.

Furnas, T. C., Single Crystal Orienter Instruction Manual, General El. Company, (1957).

Gannon, J. R. and Tilley, R. J. D. (1976). J. Microscopy, 106, 59.

Garvin, P. L., (1973). N. Jb. Mineral. Abh. 118, 235-267.

Geller, S. and Wernick, J. H. (1959). Acta Cryst. 12, 46-54.

Gjonnes, J. and Moodie, A.F. (1965). Acta Cryst. 19, 65.

Goodman, P. and Moodie, A. F. (1974). Acta Cryst. A30, 280.

Guillevic, P.J., Lestrat, H. and Grandjean, D. (1967). Acta Cryst. B32 , 1342-1345.

Graham, A. R., Thompson, R. M. and Berry, L. G. (1953). Am. Mineral. 38, 536-544.

Hamilton, W. C. (1965). Acta Cryst. 18, 502-510.

Harker, D. and Kasper, J.S., (1948). Acta Cryst. 1, 70.

Harris, D. C. and Chen, T.T. (1975) Can. Miner. 13, 411-414.

Harris, D. C., Jambor, J. L., Lachance, G. R. and Thorpe, R. I. (1968). Can. Miner. 9, 371-382.

Helmholz, L. (1936). Z. Kristallogr. 95, 129-137.

Herbert, H. K. and Mumme, W.G. (1981). N. Jb. Mineral. Mh. 2, 69-80.

Hiller, J. E. (1938). Z. Kristallogr. 100A, 128-156.

Hirsch, P., Howie, A., Nicholson, R. B., Pashley, D. W. and Whelan, M. J. (1977). Electron Microscopy of Thin Crystals, Krieger, Huntington, New York.

Hoda, S. N. and Chang, L. L. Y., (1975). Can. Mineral. 13, 388-393.

Hoda, S. N. and Chang, L. L. Y. (1975). Amer. Mineral. 60, 621-633.

Hofmann, W. (1933). Z. Kristall. 86, 225-245.

Hyde, B. G., Bagshaw, A. N., Andersson, S. and O'Keeffe, M. (1974), Ann. Rev. Mat. Sci. 4, 43-52.

Hyde, B. G., Andersson, S., Bakker, M., Plug, C. M. and O'Keeffe, M. (1979), Prog. Solid State Chem. 12, 273-327.

Iitaka, Y. and Nowacki, W. (1962). Acta Cryst. 15, 691-698.

International Tables for X-Ray Crystallography (1974). Vol.IV. Tables 2.2B and 2.3.1. Birmingham: Kynoch Press.

Jambor, J.L. (1967). Can. Miner. 9, 7-24 & 191-312.

Jambor, J.L. (1968). Can. Miner. 9, 507-521.

Jambor, J.L. (1969). Miner. Mag. 37, 442-446.

Jumas, J. C., Olivier-Fourcade, J., Philippot, E. and Maurin, M. (1980). Acta Cryst. B36, 2940-2945.

Kanishcheva, A.S., Mikhailov, Yu. N., Lazarev, V. B. and Moshchalkova, N. A. (1980). Dokl. Akad. Nauk SSSR 252, 872-875.

Karle, J. and Hauptman, H., (1950) Acta Cryst. 3, 181.

Karup-Møller, S and Makovicky, E. (1981). Can. Mineral. 19, 349-353.

Klee, W. and Schäfer, H. (1980). Mat. Res. Bull. 15, 1033-1038.

Kohatsu, J.J. (1973). PhD. Thesis, Department of Metallurgy and Materials Science, MIT.

Kohatsu, J.J. and Wuensch, B.J. (1974). Program and Abstracts, Spring Meeting, Amer. Cryst. Assoc., Berkeley, California, p 40.

Kopfmann, G. and Huber, R. (1968). Acta Cryst. **A24**, 348.

Kopfmann, G. and Huber, R. (1969). Acta Cryst. **A25**, 143.

Kupčik, V. and Veselá-Nováková, L. (1969). Tscermaks Miner. u. Petrogr. Mitt. **14**, 55-59.

Lebas, G. and Le Bihan, M. T. (1976). Bull. Soc. franç. Minér. Crist. 99, 351-360.

Lipson, H. and Cochran, W., The Determination of Crystal Structures, G. Bell and Sons, London, (1957).

Macicek, J. (1988). private communication.

Makovicky, E. (1977a). N. Jhb. Mineral. Abh. **131**, 187-207.

Makovicky, E. (1977b). Canadian Miner. **15**, 339-348.

Makovicky, E. (1981). Fortschr. Mineral. **59**,137-190.

Makovicky, E. (1983). Proc. NATO Adv. Study Inst. Ser. E83, 159-169.

Makovicky, E. (1985). Fortschr. Mineral. **63**, 45-89.

Makovicky, E. (1989). N. Jhb. Mineral. Abh. **160**, 269-297.

Makovicky, E. and Hyde, B. G. (1979). AIP Conf. Proc. 53, 99-101.

Makovicky, E. and Hyde, B. G. (1981). Structure and Bonding, 46, 101-170.

Makovicky, E. and Karup-Møller, S. (1977a). N. Jhb. Mineral. Abh. 130, 264-287.

Makovicky, E. and Karup-Møller, S. (1977b). N. Jhb. Mineral. Abh. 131, 56-82.

Makovicky, E. and Mumme, W. G. (1979). Can. Mineral. 17, 607-618.

Makovicky, E., Mumme, W. G. and Watts, J. A. (1977). Can. Mineral. 15, 339-348.

Mariano, A. N. and Chopra, K. L. (1967). Appl. Phys. Lett. 10, 282-284.

Matzat, E. (1979). Acta Cryst. B35, 133-136.

North, A. C. T., Phillips, D. C. and Mathews, F. C., (1968). Acta Cryst, A24, 351.

Nuffield, E. W. (1946). Univ. Toronto Studies, Geol. Ser. 50. 49-62.

Ohmasa, M. (1973). N. Jb. Mineral. Mh. 5, 227-233.

Ohmasa, M. and Nowacki, W. (1973). Z. Kristall. 137, 422-432.

Otto, H. H. and Strunz, H. (1968). N. Jhb. Mineral. Abh. 108, 1-19.

Petrova, I.V., Kaplunnik, L.N. Bortnikov, N.S., Pobedimskaya, E.A. and Belov, N.V. (1978). Dokl. Akad Nauk SSSR, **241**, 88-90.

Petrova, I.V., Kuznetzov, E.L., Belokoneva, A.M., Simonov, E.A., Pobedimskaya, E.A. and Belov, N.V. (1978). Dokl. Akad. Nauk SSSR **242**, 337-340.

Portheine, J. C. and Nowacki, W. (1975). Z. Kristall. **141**, 79-96.

Potel, M., Brochu, R. and Padion, J. (1975), Mat. Res. Bull. **10**, 206.

Robinson, S. C. (1948a). Univ. Toronto Studies, Geol. Ser. **48**, 54-70.

Robinson, S. C. (1948b). Econ. Geol. **43**, 293-312.

Salanci, B. (1979). N. Jb. Mineral. Abh. **135**, 315-326.

Salanci, B. and Moh, G. H. (1969). N. Jb. Miner. Abh., **112**, 63-95.

Salanci, B. and Moh, G. H., (1970). N. Jh. Mineral. Mh. **11**, 524-528.

Scherzer, O. (1949). J. Appl. Phys., **20**, 20.

Sheldrick, G. M. (1976). SHELX76. Program for crystal structure determination. Univ. of Cambridge, England.

Skarnulis, A. J., (1976), PhD Thesis, Arizona State University.

Skowron, A. and Brown, I. D. (1990a). Acta Cryst. **C46**, 527-531.

Skowron, A. and Brown, I. D. (1990b). Acta Cryst. **C46**, 531-534.

Skowron, A. and Brown, I. D. (1990c). Acta Cryst. **C46**, 534-536.

Skowron, A. and Brown, I. D. (1990d). Acta Cryst. **C46**, in press.

Skowron, A., Brown, I. D. and Tilley, R. J. D. submitted to J. Solid St. Chem.

Skowron, A. and Tilley, R.J.D. (1986a). Chemica Scripta, 26, 353-358.

Skowron, A. and Tilley, R. J. D. (1986b). Proc. XI-th Congress on Electron Microscopy, Kyoto, 1709-1710.

Skowron, A. and Tilley, R. J. D., (1989) J. Solid St. Chem. **78**, 84-92.

Skowron, A. and Tilley, R. J. D., (1989) J. Solid St. Chem. **85**, 235-250.

Smith, P. P. K. and Hyde, B. G. (1983). Acta Cryst. **C39**, 1498-1502.

Srikrishnan, T. and Nowacki, W. (1974). Z. Kristall. **140**, 114-136.

Stadelmann, P. A., (1987), Ultramicroscopy, **21**, 131.

Stout, G. H. and Jensen, L.H., X-Ray Structure Determination, John Wiley and Sons, New York, (1989).

Takeda, H. and Horiuchi, H. (1971). J. Miner. Soc. Japan **10**, 283-295.

Takèuchi, Y. (1978). Rec. Progr. Nat. Sci. Japan 3, 153-181.

Takèuchi, Y. U., Ozawa, T. and Takagi, J. (1979) Zeit. Kristallogr. **150**, 75-84.

Takagi, J. and Takèuchi, Y. (1972). Acta Cryst. B28, 649-651.

Takèuchi, Y. and Takagi, J. (1974a). Proc. Japan. Acad. 50, 76-79.

Takèuchi, Y. and Takagi, J. (1974b). Proc. Japan. Acad. 50, 222-225.

Takèuchi, Y., Takagi, J. and Yamanaka, T. (1974). Zeit. Kristallogr. **140**, 9-17.

Tideswell, N. W., Kruse, F.H. and McCullough, J. D. (1957). Acta Cryst. **10**, 99-102.

Tilley, R. J. D. and Wright, A. C. (1982). Chem. Scripta **19**, 18-22.

Tilley, R. J. D. and Wright, A. C. (1987). Chem. Scripta **27**, 459-465.

Tilley, R. D. J., Wright, A. C. and Smith, D. J. (1986). Proc. R. Soc. Lond. **A408**, 9-22.

Van Hook, H. J. (1960). Econ. Geol., **55**, 759-788.

Volk, K., Cordier, G. and Schäfer, H. (1980). Z. Naturforsch. **35b** , 134-140.

von Schnering, H.G. and Wiedemeier, H. (1981). Z. Kristallogr. **156**, 143-150.

Wagner, T. R. and O'Keeffe, M. (1988). J. Solid St. Chem. **73**, 211-216.

Wang, N. (1973). N. Jb. Mineral. Mh. **2**, 79-81.

Wang, N. (1976). N. Jb. Mineral. Abh. **128**, 167-175.

Wang, N. (1977). Can. Mineral. **15**, 115-116.

Werner, P. E., (1969), Arkiv. Kemi. **31**, 513.

Williams, T. B. and Hyde, B. G. (1988). Acta Cryst. **B44**, 467-474.

Wiedemeier, H. and von Schnering, H.G. (1978). Z. Kristallogr. **148**, 295-303.

Woolfson, M.M., An Introduction to X-Ray Crystallography, Cambridge University Press, (1979).

Wuensch, B. J. and Kohatsu J. J. (1974). Acta Cryst. B30, 2935-2937.

Wuensch, B. J. (1979). AIP Conf. Proc. **53**, 337-354.

Appendices

Table A1.1: Summary of the sample preparation and the phase analysis.

Sample number	Composition			Heat treatments: initial temp [K]	initial time [days]	final temp [K]	final time [days]	observations	X-ray diffraction analysis	Electron diffraction analysis
	PbS [mole%]	Bi_2S_3 [mole%]	Ag_2S [mole%]							
1	85.5	14.5	-	1373	2	773	21		L7,7	L7,7
2a	85.00	12.74	2.27	1373	2	1373	2		PbS, L7,7(tr)	PbS, L7,7
b						773	21		PbS, L7,7	PbS, L7,7
3a	84.80	10.71	4.46	1373	2	1373	2		PbS	PbS
						773	28		PbS	PbS
4a	79.92	19.98	0.11	1373	2	773	14		L7,7, L4,4	
b						973	14	needl.sep.	L7,7	
5a	79.82	19.96	0.22	1373	2	773	14		L7,7, L4,4(tr)	
						973	14	needl.sep.	L7,7, L4,4	
6a	79.72	19.93	0.35	1373	2	773	14		L7,7, PbS(tr)	L7,7, PbS
b						973	14		L7,7, L4,4	L4,4, L7,7
7a	79.60	19.90	0.50	1373	2	773	14		L7,7, PbS	L7,7, PbS
b						973	14	needl.sep.	L4,4, PbS, L7,7	L4,4
8a	79.47	19.87	0.66	1373	2	773	14		L7,7, PbS	
b						973	14	needl.sep.	L4,4, PbS, L4,7(tr)	L4,4
9a	79.32	19.83	0.85	1373	2	773	14		L7,7, PbS	
b						973	14	needl.sep.	L4,4, PbS, L7,7(tr)	
10a	79.15	19.79	1.07	1373	2	773	14		PbS, L7,7(tr)	
b						973	14		PbS, L7,7(tr)	
11a	78.95	19.74	1.32	1373	2	773	14		PbS, L7,7(tr)	
b						973	14	needl.sep.	PbS, L4,4	
12a	78.71	19.68	1.61	1373	2	773	14		PbS	
b						973	14	needl.sep.	PbS, L7,7, L4,4(tr)	
13	75.0	25.0	-	1373	2	773	21		L4,4	L4,4
14a	74.94	21.05	4.01	1373	2	1373	2		PbS, L4,4	L4,4, L4,5
b						773	21		PbS, L7,7	L7,7
15a	75.12	17.16	7.71	1373	2	1373	2		PbS	
b						773	28		PbS, L7,7	
16a	74.68	14.18	11.14	1373	2	1373	2		PbS,L4,4(tr),L7,7(tr)	PbS, L4,4, L7.7, L4.5
b						773	21		PbS, L7,7	PbS, L7,7

Table A1.1 cont.

Sample number	Composition			Heat treatments				observations	X-ray diffraction analysis	Electron diffraction analysis
				initial		final				
	PbS	Bi_2S_3	Ag_2S	temp	time	temp	time			
	[mole%]	[mole%]	[mole%]	[K]	[days]	[K]	[days]			
17a	65.03	33.57	1.40	1373	2	1373	2		L4,4, L7,7(tr)	L4,4, L7,7
b						773	21		L4,4	
18a	64.16	30.11	5.79	1373	2	1373	2		L4,4, L7,7	L4,4, L7,7, L4,7
b						773	28		L4,4	L4,4
21a	58.76	39.18	2.06	1373	2	773	14		L4,4, GB	L4,4, GB
b						973	14	needl.sep.	L4,4	L4,4
22	57.45	38.30	4.26	1373	2	773	14		L4,4, GB(tr)	L4,4, GB(tr)
23a	56.04	37.36	6.59	1373	2	773	14		L4,4	L4,4
b						973	14	needl.sep.	L4,4, L4,7, ?	
24a	54.55	36.36	9.09	1373	2	773	14		L4,4	L4,7, L4,4, L7,7
b						973	14	needl.sep.	L4,7, L4,4	L4,7, L4,4
25a	52.94	35.29	11.76	1373	2	773	14		L4,7, L7,7	L4,7, L7,7
b						973	14		L4,4, PbS, L4,7	
26a	51.22	34.15	14.63	1373	2	773	14		L8,8, PbS	L8,8, L7,8
b						973	14		L4,4, PbS, L4,7	L4,4, L4,7
27	49.37	32.91	17.72	1373	2	773	14		L8,8, PbS	
28	47.38	31.58	21.05	1373	2	773	14		PbS, L8,8(tr)	PbS, L8,8
29	45.21	30.14	24.66	1373	2	773	14		PbS	
30a	54.95	43.24	1.80	1373	2	1373	2		GB, L4,4	GB, L4,4, L4,5
b						773	21		GB, L4,4, ?	GB, L4,4, L7,7
31a	54.75	38.01	7.24	1373	2	1373	2		?	L4,4, L4,5, L4,7, GB
b						773	28		L4,4, L4,7, ?	L4,4, L4,7, GB
32a	56.14	31.58	12.28	1373	2	1373	2		?	L7,7, L8,8, L4,7, L4,5
b						773	21		L7,7	L7,7
34	48.7	51.30	-	1373	2	973	7		GB	GB
35	47.60	32.50	19.80	1373	2	773	7		PbS, L8,8	PbS, L8,8
36a	48.60	26.20	25.20	1373	2	1373	2		PbS	PbS
b						773	21		PbS	PbS
37	47.00	38.20	14.70	1373	2	773	7		L8,8, ?	L8,8, L4,8, L4,5, L7,8
38	47.60	35.70	16.70	1373	2	773	7		L8,8, PbS	
39	35.30	44.00	20.60	1373	2	773	7		L8,8, PbS(tr), ?	L8,8, L4,8, L4,5

Appendix 2

Geometry of the lillianite homologues

The geometry of the structure of the lillianite homologs, LN_1,N_2, can be used to find the values of N_1 and N_2 if $\underline{a}$, $\underline{b}$, γ and N_1+N_2 are known, (Makovicky and Karup-Møller, 1977a). The width of an octahedron in a galena-like slab, w, satisfies the relationship:

$$w = \left\{\frac{1}{18}\, a\, [a + (\frac{a^2-b^2}{q^2})^{1/2}]\right\}^{1/2} \qquad (A2.1)$$

where $q = \frac{N+2}{3}$, $N = (N_1 + N_2)/2$, and $\underline{a}$, $\underline{b}$ and γ are the unit cell parameters.

The angle γ between $\underline{a}$ and $\underline{b}$, see Fig. A2.1, can be calculated as:

$$\gamma = 90^{o} + \arcsin \frac{(N_1-N_2)w \cos\varepsilon - ka}{b} \qquad (A2.2)$$

where $\cos\varepsilon = 3w/a$, k is an integer such that $|(N_1-N_2)w \cos\varepsilon - ka|$ reaches its minimum value.

Comparison of calculated and measured γ, shown in Table A1, enables one to find values of N_1 and N_2.

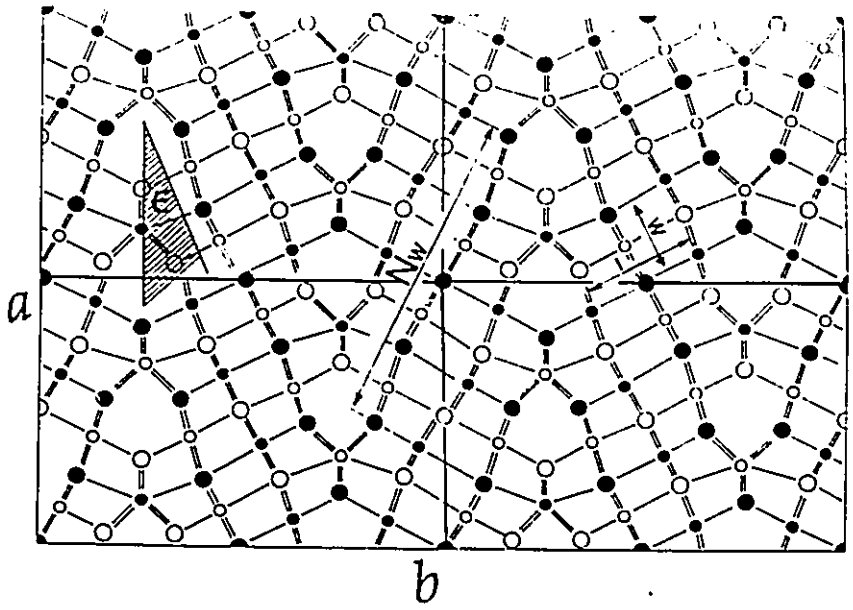

Fig. A2.1: Geometry of L4,4. w and l are 'width' and 'length' of a projected octahedron; N is the number of octahedra per slab counted in the indicated direction in the chain, ε is the angle between a and the direction of the unit chain. (after Makovicky, 1977b).

Table A2.1: Comparison of calculated and measured γ for different LN_1,N_2 homologs.

$N=N_1+N_2$ observed	Reflection corresp to $311_{(PbS)}$			Phase	Lattice parameters (Å)	Possible N_1,N_2	γ_{cal} (deg)	γ_{obs} (deg)
8	0	12	0	L4,4	a=13.54[a] b=20.65	4,4	90.0	90.0[a]
						3,5	107.2	
						2,6	93.7	
						1,7	103.4	
						0,8	97.4	
9	0	13	0	L4,5	a=13.3[b] b=21.4	4,5	99.9	99.5[b]
						3,6	95.9	
						2,7	104.1	
						1,8	91.9	
						0,9	107.9	
11	0	15	0	L4,7	a=13.46 b=25.66	5,6	98.3	
						4,7	95.3	95.55[c] 95.5[a]
						3,8	101.3	
						2,9	92.4	
						1,0	104.3	
						0,11	90.6	
12	0	16	0	L4,8	a=13.35[c] b=26.54	6,6	90.0	
						5,7	102.9	
						4,8	93.2	92.77[c] 92.5[a]
						3,9	99.7	
						2,10	96.4	
						1,11	96.4	
						0,12	96.6	

Table A2.1: cont.

$N=N_1+N_2$ observed	Reflection corresponding to $311_{(PbS)}$	Phase	Lattice parameters (Å)	Possible N_1,N_2	γ_{cal} (deg)	γ_{obs} (deg)
14	0 18 0	L7,7	a=13.67[a] b=31.37	7,7	90.0	90.0[a]
				6,8	101.4	
			a=13.459[c] b=30.194	5,9	92.4	93.35[c]
				4,10	98.9	
				3,11	94.8	
				2,12	96.5	
				1,13	97.2	
				0,14	94.1	
15	0 19 0	L7,8	a=13.5[b] b=32.3	7,8	96.7	95.5[b]
				6,9	94.1	
				5,10	99.2	
				4,11	91.6	
				3,12	101.8	
				2,13	90.9	
				1,14	99.9	
				0,15	93.5	
16	0 20 0	L8,8	a=13.7[a] b=33.05	8,8	90.0	90.0[a]
				7,9	100.4	
				6,10	92.9	
				5,11	97.5	
				4,12	95.7	
				3,13	94.6	
				2,14	98.6	
				1,15	91.7	
				0,16	101.5	

[a]-powder X-ray diffraction, present study
[b]-electron diffracion, present study
[c]-powder X-ray diffraction, Makovicky (1977b)

Appendix 3

Table A3.1: Indexed X-ray powder diffraction pattern of vikingite, L4,7. a = 13.461(3)Å, b = 25.664(4)Å, c = 4.105(1)Å, γ = 95.57(2)°.

No.	h	k	l	d_{obs}	$\sin^2\theta_{obs}$	$\sin^2\theta_{calc}$	$\delta*10^{-4}$	I_{obs}
1.	0	0	3	8.46485	0.008280	0.008184	0.96	vw
2.	2	0	0	6.68399	0.013280	0.013221	0.59	vw
3.	2	0	4	4.40686	0.030550	0.030620	0.88	vw
4.	0	0	6	4.25173	0.032820	0.032737	0.83	vw
5.	0	1	1	4.04446	0.036270	0.036118	1.52	vw
6.	1	1	1	3.87557	0.039500	0.039760	-2.59	vw
7.	-2	0	6	3.75578	0.042060	0.041921	1.39	ms
8.	1	1	2	3.72056	0.042860	0.042825	0.35	w
9.	0	0	7	3.66042	0.044280	0.044559	-2.79	vw
10.	-1	1	3	3.60213	0.045720	0.045689	0.31	w
11.	1	1	3	3.52233	0.047820	0.047708	1.12	ms
12.	2	0	6	3.43099	0.050400	0.049996	4.04	s
13.	-1	1	4	3.38692	0.051720	0.051718	0.02	s
14.	-2	0	7	3.33728	0.053270	0.053070	2.00	s
15.	1	1	4	3.29578	0.054620	0.054409	2.11	w
16.	-4	0	3	3.23562	0.056670	0.057031	-3.61	vw
17.	1	1	5	3.06780	0.063040	0.062931	1.09	vw
	-3	1	1			0.064856	1.34	
18.	3	1	0	3.02142	0.064990	0.064956	0.34	vw
19.	-2	0	8	2.99890	0.065970	0.066037	-0.67	sd
20.	-3	1	2	2.98759	0.066470	0.066575	-1.05	msd
21.	-3	1	3	2.91171	0.069980	0.070112	-1.32	msd
22.	3	1	2	2.91150	0.070490	0.070612	-1.22	sd
23.	-3	1	4	2.80510	0.075400	0.075469	-0.69	w
24.	3	1	3	2.79530	0.075930	0.076168	-2.38	vwd
25.	-4	0	6	2.77131	0.077250	0.077130	1.20	vwd
26.	-2	0	9	2.70623	0.081010	0.080824	1.86	w
27.	0	0	-11	2.32706	0.109560	0.110033	-4.73	w
	-1	1	9			0.109144	4.16	
28.	-2	0	11	2.26301	0.115850	0.115853	-0.03	w
29.	-1	1	10	2.16788	0.126240	0.126146	0.94	msd

Table A3.1 cont.

No.	h	k	l	d_{obs}	$\sin^2\theta_{obs}$	$\sin^2\theta_{calc}$	$\delta*10^{-4}$	I_{obs}
30.	2	0	11	2.13172	0.130560	0.130656	-0.96	w
31.	-6	0	5	2.12352	0.131570	0.131629	-0.59	w
32.	6	0	3	2.11001	0.133260	0.133228	0.32	ms
33.	5	1	4	2.07068	0.138370	0.138292	0.78	w
34.	-6	0	6	2.06051	0.139740	0.139613	1.27	ms
35.	-5	1	6	2.05544	0.140430	0.140483	-0.53	ms
36.	1	1	-11	2.02063	0.145310	0.144846	4.64	w
37.	-3	0	12	1.99894	0.148480	0.148451	0.29	w
38.	-5	1	7	1.98945	0.149900	0.150622	-7.22	w
39.	0	0	-13	1.96849	0.153110	0.153683	-5.73	vw
40.	-2	2	1	1.95708	0.154900	0.154290	6.10	w
41.	2	2	3	1.89987	0.164370	0.164260	1.10	w
42.	4	0	-12	1.88717	0.166590	0.167683	-10.93	vw
43.	-2	2	5	1.85016	0.173320	0.173426	-1.05	vw
44.	-6	0	9	1.84016	0.175210	0.174479	7.31	vw
45.	-2	0	14	1.80521	0.182060	0.182037	0.23	vw
46.	-4	0	13	1.77161	0.189030	0.189072	-0.42	wd
47.	2	2	6	1.76255	0.190980	0.191055	-0.75	wd
48.	4	2	0	1.75004	0.193720	0.193719	0.01	msd

Appendix 4

Table A4.1: Indexed X-ray powder diffraction pattern of L8,8.

a = 13.565(4)Å, b = 33.046(7)Å, c = 4.102(2)Å.

No.	h	k	l	d_{obs}	$\sin^2\theta_{obs}$	$\sin^2\theta_{calc}$	$\delta*10^{-4}$	I_{obs}
1.	2	6	0	4.35096	0.031340	0.032455	-11.15	vw
2.	1	0	1	3.91694	0.038670	0.038479	1.91	vw
3.	1	2	1	3.81240	0.040820	0.040652	1.68	vw
4.	1	3	1	3.60350	0.045690	0.043369	23.21	ms
5.	1	4	1	3.55481	0.046950	0.047172	-2.22	w
6.	4	0	0	3.39481	0.051480	0.051589	-1.09	vs
7.	4	1	0	3.35879	0.052590	0.052133	4.57	s
8.	0	10	0	3.30305	0.054380	0.054328	0.52	vs
9.	2	9	0	3.22257	0.057130	0.056903	2.27	msd
10.	3	0	1	3.04375	0.064040	0.064274	-2.34	msd
11.	3	2	1	2.98132	0.066750	0.066447	3.03	w
12.	3	3	1	2.92406	0.069390	0.069163	2.27	vs
13.	3	4	1	2.85378	0.072850	0.072966	-1.16	vs
14.	1	8	1	2.81859	0.074680	0.073249	14.31	s
15.	3	5	1	2.76523	0.077590	0.077856	2.66	w
16.	3	6	1	2.66894	0.083290	0.083832	-5.42	vw
17.	4	8	0	2.62122	0.086350	0.086359	-0.09	vw
18.	6	4	0	2.17992	0.124850	0.124768	0.82	msd
19.	2	15	0	2.09443	0.135250	0.135135	1.15	msd
20.	0	16	0	2.06829	0.138690	0.139080	-3.90	msd
21.	5	7	1	2.04297	0.142150	0.142484	-3.34	vsd
22.	0	4	2	1.99058	0.149730	0.149712	0.18	msd
23.	1	4	2	1.96605	0.153490	0.152936	5.54	vwd
24.	1	6	2	1.89520	0.165180	0.163802	13.78	wd
25.	1	9	2	1.77831	0.187610	0.188250	-6.40	wd
26.	4	16	0	1.76546	0.190350	0.190669	-3.19	wd
27.	6	12	0	1.74572	0.194680	0.194308	3.72	wd
28.	3	7	2	1.73956	0.196060	0.196659	-5.99	vsd
29.	1	10	2	1.72476	0.199440	0.198572	8.68	wd
30.	3	16	1	1.70772	0.203354	0.203354	0.86	vwd
31.	3	8	2	1.69765	0.205860	0.204809	10.51	vwd
32.	3	9	2	1.66669	0.213580	0.214044	-4.64	wd
33.	8	4	0	1.65404	0.216860	0.215049	18.11	wd